TECHNISCHE UNIVERSITÄT MÜNCHEN

Lehrstuhl für Flugsystemdynamik

Model-Based Quantification of Accident Probabilities from Operational Flight Data

Chong Wang, M. Sc.

Vollständiger Abdruck der von der Fakultät für Maschinenwesen der Technischen Universität München zur Erlangung des akademischen Grades eines

Doktor-Ingenieurs

genehmigten Dissertation.

Vorsitzender: Prof. Dr. phil. Klaus Bengler

Prüfer der Dissertation:
1. Prof. Dr.-Ing. Florian Holzapfel
2. Prof. Dr.-Ing. Mirko Hornung

Die Dissertation wurde am 14.02.2019 bei der Technischen Universität München eingereicht und durch die Fakultät für Maschinenwesen am 05.07.2019 angenommen.

Abstract

This thesis presents novel methods to quantify the occurrence probabilities for given accidents within the flight operations of an airline. As the number of accidents in commercial aviation has significantly decreased during the last decades while the amount of traffic has undergone tremendous growth, further improvement in operational safety has to be *predictive*. It cannot be based on changes implemented after an accident investigation simply due to the lack of accident data. Instead, hazards have to be identified well before they impact the flight operations, or even before they arise. The quantification of accident probabilities constitutes a part of this predictive component. It is an important task of any airline's Safety Management System in order to set safety targets, to benchmark with industry standards or competitors and ultimately to improve the level of safety.

This presented approach uses data that has previously been recorded on-board each aircraft within the scope of the airline's Flight Data Monitoring program. Even though the data does not contain any accident, it records deviations from nominal values – but still well within the allowed ranges – of single factors that have an influence on the outcome of potential accidents, which occurs frequently on each flight. The relationship between these so-called *contributing factors* is established by a model incorporating the behavior of the aircraft. The task is to quantify when the deviation of several factors combined will lead to an accident and how likely this is.

The presented model is dedicated to the landing phase of the flight. It includes an extensive representation of the landing gear to simulate the braking and steering on the ground. Furthermore, it includes system logics of the aircraft concerning the activation of deceleration devices, such as ground spoilers and thrust reverse. The focus of the model is the accident type of *runway excursion*, which includes the aircraft unintentionally leaving the runway off the far end (overrun) and to the side (veer-off).

For the quantification of the accident probabilities using recorded flight data based on the aircraft model, the method of *Subset Simulation* is used. It is particularly suitable for quantifying small probabilities with low computational effort. Based on the results obtained for landings at Munich airport, a thorough analysis of the contributing factors is performed and some hazards are identified.

Kurzfassung

Die vorliegende Arbeit stellt neuartige Methoden vor, um die Eintrittswahrscheinlichkeiten für bestimmte Unfälle im Flugbetrieb von Fluggesellschaften zu quantifizieren. Da die Anzahl der Unfälle in der kommerziellen Luftfahrt über die letzten Jahrzehnte gesunken ist und gleichzeitig der Verkehr jedoch stark zugenommen hat, müssen weitere Verbesserungen in der operationellen Sicherheit *prädiktiv* sein. Sie können nicht weiterhin primär aus Veränderungen bestehen, die aus Unfalluntersuchungen abgeleitet werden, da kaum Unfalldaten zur Verfügung stehen. Stattdessen müssen Gefahren erkannt werden, bevor sie sich auf den Flugbetrieb auswirken oder sogar schon bevor sie entstehen. Die Quantifizierung von Unfallwahrscheinlichkeiten ist ein Teil dieser prädiktiven Komponente. Sie ist eine wichtige Aufgabe innerhalb des Sicherheitsmanagementsystems jeder Fluggesellschaft, um Sicherheitsziele zu setzen, sich mit Branchenstandards oder Konkurrenten zu vergleichen und letztendlich, um das Sicherheitsniveau zu verbessern.

Das präsentierte Vorgehen verwendet Daten, die zuvor an Bord jedes Flugzeugs im Rahmen des Flight Data Monitoring-Programms der Fluggesellschaft aufgezeichnet worden sind. Obwohl sie keine Unfälle enthalten, zeichnen sie Abweichungen einzelner Faktoren von ihrem Nominalbereich auf, auch wenn sie sich nach wie vor im erlaubten Bereich befinden. Dies tritt auf jedem Flug häufig auf. Die Beziehung zwischen diesen sogenannten *beitragenden Faktoren* wird durch ein Modell hergestellt, welches das Verhalten des Flugzeuges widerspiegelt. Die Aufgabe besteht nun darin, zu ermitteln, wann die Abweichungen mehrerer Faktoren kombiniert zu einem Unfall führen und wie wahrscheinlich dies ist.

Das vorgestellte Model ist auf die Landephase des Fluges zugeschnitten. Es beinhaltet eine ausführliche Beschreibung des Fahrwerks, um das Brems- und Lenkverhalten am Boden abzubilden. Darüber hinaus berücksichtigt es Systemlogiken des Flugzeugs im Hinblick auf die Aktivierung von Verzögerungsvorrichtungen wie Störklappen oder Schubumkehr. Der Fokus des Modells ist der Unfalltyp *Runway Excursion*, dieser beinhaltet sowohl das Überschießen am Ende (Overrun) als auch das seitliche Verlassen (Veer-Off) der Landebahn.

Um die Quantifizierung von Unfallwahrscheinlichkeiten mithilfe von aufgezeichneten

Flugdaten basierend auf dem Flugzeugmodell durchführen zu können, wird die Methode *Subset Simulation* verwendet. Diese ist inbesondere für kleine Wahrscheinlichkeiten geeignet und ermöglicht niedrigen Rechenaufwand. Auf Basis von Ergebnissen für Landungen auf dem Flughafen München wird eine detailierte Analyse der beitragenden Faktoren durchgeführt und es werden einige Gefahren identifiziert.

Danksagung / Acknowledgments

Diese Arbeit entstand im Rahmen meiner Tätigkeit als wissenschaftlicher Mitarbeiter am Lehrstuhl für Flugsystemdynamik der Technischen Universität München, daher geht mein größter Dank an den Ordinarius, *Prof. Florian Holzapfel* für die Themenstellung, die fachliche Betreuung und das große Vertrauen. *Prof. Mirko Hornung* danke ich für die Erstellung des Zweitgutachtens und *Prof. Klaus Bengler* für die Übernahme des Prüfungsvorsitzes.

Die Fragestellung zum Thema Flugsicherheit, mit der sich diese Arbeit auseinandersetzt, entstand aus der Praxis und so muss auch die Lösung praxisorientiert sein, daher möchte ich den Industriepartnern herzlich danken. Insbesondere geht der Dank an *Manfred Müller* und *Carsten Schmidt-Moll* für die vielen Ratschläge und die intensiven Einblicke in den Flugbetrieb, die diese Arbeit maßgeblich motiviert und beeinflusst haben. *Nils Mohr* danke ich für die vielen fruchtbaren Diskussionen rund um das Thema Flugdaten, die ohne seine große Expertise unmöglich gewesen wären.

Ferner möchte ich meinen Kollegen am Lehrstuhl für Flugsystemdynamik danken, insbesondere *Monica Kleinoth-Gross* für die immerwährende Unterstützung. Den Kollegen aus der Flugsicherheitsgruppe, *Ludwig Drees*, *Javensius Sembiring*, *Lukas Höhndorf*, *Phillip Koppitz*, *Serçin Höhndorf*, *Xiaolong Wang*, *Florian Schwaiger*, *Lukas Beller* und *Stefan Schiele* danke ich für die wunderbare Zusammenarbeit in den vielen Jahren, für die vielen intensiven Gespräche, auch und gerade für die Meinungsverschiedenheiten, für die gegenseitige Unterstützung und für die Zuversicht, mit unserer Arbeit das Fliegen ein Stück sicherer gemacht zu haben. Den Kollegen *Andreas Jaroš*, *Christoph Krause*, *Christoph Göttlicher*, *Markus Hochstrasser*, *Martin E. Kügler*, *Kevin Schmiechen*, *David Löbl*, *Christopher Blum* und *Andreas Kleser* danke ich für die vielen intensiven und erkenntnisreichen fachlichen Diskussionen.

Thanks to *Lisa Nold* for proofreading this thesis and providing me valuable comments as a native speaker.

Ohne meine Familie, meine Mutter *Xia Xu*, meinen Vater *Ximing Wang* und meine Schwester *Jing Wang* und deren großartige Unterstützung und Motivation in all den Jahren wäre diese Arbeit nie entstanden. Danke, dass ihr mich ausgehalten habt.

Table of Contents

List of Figures

List of Tables

Acronyms

A/C	Aircraft
ABS	Anti-Lock Braking System
AC	Airworthiness Certificate
ACMS	Aircraft Condition Monitoring System
ADREP	Accident Reporting System
ADS-B	Automatic Dependence Surveillance - Broadcast
AGC	Airport Ground Chart
AGL	Above Ground Level
AIP	Aeronautical Information Publication
ALoSP	Acceptable Level of Safety Performance
AMC	Acceptable Means of Compliance
ANSP	Air Navigation Service Provider
AOC	Air Operator Certificate
AOG	Aircraft on-Ground
APU	Auxilliary Power Unit
ARC	Abnormal Runway Contact
ARINC	Aeronautical Radio Incorporated
ASCII	American Standard Code for Information Interchange
ASD	Accelerate-Stop Distance
ASIAS	Aviation Safety Information Analysis and Sharing
ATC	Air Traffic Control
ATCo	Air Traffic Controller
ATOL	Automatic Take-off and Landing
ATR	Avions de Transport Régional
BCD	Binary Coded Decimal
BCU	Braking Control Unit
BEA	Bureau d'Enquêtes et d'Analyses pour la Sécurité de l'Aviation Civile
BSCU	Braking Steering Control Unit
BTV	Brake To Vacate
c.o.v.	Coefficient of Variation
CAMO	Continuing Airworthiness Management Organization

CAS	Calibrated Airspeed
CATS	Causal Model of Air Transport Safety
CB	Cumulonimbus Clouds
CFIT	Controlled Flight Into Terrain
CG	Center of Gravity
CHQ/LGSA	Chania International Airport
CSV	Comma Separated Values
CVR	Cockpit Voice Recorder
DAR	Digital ACMS Recorder
DDM	Difference in Depth of Modulation
DFDR	Digital Flight Data Recorder
DFL	Dataframe Layout
DoF	Degree of Freedom
EAFR	Enhanced Airborne Flight Recorder
EASA	European Aviation Safety Agency
EBT	Evidence-Based Training
ECAM	Electronic Centralized Aircraft Monitoring
EFB	Electronic Flight Bag
EICAS	Engine Indication and Crew Alerting System
ELT	Emergency Location Transmitter
EPR	Engine Pressure Ratio
EU	European Union
FAA	Federal Aviation Administration
FADEC	Full Authority Digital Engine Control
FBW	Fly-By-Wire
FCOM	Flight Crew Operating Manual
FDAU	Flight Data Acquisition Unit
FDIMU	Flight Data Interface Management Unit
FDIU	Flight Data Interface Unit
FDM	Flight Data Monitoring
FDR	Flight Data Recorder
FEM	Finite Element Method
FH	Flight Hour
FHA	Functional Hazard Analysis
FL	Flight Level
FMEA	Failure Mode and Effects Analysis
FMS	Flight Management System
FOD	Foreign Object Damage
FODA	Flight Operations Data Analysis
FOQA	Flight Operations Quality Assurance

FSD	Institute of Flight System Dynamics
FSS	Future Sky Safety
FTA	Fault Tree Analysis
GEV	Generalized Extreme Value
GNSS	Global Navigation Satellite System
GPS	Global Positioning System
GS	Groundspeed
HAJ/EDDV	Hanover Airport
HIRO	High Intensity Runway Operation
IAE	International Aero Engines
IAS	Indicated Airspeed
IATA	International Air Transport Association
ICAO	International Civil Aviation Organization
ICDF	Inverse Cumulative Distribution Function
ILS	Instrument Landing System
IRS	Inertial Reference System
ISA	International Standard Atmosphere
ISD	Importance Sampling Density
KDE	Kernel Density Estimation
LD	Landing Distance
LDA	Landing Distance Available
LDR	Landing Distance Required
LFE	Chair of Ergonomics
LGCIS	Landing Gear Control and Indication System
LHR/EGLL	London Heathrow Airport
LOC-I	Loss of Control In-Flight
MAC	Mid-Air Collision
MAC	Mean Aerodynamic Chord
MAD/LEMD	Madrid Barajas Airport
MCMC	Markov Chain Monte Carlo
MCS	Monte Carlo Simulation
MCTOM	Maximum Certified Take-off Mass
MEL	Minimum Equipment List
METAR	Meteorological Aerodrome Report
MH	Metropolis-Hastings
MLM	Maximum Landing Mass
MRO	Maintenance, Repair and Overhaul
MSL	Mean Sea Level
MTOM	Maximum Take-off Mass
MUC/EDDM	Munich Airport

NED	North-East-Down
NLR	Netherlands Aerospace Center
NRMSE	Normalized Root Mean Square Error
NUE/EDDN	Nuremberg Airport
OEM	Original Equipment Manufacturer
OM	Operations Manual
OWE	Operating Weight Empty
PA	Predictive Analysis
PCMCIA	Personal Computer Memory Card International Association
PDF	Probability Density Function
PIC	Pilot in Command
PTF	Permit To Fly
PTU	Power Transfer Unit
QAR	Quick Access Recorder
RA	Resolution Advisory
RE	Runway Excursion
RMSE	Root Mean Square Error
ROP	Runway Overrun Protection
ROPS	Runway Overrun Protection System
ROW	Runway Overrun Warning
RPAS	Remotely Piloted Aircraft System
RTO	Rejected Take-off
RTS	Rauch-Tung-Striebel
SaMSys	Safety Management System zur Verbesserung der betrieblichen Flugsicherheit
SD	Secured Digital
SMS	Safety Management System
SOP	Standard Operating Procedure
SPI	Safety Performance Indicator
SSP	State Safety Program
TA	Traffic Advisory
TAS	True Airspeed
TC	Type Certificate
TCAS	Traffic Alert and Collision Avoidance System
TUM	Technical University of Munich
UAV	Unmanned Aerial Vehicle
US	United States
VIE/LOWW	Vienna Schwechat Airport
VLC/LEVC	Valencia Airport
WAW/LPWA	Warsaw Frederic Chopin Airport

WOW	Weight on Wheel
ZFTT	Zero Flight Time Training

Symbols and Indices

Symbols

a	Acceleration
B	Pacejka coefficient
$\mathcal{Be}$	Beta distribution
b	Wingspan
C	Capacity of a system
C	Pacejka coefficient
C_D	Drag coefficient
C_L	Lift coefficient
C_l	Roll moment coefficient
C_m	Pitch moment coefficient
C_n	Yaw moment coefficient
C_Q	Side force coefficient
$\bar{c}$	Mean aerodynamic chord
D	Demand from a system
D	Aerodynamic drag
D	Pacejka coefficient
d	Damping constant
E	Pacejka coefficient
$\mathrm{E}[\cdot]$	Expected value
$\vec{\boldsymbol{e}}$	Unit vector
$\vec{\boldsymbol{F}}$	Force vector
$f(\boldsymbol{\theta})$	Importance sampling density
g_0	Earth's gravitational constant
h	Altitude
h_R	Runway height
$I(\boldsymbol{\theta})$	Indicator function of failure for the sample $\boldsymbol{\theta}$
$\boldsymbol{I}$	Moment of inertia tensor
J	Moment of inertia
k	Drag polar coefficient
k	Spring constant
k	Controller gain
L	Aerodynamic lift
L	Aerodynamic roll moment
l	Length of the landing gear
l_0	Length of the landing gear in uncompressed state
$\boldsymbol{M}_{AB}$	Transformation matrix from B frame to A frame
$\vec{\boldsymbol{M}}$	Moment vector
M	Aerodynamic pitch moment
m	Mass
m	Number of subsets in the Subset Simulation run
N	Total number of samples
N	Aerodynamic yaw moment
N_C	Number of Markov chains
N_S	Number of samples per Markov chain
$\mathcal{N}$	Normal distribution
n	Number of contributing factors for the problem
$\vec{n}$	Normal vector
p	Probability
p	Roll angular rate
p	Air pressure
p_0	Conditional probability for Subset Simulation
p^*	Proposal distribution
Q	Aerodynamic side force

q	Pitch angular rate
$q(\boldsymbol{\theta})$	Probability density function of $\boldsymbol{\theta}$
$\mathbb{R}$	Set of real numbers
R	Gas constant
r	Yaw angular rate
$\vec{\boldsymbol{r}}$	Position vector
$r(\boldsymbol{\theta})$	Probability of failure for a given sample $\boldsymbol{\theta}$
r_T	Tire radius
S	Wing reference area
s	Tire slip
s	Acceptance ratio for the MCMC algorithm
T	Air temperature
t	Time variable
$\boldsymbol{u}$	Control variables
$\vec{\boldsymbol{V}}$	Velocity vector
V	Velocity
$\boldsymbol{x}$	State variables
x	Coordinate
y	Coordinate
z	Coordinate
α	Angle of attack
α	Confidence level
β	Angle of sideslip
γ_{Tr}	Temperature gradient in the troposphere
δ_B	Brake pedal deflection angle
ζ	Rudder deflection angle
ζ_L	Nose landing gear deflection angle
η	Elevator deflection angle
Θ	Pitch angle
$\boldsymbol{\Theta}$	Parameter random variable
$\boldsymbol{\theta}$	Parameter vector
κ	Engine mounting yaw angle
μ	Expected value / mean
μ	Friction coefficient
ξ	Aileron deflection angle
$\boldsymbol{\xi}$	Sample candidate generated during MCMC
ρ	Air density
σ	Standard deviation
σ	Engine mounting pitch angle
Φ	Bank angle
χ	Course angle
Ψ	Heading / azimuth angle
$\vec{\boldsymbol{\omega}}$	Angular velocity vector

Indices, Subscripts and Superscripts

0	Aerodynamic zero coefficient
A	Aerodynamic frame
A	Aerodynamic force
B	Body-fixed frame
B	Braking
cmd	Commanded value
E	Earth-centered-earth-fixed frame
G	Gravitation force
G	Center of gravity
GS	Groundspeed
F	Failure
I	Earth-centered-inertia frame
$\bar{K}$	Kinematic frame rotated by the kinematic bank angle around the kinematic x axis
L	Landing gear force
max	Maximum value
min	Minimum value
N	Local navigation frame
A	Aerodynamic frame
O	North-east-down frame
opt	Optimum value
P	Propulsion force

R	Aircraft reference point
R	Runway
ref	Reference value
S	Reference value at mean sea level
T	Tire coordinate frame
T	Total force
T	Tangential
W	Wind
$\parallel$	Parallel
$\perp$	Perpendicular
$\tilde{\cdot}$	Estimated value

1

Introduction

1.1 Background

Safety has always been of vital concern since the beginning of aviation. After their successful first flight in 1903, the Wright brothers were also involved in the very first fatal accident in aviation, which occurred in 1908 [Bau06]. While Orville Wright, who was the pilot, suffered severe injuries, Thomas Selfridge, who was a passenger onboard, became the very first fatality in aviation history. Since then and particularly with the beginning of commercial aviation after World War II, safety has significantly increased while the amount of traffic underwent tremendous growth at the same time. Chesley B. Sullenberger was the Pilot in Command (PIC) who performed the successful water landing with an Airbus A320 on the Hudson River in New York in 2009. He stated in an interview [Gam10] that "*... out of a 43-year career, my entire life is being judged on the basis of those 3 minutes and 28 seconds.*" This clearly shows how rarely pilots actually have to face emergency situations they train for throughout their professional life. In fact, many commercial pilots nowadays have an entire career of flying without encountering any serious event. Most hazardous situations, such as engine failures, are only known to pilots from recurrent simulator training.

Safety is of utmost significance across all aviation stakeholders. The process of obtaining an Airworthiness Certificate (AC) for an aeroplane is thoroughly regulated and mainly driven by safety considerations, which is referred to as the *Initial Airworthiness*. During the certification process, the Original Equipment Manufacturer (OEM) has to prove that certain levels of safety for all technical systems affecting the airworthiness of the aircraft are achieved. For large transport categories aeroplanes certified by the European Aviation Safety Agency (EASA), the minimum level of system reliability can be obtained from Book 2 of the CS-25 Certification Specifications [Eur18], namely in the Acceptable Means of Compliance (AMC) 25.1309. It highly depends on the con-

Severity	Qualitative Probability	Quantitative Probability per FH
No Safety Effect	N/A	N/A
Minor	Probable	$> 10^{-5}$
Major	Remote	$< 10^{-5}$
Hazardous	Extremely Remote	$< 10^{-7}$
Catastrophic	Extremely Improbable	$< 10^{-9}$

Table 1.1: *The allowed failure probabilities according to CS-25 [Eur18]*

sequence, i.e. the severity, of the respective system failure. Table 1.1 shows the corresponding acceptable failure probabilities depending on the severity of the respective failure condition.

For the most severe category, resulting in *catastrophic* consequences, which is defined as *multiple fatalities with the loss of the airplane*, the probability of failure must be 10^{-9} per Flight Hour (FH) or less. In addition, any single failure of an aircraft system must not lead to catastrophic consequences. This does not only apply to systems, but also to any hardware or software functions incorporated in the aircraft [Soc12]. These safety considerations will become clearly visible in chapter 7 where the implementations of some aircraft systems are described and discussed.

Typically, for aircraft types that are produced on a large scale, a Type Certificate (TC) is obtained for the aircraft type after certification using the prototypes that are built and flown based on a Permit To Fly (PTF). For all frames that are produced afterwards, it has to be proven that they are identical with the prototype that was certified for the TC in order to show the initial airworthiness of this particular newly-built aircraft frame. After an aircraft enters service, the airworthiness is maintained by complying, among all, to the Commission Regulation No 1321/2014 [Eur14], including its annexes, commonly referred to as *Part-M* and *Part-145*, which includes regulations about how maintenance work is to be performed. This is ensured by Continuing Airworthiness Management Organizations (CAMOs) that are also certified accordingly. The qualification of the flying personnel is regulated by Commission Regulation No 1178/2011 [Eur11b] as not only the equipment has to be airworthy, but also the crew operating it.

In contrast to obtaining initial airworthiness, there are no quantitative safety targets that the operator, along with other stakeholder involved in maintaining the continuing airworthiness, has to ensure once the aircraft enters service. The safety levels that are actually achieved for passengers in real-life flight operations are significantly lower than those shown in table 1.1 due to the environmental and operational conditions encountered during everyday flying. They are influenced by weather, traffic situation as well as pilot performance, including human errors.

While no regulatory level of operational safety exists, aviation stakeholders, such as airlines, Air Navigation Service Providers (ANSPs) and airports are obliged to define

an *Acceptable Level of Safety Performance (ALoSP)* as the safety target for their individual organization. This is guided by the International Civil Aviation Organization (ICAO) Safety Management Manual [Int13]. Especially the ALoSP expressed as a probability of suffering from an accident should be clearly set out by the organization.

The ICAO provides a crucial definition for the term *accident* [Int16]:

An occurrence associated with the operation of an aircraft which [...] takes place between the time any person boards the aircraft with the intention of flight until such time as all such persons have disembarked [...], in which:

1. *a person is fatally or seriously injured as a result of*
    - *being in the aircraft, or*
    - *direct contact with any part of the aircraft, including parts which have become detached from the aircraft, or*
    - *direct exposure to jet blast, [...]*
2. *the aircraft sustains damage or structure failure which:*
    - *adversely affect the structural strength, performance or flight characteristics of the aircraft, and*
    - *would normally require major repair or replacement of the affected component, [...]*
3. *the aircraft is missing or is completely inaccessible*

(ICAO Annex 13 [Int16])

Safety targets can also be defined by regulatory bodies. The European Union (EU) defined a safety target for commercial aviation in *Flightpath 2050 – Europe's Vision for Aviation* [Eur11a] for the European air transport system to be less than 10^{-7} accident per flight. In addition, each sovereign country can set up an individual State Safety Program (SSP). The German airline *Lufthansa* has further specified this target for its own operations to be less than 10^{-8} hull losses per flight [Rap09]. For the entire Lufthansa Group, this would imply that, on average, one hull loss would occur every 100 years based on the current amount of traffic. This is a particularly challenging goal because it is already very close to the Airworthiness Certifications requirements of 10^{-9} per flight hour. One has to keep in mind that compliance with the requirements during certification are often demonstrated by performing theoretical analyses, such as Fault Tree Analysis (FTA) or Failure Mode and Effects Analysis (FMEA). The obtained numbers do not necessarily agree with the actual numbers measured after the certified aircraft enters service.

Essentially, the responsibility for safety is shifted from the regulators to the operators. While it used to be sufficient to be compliant to regulation, airlines nowadays must

set their own safety targets and implement measures to reach the targets, taking up all the responsibility if accidents occur, even if all regulatory requirements are met with respect to the initial and continued airworthiness. From the airline's perspective, suffering from an accident is not only costly as the premium that has to be paid by the airline will increase, although the insurance will cover the direct costs of the accident [vWC]. In addition, accidents also heavily draw negative public attention. Though the current safety level in aviation is already high, public acceptance for accidents have also remarkably decreased. Media coverage of accidents are intense, which puts massive pressure on airlines to avoid such negative publicity. Especially for airlines with financial struggles, an accident with intense media coverage could be one more nail in the coffin no matter what the actual causes of the accident are [Sch15]. Prominent examples include the bankruptcy of Swissair in 2001 after the crash of the MD-11 in 1998, the takeover of Trans World Airline by American Airlines in 2001 after the crash of the Boeing 747 in 1996 or most recently the takeover of Malaysia Airlines by the State of Malaysia after losing two aircraft in 2014. These examples clearly demonstrate the importance of safety and continued improvement of the level of safety for aircraft operators.

1.2 State of the Art and Motivation

1.2.1 Safety Measurement

According to the ICAO Safety Management Manual [Int13] and the respective authorities, each organization has to set up its own safety target, or ALoSP. However, setting the target is only the first task. In order to reach the target, it has to be made measurable using so-called Safety Performance Indicators (SPIs). This implies that one has to be able to obtain its current level of safety. While this seems to be a simple task, it comes along with many challenges.

The most straightforward way to measure safety – not just for aviation – is to count the number of accidents and divide it by a reference number representing the entire operation, which, in our case, is often either the total number of flights or flight hours.

$$\text{Safety Level} = \frac{\text{Number of accidents}}{\text{Entire operations}} \tag{1.1}$$

This method is commonly used for road traffic: The total number of accidents is divided by the total number of passengers, number of trips or the amount of passenger-kilometers. As aviation has already reached a very high level of safety, accident data is very limited simply because accidents rarely occur. The annual safety report pub-

lished by the International Air Transport Association (IATA) [Int17] shows that the accident rate for the entire commercial aviation industry dropped below 2×10^{-6} per flight with the rate of hull losses below 1×10^{-6} per flight in the year 2017. In total, there were 13 hull loss accidents and 19 accidents involving fatalities in 2017. For statistical analyses, these numbers are already too low to allow for valid statements. They certainly demonstrate the high safety standards in aviation, but make it difficult to actually quantify the safety level.

Additionally, as the safety level for an individual organization has to be obtained, one cannot simply use the data from other players or the competitors. Flight operations can be much different between operators due to many reasons:

Network structure: Different airlines have different route networks. Operations at some airports or in some airspaces are associated with higher risks than others due to factors such as weather, terrain or operational constraints. A large network carrier operating from big hubs cannot be compared with regional or commuter operators.

Operating procedures: Though some parts of the Operations Manual (OM) are defined by the aircraft manufacturer, the operator can customize the way its own aircraft are operated, particularly in Part A of the OM. A more detailed description of the OMs can be found in chapter 7.

Crew selection and training: The way the pilots are chosen vary significantly among the airlines. Some airlines allow ready-entries while some insist that every pilot is trained by the airline's own flying school from the beginning. Crew members who previously worked as military fighter pilots can significantly change the way to cope with emergency situations in the cockpit and the hierarchy between the crew members.

Equipment: Differences in aircraft types and on-board equipment that are operated also influences the safety level of each individual airline.

Obviously, when looking at an individual airline, the data becomes extremely rare as a single airline simply does not have enough hull losses to make reliable statistical statements with. If an airline does not have any hull loss accidents in the recent years or even during its entire time of operation, equation (1.1) to obtain the level of safety above would simply return the value zero. However, we know that, though the number is small, it cannot be zero. Quantifying this small number, based on the fact that no accident has occurred so far, now becomes a challenge to be tackled. That is the main goal of this work.

1.2.2 Safety Management

In the ICAO Safety Management Manual [Int13], safety is defined as "*the state in which the possibility of harm to persons or of property damage is reduced to, and maintained at or below, an acceptable level through a continuing process of hazard identification and safety risk management*". Risk is defined as "*The predicted probability and severity of the consequences or outcomes of a hazard"* [Int13]. This means that risk is always a combination of how likely something is going to happen and how severe the consequences are. To be safe, or to be in the state of safety, risks have to be reduced below a level that is acceptable. To achieve this, safety has to be managed. The same ICAO document also serves as guidance material to set up a Safety Management System (SMS) within an aviation organization.

Safety management can be classified to three different categories. While **reactive** methods look at past accidents in order to prevent similar events from happening again, **proactive** methods examine the current situation in order to identify existing hazards in today's flight operations. **Predictive** methods, in contrast, look at the future in order to initiate risk mitigation actions before future hazards will begin to impose threats.

Today, safety management mostly incorporates reactive and proactive tools. As a reactive method, accident investigation is conducted on a routine basis involving a number of parties. The way to conduct accident investigation is thoroughly guided by the *Annex 13 to the Convention on International Civil Aviation* [Int16] as well as the ICAO's *Manual of Aircraft Accident and Incident Investigation* (Doc 9756) [Int15]. The improvement of aviation safety during the last decades has been significantly credited to the thorough and extensive investigations after every accident. Many additional safety features, whether technical, procedural or organizational, have been introduced after concluding the investigation of an accident and the identification of the factors contributing to it. However, the drawback of these methods is that they rely on accidents occurring in order to implement reacting procedures to prevent similar accidents from happening again in the future. As aviation becomes safer, fewer accidents occur and the chains of events leading to up to the accident have become very individual. As a result, these methods are becoming increasingly ineffective to further improve the level of safety.

Several models to determine the operational safety are already used today. The Causal Model of Air Transport Safety (CATS) [RvS+08] is well-known as well as the Bow-Tie model: both are used in operational safety management today. However, those two approaches require data of accidents to be available or at least known relationships in the causal chain of events that ultimately lead to an accident, which is, only reactive or proactive. This is also true of the *Swiss Cheese Model* developed by Reason [Rea00] to examine human errors. However, the goal has shifted from just knowing how an

accident happened towards preventing an accident from happening beforehand.

Other methods to quantify the safety level include many that are mostly used during the airworthiness certification process as they are explicitly listed as AMCs by the authorities, including FTA, Functional Hazard Analysis (FHA) and FMEA [Soc96].

In current SMSs, data is an essential enabler. Many data sources are available to the airline. One of the most important of them is the Flight Data Monitoring (FDM) system, also known as Flight Operations Quality Assurance (FOQA). Besides the well known Flight Data Recorder (FDR), a second recorder is installed on-board, the Quick Access Recorder (QAR) is routinely read out and the data is monitored. Some differences between the FDR and the QAR include the fact that the QAR is not protected against crash impacts and that the QAR, just as the name implies, can be easily read out. The data is either stored on a SD card, which can be easily removed, or it can be transferred via a Wi-Fi network at the gate or even using the 4G – possibly 5G in the future – mobile network to the airline's IT system. Besides, the data recorded on the QAR can be individually configured by the airline whereas the parameters recorded by the FDR are defined by legislation. FDM using either QAR or FDR data is common industry standard for commercial aircraft and even mandatory for all aircraft in the EU with a Maximum Certified Take-off Mass (MCTOM) of $27\,000\,\mathrm{kg}$ or more according to EU legislation [Eur08a]. As a standard approach in FDM, certain parameters are compared to given threshold values to detect violations. One example is the deviation on the Instrument Landing System (ILS) localizer and glideslope during the approach. A too high deviation, whatever the exact value is defined to according to the airline, indicates a more risky approach. The exceedance will, therefore, trigger a warning in the FDM system. Other common activities within FDM include flight path reconstruction, providing feedback to pilots whenever requested or benchmarking with other operators.

The capabilities of FDM, however, are not unlimited. Though the recordings include a large variety of parameters, the sampling rate as well as the resolution are somewhat limited, depending on the aircraft type. This is a challenge that has to be taken into account for any work performed with FDM data.

1.3 Objectives

At the Institute of Flight System Dynamics (FSD) of the Technical University of Munich (TUM), the work focuses on accident prediction. The goal is the quantification of the occurrence probabilities for given accidents, which is essential to be able to perform benchmark with the safety target that are introduced in section 1.1. Today, this is typically either not performed in standard FDM or largely based on qualitative ex-

pert judgement. The general feasibility of a novel approach developed at the FSD has already been shown that is able to quantify the occurrence probability of accidents [Dre16]. Many components of the *Predictive Analysis*, however, still have to be refined. A detailed description of the Predictive Analysis is available in chapter 4.

The Predictive Analysis is based on three fundamental pillars.

1. The main source of information is data collected from flight operations. The largest contribution is obtained from FDM data which is recorded on each and every commercial flight and read out routinely. It contains states, system parameters and characteristic values of the aircraft as timeseries data throughout the flight. Additional data is used to complete the picture, such as weather data from the Meteorological Aerodrome Report (METAR). It can be said that the data represents the **collected previous experience** from flight operations.

2. A model of the aircraft is created that is based on the understanding of the behavior of the aircraft from flight mechanics. Just as pilot training can be performed using flight simulators due to their close resemblance to the reality, the same simulation techniques can be used to predict the behavior of the aircraft. Initial conditions are provided to the model along with the control variables. The model output consists of characteristic performance indicators that are used to determine whether an accident has happened or not. The modeling contains the **knowledge** we have about the physical system of the aircraft.

3. Operating procedures are included when setting up the model. The way the crews are expected to operate aircraft systems is incorporated as well as system logics unique to specific aircraft types. This takes into account the **uniqueness** of each operator as the safety level can be very different among competitors.

Several requirements have to be fulfilled by the developed methods:

- The data that is utilized does not necessarily contain actual accidents. The method must be capable to predict the accident probabilities without any recordings containing accidents. It has to be able to *look beyond the curve*.

- The prediction must be capable to run for individual organizations, i.e. for different operators with the ability to assess their level of safety individually.

- The prediction must be capable to assess the level of safety for separate parts of the flight operations. For example, it must be possible to quantify the risk individually for each aircraft fleet or for operations at specific airports or runways.

The work presented in this thesis focuses on certain parts of the Predictive Analysis (PA). Further research is also conducted on other parts and should be considered as well by the interested reader.

1.4 Contributions

This thesis aims at developing and implementing several sub-parts of the *Predictive Analysis* developed at the FSD which is able to quantify accident probabilities of individual airlines based on recorded flight data that is accident-free, fulfilling the requirements set up in section 1.3. The following work packages were performed that are either novel by themselves or novel to be used for the application at hand along with significant modifications.

Accident probability quantification for Runway Excursion (RE)

The developed methods are able to quantify accidents that are related to Runway Excursion, including runway overrun and runway veer-off. Though the methods are used for accidents that occur during landing, they can be transferred to the same accident types that occur during take-off. Runway overrun accidents, for example, can also occur after a rejected take-off. The relevant steps include modeling as well as data analysis. In order to perform the Predictive Analysis, the relevant information has to be extracted from FDM. They include contributing factors that have an impact on whether a RE accident occurs or not. So-called *measurement functions* are implemented that extract these relevant information from recorded data. Data errors have to be accounted for in order to obtain useful results.

Establishing the *Predictive Analysis*

The Predictive Analysis consists of seven steps and is described in detail in chapter 4. This dissertation contributes to four of them with particular focus on runway excursion accidents, mainly:

- Step 1: Define (Contribution in chapter 6)
- Step 2: Model (Contribution in chapter 6)
- Step 4: Cumulate (Contribution in chapter 8)
- Step 3: Predict (Contribution in chapter 9)

Usage of simulation models related to accident quantification based on FDM data

In order to describe the motion of the aircraft on the runway, a six degree-of-freedom rigid body model of the aircraft was created based on available information from FDM. The fidelity of the model has to be chosen such that only those parameters can be

incorporated that can be obtained from FDM. However, the model still covers all the significant drivers as well as the relevant effects and relationships that are important for the accident. While flight simulation models are used for various purposes, the model includes not only the forces and moments acting on the aircraft as in classical flight simulation, but also system logics of the on-board systems, such as autobrake or spoiler extension conditions that heavily affect the performance of the aircraft. In addition, the operating procedures are included as well, which is important to reflect the way systems are used, activated and deactivated by the flight crew. This reflects individual operational distinctive features of each airline and is of high importance to perform safety assessment for individual airlines.

Introducing a landing gear model specifically for accident quantification

The aircraft model is enhanced with a landing gear model. The landing gear of the aircraft was extensively modeled as the braking force is a key driving factor for any RE accident. The entire causal chain starting from the application of the brake pressure to the friction force between the tire and the runway surface was included. Again, just like the aircraft model mentioned above, the modeling has to be based on parameters that are obtainable from recorded FDM data and other safety-related information. Using this analysis, the braking capability of the aircraft can be obtained for individual environmental conditions which is essential to assess the remaining deceleration margin. For the lateral behavior on the ground, the model includes the sideslip as well, which is particularly important when it comes to nosewheel steering and lateral control. This is of special interest for runway veer-off accidents, i.e. when the aircraft unintentionally leaves the runway to either side.

Probability distribution propagation for operational flight safety

In order to quantify the accident probability using the model described above, probability distributions have to be propagated through the model. Though classical Monte Carlo Simulation (MCS) can be used, they proved to be computationally very costly when estimating small accident probabilities. The method of Subset Simulation has been applied to civil engineering and aircraft system development problems so far, the novelty is the application to operational safety in aviation utilizing a physical model of the aircraft. The key of using this method is to minimize the covariance of the result and simultaneously reduce the computational effort that is required.

1.5 Outline

Before describing the novel method introduced in this dissertation, an overview of how the data is obtained within Flight Data Monitoring is provided in chapter 2. In chapter 3, an overview is provided about both what is currently being done with FDM with respect to safety and other applications within airlines, such as efficiency topics. In addition, the FDM data is also used by other stakeholders in aviation, such as OEMs or Maintenance, Repair and Overhaul (MRO) organizations. In chapter 4, an overview of the Predictive Analysis developed at the Institute of Flight System Dynamics is provided including a description of all seven steps. In chapter 5, an overview of the stochastic methods used in this dissertation is provided, namely the methods used to quantify the accident probability, including the classical MCS and the more sophisticated Subset Simulation. In chapter 6, the basics of flight mechanics and aircraft modeling is described, along with modeling methods of the landing gear. The implementation of the system logics and the operating procedures for different aircraft types is shown in chapter 7. In chapter 8, the relevant data is extracted from FDM and the distributions are fitted to the data that are later used for accident prediction. In chapter 9, the actual accident prediction is performed using Subset Simulations, and the obtained results are presented. Finally, chapter 10 provides a conclusion of this thesis and an outlook to future work.

Some additional information related to this work can be found in the appendices. Appendix A provides an overview of the coordinate frames used in this work when the aircraft is modeled. In appendix B, the probability distributions that are used within this work are listed. Appendix C provides some aeronautical charts of Munich Airport (MUC/EDDM) to understand the operations at this airport. Appendix D shows the data that is used to quantify the probabilities for RE at MUC/EDDM.

2

Flight Data Monitoring

2.1 Necessity for Flight Data Recording

The ability to reconstruct any accident that already occurred has been of primary concern since the early days of safety effort in aviation due to the fact that often no on-board witnesses are available to be questioned. The first Flight Data Recorders (FDRs) were introduced on military aircraft and they were made mandatory for civilian airplanes during the 1960s [Air07]. The recorders only contained the most important parameters, such as speed, altitude and the attitude. The data was written on a metal strip. It soon became obvious that the data does not necessarily have to be used in an event of an accident, but also for routine monitoring of the flight operations. During the 1960s, more advances types of recorders were installed on new generation aircraft, such as the Comet, the Boeing 707 and the Vickers VC10. When the autoland system was developed during this time, a large amount of data had to be collected to monitor and to demonstrate the safety performance of the system. The certification of the autoland system was performed using data from the newly installed Quick Access Recorder (QAR) on-board the Hawker Siddeley Trident and the Lockheed L-1011 TriStar. The data could be easily transferred from the aircraft for further processing. The Flight Data Monitoring (FDM) system rapidly developed during this time, with British Airways being the first airline to monitor all of its aircraft.

FDM, also known as Flight Operations Quality Assurance (FOQA), is a powerful tool when it comes to not just monitoring, but also improving the level of safety. FDM is part of the airline's Safety Management System (SMS) and is nowadays required by law within the European Union (EU) for all aircraft with a Maximum Certified Takeoff Mass (MCTOM) equal to or greater than $27\,000\,\mathrm{kg}$. Although FDM is currently not legally required in the United States, it is common practice for all commercial operators worldwide due to its clear benefits. Guidance material for FDM can be found in the

Acceptable Means of Compliance (AMC) of the Part-ORO issued by the European Aviation Safety Agency (EASA) [Eur12]. The European Authorities Coordination Group on Flight Data Monitoring (EAFDM) also issued recommendations [Eur17a] as well as the British Civil Aviation Authoriy (CAA) [Civ13] and the French aviation accident investigation branch, the Bureau d'Enquêtes et d'Analyses pour la Sécurité de l'Aviation Civile (BEA) [Bur05].

This chapter will describe how the flight data is recorded today and how the data can be converted from a very specific format as found on the recorder memory to meaningful engineering values, enabling the data to be processed analyzed. FDM data offers a wide range of safety and non-safety related applications, which will be explained subsequently for use-cases from both inside and outside of the airline. In addition, some current research projects and activities using FDM data that are related to this work are presented.

2.2 Data Acquisition and Recording

Recording devices on-board the aircraft include, among all, the FDR and the Cockpit Voice Recorder (CVR). Both combined are very well-known to the public as the *Black Box*. Today, the FDR is often referred to as Digital Flight Data Recorder (DFDR) as the data is nowadays stored on solid state storage devices rather than magnetic tapes commonly used on older aircraft types. The way the data is recorded and retrieved has changed as well over time.

All the parameters that are to be recorded are measured by sensors throughout the aircraft. The measured numbers are converted to digital values and sent to the aircraft's on-board buses. For the first generation of aircraft featuring a glass-cockpit and a Flight Management System (FMS), e.g. the Airbus A320, A330, A340 as well as the Boeing 757 and 767, the common standard is the Aeronautical Radio Incorporated (ARINC) 429 bus. The Flight Data Acquisition Unit (FDAU) – for Boeing aircraft – or the Flight Data Interface Management Unit (FDIMU) – for Airbus aircraft – acquires the parameters for recording from the relevant ARINC 429 buses and converts the data to the ARINC 717 format [ARI11], which is used for the recording of the data on the DFDR. Figure 2.1 shows how the data is transferred from the sensors to the recorders.

A second flight data recorder also exists on-board commercial aircraft, which is either the QAR or the Digital ACMS Recorder (DAR), which also includes the data that is provided to the Aircraft Condition Monitoring System (ACMS) in addition to data from the FDIMU or FDAU. Figure 2.2 shows the recording architecture of the Airbus A380 and its connection to the ACMS. The data available on these recorders can either be an exact copy of the DFDR or they can be individually configured [Dub14]. As

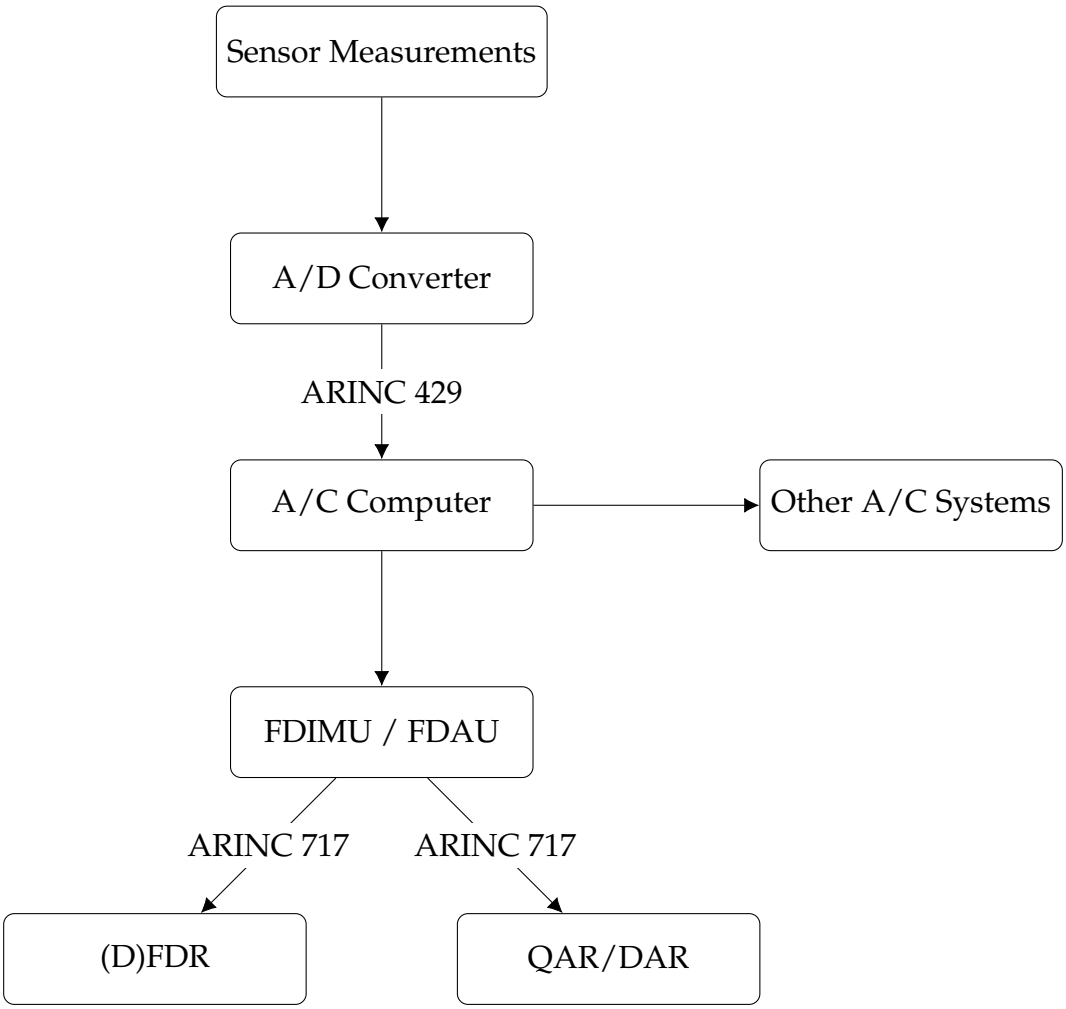

Figure 2.1: *Data flow from the sensors to the recorders*

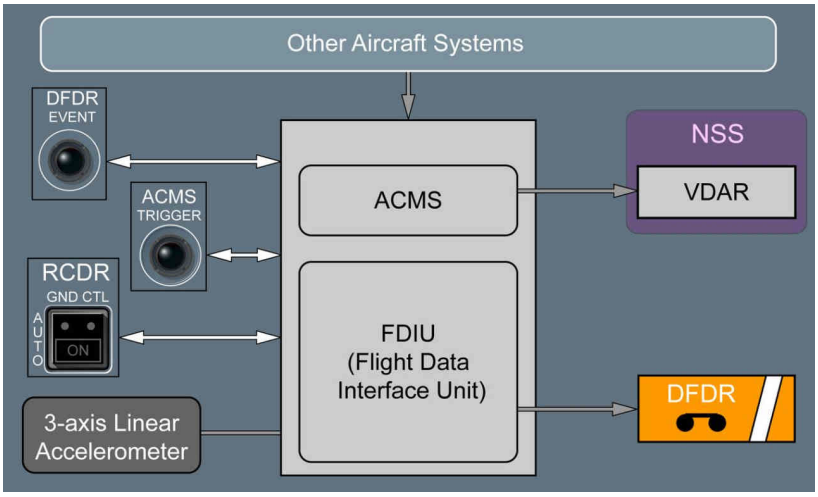

Figure 2.2: *Recording architecture on the Airbus A380 [Air11a]*

data from these recorders are used for FDM, it enables the operator of the aircraft to put individual focus according to the specific needs. In contrast, the parameters that have to be recorded on the DFDR are specified by legislation, though parameters can

be added to adapt to specific needs. Figure 2.3 shows a QAR module manufactured by *Teledyne Controls* that is installed on an aircraft. This particular model is also able to wirelessly transfer the stored data.

Figure 2.3: *A wireless QAR produced by Teledyne [Deg16]*

When it comes to the amount of recorded data, newer types of aircraft typically record more parameters simply because more parameters have to be measured and processed nowadays for other aircraft systems anyway. Especially those equipped with a Fly-By-Wire (FBW) flight control system combined with envelope protections require the input of many parameters with high reliability. However, the available amount of data is heavily limited by the data acquisition system. Airbus, for example, recently started introducing a new data acquisition and transferring system on the A320 fleet in order to allow more data being processed compared to current on-board systems [Roc17].

For the newer Airbus aircraft types, e.g. the A380 and the A350, a supplement to the ARINC 429 bus was created, allowing the data to be transferred via wireless Ethernet on the ground. On the newer types of the Boeing 777, a new on-board bus protocol, the ARINC 629, is used, which is a more capable standard compared to the ARINC 429. For example, the ARINC 629 allows a maximum transmitting speed of $2\,\mathrm{Mbps}$ while the ARINC 429 is only capable of up to $12.5\,\mathrm{kbps}$. For the Boeing 787, a newer format for flight data recording, which is the ARINC 767 [ARI09], was developed. The trend in the development is to move away from the traditional ARINC 429 protocol towards a more Ethernet-based architecture for flight data recording.

The description of the data acquisition and recording process applies to both the FDR and the QAR. The bifurcation in figure 2.1 indicate their distinctive features. There are three main differences between the FDR/DFDR and the QAR/DAR:

Crash protection: Neither the QAR nor the DAR is crash-protected, they are not designed to resist the mechanical and thermal impact. While their data are also used for accident investigation if they are still accessible, the FDR remains the only source of data if the aircraft is heavily damaged.

Data retrieval: Just as the name suggests, the data from the QAR, but also the DAR, can be easily retrieved. The data is often stored on a Personal Computer Memory Card International Association (PCMCIA) memory card or Secured Digital (SD) memory card which can easily be removed and copied to the airline's FDM system. With suitable infrastructure available at the airport, the data can also be transferred automatically via the company's Wi-Fi network at the gate or even worldwide via the 4G mobile network.

Adaptability: The operator can modify the parameters stored in a QAR whereas the data on the FDR is specified by law and must not be changed below the legally required standard.

In 2015, an Airbus A320 operated by Germanwings impacted terrain in the French Alps with high energy after deliberate actions of the First Officer. The mechanical stress acting on the airframe during the impact was enormous. Although the FDR was severely damaged from the outside, as seen in figure 2.4, the memory of the recorder was readable. The QAR was damaged and could not be read [Bur16].

Figure 2.4: *The heavily damaged, but still readable FDR of the A320 that crashed in the French Alps after recovery [Bur16]*

2.3 Data Handling

After the binary data from the recorder is transferred to the airline's IT infrastructure, some processing of the data has to be performed to make the data ready to be used for safety monitoring or other purposes. For airlines, many commercial software solutions are available on the market that provide a wide range of services from data pre-processing to safety analysis. Possible providers include SAFRAN Sagem's *Analysis Ground Station (AGS)*, Teledyne's *AirFase* as well as General Electric's *Flight Risk Management* tools, formerly a product of Austin Digital.

The main tasks of these tools include the conversion of data from binary to engineering values, the visualization of the data and the performance of safety analysis. For the first task, there are several challenges that a FDM tool has to face:

- The appropriate documentation of the Dataframe Layout (DFL) has to be available, which contains the information about how to convert from binary to engineering values. While this seems to be straightforward as it should be provided by the Original Equipment Manufacturer (OEM), the documentation is often not complete as a significant part of the knowledge is not written, but rather exchanged informally within the community.
- The tool has to be capable of processing files with large size. Each flight, in binary format, ranges from several megabytes for short-haul flights on aircraft with several hundred recorded parameters to almost $100\,\mathrm{MB}$ for long-haul flights on modern aircraft types, such as the Airbus A380, where more than 2000 parameters are recorded. While this can be easily handled by today's computational power, special attention has to be paid to the processing of data to avoid unnecessary memory allocation.
- The tool has to be capable of processing a large number of flights. The fleet of Lufthansa Passage (the mainline within the Lufthansa Group), for example, consists of about 180 short-haul and about 110 long-haul aircraft. The number of flights performed on a single day easily reaches a few thousand. The entire Lufthansa Group performs more than one million flights every year [Deu18b].

Due to the specific use-cases at the Institute of Flight System Dynamics (FSD), which is different compared to those at airlines, it was decided not to purchase a commercial solution on the market, but rather to develop a tool on their own. Unlike the application for airlines, the number of files is limited to batches coming in from airline partners rather than a live and continuous feed from operations. In addition, the main advantage of a self-developed tool is the possibility for quick and tailored customizations.

Each single flight has to be identified as the files typically contain time-continuous and looped recording, i.e. the recording restarts at the beginning of the memory once it arrives at the end, overwriting the previously recorded data. A method to split the individual flights was also developed [WMH16].

There are several types of error that should be accounted for when it comes to recorded flight data:

Measurement error: The wrong values result from incorrect measurements, mostly from erroneous sensors. Examples include incorrect position measurements due to the drift of the gyroscopes or the accelerometers of the Inertial Reference System (IRS). In addition, the measurements can contain bias and noise.

Recording error: The wrong values result from correct measurements, but the value was not correctly written on or read from the memory. This is typically caused by flipped or shifted bits.

Resolution error: As the measured values are stored digitally, the measured values have to be discretized. This introduces an error because the recorded value is typically not exactly the same as the one that was measured.

Time discretization error: Similar to the resolution error, measurements can only be recorded at discrete timepoints. This means that the time at which the value was recorded is not necessarily the same timepoint when the value was actually measured.

Dataframe error: The dataframe that is provided along with the data can be erroneous, leading to incorrect conversion to engineering values.

Recording errors are typically somewhat easier to detect as a single wrong bit will usually lead to a large deviation within a very short time frame in the engineering value, which can be detected because the value is often not physically realistic. Errors in the dataframe typically result from incorrect conversion factors or incorrect units. They can be easily detected if the units are significantly different, e.g. speed in knots instead of meters per second.

All devices involved in flight data recording should be examined and checked on a regular basis to minimize the errors described above. The sensors and measuring units should be regularly calibrated [Bur05]. The tolerated deviations from real values are provided in the EU-OPS [Eur08a].

2.3.1 The ARINC 717 Format

2.3.1.1 Format Structure

As already mentioned in section 2.2, the data on the QAR is recorded in the ARINC 717 format [ARI11] for the large majority of aircraft types currently in service except the Boeing 787 and other very new types of aircraft. In this section, the ARINC 717 format will be presented along with a tool developed at the FSD which is capable of converting the ARINC 717 binary data to engineering values.

The structure set up in ARINC 717 is defined by bits, words, subframes (SF) and frames. Each word consists of 12 bits while 4 subframes constitute one frame. The number of words per subframe varies between aircraft types. While older aircraft types only have 64 words per subframe, newer types or newly-built airplanes with modifications compared to earlier production frames can have a much higher number

Frame	Frame 1				Frame 2				...
SF	SF 1	SF 2	SF 3	SF 4	SF 1	SF 2	SF 3	SF 4	...
Word	Sync 2 3 4 5 ⋮ n	Sync 2 3 4 5 ⋮ n	Sync 2 3 4 5 ⋮ n	Sync 2 3 4 5 ⋮ n	Sync 2 3 4 5 ⋮ n	Sync 2 3 4 5 ⋮ n	Sync 2 3 4 5 ⋮ n	Sync 2 3 4 5 ⋮ n	... ... ⋮ ...
Time	1 s	1 s	1 s	1 s	1 s	1 s	1 s	1 s	...
	4 s				4 s				...

Figure 2.5: *The ARINC 717 Layout*

of words, allowing a much higher number of parameters to be recorded and also with higher frequency. For example, the Boeing 747-8, both the passenger and the freighter version, can have up to 1024 words per subframe while newer productions of the Airbus A320 can have 2048 words per subframe. The maximum recording capability is mainly limited by the FDAU / FDIMU.

The first word in each subframe is reserved for the *sync word*, which is a unique sequence of 12 bits defined in ARINC 717 in order to distinctly identify the beginning of each subframe. Of course, it cannot be entirely ruled out that the exact same 12 bits appear at other positions in the binary streams, but it is unlikely. The ARINC 717 layout is shown in figure 2.5.

The recording speed is set up in such a way that one subframe is recorded every second, meaning that one frame comprises four seconds. Depending on the aircraft type, parameters can have different recording frequencies. While the Boeing 777 and 787 have recording frequencies of 1, 2, 5, 10 and $20\,\mathrm{Hz}$, the Boeing 737 and 747 as well as all Airbus aircraft types record parameters with frequencies of 1, 2, 4, 8 and $16\,\mathrm{Hz}$. This implies that every parameter that is recorded with $1\,\mathrm{Hz}$ can be found once in each subframe. Parameters with $8\,\mathrm{Hz}$ are found 8 times in each subframe and parameters with $0.25\,\mathrm{Hz}$ can be found once in only one of the four subframes, i.e. once per frame. Parameters can also be recorded with frequencies lower than $0.25\,\mathrm{Hz}$, they are referred to as *superframe parameters* as they cannot be found in every frame. In order to distinguish each frame, a superframe counter is implemented in one of the words as a regular parameter.

The recording frequency of each parameter depends on the availability of words to be utilized on the one hand and the dynamic property of the parameter on the other hand. Highly dynamic parameters such as acceleration or angular speeds of the aircraft have a much higher recording frequency than slow-changing parameters, such as the

aircraft's mass. Other parameters might not change at all during the flight or never change at all, but they are still recorded for convenience reasons, examples include the aircraft's registration, flight number or callsign. These parameters are typically recorded as superframe parameters to minimize memory space.

2.3.1.2 Decoding Process

A key task in FDM is the conversion of the binary ARINC 717 to meaningful engineering values. In order to perform this task, one has to know which parameter is stored in which word(s) and which subframe(s) and how the relevant bits can be converted to engineering values. This information is referred to as the *Dataframe Layout (DFL)*. It has to be provided or generated by the manufacturer of the aircraft or, if the operator has made modifications to it, by the airline. A MATLAB tool was developed at the FSD that is capable of making the conversion from binary to engineering values. The DFL is stored in a database which is accessed by the tool [Moh16].

The number of bits required for each parameter does not only depend on its frequency, but also on the type of the parameter. A switch that can be either on or off only requires one bit for one value or two bits, if a valid/invalid flag is added. The position longitude of the aircraft, for example, with values ranging between $-180°$ and $180°$, requires a larger number of bits for each value which is also due to the fact that the resolution has to be sufficiently high in order to be able to record the position precisely.

Taking the position longitude as an example, it is typically recorded with 21 bits for each measurement, enabling the precision to be

$$\frac{360°}{21^2} = 0.000\,171\,661°.$$

This corresponds to a resolution of approximately $20\,\mathrm{m}$ on the surface of the earth. This precision is sufficient for airborne navigational purposes, but not for landing analysis, such as the exact detection of the touchdown point on the runway. The use of 21 bits implies that they cannot all be located in the same word, but have to be in different words since one word only contains 12 bits. A decoder will assemble the bits and convert from a binary to a signed decimal number. Numbers can also be stored as Binary Coded Decimal (BCD) which means that each digit in the decimal representation is converted to a binary number individually, requiring up to 4 bits for each digit. Letters and symbols, if they need to be recorded, are converted to binary format using the American Standard Code for Information Interchange (ASCII), thus 7 bits are required for each symbol.

Before this process can be performed for each parameter to be decoded, the bits have

to be sorted as they are stored on the memory as a long stream of ones and zeros. Using the sync words, the beginning of each subframe can be detected. The bits are then sorted into frames, subframes and words. An algorithm has been developed that sorts the bits into a 3-dimensional matrix, with the three directions being word, subframe and frame [WDH16a]. The position of the bits for each parameter is located in a repeating way:

- If the recording frequency is smaller than $0.25\,\mathrm{Hz}$, the superframe parameter is always stored in the same word(s) in the same subframe in every frame where the superframe counter has a given value.
- If the recording frequency is $0.25\,\mathrm{Hz}$, it is always stored in the same word(s) in the same subframe.
- If the recording frequency is $0.5\,\mathrm{Hz}$, it is always stored in the same word(s) in the same two subframes.
- If the recording frequency is $1\,\mathrm{Hz}$ or greater, it is always stored in the same word(s) in each subframe.

The indexing of the relevant bits now becomes much simpler when the bits are sorted.

At the FSD, flight data is available from approximately five operators that include a wide range of aircraft types. Data from almost all Airbus aircraft types featuring FBW control are available as well as data from the Boeing 747-8. All the data can be converted using the described approach.

2.3.1.3 Example Parameters

Table 2.1 shows three example parameters obtained from the DFL of an aircraft. The first parameter, the barometric altitude in feet, is coded as a binary value. It consists of 19 bits, 6 of them are located in word 852 in each subframe (SF) and each frame. This implies that a total of $2^{19} = 524288$ numbers can be expressed. However, the allowed range of the numbers is limited to a minimum of $-2000\,\mathrm{ft}$ and a maximum of $50\,000\,\mathrm{ft}$. That means after converting the binary number to decimal, the entire range has to be scaled to the interval of $[-2000; 50000]$, i.e. using a scaling factor of $\frac{50000-(-2000)}{2^{19}}$ and an offset of -2000 in order to obtain the engineering value of the barometric altitude in feet. Instead of providing the maximum and the minimum possible value, some DFLs also provide the scaling factor and the offset.

The second parameter is the lateral acceleration of the aircraft in g, i.e. scaled to the normal gravitational acceleration. It is somewhat similar to the first parameter. It is recorded every SF and every frame and has to be converted from binary to decimal

ID	Parameter	Frame	SF	Word(s)	Bit(s)	Min	Max
1	Barometric Altitude, ft	All	All	852	1-6	-2000	50000
		All	All	854	1-12		
2	Lateral Acceleration, g	All	All	69	3-12	-1	1
		All	All	197	3-12	-1	1
		All	All	325	3-12	-1	1
		All	All	453	3-12	-1	1
		All	All	581	3-12	-1	1
		All	All	709	3-12	-1	1
		All	All	837	3-12	-1	1
		All	All	965	3-12	-1	1
3	Registration Char 1	8	3	445	6-12	N/A	N/A
4	Ground Sensor	All	All	65	2	0	1

Table 2.1: *Example parameters from FDM*

using the information that the minimum and maximum values are -1 and 1, respectively. However, the difference is that this parameter can be found in 8 different words containing 10 relevant bits each. This implies that the parameter is recorded 8 times in every SF, i.e. with a frequency of $8\,\mathrm{Hz}$. Note that the difference between each word is always at an equal space of 128, which means that the frequency of $8\,\mathrm{Hz}$ is constant over the entire second.

In the documentation of the DFL, very often no reference can be found concerning whether a parameter located in several words within a subframe is simply because more than 12 bits are required to record the number or whether the frequency is higher than $1\,\mathrm{Hz}$. For this distinction, common knowledge or experience is required. First, each measurement has to have the same number of bits for every measurement. This rules out that, for example, the first parameter in table 2.1 is recorded with $2\,\mathrm{Hz}$ because the number of bits in word 852 and 854 are different. Second, when recorded with a higher frequency, the space between the words should be equal, as shown in parameter 2 in table 2.1. This also does not apply to the first parameter.

The third parameter is the first character of the registration of the aircraft. The first significant distinction is that this parameter cannot be found in every frame or SF, but only in SF 3 and only when the superframe counter is 8. For this particular DFL, this counter can reach a maximum value of 4096, which means that the counter repeats itself after $4 \times 4096 = 16\,384\,\mathrm{s}$, which is also the recording frequency of this parameter. Of course, registration character of the aircraft rarely changes – if at all. It is only logical to store it with such a low rate. In order to decode the character, one has to extract the bits 6 to 12 from word 445, which is a total of 7 bits, as the character is ASCII-coded.

The fourth parameter is the Air/Ground sensor and again recorded in every SF and every frame, resulting in a recording frequency of $1\,\mathrm{Hz}$. It is located in bit 2 of word 65.

As it is a boolean variable, only one bit is required. In this case, a value of one indicates that the aircraft is on ground and zero indicates that the aircraft is airborne. Sometimes a valid/invalid flag is added to a parameter to indicate whether the measured value is reliable, requiring an additional bit.

2.3.2 The ARINC 767 Format

A new data recording standard has been introduced to enable better performance compared to the ARINC 717, which is the ARINC 767 format [ARI09]. The ARINC 767 is currently only used on the Boeing 787 aircraft. However, it will be introduced on newly produced airframes of the Boeing 777-300ER and the Boeing 737 MAX family as well as the Boeing 777-8 and -9 at market introduction.

The ARINC 767 is used along with a new type of recorder, which is the Enhanced Airborne Flight Recorder (EAFR). The concept of frames and subframes known from the ARINC 717 is replaced by a timestamp, similar to messages that are transferred via the Automatic Dependence Surveillance - Broadcast (ADS-B) system. Each measurement is stored along with a time at with this particular measurement was obtained. This means that the recording frequency does not necessarily have to be one of the given values, but can be individual. In addition, it is possible to vary the recording frequency throughout the flight. For example, there is no need to record the wheel speed at a high sampling rate during the flight, but it can be very beneficial during take-off and landing to record this parameter with a high frequency.

The ARINC 767 is also capable of incorporating voice data, messages from datalink as well as images from on-board cameras.

2.4 FDM within the Safety Management System

Though FDM offers a rich source of data, additional information is often included within the scope of FDM. Other sources of information include radar data that is collected by Air Navigation Service Providers (ANSPs) and also ADS-B data. Weather data is collected and used in the form of Meteorological Aerodrome Report (METAR) messages. Depending on the confidentiality agreements within the company, personal data of the flight crew can be incorporated, such as previous experience or flight duty time.

Despite its importance, FDM is only one module that contributes to the overall SMS of an airline [Int13]. The implementation of a SMS requires joint effort within the company, both technical and organizational. Responsibilities are often assigned by the

appointment of staff members as safety managers. One of their key tasks is to also promote safety within the organization and to increase the awareness for safety. The gap between the safety target and the actual level of safety has to be identified and closed by implementing risk mitigation measures, such as the introduction of safety barriers or changes in training and procedures. Last but not least, safety management also includes plans to follow in the event of a crisis, e.g. when an accident has already occurred. These plans not only include the assignment of tasks and responsibilities, but also measures concerning how to communicate to the public.

3

FDM Activities Today

3.1 Introduction

Flight Data Monitoring (FDM) is a key part of the Safety Management System (SMS) of aviation stakeholders. It provides a feedback loop to allow a timely detection of any safety hazard[1] as well as any deviation from Standard Operating Procedure (SOP) [Civ13]. The effectiveness of risk mitigation actions can be monitored and quantified using FDM. If the results are not satisfying, the measures can be modified accordingly. This chapter provides an overview about how FDM data is used throughout the industry. Some research initiatives that are related to this dissertation are also presented.

3.2 Use of FDM within Airlines

FDM, also referred to as Flight Operations Quality Assurance (FOQA) or Flight Operations Data Analysis (FODA), can be used for safety improvements in various ways. When it comes to *reactive* Safety Management, it provides a possibility to review the sequence of events and the establishment of causal chains. After an accident, the authorities are informed and the flight can be reconstructed. Based on the provided information, they will decide about further steps. In addition, many minor events occur during daily flight operations. These are not serious, but still constitute an unusual situation that could, if not prevented, lead to more serious events in the future. Examples include unstablized approaches, Traffic Alert and Collision Avoidance System (TCAS) Traffic Advisory (TA) events or simply messages from the Electronic Centralized Aircraft Monitoring (ECAM) or Engine Indication and Crew Alerting System (EICAS)

[1] *Hazard* is defined by the International Civil Aviation Organization (ICAO) as *"A condition or object with the potential of causing injuries to personnel, damage to equipment or structures, loss of material, or reduction of ability to perform a prescribed function" [Int13].*

about certain on-board systems. FDM enables the safety manager to look at flights from the past to identify the contributing factors that lead to the event and to establish procedures to prevent the same or similar events from happening again in the future [Cam17].

Visualization tools create graphical images and videos of the flight along with the prevailing environmental conditions at the time of the flight. It can also be beneficial to the crew to view their own flight from a third viewer's perspective [Mor17]. Such feedback to the flight crew can also be routinely made available without the occurrence of events. Information provided to each crew member individually can include the precision of manual flight, the time to perform certain items in the procedure and, most importantly, the benchmark with other crew members in the airline [Hit17]. This also enables further development of the flight crew training program since it can be individually tailored to each person to train what is mostly required for that particular crew member. This is often referred to as Evidence-Based Training (EBT). Of course, data confidentiality agreements apply, which is further discussed in section 3.5.

FDM offers more opportunity than just replaying the past. New knowledge can be obtained by deeper analysis as part of the *proactive* Safety Management. The aim of it is to anticipate what might be happening based on the current available information and to implement countermeasures to mitigate the related risks. For example, based on previous accidents, it is well known that the wind plays a vital role when it comes to Runway Excursion (RE) accidents. Especially heavy crosswinds significantly increase the risk of suffering from a runway veer-off while tailwind increases the required landing distance, leading to higher overrun risks. A proactive SMS would analyze the wind data and implement measures before any RE accidents occur. However, although the wind is often recorded in FDM and also provided by the Air Traffic Controller (ATCo), the quality and the sampling rate is very low. Reconstructing the wind, which has high influence on the quality of the landing, is an enabler for a deeper analysis of the contributing factors to RE, particularly runway veer-offs. FDM allows unknown information that was not available in real-time during the flight to be computed afterwards using more sophisticated methods. The wind components (crosswind and tailwind) can be reconstructed for the landing phase using filter methods [van17a]. Novel techniques, such as machine learning tools, can also be used on flight data in order to detect unusual flights or flight paths rather than defining threshold values and detecting their exceedance [Oeh17]. Furthermore, the data from FDM can be enhanced since the analysis is done offline after the flight. Therefore, at each timepoint during the flight, not only the measurements in the past are available, but also those in the future. Using this information, advanced smoothing algorithm can be used to correct measurement errors in the data to enable further studies using the corrected data [Höh16] [Höh17].

Today, airlines' FDM activities are not limited to contributing to the goal of improving

the level of safety. The data can also be used to improve the efficiency of the operations, for example by analyzing and reducing fuel burn. The direct comparison of two flights is always difficult, even on the same route using the same type of aircraft because the conditions are different for each individual flight. The atmospheric conditions constantly change just as the loading is never entirely identical. A clustering method can be used to compare fuel flow between two aircraft or two aircraft fleets independent of the exact route to be flown [KSH16] [Kop17]. In recent years, experiments have been conducted to put a special coating on the outer surface of the aircraft in order to reduce aerodynamic drag [Luf]. The effect of this coating could be quantified using FDM data.

3.3 Use of FDM at Other Organizations

As FDM data are collected and, consequently, owned by airlines, data must be made available to other organizations if they wish to make use of it. While data transfer can be difficult due to legal concerns, as described further in detail in 3.5, the availability can be of great benefit for other organizations as well.

Another important field of application is the optimization of maintenance work. Data obtained from FDM is also widely used at Maintenance, Repair and Overhaul (MRO) organizations [Sor18]. With information about the flight hours, loads and other parameters relevant to the aging of the aircraft or the aircraft's components, the time to failure for the respective component can be estimated [Sor18], allowing a more efficient planning of the maintenance schedule. This method, which currently is still undergoing rapid development, is often referred to as *Predictive Maintenance*. *Big Data* processing algorithms and *Machine Learning* techniques can be utilized as well. Many big players on the MRO market have already developed products that utilize recorded data from the aircraft, including FDM data, but also data from the Aircraft Condition Monitoring System (ACMS) that is additionally stored in the Digital ACMS Recorder (DAR), to predict the failure of parts and aircraft components in order to replace them before the failure. AFI KLM E&M, the MRO subsidiary of Air France – KLM, have developed and implemented the *PROGNOS – Predictive Aircraft Maintenance* [Air17] on vital components of the aircraft, such as the engines or the Auxilliary Power Unit (APU). Lufthansa Technik developed *AVIATAR* [Luf17] that is capable of connecting the stakeholders, including airlines, Original Equipment Manufacturers (OEMs), MROs and aircraft lessors to manage the fleet, with particular focus on reliability. Of course, the FDM data has to be made available to the MRO. Due to data confidentiality issues, this is most often made possible if the MRO and the airline are different subsidiaries of the same company group.

From the point of operational efficiency, the runway occupation time after landing has

been investigated using FDM data [Her17]. The data from the on-board recorders often contain more precise position and speed data of the aircraft than the radar data that is available to the tower and ground controller. With a deeper knowledge, the arrival and departure sequence at the airport can be better planned by the ATCo. Furthermore, for Air Navigation Service Providers (ANSPs), the knowledge about the performance and the behavior of the aircraft can provide an advantage when it comes to optimizing the traffic flow. In this case, FDM data is combined and correlated with radar data, which is directly collected by the ANSP as well as weather data, such as Meteorological Aerodrome Reports (METARs).

3.4 Use of FDM Across Organizations

FDM data can also be used across organizations. In fact, the exchange of data between the operators can be greatly beneficial to all the parties involved. While the airlines are often competitors on the market, it is common industry practice to cooperate rather than to compete when it comes to safety. In the United States (US), the Aviation Safety Information Analysis and Sharing (ASIAS) program of the Federal Aviation Administration (FAA) serves as a platform to exchange data between the operators [QJ17] with all the major carriers in the US participating. A similar program called *Data4Safety* [Eur17b] is currently being implemented in the European Union (EU). This type of data exchange allows not only the exchange of experience and benchmarking, but also enables the airlines to join the effort if they face the same challenges. The International Air Transport Association (IATA) offers the Flight Data Exchange (FDX) service to its member airlines [Int18], where data can be provided by volunteer airlines that are de-identified. It can be accessed by other member airlines that take part in the program to perform, for example, benchmarking.

3.5 Data Confidentiality

Wherever data is used, confidentiality issues have to be considered. Although the way flight data is being handled varies significantly across the organizations, special care always has to be taken to guarantee that the data will not be misused for purposes other than those agreed upon.

Data de-identification is a crucial part of FDM, though anonymity is handled differently throughout the industry. The reason to de-identify the data is to prevent the capability to trace back to the people involved in the recorded flight. This is a part of the safety culture of the organization. As the top-level goal of FDM is to increase

safety, the priority should be the detection of hazardous events, rather than solving liability issues or even punishing those who are involved in the events. In order to perform safety monitoring, it is often not necessary to know the exact crew member [Civ13]. Agreements should be reached within the organization about how to proceed if it becomes beneficial to discuss the events with the involved pilots.

In order to maintain the anonymity, parameters can be erased. Most often, the date and the time as well as the aircraft's tail number are removed to reduce the possibility to trace back to a particular flight and, more importantly, a particular crew that performed the flight.

Last but not least, the data always has to be stored securely. The access is restricted to only those working with the data. This should be done by prompting for passwords and encryption of the storage device.

3.6 FDM-Related Research Effort at the FSD

3.6.1 Project SaMSys

The project *Safety Management System zur Verbesserung der betrieblichen Flugsicherheit (SaMSys)* was initiated by Deutsche Lufthansa AG in 2009 and funded by the German Federal Ministry for Economic Affairs and Energy. The project was lead by the Safety Department of Lufthansa German Airlines, with the goal being the development of novel methods to improve the operational safety level within an airline. Participants of the project include software companies as well as research institutions, including the Institute of Flight System Dynamics (FSD). The main task of the FSD was to develop and calculate Safety Performance Indicators (SPIs) with respect to the safety target that was set by the company management. Methods to quantify the occurrence probabilities of certain accidents emerged from the project [DH11]. Technical failure on-board the aircraft, leading to deteriorated performance, is also considered [DH12].

As a complementary part of the project, studies with pilots were performed during the project by the Chair of Ergonomics (LFE) at the Technical University of Munich (TUM). A large amount of data was collected during two simulator campaigns [Mül16]. The pilots were also equipped with eye-tracking devices. The manual flying skills could, therefore, be correlated with the visual behavior of the pilots. One of the research topics was how the pilots looked at the flight instruments [HGS12] as well as the way the pilots use the side stick on the Airbus aircraft [HSGB12]. The decision-making process under high workload and time pressure was also closely investigated during the second round of simulator studies [GPHB15].

The project SaMSys concluded in 2016.

3.6.2 Project Future Sky Safety

Future Sky Safety (FSS) is funded by the European Union starting in 2014 with a total duration of four years. The project is divided in several sub-projects, with the FSD being involved in *P3 – Solutions for Runway Excursions* and *P4 – Total System Risk Assessment*. Other sub-projects also look at different safety-relevant aspects such as human performance or the influence of the organizational structure on safety. The large number of project partners in FSS include airlines, OEMs, ANSPs as well as research institutions.

3.6.2.1 FSS P3 - Solutions for Runway Excursions

P3 is dedicated to Runway Excursions, including both overruns and veer-offs. The physical behavior of the aircraft plays an essential role. The focus has been to assess the aircraft's ability to stop on the runway under different runway conditions as well as its ability to maintain its direction of movement. A key point of research was the influence of runway contaminants, e.g. water, slush or snow. The approach was based on both theoretical models and experimental data. Tests were conducted with both a small business jet (Cessna Citation) as well as a large military transport aircraft (Airbus A400M). Braking tests were conducted on flooded runways in order to determine the friction coefficient [van17b]. The obtained data was used to quantify how water as contaminant leads to deterioration of the braking capability.

3.6.2.2 FSS P4 - Total System Risk Assessment

P4 is aiming at the development of a Risk Observatory that includes all stakeholders involved in the aviation transport industry, including OEMs, operators (airlines) as well as ANSPs. The idea is to present a dashboard that is capable of displaying the current risks along with a core running in the background that performs the monitoring of the trends in order to initiate risk mitigation actions in a timely manner. A key novelty of the project is the connection between the domains. While risk mitigation actions could lead to safety increase for one domain, it can also cause a deterioration of the safety levels in other domains. This project is aiming at the development of a **predictive** SMS, a tool that is able to recognize issues within the flight operations that might develop into hazards in the future.

Models to assess the safety of the flight operations exist in many domains and for most stakeholders. OEMs have models to determine the time to failure of certain compo-

nents or systems. ANSPs have models to predict mid-air conflicts for given airspaces. Models can be created based on many different principles. They could be purely data-based, such as causal models. A causal model, such as the Causal Model of Air Transport Safety (CATS) model [RvS+08], finds relationships in existing data and utilizes these to predict the outcome of future events. The alternative would be models that are based on physical relationships. When describing mechanical systems, they would use Newton's laws of motion or, for example, the Maxwell equations when it comes to electromagnetic systems.

The novel approach of this project is to develop a risk observatory for the entire aviation transport system, linking all the models. A first prototype of the risk observatory was presented [VvW] along with a look-and-feel user interface [vWVv16].

Several models were developed for different domains. For aircraft and system manufacturers, a model using the *AltaRica* language was developed [BMMP17] that is capable of quantifying the failure probability of aircraft systems based on fault tree methods. A barrier model that is referred to as the Accident Incident Model (AIM) was created to describe the sequence of events that leads to a Mid-Air Collision (MAC). The barriers in these models are actions or features that prevents the next event from occurring, which is of particular interest for an ANSP [LCM+17]. A physical model describing the motion of the aircraft during landing phase, particularly with focus on RE was developed by the FSD [WH18a]. A backbone model was created to link these models comparable to the CATS model developed by the Netherlands Aerospace Center (NLR) [RvS+08]. The connection between the backbone model, the physical model as well as the entire risk observatory was established [WMH18].

As of January 2019, the project FSS is scheduled to conclude in June 2019.

3.6.3 Project SafeClouds.eu

The project *SafeClouds.eu* is also funded by the EU. It aims at using all data that is available in aviation across all stakeholder to improve safety. A large variety of partners are involved in the project, including many airlines and research establishments. The key idea is to generate added value when data that is currently gathered by individual stakeholders in the aviation system is put together and shared across organization boundaries and analyzed together. The decoding of binary FDM data, as described in section 2.3.1 is also performed with the scope of the project [HS17].

The project SafeClouds.eu started in October 2016 and is scheduled to conclude in September 2019.

3.6.4 Fueling Policy based on FDM Data

3.6.4.1 Introduction

In addition to the aforementioned research projects, some intensive studies have been performed along with the project partner Lufthansa concerning the influence of fuel on the operational safety.

The fuel to be taken on board prior departure is regulated by law [Eur08a] and implemented by the aircraft operator [Deu13][Luf14]. It consists of the following components:

Taxi Fuel: The amount of fuel required to taxi from the gate to the take-off position. The fuel required for taxiing after landing is not included in any of these fuel components.

Trip Fuel: The amount of fuel required to fly from the origin (brake release on take-off runway) to the destination (touchdown on landing runway) under normal circumstances.

Alternate Fuel: The amount of fuel that is required to fly from the missed approach point of the destination to the landing at the planned alternate airport.

Contingency Fuel: The amount of fuel corresponding to either 5% of the trip fuel or equivalent to 5 minutes of flying time, whichever is higher. This contingency accounts for calculation errors or deviation from the planned route, such as circumnavigation of Cumulonimbus Clouds (CB).

Final Reserve Fuel: The amount of fuel that is required to fly 30 minutes at an altitude of 1500 ft Above Ground Level (AGL) at the destination airport.

Extra Fuel: Additional fuel to be taken on-board depending on the crew's decision.

Regulation requires a minimum amount of fuel to be available on-board at the time of touchdown, which corresponds to the final reserve fuel of 30 minutes of flying time. Any violation of that requirement must be reported to the authorities. On May 14, 2010, Madrid Barajas Airport (MAD/LEMD) was experiencing severe disruptions due to thunderstorms, the capacity of the airport was heavily reduced. As a result, a large number of flights diverted to Valencia Airport (VLC/LEVC). However, congestions occurred at VLC/LEVC due to its own capacity that is significantly lower than that of MAD/LEMD. Several aircraft declared emergency, two of them, a Boeing 737 and an Airbus A340, landed below the required final reserve fuel. The A340 only had $2100\,\mathrm{kg}$ of fuel remaining while its final reserve fuel should have been $2800\,\mathrm{kg}$ [Com13].

Air traffic is increasing, leading to congestions in both en-route and terminal airspaces as well as at airports. It has become a safety-relevant question whether events like

this will become more likely to happen in the future and how to adapt the procedures to the increased risk. Especially at hub airports, where traffic is grouped in several inbound and outbound waves over the day, a closure during an inbound peak could cause not only severe delays, but also possibly fuel starvation on the inbound flights if no precautions are taken.

Disruptions at airports or sometimes even a closure can be caused by weather, but also by accidents occurring on the runway. If an aircraft is disabled within the runway protection area, the runway has to be shut down until the aircraft is removed. Emergency situations on the apron can disrupt the approach flow as well. Flight operations at an airport has to be shut down if the fire department is occupied with an ongoing emergency because there would be no capacity to cope with any additional emergency situation if anything happens to other aircraft. For example, in July 2013, a Boeing 787 parked on the apron at London Heathrow Airport (LHR/EGLL) began emitting fire from the rear part of the aircraft. It was later found that the Emergency Location Transmitter (ELT) battery suffered a thermal runaway [Hra14]. While the fire department extinguished the fire, LHR/EGLL had to be closed, causing severe disruptions. Another accident occurred in 2011 at Munich Airport (MUC/EDDM). A Boeing 777 veered off the runway during landing before becoming disabled on the runway [Bun18]. One of the two runways at MUC/EDDM had to be closed for several hours, causing congestions leading to major delays and cancellations.

3.6.4.2 Approach Bottleneck

The goal of this particular research activity is to develop a tool that is capable of quantifying the risk of fuel starvation in the event of an unexpected disruption. The method that was developed has been published since 2014 [WDH16b] [Coc14] [Str17]. The idea is to perform a simulation of the approach, taking into account the capacity of the destination and the alternate airport(s) on the one hand as well as the incoming traffic on the other hand. The capacity of an airport equipped with an Instrument Landing System (ILS) is primarily limited by the wake turbulence separation between two aircraft if operating with inbound traffic only. Another limitation at some airports is the availability of (possibly high speed) taxiways. They allow landing aircraft to vacate the runway quickly to enable the next aircraft to land. This limitation was neglected because large airports are often equipped with a sufficient number of high speed exits.

It is assumed that during an emergency situation, the airport will temporarily stop departures in order to maximize the arrival capacity. Several inbound scenarios from real-life flight operations at MUC/EDDM were investigated, including both peak and off-peak hours. At the start of the simulation, aircraft heading towards MUC/EDDM begin their diversion to one of the nearby alternate airports assuming that MUC/EDDM

is closed. As airports in the vicinity have a significantly lower capacity than Munich Airport, the traffic begins to build up in the approach sector that also includes the regularly scheduled traffic heading to the alternate airports. This situation is typical for hub airports as they are mostly the only large airfield available in the area. The intention of the simulation is to determine the waiting time for each aircraft and subsequently to calculate the required fuel.

As the decision to divert is entirely up to the flight crew, there is no systematic pattern of where to divert. Crews typically choose the diversion airport by themselves. The relevant criteria could be:

- Proximity, i.e. the flying distance to it
- Remaining amount of fuel
- Availability of precision approach procedures, i.e. Instrument Landing System
- Weather at the alternate airport
- Availability of ground handling agents
- Personal preferences, such as familiarity with a particular airport.

The first alternate that is filed in the flight plan is often not necessarily the best airport to divert to, because it is most often the closest one for convenience of planning and to reduce the alternate fuel to be taken on-board [Coc14].

Based on collected data from FDM, a Monte Carlo Simulation (MCS) was conducted. The results show that depending on the diversion decision for all the aircraft involved in the scenario, severe problems can arise if the same alternate airport is used during an inbound peak. The waiting time can increase significantly, causing the amount of fuel to drop below the required final reserve if no extra fuel was taken on-board prior departure [WDH16b]. Figure 3.1 shows the result from the simulation if – in the most unfavorable event – all aircraft divert to the same alternate airport, which in this case is Nuremberg Airport (NUE/EDDN). The histogram represents the remaining amount of fuel equivalent to flight time when the aircraft touches down, with zero on the horizontal axis being exactly the required final reserve fuel, i.e. landings with negative values would violate legal regulations. One can see that a significant amount of flights landed below final reserve and some flight even landed without fuel at all, which corresponds to $-1800\,\mathrm{s}$ of remaining fuel to final reserve.

The information obtained in this study can be used to provide recommendations to flight crews during their pre-flight briefing and particularly with respect to the amount of extra fuel that should be taken on-board.

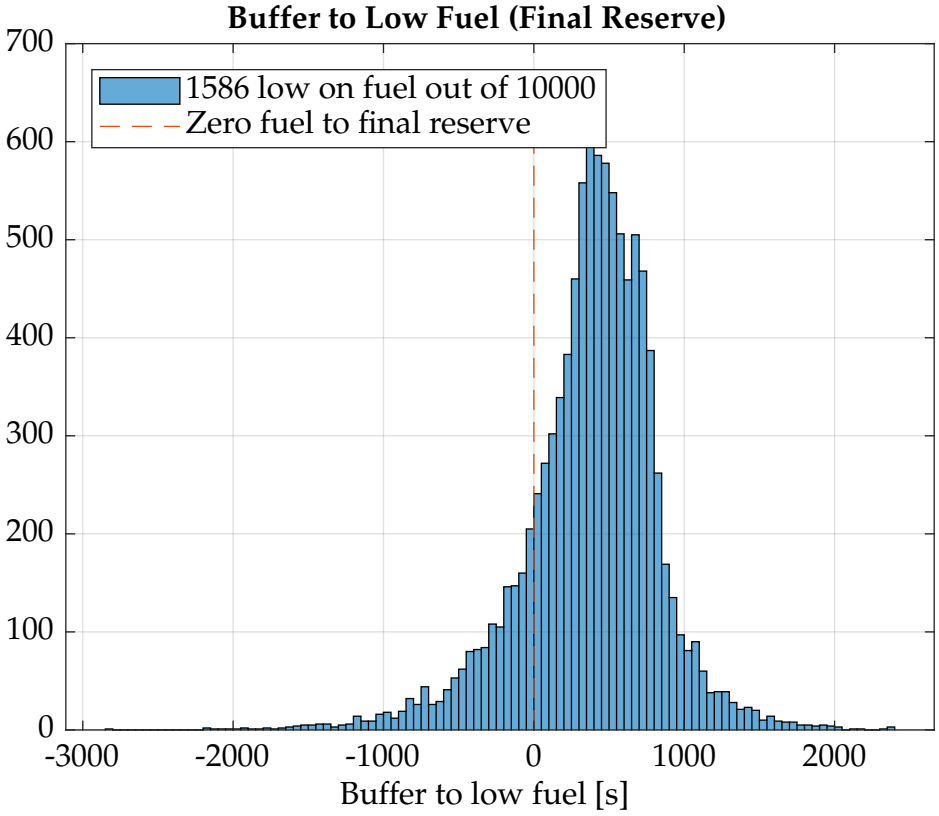

Figure 3.1: *Results of the Monte Carlo Simulation showing a significant part of the simulated flights being low on fuel at touchdown [WDH16a]*

3.6.4.3 Fuel Starvation after Technical Failures

The previous section 3.6.4.2 describes fuel emergency situations that result from disruptions at the destination airport. However, additional flight time can also be caused by issues arising on-board, particularly technical failures.

One example for technical failure contributing to fuel starvation is the Airbus A310 in 2000 that crash-landed at Vienna Schwechat Airport (VIE/LOWW) after running out of fuel [Bun06] on its way from Chania International Airport (CHQ/LGSA) in Greece to Hanover Airport (HAJ/EDDV), Germany. After take-off, the landing gear could not be retracted. While the crew was aware of the increased fuel burn, they decided to continue to MUC/EDDM rather than returning to the departure airport or land at the nearest suitable airport. However, the indication of remaining flight time shown by the Flight Management System (FMS) did not take the increased drag caused by the extended landing gear into account. When the remaining amount of fuel continued to decrease, the crew decided to divert to Vienna. The engines flamed out while on final approach to Vienna. The aircraft landed on the grassy area short of the runway, causing one main gear to collapse.

For the deeper analysis, data from simulator studies that were performed during the

SaMSys project described in section 3.6.1 were used. The situations included an approach scenario that involved two technical failures at the same time. The approach had to be aborted to allow the crew to perform the appropriate troubleshooting. At the same time, the remaining flying time with the available fuel decreased significantly as one of the failures led to the landing gear being jammed in the down position and the flaps to be frozen at the first extended position. Out of the crews that took part in the study, a significant number was not able to safely land the aircraft on time [DMSM+17] without violating the final reserve fuel of 30 minutes.

Taking into account the probability of the technical failure to occur, it was concluded that, with respect to the current regulation of 30 minutes of final reserve fuel, the safety target of less than one accident per 10 million flights set by the EU in its *Flightpath 2050* vision [Eur11a] cannot be achieved. Instead, it is suggested to increase the final reserve to a total of 45 minutes, with reporting still being mandatory if the remaining fuel drops below 30 minutes.

4

Predictive Analysis at a Glance

4.1 Introduction

In chapter 1, the terms *reactive*, *proactive* and *predictive* were already introduced and explained. The goal of this chapter is to present the *Predictive Analysis (PA)* method that was developed at the Institute of Flight System Dynamics (FSD) of the Technical University of Munich (TUM) by the Flight Safety research group and to highlight the contributions of this work with respect to each individual step of the PA.

Firstly published in 2014 [DSH+13] [DSH+14] [WDG+14], the PA aims at quantifying the probability of accidents for individual airlines based on their accident-free Flight Data Monitoring (FDM) data. This is simply because the PA method is supposed to be used by airlines that most probably have not had an accident or a statistically significant number of accidents or of a specific type of accident in their operational history. As aviation has become very safe during the last decades, this applies to most of the operators worldwide offering commercial air transport services to the public.

The PA is based on the idea that, when accidents happen in aviation, it is because several contributing factors, i.e. parameters that have an influence on whether the accident happens or not, are outside of the usual range. The vast majority of accident investigation reports shows this phenomena. The aviation system is sufficiently robust that the deviation of one single factor away from the nominal range will not lead to an accident. For example, if the approach speed is a few knots higher than usual, it will most probably not lead to an overrun since landings are performed with sufficient safety margins to account for uncertainties. The performance of an aircraft is calculated rather conservatively in order to allow some degree of deviation from the expected conditions. However, if the approach speed is higher than usual *and* the aircraft weight is higher than usual *and* the tail wind is higher than usual *and* if, still at the same time, the aircraft touches down later on the runway than usual, suffering a

Runway Excursion (RE) becomes a highly significant risk. One can see in past accident investigation reports such as the Lufthansa A320 in Warsaw in 1992 [Mai94] or the Air France A340 in Toronto 2005 [Tra05] that the combination of several deviations at the same time is what leads to an accident.

While accidents rarely can be observed in flight operations due to the high level of safety throughout the industry, the deviation of one single factor, however, can occur quite frequently, i.e. statistically significantly. *The PA uses this principle and combines these factors and their respective probabilities of deviation to obtain the probability of an accident* by inserting not only one single flight into the method, but a set of flights expressed as probability distributions, representing the airline's flight operations. The output is also a probability distribution of the incident metric. This is the key idea of the Predictive Analysis. The combination of those contributing factors, i.e the quantitative relationships between them, is established by using a model of the aircraft that is based on flight physics, i.e. equations of motion are used as the backbone.

Not all types of accidents are suitable to be investigated using the PA. It is important that the accidents can be well described by flight physics as a *physical* model is required in the process that takes into account most of the contributing factors leading to the accident. For RE and Abnormal Runway Contact (ARC)[1] accidents, the PA can well be used. These accidents are mainly driven by flight physics, or ground physics. However, other types of accidents, such as Mid-Air Collision (MAC), are not quite suitable to be analyzed by the PA. MAC[2], or *Loss of Separation* as its precursor, is mainly influenced by airspace and airway structure as well as traffic density at the current time. The flight physics will only become relevant when looking at the final avoidance maneuver shortly before the collision, which should definitely be the very last barrier preventing MAC from happening. Therefore, the PA can only focus on collision avoidance in the end game, but the emphasis when it comes to preventing MAC should be conflict avoidance, which is not covered within the scope of flight physics considerations.

The seven steps of the PA are shown in figure 4.1 and are described in the following section 4.2. These seven steps are performed in the described order, but it could become necessary to go to previous steps if the results of one particular step is not satisfying, as indicated in figure 4.1.

[1] ARC includes all ways the aircraft can contact the runway surface in a way it is not supposed to. It includes tailstrike, wing tip strike as well as hard landing.

[2] MAC, also known as *airprox*, refers to two aircraft colliding in the air or a violation of the minimum separation between two aircraft.

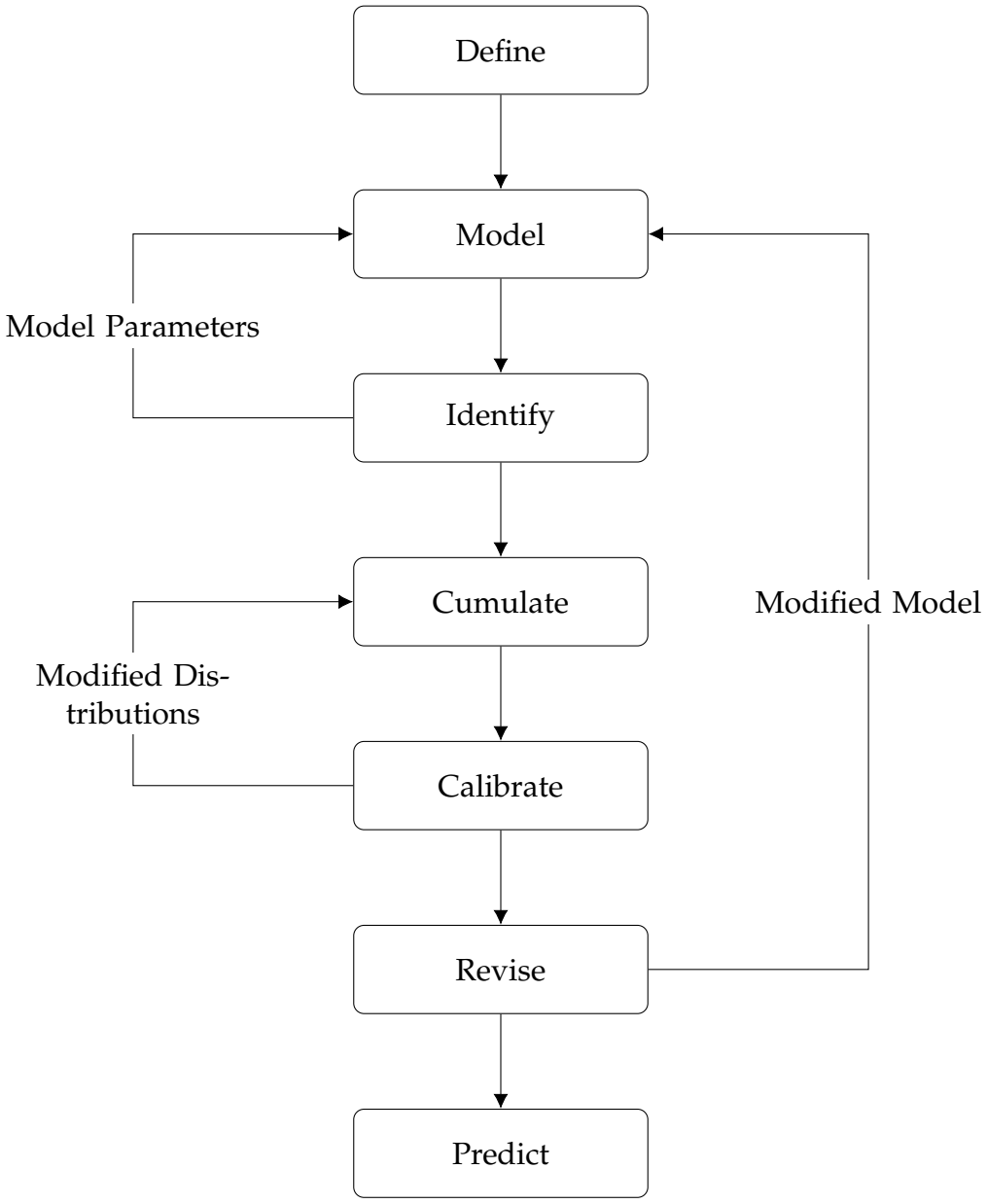

Figure 4.1: *The seven steps of the Predictive Analysis*

4.2 The Seven Steps of the Predictive Analysis

4.2.1 Step 1: Define

The first step of the PA is rather straightforward. Before the actual investigation starts, the type of accident has to be chosen. Along with it, a metric that can be used to describe whether this particular type of accident has happened or not has to be defined. This metric, referred to as the *incident metric*, is a scalar variable that indicates an accident when a certain inequality constraint is met. It must satisfy the following requirements:

1. It must be a continuous variable.
2. It describes the closeness of a particular flight to an accident.
3. If the metric has a value in a pre-defined interval, it indicates that the accident has occurred.
4. One has to be able to measure the incident metric from FDM data.

The incident metric can be chosen intuitively. For the accident type of runway overrun, it is typically chosen to be the remaining distance left on the runway after the aircraft comes to a full stop, as indicated in equation (4.1), referred to as the *stop margin*.

$$\text{incident metric}_{\text{overrun}} = \text{runway length} - \text{landing distance} \tag{4.1}$$

$$\text{stop margin} = \text{runway length} - \text{TD point} - \text{decel. distance} \tag{4.2}$$

When the incident metric becomes smaller, it implies that the remaining distance, i.e. the stop margin, becomes smaller. The landing distance can be obtained by adding (1) the distance from the runway threshold to touchdown and (2) the distance from touchdown that is required to slow down the aircraft to a full stop. If the incident metric decreases below zero, the available runway length is shorter than the distance that the aircraft uses to come to a stop. Consequently, an overrun has occurred. The incident metric can be obtained from FDM data by getting the position where the aircraft stops along with the available runway distance. Of course, in real-life flight operations, the aircraft typically does not come to a full stop on the runway. In fact, it should not because it is supposed to exit the runway as soon as possible due to safety reasons and to allow succeeding aircraft to land or to take-off with minimum delay. In order to compute this incident metric nevertheless, one can compute the distance until the aircraft's speed decreases below a certain value, which should be a sufficiently low value at which safe vacation from the runway is possible and add a constant distance to it to virtually account for coming to a full stop.

Other incident metrics are possible as well. One that also has been used is the difference between the required deceleration to come to a full stop before the end of the runway and the maximum deceleration that can be achieved given the current environmental conditions.

$$\text{incident metric}_{\text{overrun}} = \text{available deceleration} - \text{required deceleration} \tag{4.3}$$

If this incident metric becomes negative, it implies that the achievable deceleration is not sufficient to bring the aircraft to a full stop on the remaining part of the runway. An overrun is destined to happen even if the aircraft is still braking on the runway. However, though the required deceleration is simple to compute based on the remain-

ing runway and the speed of the aircraft, the deceleration that can be achieved on the runway given specific environmental conditions is somewhat difficult to obtain from FDM. More advanced methods have to be implemented to make this assessment possible.

For runway veer-off accidents, the margin between the aircraft's lateral position on the runway and the runway edge can be used as the incident metric. If this value becomes negative, the aircraft has crossed the runway edge and departed from the runway. This is similar to the stop margin for overrun. Another possibility for runway veer-off is to use the time until the aircraft crosses the runway edge if the speed and the heading are kept constant from the current time. This is similar to the use of *time to impact* in other fields of application. Compared to the first incident metric, the latter has the advantage that it takes the rate of closure into account. Imagine an aircraft that is moving closely, but parallel to the runway edge compared to another aircraft located on the centerline, but with a large deviation in heading. The latter could have a much higher risk of veer-off. Using the distance to the runway edge as the incident metric does not take this fully into account.

For ARC accidents, incident metrics can be formulated accordingly. Hard landing accidents can be described by either the aircraft exceeding a certain rate of descent during touchdown or the vertical acceleration during touchdown exceeding a certain value. These limits are provided by the Original Equipment Manufacturers (OEMs) and are measured on-board and recorded by FDM. For tailstrike accidents, where the aircraft's tail touches the ground during either take-off or landing, the tail clearance, i.e. the distance between the aircraft's tail and the runway surface, can be used as an incident metric. For most aircraft types, the OEM provides schematic drawings for tail and wing clearance depending on bank and pitch as a high bank angle close to the ground will cause the wing tip or the engine to touch the runway. Similar to the concept of *time to impact*, the time to impact of the tail on the runway, based on the aircraft's altitude and its pitch as well as their changes over time, can also be used as an incident metric for tailstrike.

It becomes obvious that there is *no right* incident metric. Usually several possibilities exist and all of them are feasible, with advantages and drawbacks for each one. However, one has to keep in mind that whatever is chosen as the incident metric, it will affect all the following steps. An incident metric might ease the work in one of the steps, but lead to great challenges in another. It is, therefore, recommended to look closely at the succeeding steps before making the decision. Of course, one can also reiterate back to this step.

4.2.2 Step 2: Model

Modeling and simulation is a task which many aeronautical engineers have to face. In a typical engineering application, modeling and simulation is popular and preferred to conducting experiments due to many reasons:

- Simulation is usually less costly than performing experiments.
- Simulation is less risky in terms of safety than experiments.
- Simulation outcomes can be an undesired state, such as an accident, which is difficult and/or very costly to achieve in real-life.

Today, modeling and simulation are not only performed to replace real-life experiments, but also to test requirements or implementations during the design phase, often referred to as *Model-Based Design*. In the operational domain, simulation is used during all phases of pilot training. Level D full flight simulators are capable of completely replacing real-life flight training during certain phases, known as Zero Flight Time Training (ZFTT). This is an impressive indication of the level of realism and fidelity achievable in simulators and it demonstrates the capability of aircraft flight dynamics simulation.

The same method of simulation is used in this step of the PA. Equations governing the dynamics of the aircraft are created based on Newton's laws of motion. Forces and moments acting on the aircraft are taken into account, serving as the backbone of the model. In addition, system logics as well as operating procedures are considered to control the forces and moments. Examples include the autobrake system, which, depending on the setting chosen by the flight crew, aims to achieve a constant value of deceleration after touchdown. Typically, different settings of the autobrake system associated with different deceleration values exist, the recommended choice is provided in the airline's operating procedures based on the Flight Crew Operating Manual (FCOM).

The required fidelity of the model heavily depends on the accident to be investigated on the one hand and the availability of data on the other hand. It is not always necessary to create a six Degree of Freedom (DoF) rigid body model for the aircraft. In contrast, other degrees of freedom, e.g. the landing gear compression or moving liquids in the fuel tank, could be added if required. However, one always has to keep in mind that whatever level of modeling is chosen, a number of model parameters are introduced. These parameters have to be obtained from the recorded FDM data, i.e. they have to be observable. This is a vital requirement to the model with respect to the next step, *Identify*, described in section 4.2.3.

The inputs of the model are the *contributing factors*, these are parameters that have

an influence on whether an accident occurs or not. Examples include wind speed, aircraft weight and the braking behavior. They have to be obtained from FDM, which is performed in the *Cumulate* step, see section 4.2.4. The output of the model is the incident metric that is used to identify whether this particular flight that was simulated constitutes an accident or not.

4.2.3 Step 3: Identify

As already mentioned in section 4.2.2, the model incorporates a number of parameters. These parameters have to be identified from the available flight data. While system identification techniques are already quite mature [MK16], they cannot be directly applied to this case. System identification and parameter estimation are most often used during flight tests in order to create a model from a newly built aircraft. For this purpose, specially equipped test aircraft are used that not only measure and record a large number of parameters relevant for the identification, but they also record with significantly higher sampling rates than what routine FDM is used to. Typical values can reach up to 100 Hz, of course, generating a much larger amount of data compared to FDM. Besides, during flight testing, dedicated flight maneuvers are flown in order to maximize the observability of certain parameters. For example, if one would intend to identify the effectivity of the ailerons, one would perform a defined step-input on the ailerons and measure, among others, the bank angle and roll rate as the system response.

The data that is available in FDM, however, is recorded with a much lower frequency, as described in section 2.2. In addition, as the data is recorded during real commercial flights, there are no dedicated system identification flight maneuvers as they would – among all – severely affect passenger comfort. These two factors constitute two major challenges one has to face in this particular step.

Work in this step has already been performed on FDM data obtained from Quick Access Recorders (QARs) [SDH13], a Bayesian approach also proved to be beneficial to identify the parameters from FDM data [SHH14].

4.2.4 Step 4: Cumulate

As already mentioned in section 4.1, not only one set of values describing one single flight is inserted into the model, but rather a batch of flights representing the operations of an airline. The data is obtained from FDM and inserted into the model as probability distributions. The path from values in the flight data to probability distributions of contributing factors that are inserted into the model is performed in this step.

When looking at the contributing factors and at how to extract them from the data, one can quickly see that most of the contributing factors are values in the flight data at certain points in time. For example, the landing weight of the aircraft has an important influence on the behavior of the aircraft and the landing performance. In order to determine the landing weight, one first has to obtain the point at which the aircraft actually lands, i.e. where it touches down on the runway. The second step would be to obtain the weight of the aircraft, which is continuously recorded, at precisely this timepoint, or at least as close as possible. The determination of certain timepoints, therefore, becomes a major task.

While detecting certain timepoints during the flight might seem easy, challenges arise when looking closer at the algorithms. Take the touchdown as an example: It seems to be obvious that there is no dispute of what a touchdown is, but how is it exactly defined? Do we required all wheels to be on the ground or just those on the main landing gear? Do we require all wheels to be spinning? Do we require the landing gears to be compressed to a certain extent? This could make a difference on a slippery runway. What about bounced landings where the aircraft becomes airborne again for a short time before touching down again? Do we consider the first or second touchdown? Even the system logics of an aircraft that detect the touchdown has different ways to process the signal, depending on the aircraft type. It is important that each timepoint is not only clearly detected, but – even more importantly – clearly defined.

After having obtained the timestamps, the next task is to obtain measurements at each specific timepoint, which is a less complex problem. By doing this for a large number of flights, a histogram can be created. For example, the vertical speed at touchdown can be extracted and visualized in a histogram for all available flights. A probability distribution is fitted to the data that is able to match the datapoints the best. One should keep in mind that, though widely used in all applications, the normal (Gaussian) distribution should be considered just like any other distributions. Especially the tails of the distributions should well represent the available data since this is the part that we are particularly interested in. The normal distribution, however, is not a heavy-tail distribution and, therefore, does not accurately represent the data if the tails are heavy.

Whenever working with data, the quality of it has to be taken into account. The values that were recorded can both be biased and contain noise. It is, therefore, desirable to remove those errors during the *Cumulate* process. Work has been performed to reduce the error in the position recording of the aircraft during the landing phase by integrating information from the Instrument Landing System (ILS) as well as by incorporating the runway and taxiway layout [KSR+18]. As the sampling frequency of FDM data typically ranges up to only $16\,\mathrm{Hz}$, a Rauch-Tung-Striebel (RTS) smoother can be used to increase the sampling frequency of those parameters that are recorded with a lower

frequency than the maximum possible [Höh16] [Höh17]. The RTS smoother makes use of the fact that the data is analyzed after the flight, i.e. offline, which also makes future measurements available for smoothing at any timestep in the recording.

4.2.5 Step 5: Calibrate

Before the obtained probability distributions from the *Cumulate* step can be used to predict the accident probability, it has to be ensured that they actually *do* represent the reality. As a direct comparison with real accidents is not possible due to lack of accident data, it should be at least ensured that the method represents the reality in the regular, accident-free area. For this purpose, a probability distribution of the incident metric is generated using Monte Carlo Simulation (MCS) based on the probability distributions of the contributing factors that are already obtained. Ideally, the probability distribution of the incident metric that is generated from simulation should be identical to the probability distribution of the incident metric directly obtained from FDM data.

However, in reality, this is often not the case. The idea of the *Calibrate* step is to reduce the distribution fitting error of both the contributing factors as model input and the incident metric as the model output [Bau16] to allow an overall optimum performance.

4.2.6 Step 6: Revise

At this stage, a model representing the aircraft has already been created in the *Model* step described in section 4.2.2. Though the fidelity of the model is carefully chosen and thus it should well represent the real behavior of the system in the scope of the particular accident type, there might be effects that are either not considered or too complex to be described by physics. Examples include parts of the behavior of the pilot, some of them might not even be aware to the pilots themselves. It has been found, for example, that pilots tend to touch down on the runway earlier if they know that the landing is more critical in terms of stop margin [WF12]. If the runway is not significantly longer than what is required by the aircraft given the circumstances, the touchdown point is much closer to the runway threshold compared to landings for which the available landing distance is much longer than the aircraft would use according to pre-landing calculations.

These dependencies, even if well known, are difficult to be described by physical equations. Instead, purely data-based methods should be used for a mathematical formulation. The concept of *Copulas* is used for this purpose. Copulas have already been widely used in finance mathematics [KHK15] [KKC18]. They are capable of describing dependencies between two or more variables as a non-linear relationship. This is

much more than what correlation coefficients are able to do. This property is essential because we are particularly interested in dependencies in the tails of the distributions as this is the area that is relevant for accident prediction. A simple correlation coefficient, however, consists of only one value that is an approximation for the entire domain.

The dependency structure in measurement data that are created in this step has already been subject to previous studies [Höh14] [HSH14] [HHD+15] [HCB+17].

4.2.7 Step 7: Predict

The very last step of the PA is the *Prediction* itself. Mathematically speaking, the goal is to propagate probability distributions through a physical model. The models that are created in section 4.2.2 are set up in a way that a single flight can be simulated, i.e. the contributing factors of one flight are inserted and one value for the incident metric is calculated by simulation. Afterwards, one can determine whether this particular flight resulted in an accident or not. The task at hand, however, is to insert probability distributions for each contributing factor and to obtain a probability distribution for the incident metric. From this distribution, by quantifying the size of a certain portion of it, the probability of an accident occurring can be obtained.

The most simple and commonly used method for such an application is the Monte Carlo Simulation. The idea of the MCS is to generate samples that are distributed according to the input distributions, simulate each sample and subsequently obtain a distribution of the output based on the sample results. While the idea of MCS is simple and easy to implement, it has a huge drawback, particularly for our application at hand: It is not suitable for quantifying small probabilities as the computational effort increases significantly. For example, in order to quantify a probability of 10^{-n}, at least $N = 10^n$ samples should be generated and simulated in order to obtain one accident – if the samples are *exactly* distributed according to the input distributions, which is only the case if the total number of simulated samples N approaches infinity: $N \to \infty$. In order to obtain a reliable value for the accident probability, the Coefficient of Variation (c.o.v.) must be smaller than one, meaning that the quantified mean value μ is larger than the standard deviation σ.

$$\text{c.o.v} = \frac{\sigma}{\mu} \tag{4.4}$$

The rule of thumb is that the number of simulated samples should be at least two orders of magnitude higher than the minimum number [AW14], i.e.

$$N = 10^{n+2}. \tag{4.5}$$

However, it is, considering the computational effort that is required, usually not feasible to quantify the probabilities that occur in our use case by applying MCS. As described in section 1.1, the safety targets are in the magnitudes of 10^{-7} to 10^{-9}, it can be assumed that the accident probabilities to be identified are in the same order of magnitude.

Various methods to reduce the number of required samples when quantifying small probabilities exist. The most commonly used method is *Importance Sampling* [AW14]. In our case, the method that has proven to be the most suitable is the *Subset Simulation*. The idea of it is to express the accident probability as a product of intermediate conditional probabilities that are much larger in value and, therefore, requiring a much smaller number of samples to be quantified. Details can be found in chapter 5.

5

Statistical Methods

5.1 Introduction

Chapter 4 presented the seven steps of the Predictive Analysis (PA). In this chapter, the statistical methods in *Step 7 – Predict* described in section 4.2.7 will be described in detail.

The task to be accomplished is to quantify which combinations of the contributing factors will lead to a Runway Excursion (RE). A model based on physical relationships, which is presented in chapter 6, is created to perform this assessment. This model essentially describes the way the contributing factors are combined and reflects the influence of them on the incident metric as defined in *Step 1: Define* in section 4.2.1. As the model contains complex and highly non-linear relationships, it is capable of simulating single flights only, rather than a set of flights with continuous input values. The task at hand now is to propagate not one single flight, but a distribution of flights through this model.

Several methods that are potentially capable of this task are presented. Some of them, such as numerical integration, are only presented for the sake of completeness because they prove to be not suitable for our problem. The method of Subset Simulation, which is a more advanced type of Monte Carlo Simulation (MCS) using a Markov Chain Monte Carlo (MCMC) method, turns out to be the method of choice. The way the samples are generated in the MCMC process is described in section 5.4.2 of this chapter. It is a non-deterministic approach.

5.2 Problem Formulation

The process of quantifying accident probabilities using physical models is – mathematically speaking – a way to determine the failure probability of an arbitrary system with its behavior and properties reflected in the given model. Failure can generally be expressed by a certain demand D to a system exceeding its capacity C [AB01]:

$$D > C. \tag{5.1}$$

In the RE example, the demand could be the distance required to stop the aircraft on the runway or the maximum lateral deviation from the runway centerline during deceleration. The corresponding capacity is the runway length and the runway width, respectively. If the latter exceeds the former, a RE accident has occurred.

The goal now is to quantify the size of the hyperplane in which the failure F occurs.

$$p_F = p\left(D > C\right) = \iiint_F p\left(\boldsymbol{\theta}\right) \mathrm{d}\boldsymbol{\theta} \tag{5.2}$$

In equation (5.2), p_F is the probability of failure, $p\left(\boldsymbol{\theta}\right)$ is the probability that a sample consisting of the input vector $\boldsymbol{\theta} \in \mathbb{R}^n$ is located in the failure region.

The failure probability can also be expressed as an expectation:

$$p_F = E\left[r\left(\boldsymbol{\Theta}\right)\right] = \int r\left(\boldsymbol{\theta}\right) q\left(\boldsymbol{\theta}\right) \mathrm{d}\boldsymbol{\theta}, \tag{5.3}$$

where $r\left(\boldsymbol{\theta}\right)$ is the probability of failure if $\boldsymbol{\Theta} = \boldsymbol{\theta}$ [AW14]. Coming back to our problem again using RE as an example, $\boldsymbol{\theta}$ would be a set of multi-dimensional model inputs containing contributing factors such as the wind speed, the aircraft weight etc., one component for each contributing factor. $q\left(\boldsymbol{\theta}\right)$ is the Probability Density Function (PDF) of how $\boldsymbol{\theta}$ is distributed and $r\left(\boldsymbol{\theta}\right)$ indicates the probability of suffering from a RE if $\boldsymbol{\Theta} = \boldsymbol{\theta}$.

In our case, $r\left(\boldsymbol{\theta}\right)$ can be viewed as an indicator function with a value of either zero or one that indicates whether $\boldsymbol{\theta}$ is a failure sample or not, i.e. $r\left(\boldsymbol{\theta}\right)$ becomes $I\left(\boldsymbol{\theta} \in F\right)$ which determines whether $\boldsymbol{\theta}$ lies in the failure region or not. $I\left(\boldsymbol{\theta} \in F\right)$ would use the model output, which is either the lateral deviation on the runway or the landing distance that is actually required for each landing to determine whether it takes the value zero or one. Equation (5.3) then changes to

$$p_F = \int I\left(\boldsymbol{\theta} \in F\right) q\left(\boldsymbol{\theta}\right) \mathrm{d}\boldsymbol{\theta}. \tag{5.4}$$

The aim of this chapter is to find a suitable method to quantify the integral in equation (5.3) or (5.4). As always when performing uncertainty quantification using non-deterministic tools, the method should minimize computational effort and simultaneously minimize the Coefficient of Variation (c.o.v.), which is defined in equation (5.5). μ is the expected value resulting from the method and σ is the standard deviation.

$$\text{c.o.v.} = \frac{\sigma}{\mu} \tag{5.5}$$

The following section 5.3 will present several possible ways to solve for the integral in equation (5.3). The method that is used for our problem, the *Subset Simulation*, is presented section 5.4.

5.3 Failure Quantification

5.3.1 Analytical Method and Numerical Approximation

For some problem formulations, one is able to analytically describe the area in which the failures occur just by simply looking at the mathematical description incorporated in the model. However, if the model is complex or if the dimension of the inputs increases, this becomes an increasingly difficult task. The analytical propagation of probability distributions through models is possible only if (a) all distributions are Gaussian and (b) the equations governing the model are linear. None of these two conditions are fulfilled in our case. The model that describes the behavior of the aircraft during landing phase is highly non-linear and the input distributions are often non-Gaussian. Some distributions can be Kernel Density Estimations (KDEs) and, therefore, an analytical description of their PDFs can be very difficult to obtain.

Every integral can be approximated by summing up a discrete number of contributions, same can be done for equation (5.3). The entire domain in which $\boldsymbol{\theta} \in \mathbb{R}^n$ lies can be divided up into a discrete number of intervals for each dimension, creating a discrete number of hypercubes $\Delta\boldsymbol{\theta} = \Delta\theta_1, ..., \Delta\theta_n$ that are disjoint. The contribution of each of those hypercubes can be computed and summed up. However, for large dimensions, i.e. if n is high, the resulting number of hypercubes increases exponentially, making this method inefficient for high dimensions [AW14].

5.3.2 Monte Carlo Simulation

A common method to approximate the value of an integral is the direct MCS [Geo96], which has proven to be robust for complex problems and particularly for complex ge-

ometries of the failure domain. Besides, the MCS is also suitable for high-dimensional problems [RK17].

The idea of MCS is to generate samples distributed according to the input distributions, evaluate those samples using the model and count the number of samples in the failure domain to estimate the probability of failure. Equation (5.3) can then be re-written by replacing the integral with a sum.

$$p_F \approx \frac{1}{N} \sum_{i=1}^{N} I\left(\boldsymbol{\theta}\right) \tag{5.6}$$

N is the total number of samples and $I\left(\boldsymbol{\theta}\right)$ is the indicator function where $I\left(\boldsymbol{\theta}\right) = 1$ if $\boldsymbol{\theta}$ is a failure sample.

Unfortunately, the MCS has a severe drawback which the quantification of small probabilities. The number of samples N that is required is inverse proportional to the probability that is to be quantified [AB01], i.e.

$$N \propto \frac{1}{p_F}. \tag{5.7}$$

As our problem is about the quantification of small failure probabilities, the computational effort would be tremendously high if the direct MCS method is used.

5.3.3 Importance Sampling

Importance Sampling is an enhancement to the MCS to tackle rare event problems. The idea is that, most often, the failure samples are concentrated in a certain region or several regions. A separate distribution is introduced to generate more samples in these regions, which is referred to as the Importance Sampling Density (ISD) $f\left(\boldsymbol{\theta}\right)$ [AW14]. Using the ISD, equation (5.3) can be modified as follows:

$$p_F = E\left[r\left(\boldsymbol{\Theta}\right)\right] = \int r\left(\boldsymbol{\theta}\right) p\left(\boldsymbol{\theta}\right) \mathrm{d}\boldsymbol{\theta} = \int \frac{r\left(\boldsymbol{\theta}\right) p\left(\boldsymbol{\theta}\right)}{f\left(\boldsymbol{\theta}\right)} f\left(\boldsymbol{\theta}\right) \mathrm{d}\boldsymbol{\theta} = E\left[\frac{r\left(\boldsymbol{\Theta'}\right) p\left(\boldsymbol{\Theta'}\right)}{f\left(\boldsymbol{\Theta'}\right)}\right]. \tag{5.8}$$

In this case, $\boldsymbol{\Theta'}$ is distributed according to f rather than p. The ISD f can be chosen such that many samples can be generated in the failure region [Sri14].

The challenge of importance sampling is to create a suitable ISD, which is only possible if the failure region is well-known and can also be easily described. If the problem contains a large number of random variables, it becomes more challenging to apply importance sampling.

5.4 Subset Simulation

5.4.1 Derivation of the Subset Simulation

The method of Subset Simulation was firstly published in 2001 [AB01]. The idea of Subset Simulation is to express the failure probability as a product of several conditional failure probabilities. As these individual conditional probabilities can be chosen to be large, only a relatively small number of samples is required to quantify them.

$$\begin{aligned} p_F &= p\left(F_m\right) = p\left(\bigcap_{i=1}^{m} F_i\right) = p\left(F_m|\bigcap_{i=1}^{m-1} F_i\right) p\left(\bigcap_{i=1}^{m-1} F_i\right) \\ &= p\left(F_m|F_{m-1}\right) p\left(\bigcap_{i=1}^{m-1} F_i\right) \\ &= p(F_1) \prod_{i=1}^{m-1} p\left(F_{i+1}|F_i\right) \end{aligned} \tag{5.9}$$

In equation 5.9, $p\left(F_i\right)$ represents the failure probability at each subset-level. The failure thresholds on each of those sub-levels are selected such that the conditional failure probabilities $p\left(F_m|F_{m-1}\right)$ are sufficiently large. Using the idea from equation (5.1), equation (5.9) can be re-written as follows:

$$p_F = p\left(D > C\right) = p\left(D > C_1\right) \cdot \prod_{i=2}^{m} p\left(D > C_i\right). \tag{5.10}$$

Depending on the chosen conditional probability $p_0 = p\left(F_m|F_{m-1}\right)$ for each subset level i, the $N_S = p_0 N$ samples that are the closest to the failure region are selected, with N being the total number of samples in each subset. Using those samples, referred to in the following as *seeds*, the samples for the next subset are generated. The Subset Simulation method requires samples to be created conditionally based on existing samples. An efficient way to generate the samples is to use MCMC, which is a class of *Random Walk* algorithms. Ways to perform this generation is presented in the following section 5.4.2. The total number of samples N and the conditional probability p_0 has to be chosen such that p_0 is sufficiently large that it can be quantified using a reasonable number of samples. The number of chains N_C in each subset is, subsequently, $N_C = p_0^{-1}$. The values must be chosen such that N, N_C and N_S are integers.

One has to keep in mind that, for the Subset Simulation, it has to be ensured that the newly generated samples in step $i+1$, even though accepted by the Random Walk algorithm, still have to be located inside the previous failure domain, i.e. $\boldsymbol{\theta}_{i+1} \in F_i$. Otherwise, it has to be rejected as well after the evaluation of this sample, returning back to the seed.

Just like the original direct MCS method, failure quantification using Subset Simulation comes along with a certain degree of error. The estimated failure probability $\tilde{p}_F$ is computed using the number of samples n_i in each subset that are located in the failure domain, which is derived from equation (5.9). Consequently, they only represent an approximation of the real failure probability value.

$$\begin{aligned} \tilde{p}_F &\approx p_F = p(F_1) \prod_{i=1}^{m-1} p\left(F_{i+1}|F_i\right) && (5.11) \\ &= \tilde{p}(F_1) \prod_{i=1}^{m-1} \tilde{p}\left(F_{i+1}|F_i\right) \\ &= \prod_{i=1}^{m} \frac{n_i}{N} = p_0^{m-1} \cdot \frac{n_m}{N} && (5.12) \end{aligned}$$

Going back to the investigation of runway excursion, each intermediate failure threshold C_i can represent different available runway lengths. For example, $p\left(F_1\right)$ could be the probability that only 1000 meters of runway is remaining, $p\left(F_2|F_1\right)$ would be the conditional probability that only 800 meters is remaining given that less than 1000 meters is remaining. This iterative process continues until the subset arrives at the point for which the probability of less than zero distance is remaining is considered, which implies that an excursion occurred. However, one has to keep in mind that in this case, the threshold values are not fixed beforehand. Instead, they are defined in such a way that the values for the conditional probabilities $p\left(F_{i+1}|F_i\right)$ are always constant and sufficiently large that they can be quantified using a reasonable number of samples and returning a low c.o.v..

5.4.2 Sampling Methods

5.4.2.1 Metropolis Algorithm

The Metropolis-Hastings algorithm was firstly introduced by Metropolis et al in 1953 [MRR+], scientists in the Los Alamos Scientific Laboratory (later Los Alamos National Laboratory) in New Mexico, United States. It was generalized by Hastings in 1970 [Has70]. The goal is to generate samples that are distributed according to a given distribution $f_\pi\left(\boldsymbol{x}\right)$ which does not have to be a standard type of probability distribution. In fact, the function $f_\pi\left(\boldsymbol{x}\right)$ only has to be non-negative for all $\boldsymbol{x}$ and does not even necessarily have to integrate to one. It only has to be proportional to a function $f\left(\boldsymbol{x}\right)$ that does integrate to one [AW14], representing the PDF.

$$f_\pi\left(\boldsymbol{x}\right) = \frac{f\left(\boldsymbol{x}\right)}{\int f\left(\boldsymbol{z}\right) \mathrm{d}z} \tag{5.13}$$

The orignal algorithm proposed in 1953 [MRR+] requires the use of a *proposal distribution* $p^*(\boldsymbol{x};\boldsymbol{v})$ which has to be a symmetric function, i.e. $p^*(\boldsymbol{x};\boldsymbol{v}) = p^*(\boldsymbol{v};\boldsymbol{x})$. Of course, there must be efficient ways to generate samples from $p^*(\boldsymbol{x};\boldsymbol{v})$.

The Metropolis algorithm is performed as follows:

1. From the existing sample $\boldsymbol{\theta}_i$, generate a candidate sample $\boldsymbol{\xi}$ using the proposal distribution $p^*(\cdot;\boldsymbol{\theta}_i)$.
2. Calculate $s = \frac{f(\boldsymbol{\xi})}{f(\boldsymbol{\theta}_i)}$, set $a = \min(1, s)$.
3. Accept $\boldsymbol{\xi}$ as the new sample with probability a and set the new sample to $\boldsymbol{\theta}_{i+1} = \boldsymbol{\xi}$; Reject $\boldsymbol{\xi}$ as the new sample with probability $1 - a$ and set the new sample to $\boldsymbol{\theta}_{i+1} = \boldsymbol{\theta}_i$ [1].
4. Evaluate $r(\boldsymbol{\theta})$. Accept the new sample $\boldsymbol{\theta}_{i+1}$ if $\boldsymbol{\theta}_{i+1}$ lies in the failure space, i.e. $\boldsymbol{\theta}_{i+1} \in F_i$ or $r(\boldsymbol{\theta}) = 1$; otherwise reject $\boldsymbol{\theta}_{i+1}$ and set $\boldsymbol{\theta}_{i+1} = \boldsymbol{\theta}_i$.

The Metropolis algorithm will generate samples with f_π as their stationary distribution. This implies that if the initial samples $\boldsymbol{\theta}_k$ are distributed according to f_π, the samples of the next step $\boldsymbol{\theta}_{k+1}$ will also be distributed according to f_π. If $\boldsymbol{\theta}_k$ is not distributed according to f_π, the following samples that are generated are only asymptotically distributed according to f_π as $k \to \infty$.

5.4.2.2 Metropolis-Hastings Algorithm

The generalization performed by Hastings [Has70] allows the use of non-symmetric proposal distributions. The modified algorithm for a generalized proposal function $p^*(\boldsymbol{x};\boldsymbol{v})$ is as follows:

1. From the existing sample $\boldsymbol{\theta}_i$, generate a candidate sample $\boldsymbol{\xi}$ using the proposal distribution $p^*(\cdot;\boldsymbol{\theta}_i)$.
2. Calculate $s = \frac{p^*(\boldsymbol{\theta}_i;\boldsymbol{\xi}_i)\cdot f(\boldsymbol{\xi})}{p^*(\boldsymbol{\xi};\boldsymbol{\theta}_i)\cdot f(\boldsymbol{\theta}_i)}$, set $a = \min(1, s)$.
3. Accept $\boldsymbol{\xi}$ as the new sample with probability a and set new sample to $\boldsymbol{\theta}_{i+1} = \boldsymbol{\xi}$; Reject $\boldsymbol{\xi}$ as the new sample with probability $1 - a$ and set the new sample to $\boldsymbol{\theta}_{i+1} = \boldsymbol{\theta}_i$.
4. Evaluate $r(\boldsymbol{\theta})$. Accept the new sample $\boldsymbol{\theta}_{i+1}$ if $\boldsymbol{\theta}_{i+1}$ lies in the failure space, i.e. $\boldsymbol{\theta}_{i+1} \in F_i$ or $r(\boldsymbol{\theta}) = 1$; otherwise reject $\boldsymbol{\theta}_{i+1}$ and set $\boldsymbol{\theta}_{i+1} = \boldsymbol{\theta}_i$.

[1] This implies a random number has to be sampled from a uniform distribution defined on the interval $[0, 1]$. If the sampled value is smaller or equal a, the candidate $\boldsymbol{\xi}$ is accepted. If not, the candidate is rejected.

One can see that only step 2 is modified to take into account the ratio of the two values of the proposal distribution. If $p^*(\boldsymbol{x};\boldsymbol{v})$ is symmetric, i.e. $p^*(\boldsymbol{x};\boldsymbol{v}) = p^*(\boldsymbol{v};\boldsymbol{x})$, the Metropolis-Hastings (MH) algorithm reduces to the original Metropolis algorithm.

The choice of the proposal distribution determines how fast the Markov Chain moves. Typical choices of symmetric distributions include uniform, Gaussian, triangular or exponential distributions. The key, however, is the spread or the width of the distribution rather than the shape. If it is chosen to be wide, many candidates are generated far away from the original starting sample which, in the first place, implies that the Markov Chain would move fast and quickly explore the entire domain. However, if the spread is chosen to be too wide, many candidates could be rejected, resulting in no movement of the Markov Chain at all. The key, therefore, is to set up the parameters such that the acceptance ratio of the newly generated candidate samples is maximized. The acceptance ratio s_i for the i-th chain is formulated in equation (5.14) when using the generalized MH algorithm.

$$s_i = \frac{p^*(\boldsymbol{\theta}_i;\boldsymbol{\xi}_i)\cdot f(\boldsymbol{\xi})}{p^*(\boldsymbol{\xi};\boldsymbol{\theta}_i)\cdot f(\boldsymbol{\theta}_i)} \tag{5.14}$$

The first terms in both the numerator and denominator disappear if a symmetric proposal distribution according to the original Metropolis algorithm is used.

5.4.2.3 Component-Wise MH Algorithm

The original MH algorithm can lead to significant difficulties when applied to high-dimensional problems. This is due to the fact that the proposal distribution, which is a multi-dimensional distribution, is a product of one-dimensional distributions [AW14]:

$$p^*(\boldsymbol{x};\boldsymbol{v}) = \prod_{k=1}^{n} p_i^*(\boldsymbol{x}_i;\boldsymbol{v}_i)\,, \tag{5.15}$$

where n is the dimension of the problem.

The acceptance ratio according to equation (5.14) is also the product of the acceptance ratios of each of the components:

$$s_k = \prod_{k=1}^{n} r_k = \prod_{k=1}^{n} \frac{p_k^*(\theta_k;\xi_k)\cdot f_k(\xi_k)}{p_k^*(\xi_k;\theta_k)\cdot f_k(\theta_k)} \tag{5.16}$$

One can see that as the dimension n increases, the acceptance ratio will continuously decrease and tend towards zero which makes the original MH algorithm unusable for high-dimensional problems. To cope with this problem, a component-wise MH algorithm is introduced [AB01]. Every component of $\boldsymbol{\theta}_i$ is sampled, accepted or rejected

individually. The algorithm can be written as follows:

1. Using the existing sample $\boldsymbol{\theta}_i = \left[\theta_i^{(1)}, ..., \theta_i^{(k)}\right]$, generate a candidate sample $\boldsymbol{\xi} = \left[\xi^{(1)}, ..., \xi^{(k)}\right]$. Repeat for every component $k = 1, ..., n$:
   (a) Generate $\xi^{(k)}$ using the proposal distribution $p_k^*\left(\cdot; \theta_i^{(k)}\right)$
   (b) Calculate $s_k = \frac{p_k^*\left(\theta_i^{(k)}; \xi^{(k)}\right) \cdot f_k\left(\xi^{(k)}\right)}{p_k^*\left(\xi^{(k)}; \theta_i^{(k)}\right) \cdot f_k\left(\theta_i^{(k)}\right)}$, set $a = \min\left(1, s_k\right)$.
   (c) Set $\xi^{(k)}$ as the new component of the sample with probability a and set the new sample $\theta_{i+1}^{(k)} = \xi^{(k)}$; Reject $\xi^{(k)}$ as the new component of the sample sample with probability $1 - a$ and set the new sample $\theta_{i+1}^{(k)} = \theta_i^{(k)}$.
2. Evaluate $r\left(\boldsymbol{\theta}\right)$. Accept the new sample $\boldsymbol{\theta}_{i+1}$ if $\boldsymbol{\theta}_{i+1}$ lies in the failure space, i.e. $\boldsymbol{\theta}_{i+1} \in F_i$ or $r\left(\boldsymbol{\theta}\right) = 1$; otherwise reject $\boldsymbol{\theta}_{i+1}$ and set $\boldsymbol{\theta}_{i+1} = \boldsymbol{\theta}_i$.

The component-wise MH algorithm significantly increases the acceptance ratio of each sample as only one component of a sample has to be accepted in order to accept the entire sample. However, samples are created in the Markov chain that are more correlated as there will be samples that only differ in some, possibly even a few, but not all components.

5.4.2.4 Infinity Sampling

As mentioned in the previous section 5.4.2.1, the key of the MH algorithm is to set up the proposal distribution such that the maximum acceptance ratio can be achieved as this indicates that the Markov Chain is moving the quickest. The component-wise MH already introduces a method to significantly increase the acceptance ratio compared to the original MH. However, the samples obtained from the component-wise MH are often correlated as very often, only one or a few components of the sample is actually changed when using the component-wise MH, resulting in many samples being identical in the other components. Two research groups simultaneously proposed a new sampling method in 2015 to cope with this issue. It was named *Subset Infinity* [PA15] and *Conditional Sampling* [PBZS15], by each group, respectively.

The idea of this algorithm is that every random variable can be expressed by a linear combination of a infinite number of Gaussian random variables. In order to simplify the algorithm, the samples are transformed into the standard normal ($\boldsymbol{U}$) space. The existing sample $\boldsymbol{\theta}_k$ and the candidate that is generated $\boldsymbol{\xi}$ are transformed to $\boldsymbol{U}$-space with zero mean and unit variance. The samples can be then generated as follows:

1. Set $a = \sqrt{1 - \boldsymbol{\sigma^2}}$, $\boldsymbol{\sigma} = [\sigma_1, ..., \sigma_n]$ are the standard deviations for each of the components of $\boldsymbol{\theta}$.

2. Generate a new candidate sample $\boldsymbol{\xi}$ according to the Gaussian distribution $\mathcal{N} \sim (\boldsymbol{a\theta}_k, \boldsymbol{\sigma})$
3. Set the new sample $\boldsymbol{\theta}_{k+1} = \boldsymbol{\xi}$ if $\boldsymbol{\xi}$ lies in the failure space, i.e. $\boldsymbol{\xi} \in F_k$, otherwise reject $\boldsymbol{\xi}$.

This procedure is repeated for every sample during every step of the Subset Simulation.

5.4.2.5 Dependency Sampling

Throughout this work, the contributing factors are considered to be independent, which is only an approximation of the true world. It is, however, possible to incorporate dependency structures into the input distributions by using Copulas, see section 4.2.6, and multi-dimensional distributions [HWK+18]. The details are further explored in separate research efforts.

5.4.3 Post-Processing

The Subset Simulation provides an estimate of the failure probability $\tilde{p}_F$ of a system given certain input distributions shown in equation (5.12). However, it is also important to provide a measure that is capable of describing the confidence of this value. The inventors of the Subset Simulation proposed a Bayesian post-processor in 2011 [ZBAK12] that is able to quantify the confidence of the result coming out from the Subset Simulation. Using equation (5.12), each intermediate failure probability $p(F_1), ..., p(F_m)$ is considered as a stochastic variable using the Bayesian approach.

The final failure probability p_F can then be described as a stochastic variable that is distributed according to a Beta distribution $\mathcal{Be}$ [ZBAK12].

$$p_F \sim \mathcal{Be}(a, b), \tag{5.17}$$

with the parameters a and b being

$$a = \frac{\prod_{i=1}^{m} \frac{n_i+1}{N+2} \left(1 - \prod_{i=1}^{m} \frac{n_i+2}{N+3}\right)}{\prod_{i=1}^{m} \frac{n_i+2}{N+3} - \prod_{i=1}^{m} \frac{n_i+1}{N+2}} \tag{5.18}$$

$$b = \frac{\left(1 - \prod_{i=1}^{m} \frac{n_i+1}{N+2}\right) \left(1 - \prod_{i=1}^{m} \frac{n_i+2}{N+3}\right)}{\prod_{i=1}^{m} \frac{n_i+2}{N+3} - \prod_{i=1}^{m} \frac{n_i+1}{N+2}}. \tag{5.19}$$

The Beta distribution is defined only on the interval $[0; 1]$ with both parameters $a, b > 0$.

The expected value or the failure probability and its square can be given as [ZBAK12]:

$$\mathrm{E}\left[p_F\right] = \prod_{i=1}^{m} \frac{n_i + 1}{N + 2} \tag{5.20}$$

$$\mathrm{E}\left[p_F^2\right] = \prod_{i=1}^{m} \frac{(n_i + 1)(n_i + 2)}{(N + 2)(N + 3)} \tag{5.21}$$

The variance of the failure probability can be computed as follows:

$$\mathrm{Var}\left(p_F\right) = \mathrm{E}\left[p_F^2\right] - \left(\mathrm{E}\left[p_F\right]\right)^2. \tag{5.22}$$

Equation (5.22) provides a measure to describe how confident we are about the results obtained in the Subset Simulation. One can see that with increasing number of total samples N, the variance decreases, which is consistent also with the experiences previously made with direct MCS.

The span of the confidence interval, which is typically two-sided, can also be derived from the Beta distribution using the Inverse Cumulative Distribution Function (ICDF) F^{-1} by computing the values $F^{-1}\left(\frac{\alpha}{2}\right)$ and $F^{-1}\left(1 - \frac{\alpha}{2}\right)$ for a given confidence level α [FHK+16]. α is typically chosen to be 0.05.

5.5 Current Use of Subset Simulation

Since its introduction in 2001, the method of Subset Simulation has become increasingly popular in many engineering fields. Most of the applications involve civil engineering or geodesy since Subset Simulation has become the tool of choice when it comes to quantifying small probabilities, i.e. rare events, for high-dimensional problems.

Subset Simulation has been used for safety assessment of pipelines that are buried underground [KT16]. This particular application has two very important similarities with our problem of quantifying aviation accident probabilities: The rare occurrence and the severe consequence when it occurs. The contributing factors to the failure of pipelines are mainly the loading on the structure from both inside and the outside of the pipeline as well as corrosion. A precise safety assessment can help to reliably determine maintenance cycles to predictively take actions before a pipeline actually fails. Because the threat of earthquakes, which is a rare, but highly severe event, represents a significant contributing factor, underwater pipelines are subject to safety assessments using Subset Simulation as well. A physical model can also be used here, describing the pipeline as a Timoshenko beam [LZK18]. The stability of offshore structures in general is a frequent subject of safety assessment using Subset Simulation. The motion of

the sea can be described using a given power spectrum density function [LH17], which also serves as the input into the Subset Simulation.

Rare events can also include natural disasters. Landslides, for example, occur very rarely, but with severe consequences. In order to determine the probability of the failure of rock slopes, Subset Simulation has been used [JHZ17]. For structural reliability analysis, very often the Finite Element Method (FEM) is used for the modeling of the object as it can be well combined with Subset Simulation in order to determine the failure of building structures [PHD+09].

Subset Simulation has also been applied in the field of aviation, mostly during the development process of aerial systems. For example, in order to certify flight control algorithms used for aerial refueling, the system has to achieve a certain level of precision and availability. This can be shown by quantifying the probability of violation using Subset Simulation [LH15]. With the increasing use of Remotely Piloted Aircraft Systems (RPASs) in the airspace, the risk of collision has significantly increased. To counter this, systems have to be built into the RPASs that have to achieve a certain performance level such that the risk of collision is sufficiently low, which the Subset Simulation is used to asses [MMAR16]. The first application using Subset Simulation to quantify accident probabilities for operational flight safety related to this work was published in 2014 [WDH14] using a 3 Degree of Freedom (DoF) model for runway overrun, i.e. considering the longitudinal motion only.

6

Flight Mechanics and Model Build-up

6.1 Coordinate Frames and Transformation

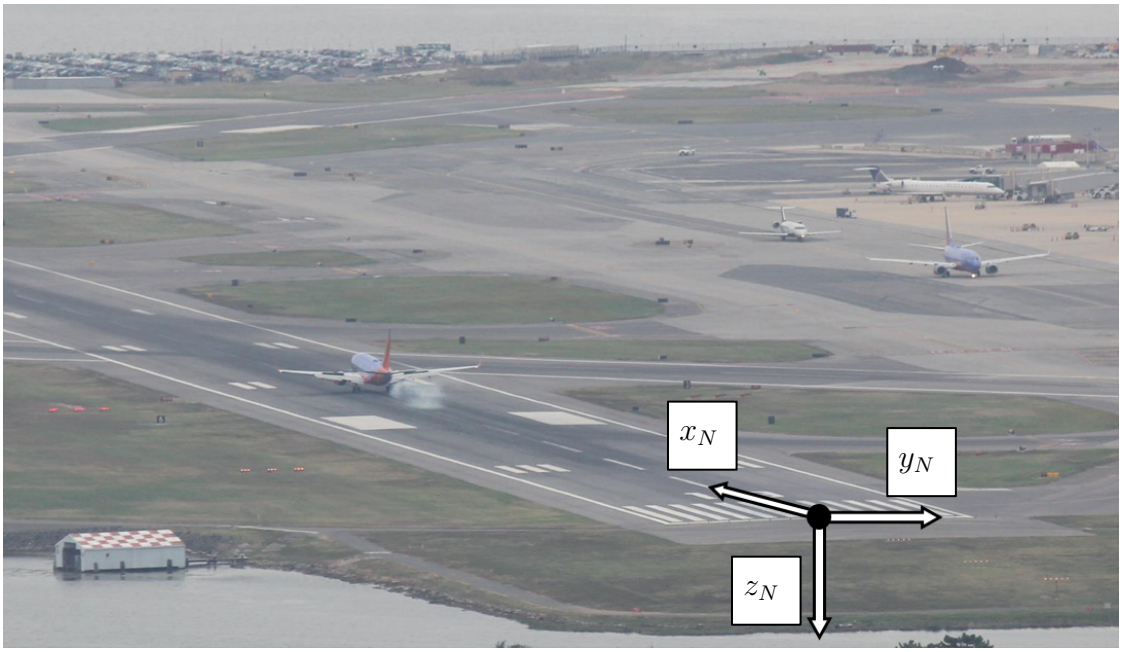

Figure 6.1: *Definition of the local navigation coordinate frame N*

Before setting up the model of the aircraft, it has to be clarified which coordinate frames are used. As the landing phase is considered during this work, the coordinate frame that is of primary interest is a local navigation frame N, which is illustrated in figure 6.1. Its origin is located on the runway centerline at the runway threshold. Its x axis is pointing towards the far end of the runway and parallel to it. The z axis is parallel to the z axis of the North-East-Down (NED) (O) frame, pointing to the direction of the earth's gravitation. The y axis is pointing to the right, perpendicular to the runway direction and the direction of gravitation. For the N frame, it can be beneficial to move the origin of the coordinate frame translationally along the x axis to the touchdown point of the

aircraft, however, still located on the runway centerline. The reason is that the braking phase is considered, which starts at the point of touchdown. This only changes the reference point, but not the physical behavior. The N frame can be obtained by rotating the North-East-Down (O) frame by the runway heading Ψ_R around the z axis using the transformation matrix $\boldsymbol{M}_{NO}$. The z component is often neglected since it is parallel for both frames.

$$\boldsymbol{M}_{NO} = \begin{pmatrix} \cos\Psi_R & \sin\Psi_R & 0 \\ \sin\Psi_R & \cos\Psi_R & 0 \\ 0 & 0 & 1 \end{pmatrix} \tag{6.1}$$

Within the scope of this work, N is considered to be an inertial frame. This assumption can be made due to the relatively small speed of the aircraft compared to the earth's rotation during the landing as well as the fact that only short distances are covered during this relevant time period. Newton's laws are thus valid, the force and moments can directly be integrated.

6.2 Aircraft Model

The nomenclature of the variables for forces and moments is defined in equation (6.2).

$$\left(\vec{\boldsymbol{F}}^{\text{Reference point}}_{\text{Type of force}}\right)_{\text{Reference frame}} \tag{6.2}$$

The total force $\left(\vec{\boldsymbol{F}}^{G}_{T}\right)_B$ acting on the aircraft is obtained by summing up the four types of forces: aerodynamics A, gravitation G, propulsion P and landing gear L. In this particular case, the forces are provided in the body fixed coordinate frame B. Different reference points are used for each of the forces. While the gravitational forces act on the Center of Gravity (CG) G, the aerodynamic forces act at the aerodynamic reference point A, the propulsion forces act at the propulsion reference point P and the landing gear forces act at the landing gear reference point L. Of course, the landing gears can also be treated separately, resulting in individual landing gear forces and reference points. Same applies to the engines.

The total force acting on the aircraft can be given as:

$$\left(\vec{\boldsymbol{F}}_T\right)_B = \sum\left(\vec{\boldsymbol{F}}\right)_B = \left(\vec{\boldsymbol{F}}^{A}_{A}\right)_B + \left(\vec{\boldsymbol{F}}^{G}_{G}\right)_B + \left(\vec{\boldsymbol{F}}^{P}_{P}\right)_B + \left(\vec{\boldsymbol{F}}^{L}_{L}\right)_B = \begin{pmatrix} X_T \\ Y_T \\ Z_T \end{pmatrix}_B . \tag{6.3}$$

However, the same forces can also be expressed with respect to a same reference point

R that is defined for the entire aircraft:

$$\left(\vec{\boldsymbol{F}}_T^R\right)_B = \sum \left(\vec{\boldsymbol{F}}^R\right)_B = \left(\vec{\boldsymbol{F}}_A^R\right)_B + \left(\vec{\boldsymbol{F}}_G^R\right)_B + \left(\vec{\boldsymbol{F}}_P^R\right)_B + \left(\vec{\boldsymbol{F}}_L^R\right)_B = \begin{pmatrix} X_T^R \\ Y_T^R \\ Z_T^R \end{pmatrix}_B . \tag{6.4}$$

From the perspective of physical modeling, using the CG G as the reference point seems to be the straightforward choice. Typically, this approach poses some problems since the CG moves during the flight as the mass of the aircraft changes when the amount of fuel decreases. In our case, however, since the time frame to be considered is relatively small, it is a valid assumption to have a fixed CG that is used as the reference point. Using the CG offers some convenient simplifications concerning the mathematical formulations.

Same applies to the moments acting on the aircraft. The moment is obtained from the forces by multiplying with their respective lever arm.

$$\left(\vec{\boldsymbol{M}}_T\right)_B = \sum \left(\vec{\boldsymbol{M}}\right)_B = \left(\vec{\boldsymbol{M}}_A\right)_B + \left(\vec{\boldsymbol{M}}_G\right)_B + \left(\vec{\boldsymbol{M}}_P\right)_B + \left(\vec{\boldsymbol{M}}_L\right)_B = \begin{pmatrix} L_T \\ M_T \\ N_T \end{pmatrix}_B \tag{6.5}$$

$$\left(\vec{\boldsymbol{M}}_T^G\right)_B = \sum \left(\vec{\boldsymbol{M}}^G\right)_B = \left(\vec{\boldsymbol{M}}_A^G\right)_B + \left(\vec{\boldsymbol{M}}_G^G\right)_B + \left(\vec{\boldsymbol{M}}_P^G\right)_B + \left(\vec{\boldsymbol{M}}_L^G\right)_B \tag{6.6}$$

$$= \sum_i \left(\vec{\boldsymbol{r}}^{GR_i}\right)_B \times \left(\vec{\boldsymbol{F}}_i^{R_i}\right)_B \tag{6.7}$$

$$= \left(\vec{\boldsymbol{r}}^{GA}\right)_B \times \left(\vec{\boldsymbol{F}}_A^A\right)_B + \left(\vec{\boldsymbol{r}}^{GP}\right)_B \times \left(\vec{\boldsymbol{F}}_P^P\right)_B + \left(\vec{\boldsymbol{r}}^{GL}\right)_B \times \left(\vec{\boldsymbol{F}}_L^L\right)_B + \underbrace{\left(\vec{\boldsymbol{r}}^{GG}\right)_B}_{=0} \times \left(\vec{\boldsymbol{F}}_G^G\right)_B \tag{6.8}$$

In equation (6.5), the forces and moments are summed up, taking into account the respective coordinate frames. The moments consist of forces with their respective lever arms, see equation (6.7). If the CG is used as the reference point, the summand describing the moments resulting from the gravitational forces reduces to zero since the lever arm $\left(\vec{\boldsymbol{r}}^{GG}\right)_B$ is zero, see equation (6.8). Each of the summands could possibly consist of several summands themselves with different reference points. Examples include several forces and moments resulting from several engines or landing gears. The total force is transformed into the inertial frame N using the transformation matrix $\boldsymbol{M}_{NB}$. A flat, non-rotating earth is assumed, i.e. $\vec{\boldsymbol{\omega}}^{IE} = \vec{\boldsymbol{\omega}}^{EO} = 0$.

Figure 6.2 shows a Boeing VC-25A shortly after touchdown on the runway. The thrust reverse is deployed as well as the ground spoilers. The flaps and slats typically remain in the landing configuration until the aircraft vacates the runway. All the sources of forces and moments acting on the aircraft during landing are visible in this picture.

Figure 6.2: *A Boeing VC-25A after touchdown on the runway. The deceleration devices are clearly visible.*

6.2.1 Aerodynamics

The aerodynamic is an important feature of every aircraft, not just in the air, but also on the ground. The aerodynamic configuration of an aircraft can significantly change throughout and between the flight phases. During take-off, it is important to generate as much lift as possible, but keeping the drag to a minimum, leading to a compromise that typically is a partial extension of the high-lift system. During cruise, it is important to reduce the drag to a minimum and to obtain the optimum lift-to-drag ratio to reduce fuel burn. During the approach, the lift should be maximized while the drag can be higher than during take-off. After touchdown down on the ground, the objective is to maximize drag while destroying the lift as much as possible. The drag contributes to the slow-down of the aircraft while the reduced lift augments the effect of wheel brakes as the aircraft is pressed on the ground. In the following section, a model of these variations of the aerodynamic is presented.

6.2.1.1 Aerodynamic Forces

For the aerodynamic forces acting on the aircraft, the following model is chosen:

$$C_L = C_{L0} + C_{L\alpha} \cdot \alpha + C_{L\eta} \cdot \eta + \Delta C_{L,\text{Flaps}} + \Delta C_{L,\text{Spoiler}} \tag{6.9}$$

$$C_D = C_{D0} + k \cdot C_L^2 + \Delta C_{D,\text{Spoiler}} + \Delta C_{D,\text{Flaps}} + \Delta C_{D,\text{Gear}} \tag{6.10}$$

$$C_Q = C_{Q0} + C_{Q\beta} \cdot \beta + C_{Q\zeta} \cdot \zeta. \tag{6.11}$$

Equation (6.9) shows what the lift coefficient C_L is composed of. A linear dependency to the angle of attack α is assumed as well as to the elevator deflection η. Furthermore, the extension of the flaps during landing will cause an increase of the lift coefficient

while the extension of the spoilers will cause a decrease of it. It is assumed that the extension of the landing gear does not change the aerodynamic lift. As the aircraft is already on the ground, the ground effect is already a part of the model above.

For the drag coefficient C_D in equation (6.10), a quadratic drag polar is introduced using the factor k to describe the induced drag. The extension of the spoilers and the flaps causes additional drag as well as the extension of the landing gear. The landing gear does not affect the lift coefficient.

The side force coefficient C_Q in equation (6.11) is only dependent on the side slip angle β and the rudder deflection ζ. In this case, as the aircraft is assumed to be symmetric, C_{Q0} is set to zero.

As only the landing phase is considered, the configuration of the aircraft does not change in the meantime. The only change in aerodynamics occurs when the spoilers are deployed shortly after touchdown. To extract the parameters above from recorded flight data, it is useful to introduce a single zero lift coefficient C_{L0} and a zero drag coefficient C_{D0} for the final configuration, i.e. flaps extended to landing configuration and gear down. Thus, equations (6.9) to (6.11) simplify to the following:

$$C_L = C_{L0,\text{Final}} + C_{L\alpha} \cdot \alpha + C_{L\eta} \cdot \eta + \Delta C_{L,\text{Spoiler}} \tag{6.12}$$

$$C_D = C_{D0,\text{Final}} + k \cdot C_L^2 + \Delta C_{D,\text{Spoiler}} \tag{6.13}$$

$$C_Q = C_{Q\beta} \cdot \beta + C_{Q\zeta} \cdot \zeta. \tag{6.14}$$

The aerodynamic forces are computed using equation (6.15). ρ refers to the prevailing air density, $\vec{\boldsymbol{V}}_A$ is the aerodynamic velocity of the aircraft and S is the reference wing area of the aircraft. The wind speed is included by subtracting it from the kinematic speed, i.e. the Groundspeed (GS) in order to obtain the aerodynamic speed $\vec{\boldsymbol{V}}_A$, which is the True Airspeed (TAS). The Indicated Airspeed (IAS) can be used in this equation instead of the TAS if the density is substituted with the air density at Mean Sea Level (MSL), $\rho_0 = 1.225\,\mathrm{kg\,m^{-3}}$.

$$\left(\vec{\boldsymbol{F}}_A^R\right)_A = \begin{bmatrix} -D \\ Q \\ -L \end{bmatrix}_A = \frac{1}{2}\rho \left|\vec{\boldsymbol{V}}_A\right|^2 S \begin{bmatrix} -C_D \\ C_Q \\ -C_L \end{bmatrix}_A \tag{6.15}$$

6.2.1.2 Aerodynamic Moments

For the aerodynamic roll moment coefficient C_l, the pitch moment coefficient C_m and the yaw moment coefficient C_n, the following model is introduced:

$$C_l = \underbrace{C_{l0}}_{=0} + C_{l\beta} \cdot \beta + C_{l\xi} \cdot \xi + C_{lp} \cdot p \tag{6.16}$$

$$C_m = C_{m0} + C_{m\alpha} \cdot \alpha + C_{m\eta} \cdot \eta + C_{mq} \cdot q \tag{6.17}$$

$$C_n = \underbrace{C_{n0}}_{=0} + C_{n\beta} \cdot \beta + C_{n\zeta} \cdot \zeta + C_{nr} \cdot r. \tag{6.18}$$

Each of the three coefficient has a first $C_{\cdot 0}$ term, which can be assumed to be zero for the roll coefficient in equation (6.16) and for the yaw coefficient in equation (6.18) since the aircraft is symmetric. The roll moment coefficient is linearly dependent on the angle of sideslip β, the aileron deflection ξ as well as the roll rate p. The pitch moment is dependent on the angle of attack α, the elevator deflection η and the pitch rate q. For the yaw moment, a linear relationship is assumed for the angle of sideslip β, the rudder deflection ζ as well as the yaw rate r, as these values are typically small. The last term in each equation represents a damping moment since it is dependent on each of the respective angular rates.

The aerodynamic moments are computed in equation (6.19). They are given in the body-fixed frame B.

$$\left(\vec{\boldsymbol{M}}_A^R\right)_B = \frac{1}{2}\rho \left|\vec{\boldsymbol{V}}_A\right|^2 S \begin{bmatrix} \frac{b}{2}C_l \\ \bar{c}C_m \\ \frac{b}{2}C_n \end{bmatrix}_B \tag{6.19}$$

As the moment coefficients are dimensionless, the values have to be multiplied with a characteristic length of the aircraft in addition to the dynamic pressure and the wing reference area. For the pitch moment, this is the half-wingspan $\frac{b}{2}$ and for the roll moment and yaw moment, this is the Mean Aerodynamic Chord (MAC) $\bar{c}$.

6.2.1.3 Frame Transformation

As the aerodynamic forces and moments are typically computed in the aerodynamic frame, they have to be transformed into the body-fixed coordinate frame B according to equations (6.20) and (6.21).

$$\left(\vec{\boldsymbol{F}}_A^R\right)_B = \boldsymbol{M}_{BA} \cdot \left(\vec{\boldsymbol{F}}_A^R\right)_A \tag{6.20}$$

$$\left(\vec{\boldsymbol{M}}_A^R\right)_B = \boldsymbol{M}_{BA} \cdot \left(\vec{\boldsymbol{M}}_A^R\right)_A \tag{6.21}$$

It uses the rotation matrix $\boldsymbol{M}_{BA}$.

$$\boldsymbol{M}_{BA} = \begin{bmatrix} \cos\alpha\cos\beta & -\cos\alpha\sin\beta & -\sin\alpha \\ \sin\beta & \cos\beta & 0 \\ \sin\alpha\cos\beta & -\sin\alpha\sin\beta & \cos\alpha \end{bmatrix} \tag{6.22}$$

6.2.2 Gravitation

Gravitation consists of the gravity forces of the earth and the centrifugal forces that depends on the radius to the earth's rotational axis. The gravitation is given in the navigation (N) frame. The gravitational forces always act at the CG and in the direction of the z axis of the O and N frame.

$$\left(\vec{\boldsymbol{F}}_G^G\right)_O = g_0 \begin{bmatrix} 0 \\ 0 \\ 1 \end{bmatrix}_O \tag{6.23}$$

It can be transformed into the body-fixed frame using the rotational matrix $\boldsymbol{M}_{BO}$,

$$\left(\vec{\boldsymbol{F}}_G^G\right)_O = \boldsymbol{M}_{BO} \cdot \left(\vec{\boldsymbol{F}}_G^G\right)_O \tag{6.24}$$

with

$$\boldsymbol{M}_{BO} = \begin{bmatrix} \cos\Psi\cos\Phi & \sin\Psi\cos\Theta & -\sin\Theta \\ \cos\Psi\sin\Theta\sin\Phi - \sin\Psi\cos\Phi & \sin\Psi\sin\Theta\sin\Psi + \cos\Psi\cos\Phi & \cos\Theta\sin\Phi \\ \cos\Psi\sin\Theta\cos\Phi + \sin\Psi\sin\Phi & \sin\Psi\sin\Theta\cos\Phi - \cos\Psi\sin\Phi & \cos\Theta\cos\Phi \end{bmatrix}. \tag{6.25}$$

As the CG is used as the reference point, the gravitational forces do not cause any moment to the aircraft since the lever arm is zero.

6.2.3 Propulsion

The propulsion provides reverse thrust during the deceleration phase after touch-down. In the case of a turboprop engine, the reverse thrust is achieved by propeller reverse.

As a simplification, the rotational speed of the low pressure shaft ω_{N1}, along with the density of the air ρ, is used to determine the thrust force. A constant k_P is introduced as well as the exponent n_ρ to characterize the influence of the air density.

$$\left(\vec{\boldsymbol{F}}_P^R\right) = k_P \cdot \omega_{N1} \cdot \left(\frac{\rho_S}{\rho}\right)^{n_\rho} \tag{6.26}$$

The engines are mounted on the aircraft with a fixed yaw angle κ_P and a pitch angle σ_P. By assuming that $\kappa_P = \sigma_P = 0$, the B frame becomes identical to the propulsion frame P of the aircraft. The engine model that is used is a simple approximation of the real behavior of the propulsion system that is able to deliver the fidelity required for this use-case. Of course, the fidelity of the engine model can be increased if required [KWH+19].

6.3 Landing Gear Model

The landing gear model is a central part of this work as the gear has an important role during landing. The task of the landing gear is to absorb the energy of the vertical motion of the aircraft during touchdown and, subsequently, to dissolve the energy of the aircraft's horizontal motion by applying the brakes until the speed is sufficiently low to exit the runway via available taxiways. The gear has to apply lateral forces that enable traction as well. Last but not least, the landing gear supports the aircraft on the runway surface by applying vertical forces.

6.3.1 Model Build-up

The landing gear is modeled as a mass-spring-damper assembly shown in figure 6.3. An additional degree of freedom, which is the vertical position of the landing gear, is introduced. For the modeling purpose, a landing gear-fixed coordinate frame L is introduced containing the axes x_L, y_L and z_L. The y_L axis always points parallel to the rotational axis of the wheel while the z_L axis points perpendicular to the contact surface. The x_L axis is perpendicular to the y_L and the z_L axis, shown in equation (6.27). The unit vectors of the coordinate frame $\vec{\boldsymbol{e}}_{x_L}$, $\vec{\boldsymbol{e}}_{y_L}$ and $\vec{\boldsymbol{e}}_{z_L}$ are related as follows:

$$\vec{\boldsymbol{e}}_{x_L} = \vec{\boldsymbol{e}}_{y_L} \times \vec{\boldsymbol{e}}_{z_L}. \tag{6.27}$$

The contact force between the tire and the ground surface is obtained from the compression of the tire, depending on the spring constant of the tire k_T based on the height of the aircraft reference point and the aircraft's attitude.

The position of each landing gear $\left(\vec{\boldsymbol{r}}^{L^i}\right)_N$ with $i = \{\text{nose; main left; main right; ...}\}$ relative to the N frame can be determined by obtaining the position of the landing gear relative to the aircraft's reference point in the B frame and the position of the reference

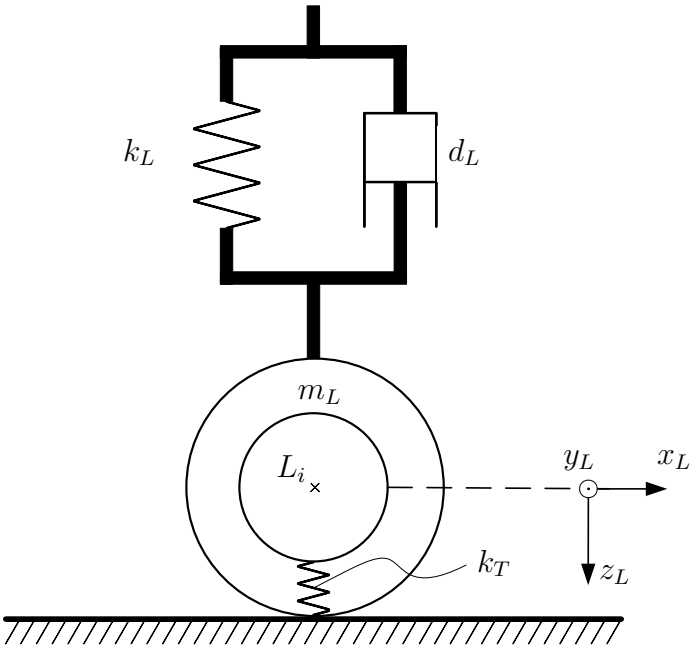

Figure 6.3: *The model of the landing gear*

point in the N frame. The height above the runway reference point can be determined by taking the position in the B frame and transforming it into the N and taking the z component.

$$\left(\vec{\boldsymbol{r}}^{L^i}\right)_B = \left(\vec{\boldsymbol{r}}^{R}\right)_B + \left(\vec{\boldsymbol{r}}^{RL^i}\right)_B \tag{6.28}$$

$$\left(\vec{\boldsymbol{r}}^{L^i}\right)_N = \boldsymbol{M}_{NB} \cdot \left(\vec{\boldsymbol{r}}^{L^i}\right)_B = \begin{bmatrix} x^{L^i} \\ y^{L^i} \\ z^{L^i} \end{bmatrix}_N \tag{6.29}$$

As the runway does not necessarily have to be flat, a model of the runway is used to determine the height of the runway h_R at a given point (x_N, y_N). It is important to know that the height is defined to be positive in the direction of the negative z axis of the N frame as the z axis is pointing downwards.

$$h_R = f(x_N, y_N) \tag{6.30}$$

The compression Δl^i of the landing gear can be obtained by determining the position of each landing gear relative to the local runway surface.

$$\Delta l^i = l_0^i - \left(z^{L_i} + h_R^i\left(x_N^i, y_N^i\right)\right) \tag{6.31}$$

l_0^i is the length of the landing gear in the uncompressed state.

The gear compression as well as its derivatives can be used in the following to deter-

mine the forces acting on the landing gear. They are each divided into three components. The first component $F_{Li,\perp}$ is the force that is perpendicular to the contact plane, i.e. the runway surface. This force is typically acting vertically on the aircraft, ensuring it does not sink into the runway. The second component $F_{Li,\parallel x}$ is the braking force. It acts in the longitudinal direction of the tires which is the same as the longitudinal direction of the aircraft for the landing gears that do not have steering control (main gears). For the nose gear, the direction has to be computed depending on the deflection of the steering control. The third component $F_{Li,\parallel y}$ acts tangential to the runway surface, but perpendicular to the braking forces. It consists of the forces that ensure that the aircraft stays on the track in the longitudinal direction.

The three components and the way they are modeled are described further in detail in the sections 6.3.2 to 6.3.4.

6.3.2 Landing Gear Normal Forces

The force normal to the contact surface acting on the landing gear $F_{Li,\perp}$ can directly be computed using the compression of the tire. Since the aircraft considered is on the ground, we assume that both the pitch and the bank angle are small. Therefore, the force acting normal to the contact surface is parallel to the landing gear strut.

The equation of motion of the landing gear can then be derived using the principle of equilibrium of forces, as shown in equation (6.32). Δl_i is substituted by l_i in the following equations.

$$\begin{aligned} m_{Li}\ddot{l}_i &= -c_i l_i - d_i \dot{l}_i + F_{Li,\perp} \\ m_{Li}\ddot{l}_i &= -c_i l_i - d_i \dot{l}_i - l_i \cdot k_T \end{aligned} \tag{6.32}$$

The damper and spring characteristics, d and k, are not necessarily constant, but can be dependent on the gear compression, i.e. $d\left(l_i\right)$ and $k\left(l_i\right)$. A typical landing gear, for example, becomes stiffer with higher compression.

Equation (6.32) is used to compute the vertical acceleration of the landing gear based on the current state, i.e. vertical position and speed. By integrating the acceleration, the vertical speed and position are obtained.

6.3.3 Landing Gear Longitudinal Forces

6.3.3.1 Tire Rotational Dynamics

The longitudinal force acting on each landing gear is typically the braking force. As they are friction forces, they depend on the normal force between the tire and the runway surface, which was described in section 6.3.2, and the friction coefficient. The friction coefficient μ_x in the longitudinal direction can be controlled by the application of the brake pedals δ_B or – in case of the use of autobrake – an equivalent degree of braking action corresponding to a given brake pedal deflection.

$$F_{Li,\parallel x} = \mu_x \left(\delta_B\right) F_{Li,\perp} \tag{6.33}$$

When modeling the ground forces, the slope and bank of the runway surface has to be taken into account. Therefore, the normal vector $\vec{n}$ at each contact point has to be computed. All friction forces have to be within the plane perpendicular to the normal vector. This can cause one of the most common mistakes when performing contact force modeling. If the normal vector is not considered and a slope is introduced, the aircraft will behave as if it is standing on a staircase: tilted, but still with vertical contact forces only.

In order to obtain the exact relationship between the brake pedal and the friction coefficient, it is assumed that the moment acting on the braking disc M_B is proportional to the brake pedal deflection that is applied using the constant coefficient k_B.

$$M_B = k_B \cdot \delta_B \tag{6.34}$$

The speed of the wheel is controlled by the braking system by applying a torque on the wheel via the braking discs. In order to obtain the wheel speed, the rotating part of the wheel and tire, including the braking disc, is taken into account using the equilibrium of moments.

$$J_W \cdot \ddot{\omega}_W = -r_T \cdot F_{Li,\parallel x} + M_B \tag{6.35}$$

J_W is the moment of inertia of the entire rotating assembly, r_T is the radius of the tire and M_B is the torque applied on the wheel by the braking discs. The wheel speed V_W can be obtained from the wheel angular speed ω_W.

$$V_W = \omega_W \cdot r_T \left(t\right) \tag{6.36}$$

As shown in figure 6.3, the ground contact force relies on the deformation of the tire. Therefore, the tire radius r_T can change significantly over time depending on the com-

pression, which is indicated in equation (6.36).

Figure 6.4 shows the braking disc on one of the main landing gears of a Boeing 777-300ER. The tire, the braking disc assembly as well as the hydraulic actuators are shown, which push the braking disc in the direction of the wheel, building up the braking torque. The wear indicator pin, which is the long pin pointing towards the braking disc, is clearly visible. If the right end of the pin is close to the fixation, it indicates that the braking disc is worn out and should be exchanged.

Figure 6.4: *Braking disc on the main landing gear of a Boeing 777-300ER*

6.3.3.2 Slip-Friction Curve

The moment acting on the braking disc controls the speed of the tire. Hans B. Pacejka and his team developed a model that is able to describe the relationship between the slip s and the friction coefficient μ [Pac12] [BNP87], shown in equation (6.37).

$$\mu(s) = D \cdot \sin\left(C \cdot \arctan\left(B \cdot (1-E) \cdot s + E \cdot \arctan\left(B \cdot s\right)\right)\right) \tag{6.37}$$

B, C, D and E are parameters that can be used to adapt the curve to match the environmental conditions. The slip s is defined as the difference between the tire speed and the road surface speed, normalized to the surface speed, see equation (6.38). For aircraft tires, as the wheels are not powered, the slip will always be positive since the wheel speed cannot become faster than the groundspeed. The slip can also not reach values above 1 since no change of direction of motion is considered.

$$s = \frac{V_{\text{Groundspeed}} - V_{\text{Wheel}}}{V_{\text{Groundspeed}}} \tag{6.38}$$

Equation (6.37) is sometimes also referred to as the *Magic Formula* because there is no physical motivation behind its derivation. However, it has become a standard for friction and tire modeling, particularly in the automotive industry because of its close resemblance to the reality. The exact shape of the curve is influenced by the surface of the runway, the tire tread, runway contaminant, if applicable, the groundspeed as well as the tire pressure [Eng95].

Figure 6.5 shows a typical curve based on the friction model described in equation (6.37). For small slip values, the curve is approximately linear with a high gradient. As the slip increases, the gradient decreases and it reaches its maximum before decreasing again. For this particular example, the maximum is located at approximately $s = 0.2$. The friction coefficient decreases until a slip value of $s = 1$ is reached, i.e. the tire is completely skidding on the runway surface.

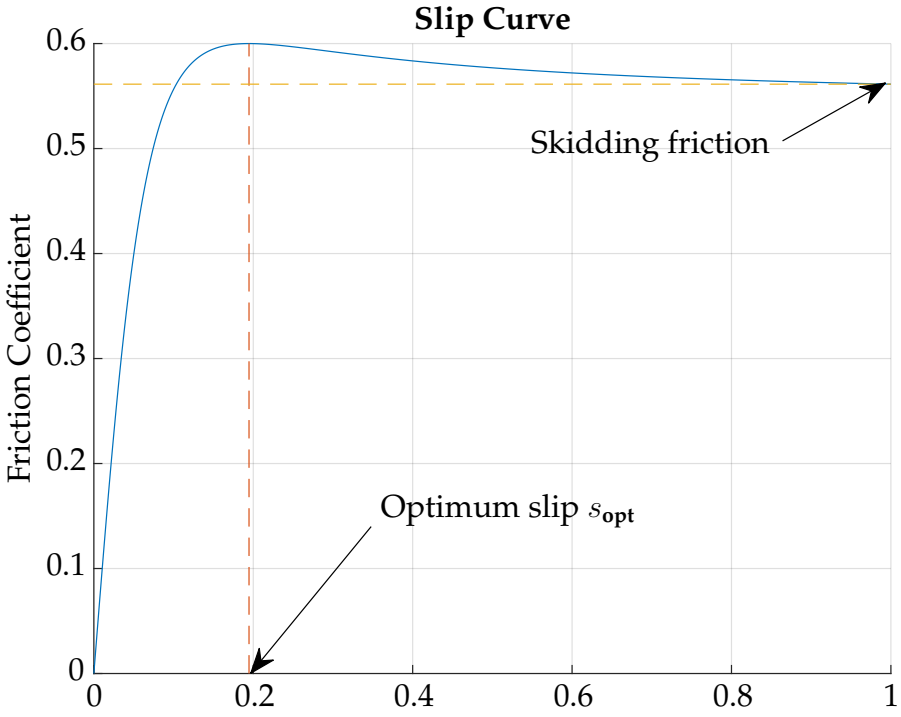

Figure 6.5: *An example friction curve based on Pacejka's model*

The maximum slip s_{opt} divides the friction curve into a left part and a right part. On the left part, a stable behavior with respect to the rotational dynamics of the tire can be observed. When the wheel speed decreases, the slip will increase if the groundspeed remains constant. A higher slip will lead to a higher friction coefficient and subsequently a higher friction, resulting in a higher braking force. The friction force speeds up the wheel again and we obtain an asymptotically stable behavior.

On the right side of the curve, however, it becomes obvious that the behavior becomes unstable when the slip becomes larger than the optimum value s_{opt}. When the braking

pressure and subsequently the moment on the braking disc is increased, the moment leads to a decrease of the wheel speed. The lower wheel speed results in a higher slip value. The higher slip value leads to a *lower* friction coefficient and, thus, a lower braking force which acts against the deceleration of the wheel. This will result in an even lower tire speed and higher slip. The wheel will lock instantaneously and start skidding over the runway. In order to move back to the left side of the slip curve, the braking pressure has to be released until the wheel speeds up again. This behavior is an analogy to the dependency between the angle of attack α and the lift coefficient C_L. After the maximum lift coefficient $C_{L,\text{max}}$ is reached, the lift decreases again when the angle of attack is further increased. The effect of the ailerons are now inverted, leading to a highly dangerous and, therefore, undesired state.

Most cars manufactured today as well as large aeroplanes are equipped with an Anti-Lock Braking System (ABS). The goal of the ABS is to make sure the slip never exceeds the value at which the maximum friction coefficient is achieved. While the certification specifications for large aeroplanes [Eur18] require the efficiency of the braking system to achieve certain values, it does not explicitly require the installation of ABS. However, from the aircraft performance point of view, the Original Equipment Manufacturer (OEM) will most likely install anti-skid systems in order to achieve the required Accelerate-Stop Distances (ASDs) or Landing Distances (LDs). The regulations for all-weather operations ("CS-AWO") [Eur03] specify that "*an antiskid braking system is considered to be essential*" when (possibly automatic) landings are performed without decision heights. Due to the low visibility in these situations, the pilot is likely to aggressively use the brakes, which increases the risk of skidding. On most modern commercial aircraft, an autobrake system is available which can only be activated along with an ABS to ensure the autobrake does not apply too much brake pressure, causing the tires to skid. In fact, the risk of tire burst increases significantly if the tire is skidding. Of course, the local wear-out increases as well, leading to a shorter lifetime for the tire.

The four figures 6.6 to 6.9 show how the shape of the curve is influenced by the four parameters B, C, D and E. For each figure, one parameter is varied. The default parameter values for this particular example are as set follows:

$$\begin{aligned} B &= 8 \\ C &= 2 \\ D &= 0.6 \\ E &= 1. \end{aligned}$$

Figure 6.6 shows the slip curve for different values of B. This parameter does not influence the maximum friction that can be achieved. It rather changes the gradient

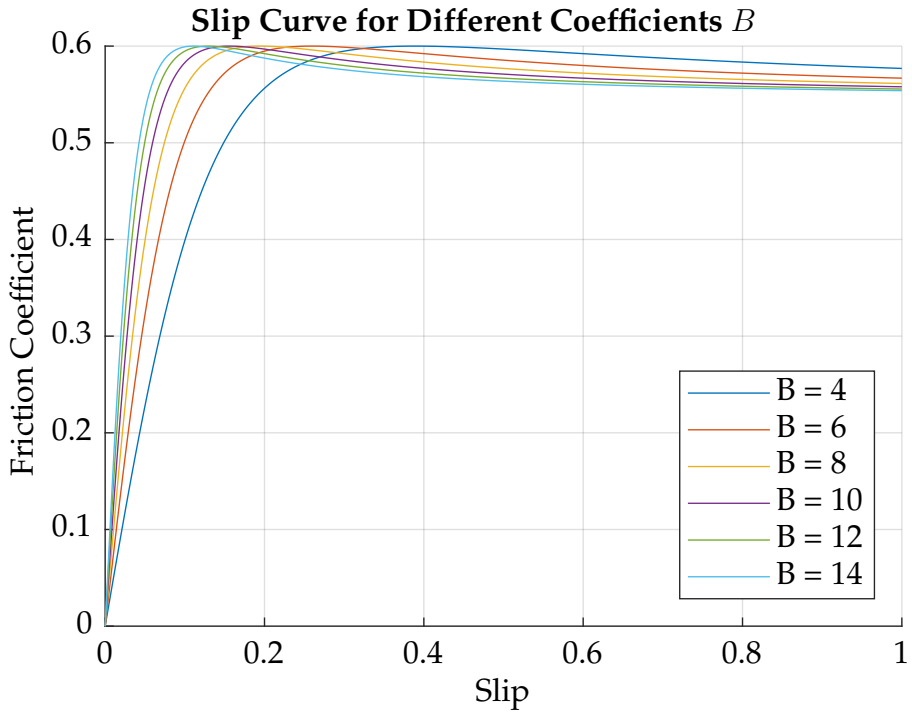

Figure 6.6: *Pacejka's curve for different values of parameter B*

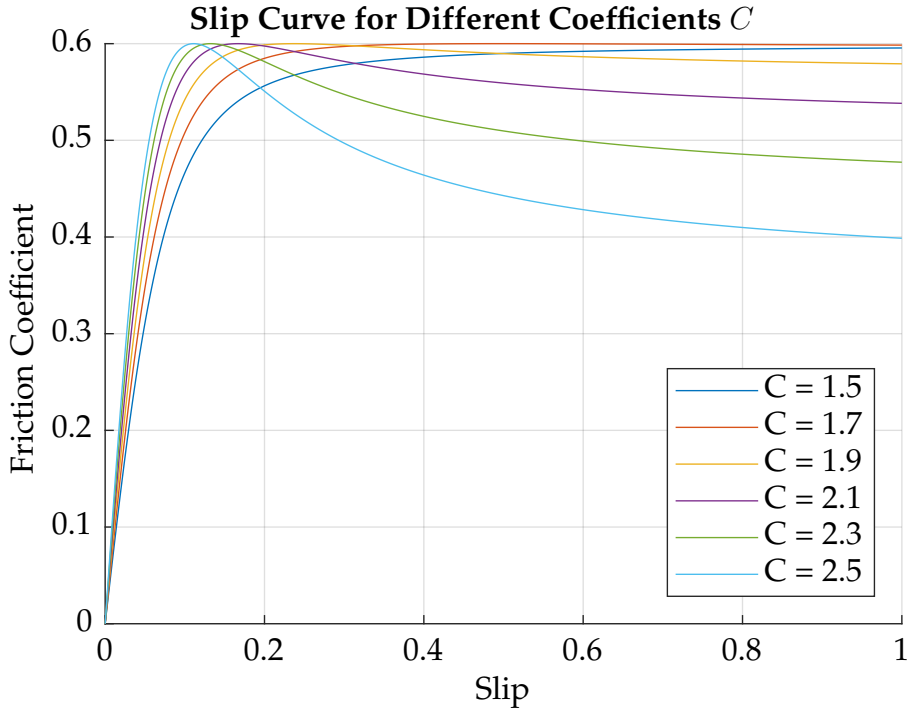

Figure 6.7: *Pacejka's curve for different values of parameter C*

of the curve for small slip values but also slightly moves the slip value at which the maximum braking coefficient is achieved to the right as B increases.

In figure 6.7, the coefficient C is varied. The most significant influence is how the curve decreases after reaching its maximum. For higher values of C, the friction decreases

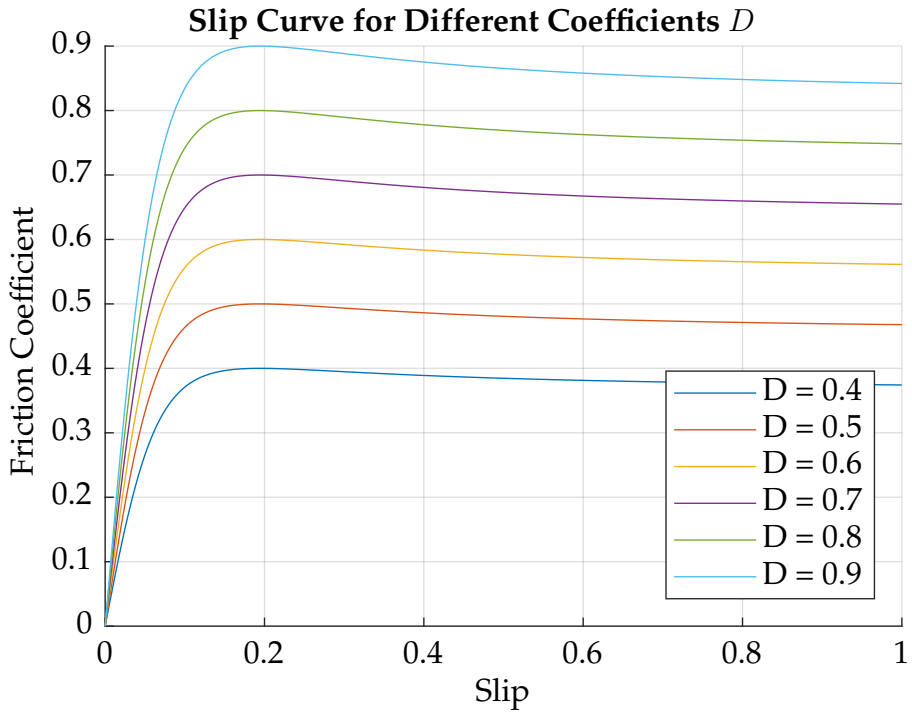

Figure 6.8: *Pacejka's curve for different values of parameter D*

significantly when the slip moves towards 1. For lower values of C, the maximum friction coefficient moves towards higher slip values or even reaches its maximum when the wheel is skidding. For higher values of C, the unstable behavior of the wheel, as described above, becomes more severe as the negative gradient after s_{opt} becomes steeper.

The influence of the parameter D, shown in figure 6.8 can directly be interpreted from equation (6.37). It is a scaling parameter and D directly represents the maximum friction coefficient that can be achieved.

The most significant influence of the parameter E, as shown in figure 6.9, is the skidding friction coefficient and the gradient of the curve right of the maximum, while the part left of s_{opt} is barely affected by E.

6.3.4 Landing Gear Lateral Forces – Unbraked Wheel

The lateral forces acting on the tires are generated when the aircraft moves into the lateral direction, which is usually not the dominant part of the motion. A method very similar to describing the longitudinal forces in section 6.3.3 is used. Instead of using the slip as the independent variable, the sideslip angle β_T between the direction of movement of the aircraft and the longitudinal direction of the tire is used.

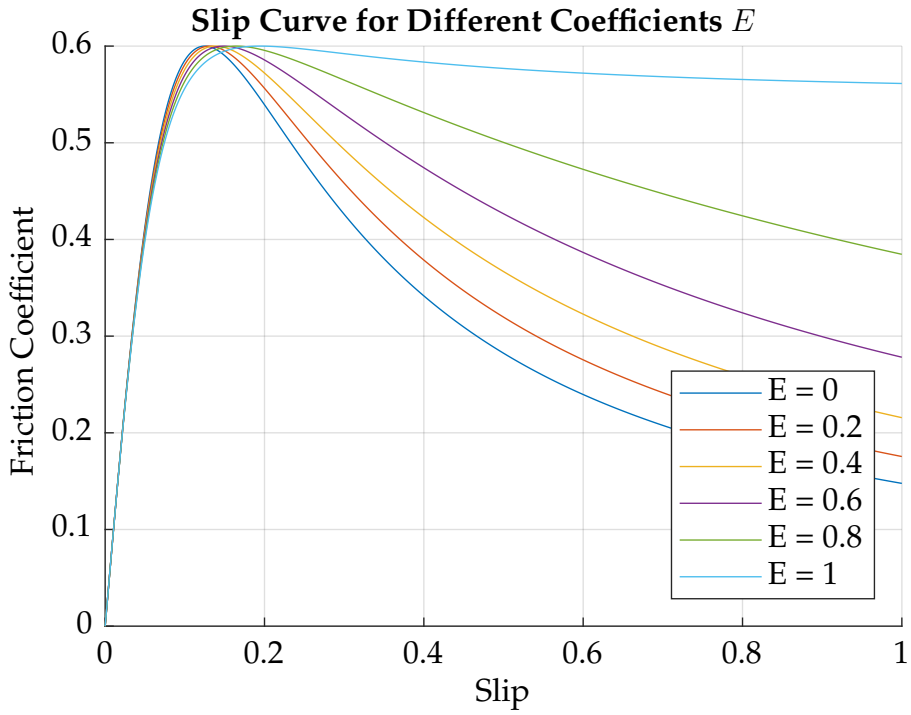

Figure 6.9: *Pacejka's curve for different values of parameter E*

$$F_{Li,\|y} = \mu_y\left(\beta_T\right) \cdot F_{Li,\perp} \tag{6.39}$$

The lateral force friction coefficient μ_y can be obtained using a very similar model as equation (6.37) [Pac12].

$$\mu_y\left(\beta_T\right) = D \cdot \sin\left(C \cdot \arctan\left(B \cdot (1-E) \cdot \frac{2\beta_T}{\pi} + E \cdot \arctan\left(B\frac{2\beta_T}{\pi}\right)\right)\right) \tag{6.40}$$

The sideslip angle is normalized to $\frac{\pi}{2}$. Like the longitudinal forces, a very similar curve as shown in figure 6.5 is obtained. The difference is that the horizontal axis shows the sideslip angle and that the interval for possible values is limited to $\beta_T \in \left[-\frac{\pi}{2}; \frac{\pi}{2}\right]$, or $[-90°; 90°]$. This means that the lateral forces increase with an increasing sideslip angle until a maximum value. When the sideslip angle is $\pi/2$, the tire is effectively skidding over the runway surface. The curve is symmetric since the behavior of the aircraft is equal regardless of skidding to the left or the right, as shown in figure 6.10.

The modeling of the lateral landing gear forces is important for two reasons. First, the lateral force on the main landing gear contribute to the directional stability of the aircraft on the ground. Second, the lateral forces on the nose landing gear are essential for steering on the ground, particularly at low speed. Of course, steering can also be achieved by differential braking on the main landing gear or by the rudder if the dynamic air pressure is sufficiently high.

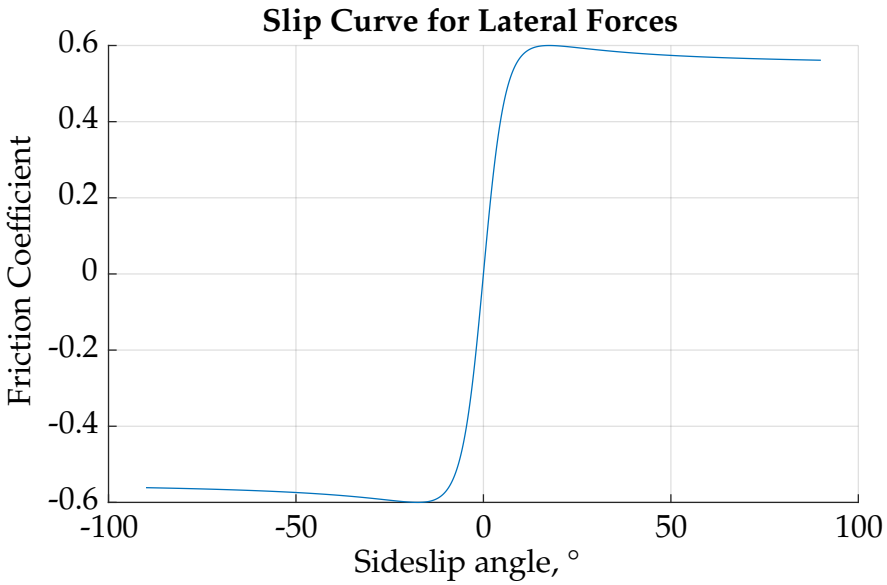

Figure 6.10: *Pacejka's curve for lateral forces*

6.3.5 Combination of Sideslip and Braking

When the sideslip β_T and the longitudinal slip s occur at the same time, which can only be the case for the main landing gear during braking, the velocity of the tire V_T can be divided into two components. One of them, $V_{T,\parallel}$, is acting parallel to the velocity relative to the ground V_{GS}, the other one is acting perpendicular to it $V_{T,\perp}$, i.e. in the x and the y axis of the kinematic frame K. The components are shown in figure 6.11 and are described in equation 6.41 using the transformation matrix $\boldsymbol{M}_{KL}$. Since the z components of both coordinate frames are parallel, it will be neglected in the following.

$$\begin{pmatrix} V_{T,\parallel} \\ V_{T,\perp} \end{pmatrix}_K = \boldsymbol{M}_{KL} \cdot \begin{pmatrix} V_T \\ 0 \end{pmatrix}_T = \begin{pmatrix} \cos\beta_T & \sin\beta_T \\ -\sin\beta_T & \cos\beta_T \end{pmatrix} \cdot \begin{pmatrix} V_T \\ 0 \end{pmatrix}_T = V_T \begin{pmatrix} \cos\beta_T \\ -\sin\beta_T \end{pmatrix} \tag{6.41}$$

The perpendicular component $V_{T,\perp}$ corresponds to a skidding friction while the parallel component $V_{T,\parallel}$ can be modeled using Pacejka's curve as described in section 6.3.3. Both the longitudinal and the lateral forces for a braked wheel can then be obtained. Using the definition of friction force in equation (6.33) and the definition of the slip in equation (6.38), both components of the speed $V_{T,\parallel}$ and $V_{T,\perp}$ will cause a friction force.

$$\left(\vec{\boldsymbol{F}}_{Li}\right)_K = F_{Li,\perp} \cdot \begin{pmatrix} \mu\left(s\left(V_{\text{Tire}} = V_{T,\parallel}\right)\right) \\ \mu\left(s = 1\right) \end{pmatrix}_K \tag{6.42}$$

By transforming the forces back to the L frame, the friction force on the landing gear

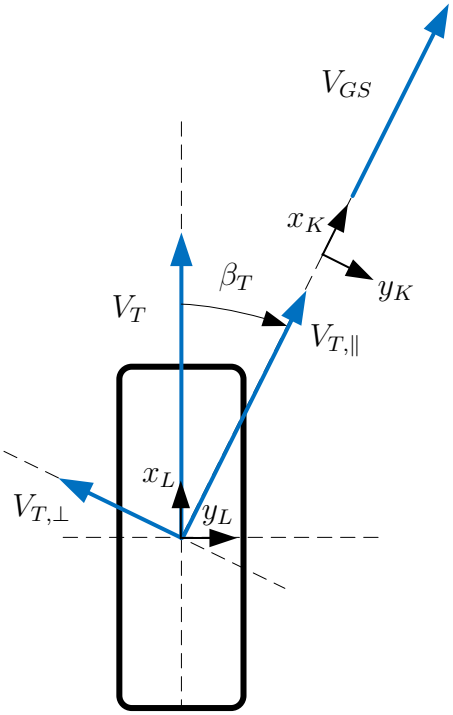

Figure 6.11: *The motion of the single wheel and the coordinate frames*

in the landing gear frame can be obtained.

$$
\begin{aligned}
\left(\vec{\boldsymbol{F}}_{Li}\right)_L &= \boldsymbol{M}_{LK} \cdot \left(\vec{\boldsymbol{F}}_{Li}\right)_K \\
&= F_{Li,\perp} \cdot \boldsymbol{M}_{KL}^T \cdot \begin{pmatrix} \mu\left(s\left(V_{\text{Tire}} = V_{T,\parallel}\right)\right) \\ \mu\left(s=1\right) \end{pmatrix}_K \\
&= F_{Li,\perp} \cdot \begin{pmatrix} \cos\beta_T & -\sin\beta_T \\ \sin\beta_T & \cos\beta_T \end{pmatrix} \cdot \begin{pmatrix} \mu\left(s\left(V_{\text{Tire}} = V_{T,\parallel}\right)\right) \\ \mu\left(s=1\right) \end{pmatrix}_K \qquad (6.43) \\
&= F_{Li,\perp} \cdot \begin{pmatrix} \mu\left(s\left(V_{\text{Tire}} = V_T\cos\beta_T\right)\right)\cos\beta_T - \mu\left(s=1\right)\sin\beta_T \\ \mu\left(s\left(V_{\text{Tire}} = V_T\cos\beta_T\right)\right)\sin\beta_T + \mu\left(s=1\right)\cos\beta_T \end{pmatrix}_L \qquad (6.44)
\end{aligned}
$$

For any landing gear with a steering feature, particularly the nose gear, the gear coordinate frame L does not coincide with the aircraft's body-fixed frame B, making an additional transformation necessary using the nosewheel deflection angle ζ_L. This is shown in figure 6.12. The transformation matrix $\boldsymbol{M}_{LB}$ is as follows:

$$
\boldsymbol{M}_{LB} = \begin{pmatrix} \cos\zeta_L & \sin\zeta_L \\ -\sin\zeta_L & \cos\zeta_L \end{pmatrix}. \qquad (6.45)
$$

The forces of the respective landing gear is thus:

$$
\left(\vec{\boldsymbol{F}}_{Li}\right)_B = \boldsymbol{M}_{BL} \cdot \left(\vec{\boldsymbol{F}}_{Li}\right)_L. \qquad (6.46)
$$

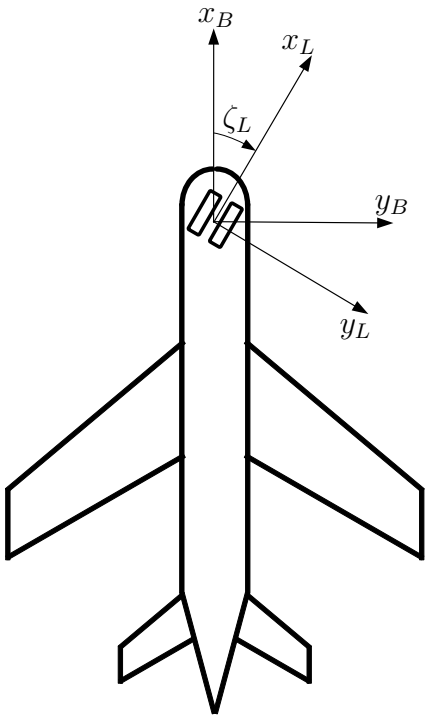

Figure 6.12: *Transformation of the nose gear forces to body-fixed frame*

As $\boldsymbol{M}_{LB}$ is a rotational matrix, $\boldsymbol{M}_{LB} = \boldsymbol{M}_{BL}^T$ applies. It reduces to the identity matrix if there is no deflection of the wheel, i.e. $\zeta_L = 0$.

6.3.6 Landing Gear Model Assembly and Integration

After all the components of the forces acting on the landing gear strut have been described, it is possible to assemble the forces $\left(\vec{\boldsymbol{F}}_L^G\right)_B$ and moments $\left(\vec{\boldsymbol{M}}_L^G\right)_B$ and to describe their influence on the entire aircraft. The CG G is chosen as the reference point. The number of elements depends on the number of landing gears.

$$\begin{aligned}\left(\vec{\boldsymbol{F}}_L^G\right)_B &= \sum_i \left(\vec{\boldsymbol{F}}_{Li}^G\right)_B \\ &= \sum_i F_{Li,\perp} \boldsymbol{M}_{BL_i} \begin{pmatrix} \mu\left(s\left(V_{\text{Tire}} = V_{Ti}\cos\beta_{Ti}\right)\right)\cos\beta_{Ti} - \mu\left(s=1\right)\sin\beta_{Ti} \\ \mu\left(s\left(V_{\text{Tire}} = V_{Ti}\cos\beta_{Ti}\right)\right)\sin\beta_{Ti} + \mu\left(s=1\right)\cos\beta_{Ti} \\ 1 \end{pmatrix}_B\end{aligned} \tag{6.47}$$

The resulting moments from the landing gear forces are obtained using the vector from the CG to the respective contact points between the landing gear and the ground sur-

face, which can be found in equation (6.29).

$$\left(\vec{\boldsymbol{M}}_L^G\right)_B = \sum_i \left(\vec{\boldsymbol{M}}_{Li}^G\right)_B = \left(\vec{\boldsymbol{r}}^{GL^i}\right)_B \times \left(\vec{\boldsymbol{F}}_{Li}^G\right)_B \tag{6.48}$$

6.3.7 Landing Gear Model Simplifications

Some aspects of the landing gear are not included in the model as they are not considered to be significant for the current problem.

Delays in the hydraulic system are not considered. In the model, it is assumed that there is no delay between the movement of the brake pedals in the cockpit or the braking command of the autobrake and the application of braking torque on the braking disc. This is a valid assumption because the reaction time of the hydraulic system is much shorter than that of the systems considered in the model. Estimations have shown that only a very small amount of hydraulic fluid has to move through the pipes in order to apply forces on the braking discs since hydraulic fluids are non-compressible. Delays by inertia can, therefore, be neglected. Furthermore, the purpose of the simulation is to examine the deceleration behavior of the aircraft rather than the control behavior of the hydraulic system. The reaction time of the former is much longer than that of the latter, thus allowing the time delay in the hydraulic system to be neglected.

While the landing gear strut has a degree of freedom in the vertical direction, no elasticity in the longitudinal or lateral direction is considered. The spring and damper model in the vertical direction has to be introduced to be able to compute the vertical forces. The main drawback of including such a landing gear model is the stiffness of the landing gear compared with the behavior of the rest of the aircraft. The use of spring and damper in the longitudinal and lateral direction does not provide any benefit for our application. They could be introduced if one would be interested in investigating the following aspects, which can be relevant in the scope of flight operations safety assessment focusing on the landing.

Touchdown analysis: At the moment of touchdown, not only is there a peak in vertical acceleration. When the wheels spin up at touchdown, an acceleration in the longitudinal direction can be measured. If the wheel is not perfectly aligned with the direction of motion, a lateral acceleration also occurs. These forces will cause high frequency oscillations of the landing gear structure. Introducing a respective degree of freedom will enable further investigation.

ABS activation: One of the possible implementations of the ABS system would be a bang-bang controller. Application of braking will lead to oscillation of the landing gear in the longitudinal direction. The frequency of the ABS controller should

be carefully chosen that it does not excite the eigenfrequency of the landing gear strut in the longitudinal direction as it could lead to increased wear-out, thus reduced life-time or even heavy damage and failure of the strut [Wan00].

As none of those two phenomenons are relevant to our problem, there is no necessity to introduce additional degrees of freedom for the landing gear.

6.3.8 Landing Gear Model Validation

A validation of the landing gear model based on available Flight Data Monitoring (FDM) data was performed based on a simplified aerodynamic and propulsion model [WH18a]. The contribution of the braking force to the total deceleration during landing is extracted. Furthermore, the available data was used to perform a non-linear regression based on Pacejka's friction curve [WH18b]. Friction data from other studies was available [Eng95] for given runway surfaces.

Algorithm 1 Groundspeed Estimation Algorithm [WH18a]

1: *loop*: For each timestep t
2: Compute new groundspeed $\tilde{V}_{GS}(t)$ from previous groundspeed $V_{GS}(t-1)$ and previous longitudinal acceleration $a_x(t-1)$
3: Obtain new tire speed $V_{\text{Tire}}(t)$ from measurement
4: **if** $\tilde{V}_{GS}(t) < V_{\text{Tire}}(t)$ **then**
5: Set $V_{GS}(t) = V_{\text{Tire}}(t)$.
6: **else**
7: Set $V_{GS}(t) = \tilde{V}_{GS}(t)$.

The groundspeed has to be obtained to compute the slip value. For this purpose, the method described in algorithm 1 is used along with the aircraft's yaw rate to account for different wheel groundspeeds during turns [WH18a]. In fact, the groundspeed in turns can also be estimated from measurements of the yaw rate and lateral acceleration, but it can only be reliably done when the aircraft is in a turn, which is rarely the case during deceleration on the runway. The actual groundspeed and the obtained wheel speed for one example flight are shown in figure 6.13. The difference between the two curves is clearly visible during the phase where heavy braking is applied.

Figure 6.14 shows the data points for a recorded landing [WH18a]. The red line depicts the friction value based on the wheel slip as computed from the model described in this section. The blue circles indicate the values that were actually measured from this particular landing. The line connects the data point in chronological order. The data is separated in three different clusters based on the groundspeed as the slip curve changes along with the speed. Each sub-figure represents an other interval of $10\,\mathrm{m\,s^{-1}}$.

First of all, one can see that the datapoints are all located in the left part of the friction

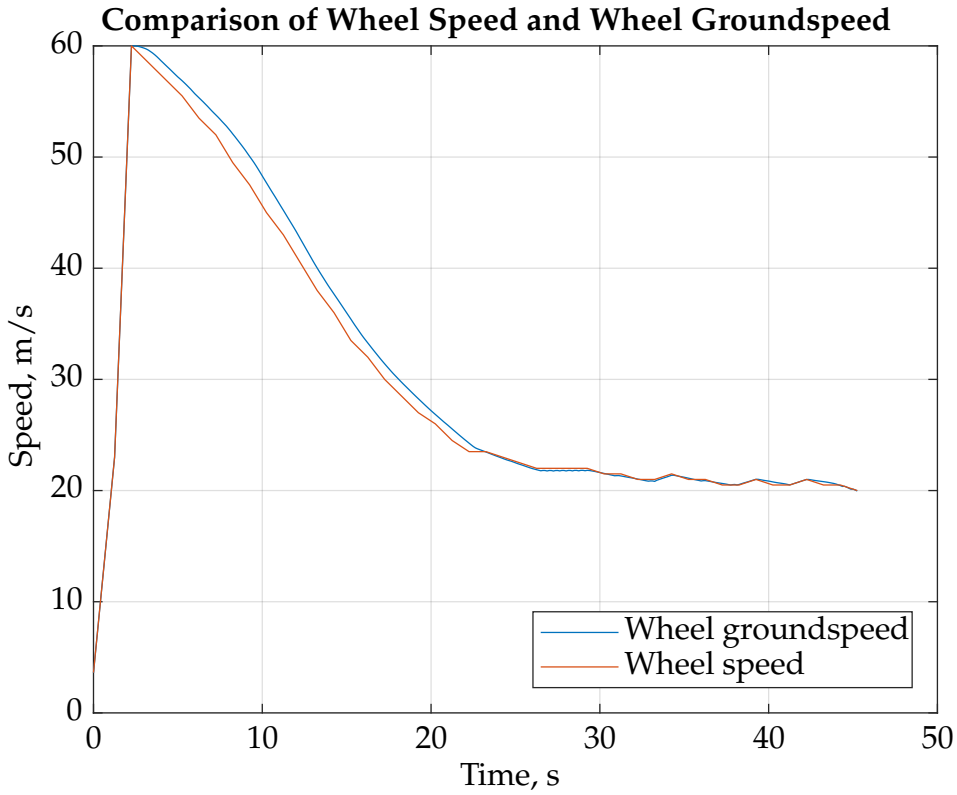

Figure 6.13: *Comparison of wheel speed and wheel groundspeed [WH18a]*

curve where an almost linear relationship is valid between the slip and the friction coefficient. Though the data does not perfectly follow the values as predicted by the model, it actually fits the model quite well. Particularly for the highest speed interval in figure 6.14c, it is very close to the prediction, indicating a high validity of the model. To assess the quality of the fitting, the Root Mean Square Error (RMSE) as well as the Normalized Root Mean Square Error (NRMSE), which are defined in equations (6.49) and (6.50) [DS12], are computed for every speed interval.

$$\text{RMSE} = \sqrt{\frac{\sum_{i=1}^{n} (\tilde{x}_i - x_i)}{n}} \tag{6.49}$$

$$\text{NRMSE} = \frac{\text{RMSE}}{\max\{x_i\} - \min\{x_i\}} \tag{6.50}$$

In both equations, i is the i-th data point out of a total of n data points. A value with a tilde $\tilde{x}$ indicates that it was measured while a value without a tilde was obtained from the model.

Speed Range, $\mathrm{m\,s^{-1}}$	30 to 40	40 to 50	50 to 60
RMSE, -	0.0033	0.0055	0.0028
NRMSE, -	0.2315	0.169	0.0494

Table 6.1: *Goodness of fit indicators for the slip curve*

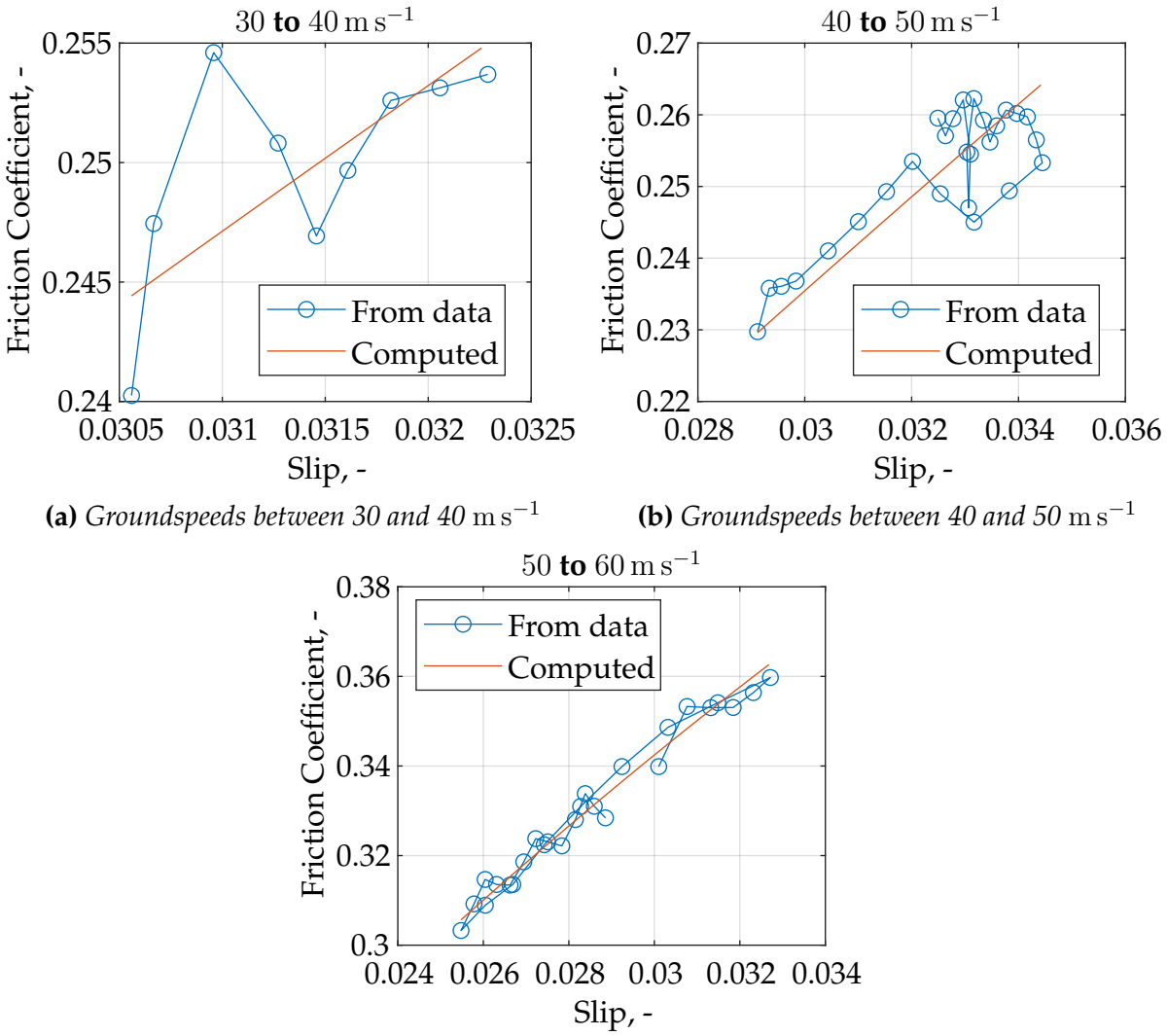

(a) *Groundspeeds between 30 and 40* $\mathrm{m\,s^{-1}}$

(b) *Groundspeeds between 40 and 50* $\mathrm{m\,s^{-1}}$

(c) *Groundspeeds between 50 and 60* $\mathrm{m\,s^{-1}}$

Figure 6.14: *Comparison of measured and computed friction coefficient [WH18a]*

The NRMSE can be interpreted as the RMSE normalized to the interval width of the occurring data. The computed values for the three speed intervals are shown in table 6.1. One can see that the the fitting is particularly good for the highest speed interval and worse for the lower speed intervals, which is consistent with observations made in figure 6.14. The NRMSE shows that the error corresponds to $23\,\%$ of the data range for the speed interval of 30 to $40\,\mathrm{m\,s^{-1}}$ and decreases to $5\,\%$ for the highest speed interval.

Taking a closer look at figure 6.14, especially figure 6.14b and the way the data points are connected chronologically, one comes to the conclusion that there seems to be some hysteresis behavior. The values for the friction coefficient are located significantly below the fitted red line when the slip increases and they are located at or above the red line when the slip decreases, except one single data point. There is, however, no plausible explanation for the hysteresis. It could be the result of different friction behavior depending on whether the wheel is being accelerated or decelerated.

6.4 Integration

In the last sections, all the forces acting on the aircraft, with particular focus on the landing gear forces, have been presented. The forces are summed up, taking into account different coordinate frames, including aerodynamics, propulsion, gravitation and landing gear. They are used to obtain the speed and the position of the aircraft by integration of $\left(\dot{\vec{V}}^{R}\right)^{NB}$ shown in equation (6.51).

$$\sum\left(\vec{F}_T^G\right) = m\left[\left(\dot{\vec{V}}^{R}\right)^{NB} + \left(\vec{\omega}^{NB}\right)\times\left(\vec{V}^{R}\right)^{E} + \left(\dot{\vec{\omega}}^{NB}\right)^{B}\times\left(\vec{r}^{RG}\right) + \left(\vec{\omega}^{NB}\right)\times\left[\left(\vec{\omega}^{NB}\right)\times\left(\vec{r}^{RG}\right)\right]\right] \tag{6.51}$$

For the rotational dynamics of the aircraft, all moments acting on the aircraft are summed up. Using the sum of the moments, the derivative of the angular rates can be computed, as shown in (6.52).

$$\begin{pmatrix}\dot{p}\\ \dot{q}\\ \dot{r}\end{pmatrix}_B = \left(\dot{\vec{\omega}}_K^{OB}\right)_B^B = \left(\boldsymbol{I}^G\right)_{BB}^{-1}\cdot\left[\sum\left(\vec{M}_T^G\right)_B - \left(\vec{\omega}_K^{OB}\right)_B\times\left(\boldsymbol{I}^G\right)_{BB}\cdot\left(\vec{\omega}_K^{OB}\right)_B\right] \tag{6.52}$$

The attitude of the aircraft $[\Phi,\Theta,\Psi]^T$ is obtained based on the angular rates.

$$\begin{bmatrix}\dot{\Phi}\\ \dot{\Theta}\\ \dot{\Psi}\end{bmatrix} = \begin{bmatrix}1 & \sin\Phi\tan\Theta & \cos\Phi\tan\Theta\\ 0 & \cos\Phi & -\sin\Phi\\ 0 & \frac{\sin\Phi}{\cos\Theta} & \frac{\cos\Phi}{\cos\Theta}\end{bmatrix}\cdot\begin{bmatrix}p\\ q\\ r\end{bmatrix} \tag{6.53}$$

The starting point of the simulation is the moment when the aircraft touches down on the runway. The initial states can be extracted from FDM data, which is described in chapter 8.

6.5 Implementation Issues

The most significant challenge one has to face during the implementation of the model is the difference in stiffness of the subsystems in the model. Particularly the landing gear has much higher eigenfrequencies than the other components of the airframe. Higher eigenfrequencies call for smaller timesteps when making time-discrete computational simulation, however, smaller timesteps significantly increase the computa-

tional effort at the same time while being unnecessary for components that have low stiffness.

When looking at the moment of touchdown, the wheel speed increases from zero to approximately the groundspeed of the aircraft in a very short interval of time. If the time step of the simulation is significantly greater than the time required for the speed-up of the wheel, it can cause major problems in the simulation. After the angular acceleration of the wheel is obtained, the solver would take the value and obtain the angular speed of the wheel in the next step by forward integration. However, when the time step is too large, it will cause the computed wheel speed to be significantly higher than the groundspeed of the aircraft in the next timestep as the acceleration is high, which is simply unrealistic and will also lead to severe problems during the next time step because the computed friction forces will go out of bound. A possible solution without increasing the computational effort is limiting the values the variables can reach. In this case, the wheel speed or the angular acceleration can be limited. However, the limit values have to be carefully chosen to ensure no desired effect is ignored in the simulation. As the wheels are not powered, unlike for cars, their speed cannot be higher than the current groundspeed. In addition, as the aircraft is moving forward, the wheel speed cannot be smaller than zero. These two values are used as limits to stabilize the simulation of the rotational dynamics of the wheel. In addition, the slip of the wheel is limited to the interval of $s \in [0; 1]$.

7

System Logics, Operating Procedures and Pilot Behavior

7.1 Introduction

As already mentioned in section 1.2.1, differences among aircraft operators can be traced back to several factors, including *network structure*, *operating procedures*, *operating crew* and *equipment*. Two of them, *network structure* and *crew* are reflected in the collected Flight Data Monitoring (FDM) data. Not only can the data be separated according to airport and runway, but the data also contains the specific behavior of the pilots. For example, the ability and quality of the crew to perform a manual Instrument Landing System (ILS) approach can be directly derived from the data, specifically the deviations on the glideslope and the localizer. In this chapter, we focus on how to incorporate the remaining two factors, (1) *equipment*, i.e. aircraft type-specific behavior, and (2) *operating procedures*, which also includes the behavior of the flight crew.

In order to include different types of aircraft, system logics have to be considered in the modeling as they reflect the behavior of the aircraft during certain situations. It incorporates the individual properties of each aircraft type. In this chapter, some system logics of the aircraft types that are relevant to the current work are presented. They include the Boeing 737 as well as the Airbus Fly-By-Wire (FBW) aircraft types, i.e. A320 family, A330, A340, A350 and A380. In most cases, the logics on the various Airbus aircraft types are very similar, varying only in the number of landing gears, control surfaces and engines. Information about the system logics can be found in the Flight Crew Operating Manual (FCOM) [Air11a], which is an extensive document provided to the operator by the Original Equipment Manufacturer (OEM) that contains detailed descriptions of the on-board technical systems.

Another factor that can lead to differences is the way the aircraft is operated, which

can be different depending on the airline. The information is mainly extracted from the Operations Manuals (OMs). The OM is written by the operator based on the information provided by the manufacturer. It consists of four parts, which is required by legislation [Eur08a] within the scope of obtaining the Air Operator Certificate (AOC) [Eur08b].

Part A: General information and company procedures with no reference to specific aircraft types. It is intended to establish Standard Operating Procedures (SOPs) to ensure safe and efficient flight operations.

Part B: Operating procedures for specific aircraft types. Typically, there is one specific OM-B for a specific aircraft type, a specific aircraft family, or a set of aircraft types that are operated by the same group of pilots. When aircraft types are grouped together in one document, they often share very similar cockpits and other onboard systems, such as the Airbus A330 and A340.

Part C: Operating procedures for specific airspaces, routes and airports. For example, it contains the potential hotspots and commonly made errors at each airport. It also includes the contact information of the ground staff at each airport within the operators network.

Part D: Procedures for training of the personnel.

In this chapter, some items from the OM, the FCOM and other relevant documents that contribute to the accident types of Runway Excursion and Abnormal Runway Contact are presented. These are particularly items that are used during landing and deceleration.

7.2 Ground Spoiler Extension Logics

7.2.1 Airbus FBW Aircraft

Figure 7.1 shows the ground spoiler extension logics for the Airbus A320 family [eas12], which has been in use until an update in 2010. The A320 has five spoilers on each wing that are numbered from 1 to 5, beginning with the inbound spoiler. The spoilers 2, 3 and 4 are used as speed brakes when airborne while all spoilers are used as ground spoilers [Deu09a]. Depending on the exact control law version of the aircraft, both ailerons are also deflected upwards to support the ground spoiler function. Figure 7.2 depicts the difference. While on the particular A320 shown in 7.2a, all spoilers are extended, the aileron at the very outbound position of the wing, does not change in deflection as it is used for roll control only. For the A350 on the right in 7.2b, however, the aileron is also deflected upwards to support the aerodynamic effect of the spoilers.

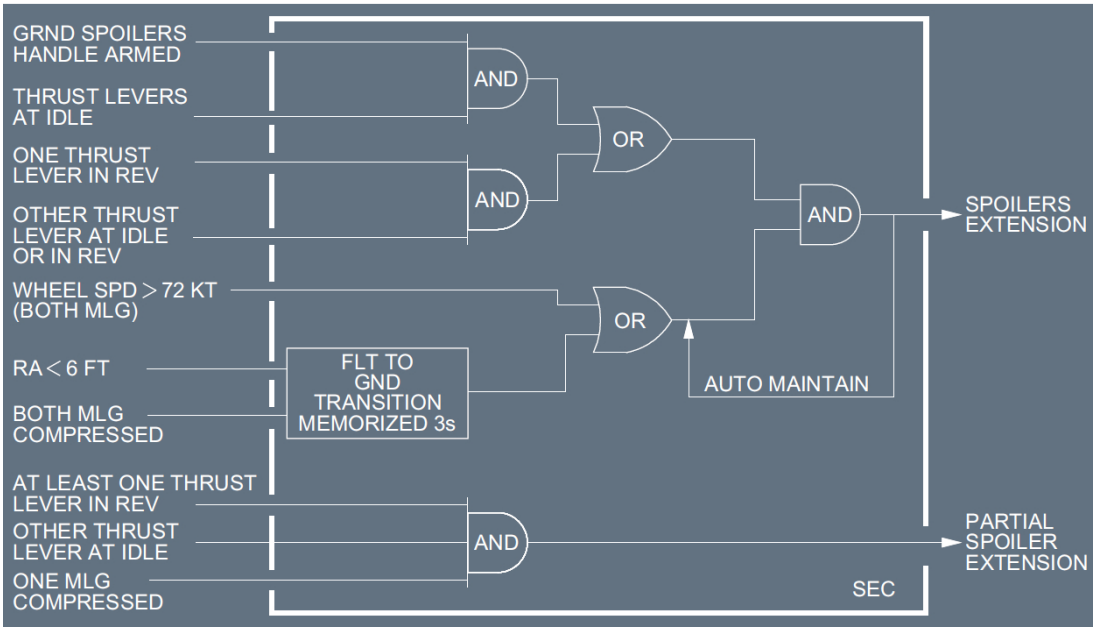

Figure 7.1: *The spoiler extension logic on the Airbus A320 [eas12]*

This also occurs on the opposite wing, leading to an atypical symmetric deflection of the ailerons.

(a) *Spoiler deployment on the Airbus A320 with no use of the aileron*

(b) *Spoiler deployment on the Airbus A350 with ailerons deflected upwards*

Figure 7.2: *Wing view after touchdown showing the extension of the ground spoilers for two different Airbus aircraft types*

For safety reasons, Airbus includes a state for the spoilers referred to as *Partial Extension*, which is visible in the lower logic branch in figure 7.1. When only one thrust lever is in reverse with the second one being in idle and only one landing gear is compressed, the spoilers are only partially deployed, which means that the deflection of the spoiler surfaces are limited to $10°$. Only if the conditions in the upper branch are fulfilled, the spoilers will completely extend. The motivation for this implementation lies in the requirements set out by the certification specifications [Eur18]. Both the unintended full deployment of ground spoilers during flight and not deploying the ground spoilers after landing or during Rejected Take-off (RTO) could result in *catastrophic* consequences, implying that such an event must not occur with a probability of more than

1×10^{-9} per Flight Hour (FH). This would impose a very high requirement concerning the quality and reliability of the signals coming from Weight on Wheel (WOW) sensors as wrong signals sent from them could lead to one of the described failure conditions above. Besides, it would violate the certification requirement that a single failure must not result in a catastrophic failure condition under any circumstances. Multiple redundant sensors could become necessary. In order to be able to use lower quality signals, the state of partial extension is introduced. Wrong signal from a single sensor can only lead to a partial spoiler extension, which will not lead to Loss of Control In-Flight (LOC-I) if it occurs in the air. Besides, if the aircraft has already touched down with one single landing gear, the partial deployment of the spoilers will aid to the fulfilment of the conditions for full extension as it reduces the lift and eases the touchdown with the remaining landing gear.

The condition for which the landing gear is considered compressed, i.e. when the WOW signal is positive, has to be carefully chosen. In 1993, a Lufthansa A320 overran the runway at Warsaw Frederic Chopin Airport (WAW/LPWA) during landing [Mai94]. The threshold value for the A320 in order to generate the compressed signal was set to be $5.8\,\mathrm{t}$ per main landing gear. As the aircraft touched down very softly and the wheels did not spin up due to a very wet runway, the spoilers did not extend, nor did the autobrake activate. Thrust reverse was also not available since the aircraft system did not detect the ground condition. This greatly contributed to the overrun accident, along with a late touchdown and a high approach speed, after which Airbus lowered the threshold value for landing gear compression to $2\,\mathrm{t}$ per landing gear [Aus13].

The logic shown in figure 7.1 was modified in 2010 [BS10] to reduce the risk of hard landing. This is caused by the pilot not retarding the thrust levers prior to touchdown, leading to the aircraft bouncing off the runway and becoming airborne again. When the pilot retards the thrust levers during the bounce, the spoiler extension conditions are fulfilled since the radio altitude and the landing gear compressed conditions are memorized for three seconds. This leads to the aircraft touching down hard on the runway for second time because the lift is suddenly lost when the spoilers extend after bouncing off the ground. With this modification, Airbus changed the conditions for the thrust levers to enable a partial condition to both of them being at or below the climb thrust notch, which is the same position as when the auto-thrust function is in use [BS10]. The logic is deployed on all newly produced aircraft and can also be updated to frames that previously left the production sites. 4 Very similar logics are used on all Airbus FBW aircraft, including the A330 and A340 [Deu09b], the A380 as well as the A350 [Air11b]. Differences exist in the number of spoilers, engines and landing gear struts in the signal logics. On the A380, for example, the partial extension of the spoilers requires one of the four main landing gears to be compressed and one of the

four thrust levers in reverse while the remaining three are at idle. The full extension of the spoilers requires three landing gears to be compressed and at least one thrust lever in reverse while at least two of the remaining three are below climb power [Air11a]. At least three thrust levers in idle position is also accepted for the thrust setting to trigger partial or full extension. On the A380, there are eight ground spoilers available on each wing in addition to the ailerons that are also deflected upwards to support the spoilers. There are three adjacent ailerons on the Airbus A380 on each wing that can be controlled independently.

7.2.2 Boeing 737 NG

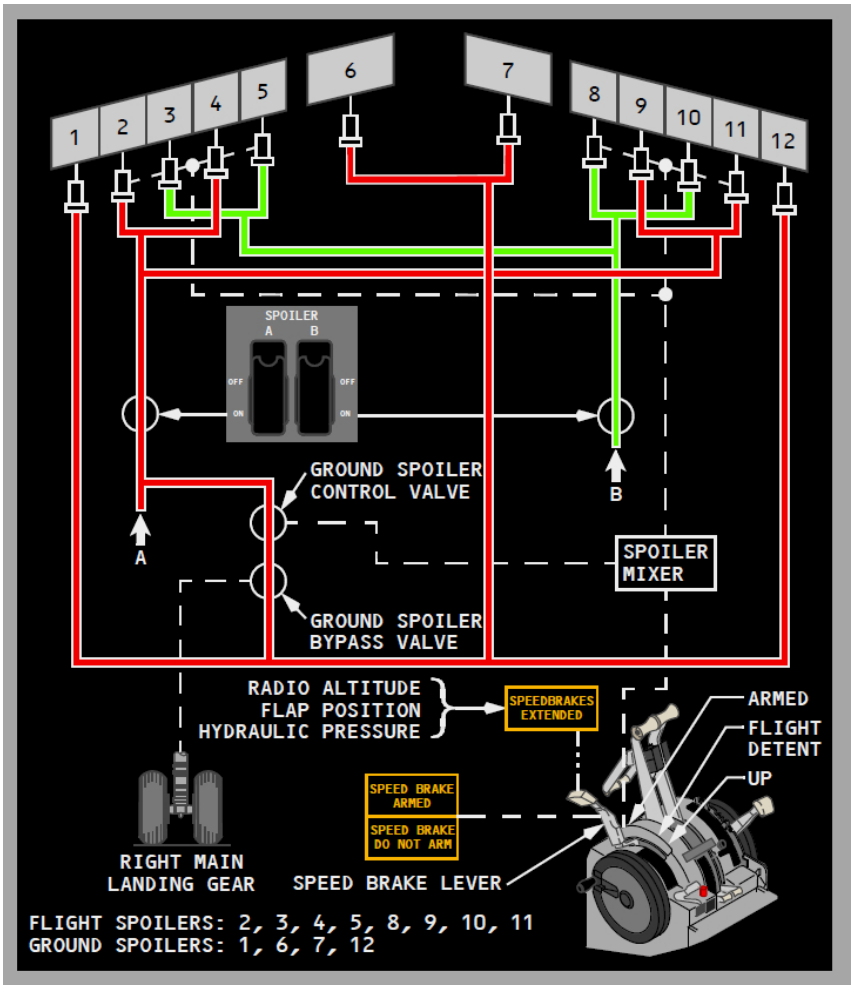

Figure 7.3: *The spoiler extension logic on the Boeing 737 NG [The09]*

Figure 7.3 shows the system architecture of the ground spoilers for the Boeing 737 New Generation (NG) aircraft [The09], which includes the 737-600 to 737-900 series. The 737 has twelve spoilers in total, numbered 1 to 12 from left to right. Eight of them are used as flight spoilers and ground spoilers, four more are used as ground spoilers only. The main difference in the architecture compared to the A320 is that the flight spoilers will

deploy if any of the two main landing gears is compressed. The ground spoilers will only deploy if the right main landing gear is compressed. In addition, the following conditions have to be met simultaneously [The09]:

- The ground spoilers are armed using the speed brake lever.
- The radio altitude is smaller than $10\,\mathrm{ft}$.
- Both thrust levers are at idle.
- The measured wheel speeds on the main landing gear wheels are higher than $60\,\mathrm{kn}$.

When looking at the safety considerations, one can see that the safety requirements on the compression sensor on the right main landing gear must be significantly higher than for the left main gear. While a wrong signal from the left gear could trigger the extension of the flight spoilers, it can be assumed that the aircraft is still controllable and maneuverable if only the flight spoilers are extended. It is comparable to the concept of partial deployment at Airbus except that Boeing's understanding of partial is that only a certain number of spoilers deploy rather than all spoilers, but with a limited deflection angle.

7.3 Braking System and Autobrake

7.3.1 Airbus FBW Aircraft

Figure 7.4 shows the braking system of the Airbus A320. The braking is controlled by the Braking Steering Control Unit (BSCU). The naming of it clearly indicates that it does not only control the braking of the aircraft, but also the steering on the ground as asymmetric braking can be used to control the yaw axis of the aircraft. This is particularly useful at high speeds when the nosewheel steering is not effective or when very small turn radii have to be achieved at low speed on ground.

The braking system is using power from two of the three on-board hydraulic systems, yellow and green. For the default case, the green system is used. If the green hydraulic system has failed, the yellow hydraulic system is automatically selected to power the braking pressure. In addition, a Power Transfer Unit (PTU) interconnects the green and the yellow hydraulic system [eas12] by pressurizing one system using the power from the other if the difference in pressure between the two systems increases above $500\,\mathrm{psi}$. The Anti-Lock Braking System (ABS) is available unless the BSCU has failed or if both hydraulic systems are low on pressure. In this case, a brake accumulator is available that temporarily provides limited braking pressure [eas12]. It stores the

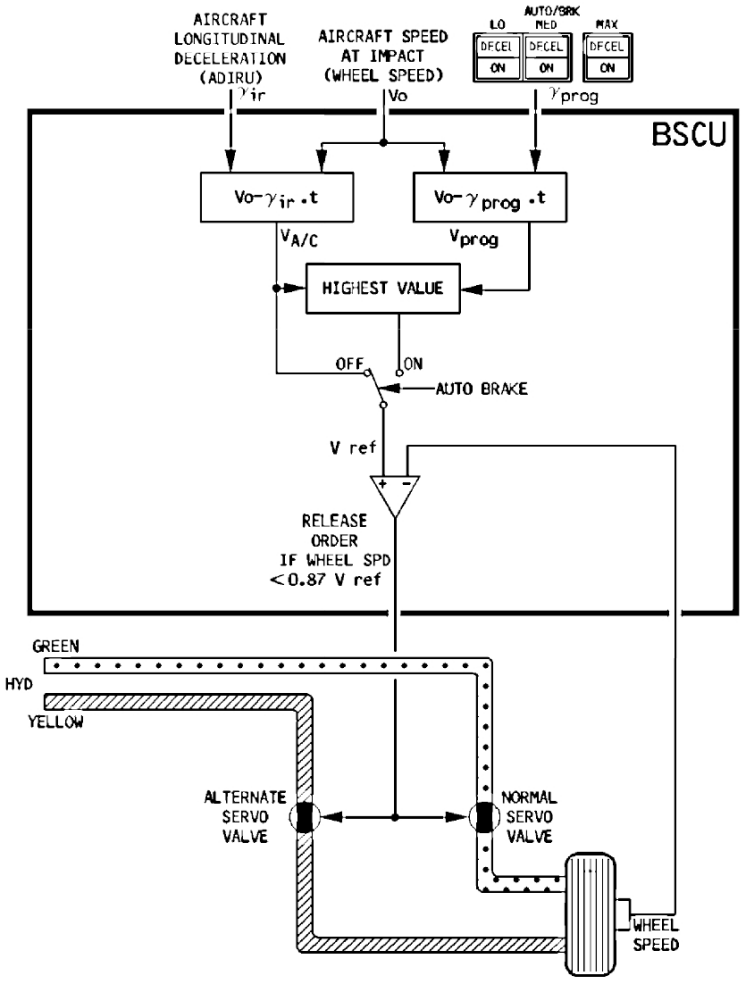

Figure 7.4: *An overview of the braking system of the Airbus A320 [eas12]*

pressure as long as the hydraulics are operating normally and releases the energy in case of failure.

Figure 7.4 illustrates the principle of ABS. It is activated when the wheel speed is below 0.87 of the reference ground speed, i.e. when the slip increases above 0.13. In that case, the BSCU commands the brake pressure to be reduced in order to lower the slip. Obtaining the reference ground speed is a challenge as measurements using the Global Navigation Satellite System (GNSS) are not very reliable. In this case, the ground reference speed is obtained by taking the wheel speed shortly after touchdown as initial value. At that time, the wheel should approximately have the same speed as the Groundspeed (GS) as no braking has been applied yet. The continuous values for the GS are obtained by integrating the longitudinal acceleration, i.e. making use of the principles of inertial navigation.

An autobrake system is available that commands a constant deceleration value that is pre-selected by the pilot prior landing. On the A320, there are two settings available for landing, *LO* and *MED*. The corresponding deceleration values are depicted in table

Setting	Deceleration $[\mathrm{m\,s^{-2}}]$
LO	1.7
MED	3.0

Table 7.1: *Autobrake settings and corresponding deceleration values on the Airbus A320 family [Deu09a], A330 and A340-300 [Deu09b]*

7.1. In addition, a *MAX* setting is available which is only used for RTO for which the maximum braking capability is applied with no specific deceleration target value. The autobrake has to be armed in order to have it activated when certain conditions are met. For the activation after landing, the same conditions have to be met as for the full extension of the ground spoilers, described in section 7.2.1 above.

On the Airbus A330 and A340, the architecture is very similar [Deu09b]. Braking pressure is supported by the green hydraulic system as the primary source and the blue hydraulic system as the secondary source. The two settings for landing with autobrake, *LO* and *MED* in table 7.1 are also available on all versions of the A330 and the A340-200 and -300 series with the same deceleration values. On the A340-500 and -600, five different settings are available, the deceleration values are shown in table 7.2. Another dedicated *RTO* mode is used for take-off. On the A330 and A340, the maximum slip value before the activation of the ABS is set to be 0.12, slightly lower compared to the A320 family.

Setting	Deceleration $[\mathrm{m\,s^{-2}}]$
LO	1.8
2	2.2
3	2.6
4	3.0
HI	3.5

Table 7.2: *Autobrake settings and corresponding deceleration values on the Airbus A340-500 and -600 [Deu09b]*

On the Airbus A380, only four selection options are available for the autobrake, still covering the same range with respect to deceleration value. In addition, a Brake To Vacate (BTV) function is introduced for the autobrake. After the selection of the airport, the system indicates the earliest point on the runway at which the aircraft can vacate the runway for the two cases when the runway is either dry or wet. Based on the available weather information, the crew can select a taxiway that is located beyond the respective point. The autobrake system will slow down the aircraft such that it can safety vacate the runway at the selected taxiway, optimizing brakes and tire wear as well as passenger comfort. In addition, a new system called Runway Overrun Protection System (ROPS) is installed that continuously monitors the landing distance and the remaining runway distance to provide a real-time landing performance update to

the pilots and trigger additional actions [Air11a] if necessary. It is a combination of Runway Overrun Warning (ROW), which computes the distance that is still required on the fly and Runway Overrun Protection (ROP), which prompts the crew to apply maximum braking and maximum reverse until full stop, which is typically not recommended in the SOP due to a higher risk of Foreign Object Damage (FOD) to the engine. Alternatively, if a long landing is performed, i.e. touching down too late on the runway, the system can also recommend the pilot to perform a go-around if the aircraft has not been on the ground yet.

On the Airbus A350, there is only one autobrake setting that can be selected, which is *MED*, corresponding to a deceleration of $3\,\mathrm{m\,s^{-2}}$ [Deu18a]. However, it is recommended to use the BTV function only for all landings, combined with ROPS [Air11b], which is standard equipment on the A350. The runway condition, i.e. *dry*, *wet* or *contaminated*, has to be pre-selected prior landing based on the information available to the flight crew.

7.3.2 Boeing 737 NG

On the Boeing 737 NG, the braking pressure is provided by two hydraulic systems with hydraulic B as the primary and hydraulic A as the alternate source of power [The09]. A brake accumulator is also available that support limited braking power in case both hydraulic systems have failed.

Just like on the Airbus aircraft, the ABS reduces the braking pressure when the skidding of a wheel is detected. Unfortunately, the exact values that lead to the activation of the ABS could not be found. The release of braking pressure is done individually for each wheel.

As for the autobrake, there are four settings that can be used for landing, the corresponding deceleration values are given in table 7.3. The target deceleration for the *MAX* setting varies depending on the GS of the aircraft. In addition, there is also an autobrake mode for RTO, which is explicitly armed prior departure.

Setting	**Deceleration** $[\mathrm{ft/s^2}]$	**Deceleration** $[\mathrm{m\,s^{-2}}]$
1	4	1.22
2	5	1.52
3	7.2	2.19
Max (below $80\,\mathrm{kn}$)	12	3.66
Max (above $80\,\mathrm{kn}$)	14	4.27

Table 7.3: *Autobrake settings and corresponding deceleration values on the Boeing 737 NG [Bra99]. As the original values are provided in* $\mathrm{ft/s^2}$ *in the Boeing FCOM, a conversion to* $\mathrm{m\,s^{-2}}$ *is provided to enable direct comparison with the Airbus values.*

The activation of the autobrake during landing is triggered when both thrust levers are pulled back to at least idle and when the wheels on the main landing gears have spun-up to $60\,\mathrm{kts}$ or above. This condition is very similar to the deployment of the spoilers described in section 7.2.2 above. However, unlike the logics for ground spoiler extension, both the radio altitude and the landing gear compression are not taken into account.

For all aircraft types previously mentioned, a *touchdown protection* is implemented that ensures the release of the brakes before touchdown until wheel spin-up. Landing with locked wheels will result in immediate tire bursts and must be avoided.

7.4 Landing Distance and Target Speed Computation

For each landing, the speed that should be kept during final approach is determined based on values indicated in the OM Part B for each individual aircraft type. Table 7.4 shows the reference speed V_{ref} of the Airbus A380 [Air11a] depending on the weight of the aircraft, the flaps and slats configuration as well as the position of the Center of Gravity (CG). The exact values for each individual landing can be obtained by interpolating the values. In today's flight operations, these tables are implemented in the flight crew's Electronic Flight Bag (EFB), the values are determined typically before beginning the approach. The final speed that should be kept during approach V_{app} as Indicated Airspeed (IAS) is computed as follows according to Airbus:

$$V_{\mathrm{app}} = V_{\mathrm{ref}} + \min\left\{\frac{1}{3}V_{\mathrm{Headwind}}, 15\,\mathrm{kts}\right\} + \Delta V_{\mathrm{C}}, \tag{7.1}$$

where V_{Headwind} is the speed of the headwind that should be accounted for by adding one third of it to the approach speed. However, this increment is limited to $15\,\mathrm{kn}$ on the A380. V_{C} is a speed correction increment added to the crew's discretion to account for local weather conditions, such as turbulences or wind shear, it is typically a few knots.

Weight ($1000\,\mathrm{lb}$)	CONF 3		CONF FULL	
	20 % CG	43 % CG	20 % CG	43 % CG
600	120	120	120	120
700	128	124	125	121
800	137	133	133	130
900	145	141	141	138
1000	153	149	149	145
1100	160	156	157	152
1200	168	163	164	159

Table 7.4: *Reference speeds (V_{ref}) in knots on the Airbus A380 [Air11a]*

A factor k_{Failure} is used as a multiplier to the obtained results to account for system failures that affect the controllability or the braking capability of the aircraft. Examples include the failure of the yaw damper, jamming of the horizontal stabilizer, ice accretion or when the flight control system enters the Alternate Law or Direct Law. As the flight envelope of the aircraft becomes smaller and, in the case of leaving the Normal Law, the envelope protections successively become unavailable when these failures occur, it is logical to increase the approach reference speed of the aircraft to have a larger margin to the stall speed and to account for larger uncertainties and errors in the sensor measurements.

Similar computation is performed by the crew to assess the expected landing distance that is required. Typically, tables are available that use input parameters such as the aircraft's weight at landing, the wind, the runway condition (dry, wet or contaminated) and the airport elevation, adjustments may be made if the landing is performed by the autopilot. In addition, just as the computation of the approach speed, corrections have to be made for failures that affect the deceleration capability. Examples include inoperability of spoilers, even single spoiler surfaces, failure of hydraulic systems that could affect both the braking performance and spoiler operation or the unavailability of the ABS. System logics have to be considered as well, as there are inter-dependencies between the systems. For example, on all Airbus aircraft, if one spoiler surface fails, the symmetric spoiler on the other wing is also inhibited in order to avoid asymmetry.

In daily flight operations, the crew typically does not use value tables as shown in table 7.4. Instead, a computer tool is used that is provided either directly by the aircraft manufacturer or created by the operator with information supported by the manufacturer. The advantage is not only the quicker computation process but the ability to quickly evaluate different options and make the best decision. For example, landings can typically be conducted with several possible flap settings. Higher settings (flaps and slats further extended) allow lower approach speeds, but the aircraft will become more sensitive to turbulence and gusts during the approach due to a lower wing load. Lower settings often have a higher risk of tailstrike due to the higher angle of attack during approach, but offer better aerodynamic efficiency a reduce the level of noise. Using the provided calculation tool, the crew is able to explore different options quickly and decide based on all relevant constraints.

7.5 Thrust Reverse

During certification flight testing, the Landing Distance (LD) as well as the Accelerate-Stop Distance (ASD) after a RTO must be obtained without the use of thrust reverse. They present an additional deceleration device providing extra safety margin. During

daily flight operations, however, thrust reverse is routinely used, though some airports require the operators to restrict the use of thrust reverse as much as necessary due to noise abatement procedures [Emi13]. Often, thrust reverse is not used in full, but in idle only, depending on local airport regulations. Penalty fines could be placed if rules are violated without the necessity to use full reverse based safety considerations.

A failure of the thrust reverse during deceleration phases on the ground will only lead to the loss of deceleration capabilities that were not accounted for during performance calculation in the first place, which means that the consequences are manageable. In fact, the thrust reverse is typically not even an item on the Minimum Equipment List (MEL), meaning that aircraft can be dispatched if reverse is not functioning properly and, therefore, deactivated, though operational restriction may apply. However, the contrary case, meaning that the thrust reverse deploy during flight phases at which it is not supposed to deploy, could lead to catastrophic consequences. The crash of a Lauda Air Boeing 767-300ER near Bangkok in 1991 [Air93] was caused by an inadvertent deployment of the thrust reverse on the number one engine. The aircraft was climbing through Flight Level (FL) 310 at a speed of Mach 0.78 when the reverse activated. The aircraft entered a stall due to high asymmetric thrust and broke apart at an altitude of $4000\,\mathrm{ft}$ due to excessive load and buffeting.

On the Airbus A320 family, except the A318, two engine types are available for customer selection, the CFM International CFM56-5 and the International Aero Engines (IAE) V2500. On the A318, the smallest aircraft type in the family, the IAE engine is not available. Instead, the customer can choose between the CFM56-5 and Pratt & Whitney's PW6000. The engine control architecture and the actuation logic, however, are very similar for all engine types. The engine is controlled by a Full Authority Digital Engine Control (FADEC) system with two redundant channels. The deployment of a thrust reverse requires the operating FADEC channel to be operating and sending the reverse deployment signal, both main landing gears to be compressed and the thrust lever to be set to reverse for the respective engine [eas12]. Gear compression signal is provided by the Landing Gear Control and Indication System (LGCIS), the same source is used for the WOW signal required for the activation of the autobrake and the extension of the ground spoilers.

On the Airbus A330 and A340, the logics are very similar. Though the A340 has a center body landing gear, it is not required to have a compressed center gear for reverser deployment [Deu09b]. In fact, the A340 can even be dispatched with weight restrictions if the body gear is retracted and not operating. On the A340-200 and -300, no braking system is installed on the body gear which consists of two wheels only, while for the A340-500 and -600, the center gear is a two axis bogie with brakes installed. On the A340, for the outbound engines (1 and 4), an interlock is implemented that limits the reverse on an engine to idle if the reverse of the corresponding outbound engine

is not in the deployed and locked position. This reduces the magnitude of possible asymmetric thrust and avoids uncontrollably high yaw rates.

On the Airbus A380, thrust reverse is only available on the two inbound engines (number 2 and 3). The outbound engines are approximately 26m away from the fuselage center [Air16], which means that, depending on the runway width and the location of the aircraft on the runway, they could be well located beyond the runway shoulder. Thus, the thrust reverse was not installed in order to avoid FOD. The deployment logic on the A380 is very similar to those on the previously mentioned Airbus aircraft types. However, it is structured in three lines of defense, each of them is controlled and monitored by an individual system to prevent inadvertent reverse deployment during flight. In addition, two protection measures are introduced on the A380 [Air11a] to limit the effect of inadvertent deployment:

Idle Protection: The FADEC monitors the position of the thrust reverse translating cowl. If it is deployed by more than $5\,\%$ and reverse is not selected on the thrust lever, the FADEC automatically reduces the thrust on the engine to idle. This measure is to cope with inadvertent deployment in-flight.

Auto-Idle Protection: Since the outbound engines are not equipped with thrust reverse, it is possible to select a thrust above idle on the outbound engines while the inbound engines are in reverse. In this case, the FADEC reduces the thrust of the outbound engines to idle without manual interaction.

To sum it up, it becomes obvious that the considerations behind the actuation logics of the thrust reverse is more focused on preventing inadvertent deployment during the flight rather than ensuring a high availability of the reverse on ground. The reason behind this is that the consequences of the former are much more severe than that of the latter, as shown in previous accidents. This is significantly different compared to the logics of spoiler deployment or autobrake activation.

7.6 Pilot Behavior

7.6.1 Modeling of the Pilot Behavior

Although the focus of this work is not human performance, it should be addressed due to the strong influence of the behavior of the flight crew on the occurrence and on the outcome of an accident. The intention, however, is not to assess human factors by creating a model representing the pilot, but rather to incorporate interactions with the pilot wherever possible and wherever this can be observed in FDM data. For example, it was visible in the FDM data that pilots tend to touch down significantly earlier on

the runway if the landing is more critical with respect to runway length [WF12]. The behavior should also be reflected in the model.

Several parts of the model include pilot interactions and they are explained in the succeeding sections.

7.6.2 Braking Behavior

After touching down, the primary objective is to slow down the aircraft in order to be able to safely vacate the runway. To achieve this goal, the pilot either applies deceleration devices manually or they are automatically activated if the given conditions are fulfilled. The brakes, which are the most effective means to decelerate, are applied by the pilot or are activated by the autobrake system, which was described in section 7.3. The use of the BTV system on the Airbus A380 and A350 already suggests that the braking behavior heavily depends on the location of the taxiway that is used to vacate the runway. The top-level goal is to minimize brake wear and the time required to taxi to the gate while avoiding unnecessary risks for Runway Excursion (RE). Figure 7.5 shows the southern part of Munich Airport (MUC/EDDM) along with the runway 08R/26L. As both passenger terminals are located close to the eastern part of the runway, the braking action is typically higher when landing in western (26) whereas in eastern direction (08), a long roll-out can be performed, if traffic permitting, to minimize taxi time on the ground. This behavior can actually be observed in the available flight data, the details are described in section 9.2.2.1. A full airport chart of MUC/EDDM can be found in the appendix C.

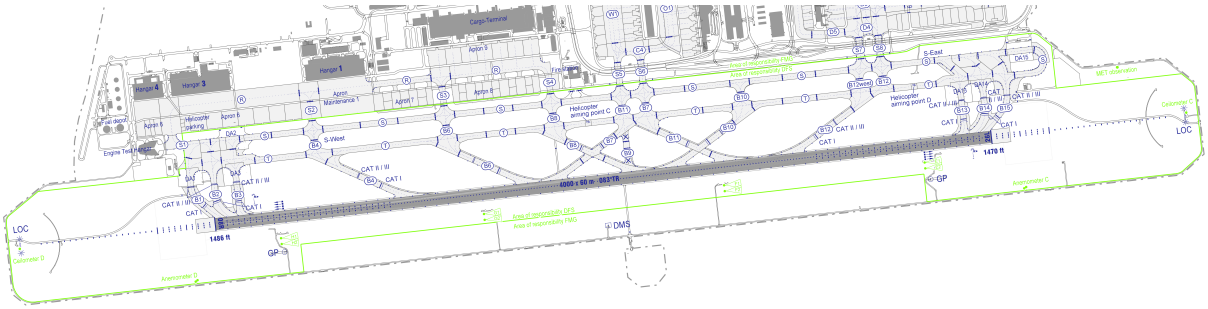

Figure 7.5: *The taxiway layout of the southern runway (08R/26L) at MUC/EDDM (north-up orientation) [DFS18]*

In order to compare the model output with FDM data, the actual landing distance has to be extracted from the data. However, it is not directly possible to obtain the actual landing distance used to come to a full stop because the aircraft never comes to a full stop on the runway unless during an emergency. To overcome this issue, the time point at which the pilot stops braking during landing roll is extracted. It is assumed that the pilot would only terminate braking action if a sufficiently safe low speed is already

reached to exit the runway via the next suitable taxiway. In order to determine the actual required landing distance, a full braking, using the maximum available braking action under the given condition, is simulated from this point to compute a distance that the aircraft would hypothetically use if it had to stop on the runway.

7.6.3 Steering Behavior

In order to quantify the risk of runway veer-off, the steering behavior of the pilot on the ground has to be considered. The task can be considered a control task with the objective to be as close to the runway centerline as possible. The control inputs are nosewheel steering, rudder deflection, asymmetric braking as well as asymmetric thrust. However, in our use case, only the first two, nosewheel steering and rudder, shall be used. In contrast, the application of differential thrust is not recommended. Figure 7.6 shows the runway veer-off accident which occurred at MUC/EDDM in 2011 [Bun11] [Bun18]. The aircraft departed the runway to the left during the landing roll-out. However, due to overcorrection by the pilot, the aircraft returned to the runway, but crossed the runway edges again to the right before coming to a full stop.

Figure 7.6: *The RE (veer-off) accident at MUC/EDDM in 2011 [Bun11]. The tire markings are well visible.*

For the implementation of a ground controller, a control algorithm developed by other researchers for the application on an Unmanned Aerial Vehicle (UAV) performing Automatic Take-off and Landing (ATOL) is used [SH17]. Using the lateral deviation on the runway, i.e. the distance to the runway centerline alone will lead to frequent overshoots and augmenting oscillations around the centerline. The idea of this controller is to have three cascaded loops, controlling the lateral deviation, the heading and the yaw rate, respectively, in the outer, the middle and the inner loop. Figure 7.7 shows the

structure of the controller. δ_{cmd} is the variable for the control input in general, which can be both the nosewheel deflection and the rudder. For the implementation, the control inputs have to be limited in order to be realistic. In our case, the nosewheel deflection was limited to $\zeta_L \in [-30°; 30°]$ and the rudder deflection was limited to $\zeta \in [-60°; 60°]$.

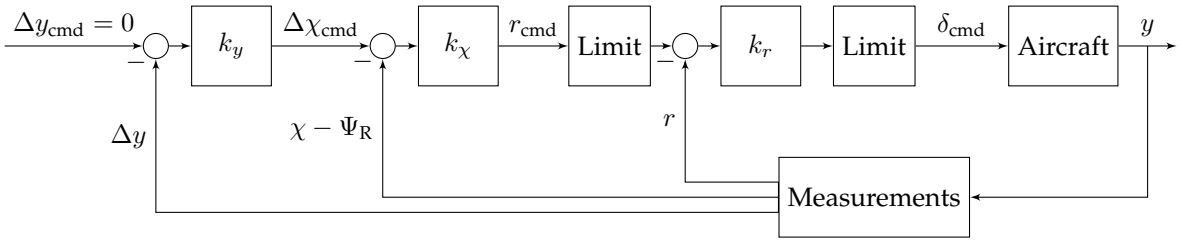

Figure 7.7: *The cascaded ground controller used to reduce lateral deviation [SKHH18]*

The controller gains k_y, k_χ and k_r have to be obtained and adjusted. A heuristic approach is used. For this purpose, all the gains are first set to reasonable values with the correct sign that are, if in doubt, rather small in magnitude. Starting from the inner loop to the outer loop, the values of the gains are slowly increased so that the system is still stable without overshooting. In general, the gains become increasingly smaller from the inner to the outer loop. Gain scheduling over the speed is not performed as the previous work has shown that the performance is sufficiently high [SKHH18], which is also confirmed in this case.

Figure 7.8 shows the performance of the ground lateral controller during a simulated landing for which the initial touchdown point was set to $20\,\text{m}$ right to the runway centerline. In 7.8a, both control variables, the rudder and the nosewheel, are shown. As the aircraft is significantly off the centerline at the beginning of the simulation, both variables are at their saturated value, being $-30°$ and $60°$, respectively. One has to keep in mind that a deflection to the right is indicated by a positive value for the nosewheel deflection and a negative value for the rudder since the nosewheel is located in front of the origin of the body-fixed coordinate frame B and the rudder behind it. The commanded inputs converges to zero as time progresses and the aircraft approaches the centerline. The discontinuity during the beginning of the simulation is caused by numerical instabilities resulting from the touchdown and the speed-up of the wheels.

The actual and the commanded yaw rate is shown in figure 7.8b. As the yaw rate is separated from the control inputs by only one integration, it is fairly dynamic and follows the commanded value very well. A negative yaw rate is commanded in order to turn the aircraft to the left towards the centerline when the lateral position offset is positive, i.e. to the right. The actual and commanded heading in 7.8c are also quite close to each other, although not as perfectly aligned as the yaw rate. The values for the heading is corrected such that the runway heading is exactly zero. Figure 7.8d finally shows the ultimate target variable, which is the lateral deviation from the centerline. The commanded value is not explicitly shown as it is represented by the horizontal zero

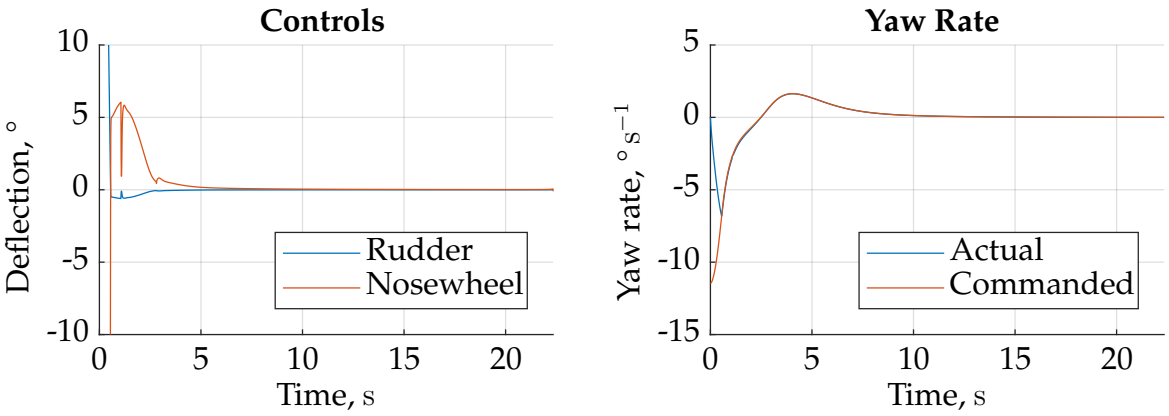

(a) *Control variables*

(b) *Commanded and actual yaw rate*

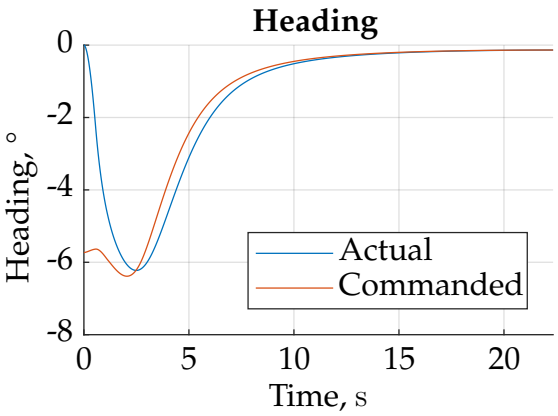

(c) *Commanded and actual heading*

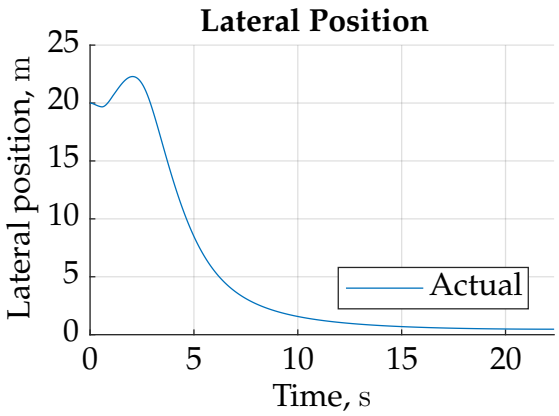

(d) *Lateral deviation from the centerline*

Figure 7.8: *The lateral controller behavior for a simulated landing*

line. The increase of deviation, which is also visible in the heading plot, results from slightly asymmetric braking action caused by oscillations during touchdown. However, after ground contact is thoroughly established, the deviation decreases quickly as the aircraft converges towards the centerline without overshooting. Although stationary accuracy cannot be achieved using this control structure due to the missing integral component, simulations showed that the performance is sufficiently close to reaching the runway centerline even under constant crosswind conditions. The lack of stationary accuracy would only lead to large deviations if the constant crosswind component is high [SHH18] [SKHH18].

8

Distribution Cumulation

8.1 Introduction

In this chapter, the relevant contributing factors for Runway Excursion (RE) and Abnormal Runway Contact (ARC) are extracted from recorded Flight Data Monitoring (FDM) data. Within the scope of this work, only the RE data is further processed for the *Predict* step. The data for ARC, however, is also useful to demonstrate the methods and the algorithms that are implemented.

As already pointed out in section 4.2.4, a distinction between *timepoints* and *measurements* is necessary. Timepoints can be considered as indexes that are used as markers for each flight to indicate certain characteristic events such as touchdown or the application of brakes. Measurements utilize the information provided by timepoints in order to extract relevant information from FDM data at these specific times during the flight. Measurements can directly utilize a single recorded value, such as the speed at touchdown, a series of values, such as the average brake pressure during deceleration or even a timespan, such as the time elapsed between touchdown and the application of brakes.

First, a way to enhance the data and to improve the data quality is presented. For each measurement, the way it is computed, i.e. the algorithm, is described. As data processing always has to account for measuring and recording error, it is necessary to limit the values that are extracted to a range that is physically feasible. As the last part of this chapter, the fitting of probability distributions to the obtained data is presented. These distributions ultimately serve as the input to the last part of the Predictive Analysis (PA): *Predict*.

The detailed data, including histograms as well as the fitted distributions, can be found in the appendix part D.

8.2 Data Enhancement

The FDM data that is used, just like any data, contains error that result from both measuring and recording. The details are described in section 2.3. Particularly the position data could be very inaccurate for landing analysis. The position on-board an aircraft is obtained by fusing information from the Global Navigation Satellite System (GNSS) and the Inertial Reference System (IRS) within the Flight Management System (FMS). While the GNSS position offers long-term stability, it is not sufficiently accurate to precisely determine the touchdown point of the aircraft. On the other hand, position solutions from the IRS is very precise right after initialization, but starts to drift over time as the error in the acceleration and angular rate measurements is integrated, resulting in trajectories that are shifted as time progresses. The service standards that can be achieved using the United States (US) Global Positioning System (GPS) is published by the US government [Nat08]. In the last issue from 2008, the accuracy that could be achieved was given to be $17\,\mathrm{m}$ in horizontal position and $37\,\mathrm{m}$ in vertical position. The numbers given mean that in at least $99\,\%$ of the time, the position solution is obtained such that the $95\,\%$ confidence interval is located within this boundary. In addition, the resolution of the recorded position parameter only allows a precision of approximately $20\,\mathrm{m}$, as already described in chapter 2. Clearly, this is not sufficient to obtain the position, particularly the lateral position, during landing as commercially used runway have a typical width between 30 and $60\,\mathrm{m}$.

In order to obtain a more precise position and speed data during the approach and landing of the aircraft, information from several sources of information can be combined. Besides the position and the speed itself that contain large uncertainty, available measurements include the aircraft's attitude, angular rates, barometric altitude, radio altitude as well as deviations measurements from the Instrument Landing System (ILS) glideslope and localizer. Using a Rauch-Tung-Striebel (RTS) smoother, the data is enhanced by making the measurements kinematically compatible to each other [Höh16]. Especially the lateral position with respect to the runway becomes much more precise by including measurements of the localizer. As the localizer measures the Difference in Depth of Modulation (DDM), which is proportional to the angular deviation from the runway centerline, the position can only be obtained by including the distance of the localizer antenna relative to the runway. The longitudinal position can be corrected by comparing the point at which the aircraft vacates the runway with the available taxiways and shifting the trajectory to fit to the taxiways, assuming the aircraft is precisely on the taxiway centerline.

The results from the implemented measurements are based on the enhanced data using the methods described above [Höh17]. This is of high importance, particularly for the examination of runway veer-off accidents since the lateral position is not sufficiently

precise in the original data. The exact positions of the sensors, including radio altimeter, ILS glideslope and localizer receiver antennae as well as barometric altitude, are required for the smoothing. They can be obtained from datasheets provided by Airbus for its aircraft types A319 [Air18b], A320 [Air18c], A321 [Air18d], A330 [Air18e], A340-300 [Air18g], A340-600 [Air18f], A380 [Air16] and A350 [Air18h].

8.3 Implemented Measurements

8.3.1 Operational Parameters

8.3.1.1 Touchdown Point

The logics for spoiler deployment also include a proper detection of the touchdown point, it is described in section 7.2. When detecting the touchdown point, it is important that the same logics are used as on-board the aircraft which means the same signals are used as described in figure 7.1. The algorithm has to be adapted to the aircraft type, also taking into account multiple landing gears if applicable, such as on the Airbus A380 in figure 8.1.

Figure 8.1: *An Airbus A380 touching down on the runway with multiple landing gears. The glideslope antenna is visible on the left which is located abeam the desired touchdown point.*

8.3.1.2 Aircraft Landing Mass and Balance

The mass of the aircraft at touchdown and the location of the Center of Gravity (CG) is a strong contributing factor to any runway related accident. The CG is typically given in percentage of the Mean Aerodynamic Chord (MAC). Both the mass and the CG are limited by the flight envelope. Each aircraft is certified with a Maximum Landing Mass (MLM) and a range of permitted positions for the CG.

8.3.1.3 Landing Speeds

The speed of the aircraft at landing heavily contributes to RE accidents. The cumulation of the landing speed itself, however, proves to be not viable as the landing target speed varies among the flights depending on operational and environmental conditions. The calculation of the landing speed is described in section 7.4. The actual landing speed again deviates from the target landing speed. This means that when looking at the landing speed itself as a distribution, it is a distributed value of a distributed value which further increases the uncertainty. Besides, the approach speed depends on many other contributing factors. If it is directly used later during sampling, this dependency has to be taken into account as well.

As an alternative approach, the deviation from the approach speed target is used as the input. It can be obtained by subtracting the respective target approach speed from the actual speed at touchdown for every flight. The target approach speed is either directly recorded in FDM or it can be computed using the Operations Manuals (OMs) Part B, the required inputs, such as mass, CG, temperature, wind speed and direction, are available from FDM.

For the simulation model, the groundspeed V_{GS} is required as this is the kinematic speed used for the numerical integration. The True Airspeed (TAS) V_{TAS} is required to compute the aerodynamic forces. However, the approach speed is always expressed as Indicated Airspeed (IAS) V_{IAS} since this is also the measured speed directly available in the cockpit. A conversion from V_{IAS} to V_{TAS} and to V_{GS} becomes necessary. As the speeds during landing do not exceed an equivalence of Mach 0.3, the conversion can be performed under the assumption of an incompressible flow, making only the correction for air density necessary:

$$V_{\text{TAS}} = V_{\text{IAS}} \cdot \sqrt{\frac{\rho_s}{\rho}}, \tag{8.1}$$

where ρ is the prevalent air density and $\rho_S = 1.225\,\mathrm{kg\,m^{-3}}$ is the reference air density according to the International Civil Aviation Organization (ICAO) Standard Atmosphere (ISA) at Mean Sea Level (MSL). V_{GS} can be obtained by subtracting the headwind component from V_{TAS}.

8.3.1.4 Flare Height

For this particular measurement, but also for any succeeding measurement involving the flare maneuver, such as the vertical acceleration during flare, the first task is to detect the flare. The method used is based on two models: one describing the trajectory of the flare and the second describing the trajectory on the ILS glideslope. The idea

is to use data points on the trajectory during final approach and fit the data to both models, obtaining the fitting error as Root Mean Square Error (RMSE). The error for the glideslope model increases when the flare is initiated, at the same time, when going backwards from the touchdown point, the error of the flare model should increase when data points from the glideslope are added [DHSH13].

When the sum of both errors is computed, an ideal flare is initiated at the point at which the sum of both errors reaches a minimum. Figure 8.2 shows both RMSE curves as well as the sum for an ideal flare, indicating where the flare maneuver was initiated.

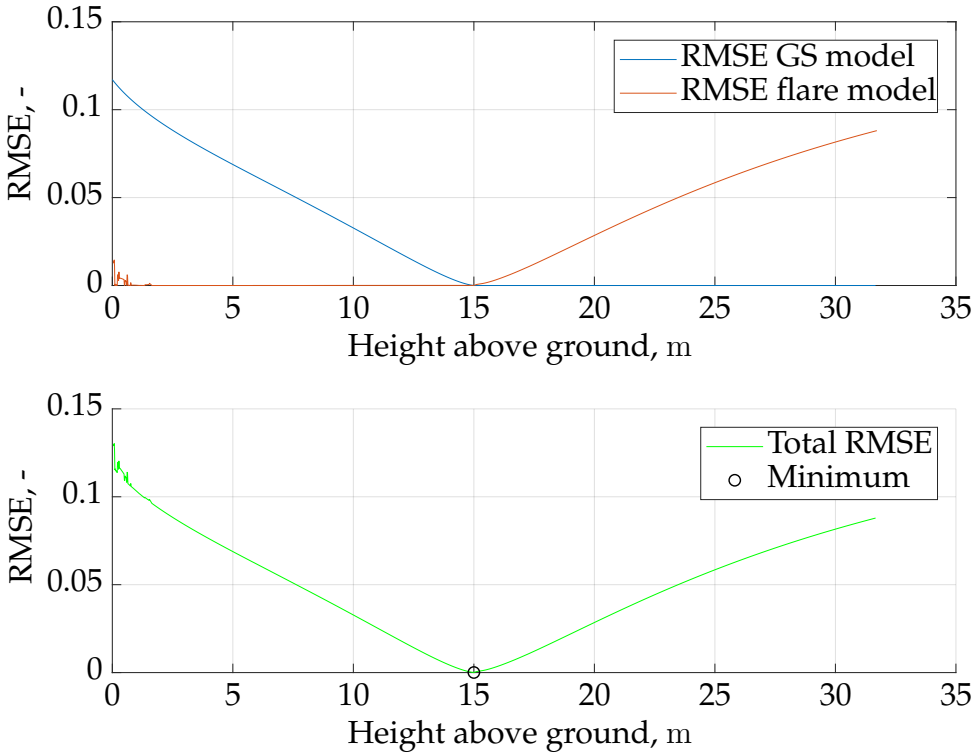

Figure 8.2: *Flare detection using a flare and a glideslope model [WDH16a]*

Of course, most real-life flare maneuvers look different than in figure 8.2. In some cases, the pilot pulls gently on the stick in order to test the aircraft response early during the approach long before the actual flare, which could be erroneously detected as the actual one [WDH16a].

8.3.2 Environmental Parameters

8.3.2.1 Wind

The wind speed V_W and the wind direction, i.e. where the wind is coming from $-\chi_W$, are important contributing factors to the landing performance. χ_W always indicates the

direction into which the wind is blowing. Both are recorded in FDM. As the absolute wind direction is not important for landing analysis but rather the relative direction to the aircraft's heading and runway heading, the headwind $V_{\text{W,head}}$ and the crosswind $V_{\text{W,cross}}$ components based on the aircraft's heading Ψ are computed using equations (8.2) and (8.3).

$$V_{\text{W,head}} = -V_W \cos(\chi_W - \Psi) \tag{8.2}$$

$$V_{\text{W,cross}} = V_W \sin(\chi_W - \Psi) \tag{8.3}$$

The direction of the crosswind is defined such that wind blowing towards the right of the aircraft is considered to be positive.

8.3.2.2 Atmospheric Conditions

The atmospheric conditions during landing include the temperature, the air density as well as the air pressure. If only two of the values are known, the third can be computed using the ideal gas law in equation (8.4).

$$p = \rho R T \tag{8.4}$$

$R = 287.058\,\text{J}\,\text{kg}^{-1}\,\text{K}^{-1}$ is the gas constant for air, whereas p is the static pressure, ρ is the air density and T is the static air temperature.

For the static air pressure, it is important to know that it is typically directly measured, but not recorded. Instead, it is converted to the barometric altitude using the ICAO standard atmosphere. The air data sensors on the Airbus A350 is shown in figure 8.3. The visible probes include the sideslip and angle of attack sensor, the static port, the Pitot tube and the total air temperature sensor.

The static pressure p can then be converted using the recorded barometric altitude h_{baro} and the reference pressure p_{QNH}, which is recorded using the definition of the ICAO standard atmosphere:

$$\frac{p}{p_{\text{QNH}}} = \left[1 + \frac{\gamma_{\text{Tr}}}{T_s} \cdot h_{\text{baro}}\right]^{\frac{-g}{R\gamma_{\text{Tr}}}}. \tag{8.5}$$

Equation (8.5) is only valid for the troposphere, i.e. the altitude above MSL is $11\,000\,\text{km}$ or lower, which is valid for all the considered landings. The reference parameters for the standard atmosphere are presented in table 8.1.

Figure 8.3: *Air data sensors on the left side of the nose of the Airbus A350. The static port is located right below the windows surrounded by the red dashed line.*

Parameter	Symbol	Value
Reference temperature at MSL	T_s	$288.15\,\mathrm{K}$
Temperature gradient	γ_{Tr}	$-6.5 \times 10^{-3}\,\mathrm{K\,m^{-1}}$
Gravitational constant	h_g	$9.806\,65\,\mathrm{m\,s^{-2}}$
Universal Gas Constant	R	$287.05\,\mathrm{J\,kg^{-1}\,K^{-1}}$

Table 8.1: *Values for the troposphere defined in the ICAO standard atmosphere*

8.3.3 Time Measurements

8.3.3.1 Spoiler Deployment

Though the spoiler deployment is triggered by internal system logics of the aircraft after armed by the flight crew, the time at which the spoilers are extended after touchdown can slightly vary. The time that elapses between touchdown and the deployment of the spoilers is, therefore, extracted from FDM as a measurement and incorporated in the model.

8.3.3.2 Brake Application

The same time measurement is extracted for the application of braking as well. While the use of autobrake certainly leads to a smaller variance of the time between touchdown and brake application, this value can have a much higher spread when brak-

ing is performed manually. It does not only depend on the pilot's performance, but also operational aspects, such as the location of the taxiways and the location of the expected parking position relative to the runway. If the terminal building and the associated parking position is more towards the end of the runway and high-speed exits are available, the pilot could somewhat delay the braking or reduce the braking action.

8.3.3.3 Reverser Deployment

The application of reverse thrust also impacts the landing performance. In this case, it is not only important when reverse thrust was deployed relative to touchdown, but also how much reverse thrust was applied. Therefore, the exact position of the thrust lever on the reverse scale is required.

8.4 Distribution Fitting

For the propagation using Subset Simulation, as described in section 5.4, the data has to be inserted as Probability Density Functions (PDFs). Distributions fitting is carried out on the available data. The distributions that are used are listed in the appendix B. In order to determine the distribution that fits best, a least-square method is used. For each fitted distribution, a Kolmogorov-Smirnov test [Reu09] is performed. The p value of the null hypothesis (i.e. the data is distributed according to the fitted distribution) for each fit is also shown in the figures in appendix B.

In addition to the defined distributions, Kernel Density Estimation (KDE) can be utilized to fit a non-parametric distribution to the data. The advantage of KDE is that it can closely follow the available data. However, this implies that it also includes spikes and outliers in the data used for fitting that might not be representative of the actual distribution of values. In chapter 9, both fitting methods will be used in order to enable a comparison of the results.

Some of the timepoint data, especially the spoiler deployment and the reverser deployment, are not very well fitted by the respective distributions, particularly because they are discretized to certain values or are multi-modal. This is mainly due to the measuring process of the parameters. The spoiler position, for example, is recorded with a frequency of $1\,\mathrm{Hz}$. This means that a deployment of the spoilers can only be detected with a precision of $1\,\mathrm{s}$ in time. Therefore, the continuous distribution is, nevertheless, used as it represents the real behavior better than a KDE that follows the data more closely.

After the fitting, the distributions should be truncated, if applicable, to values that are

realistic from a flight dynamics point of view. Many parametric distributions, by nature, do not have either a lower or an upper boundary, or both, to its domain. However, this does not mean that the values of the samples that are generated from the distributions should be unbounded. For many contributing factors, such as the aircraft mass or the temperature, there are boundaries that cannot be exceeded without getting values that are just not realistic. The distributions, therefore, should be truncated within certain values. These boundaries have to be carefully chosen such that:

1. They can prevent physically unrealistic samples to be generated from the distributions;

2. Samples can still be generated in the tails of the distributions since these are the particularly interesting samples that can lead to accidents.

Direction	Condition	Limit, kn	Limit, $\mathrm{m\,s^{-1}}$
Headwind		30	15.4
Tailwind	Dry or wet runway	10	5.1
	Contaminated runway	5	2.6
Crosswind	Manual landing	30	15.4
	Automatic landing	20	10.3

Table 8.2: *Wind limits during landing for the Airbus A320 [Deu09a]*

These two criteria drive the choice of the truncation values in table 8.3 into contrary directions and suitable compromises have to be found. In addition, limits set by the operator in the Standard Operating Procedure (SOP) can be used as a reference, particularly for operational factors. For example, the certified wind limits for the A320 family are shown in table 8.2. The limits are different depending on headwind, tailwind or crosswind and certain conditions, e.g. runway surface or whether the landing is performed manually or automatically. Landings outside of the given wind conditions must not be performed, but this does not mean that landings actually never happen under these circumstances. Another example is the touchdown distance. While the operator specifies that touchdown should be achieved at $300\,\mathrm{m}$ and no later than $900\,\mathrm{m}$ beyond the threshold [Deu13], it may be expected that some few landings touchdown beyond that point, particularly since the runway length at Munich Airport (MUC/EDDM) is $4000\,\mathrm{m}$. For the heading deviation at touchdown, the so-called crab-angle, a maximum value of $10°$ is allowed. Airbus requires the crab angle to be no more than $5°$ at touchdown [Air08]. In general, if these limits cannot be fulfilled, a landing must not be performed. However, that does not actually mean that landings are never performed under these conditions. Limits could be exceeded shortly before touchdown after complying with them throughout the entire approach. In these cases, pilots could decide to continue the landing. Previous accidents have also shown that some of them are caused by the flight crew not realizing or even ignoring that limits have been exceeded.

The values can also be chosen individually for different airports and aircraft types, if necessary. For example, the value for the aircraft mass that is shown applies to the Airbus A320 family. Other values have to be used when other aircraft types are considered. Individual values for the A319, A320 and A321 can also be introduced if necessary.

Contributing Factor	**Unit**	**Lower Limit**	**Upper Limit**
Average brake pressure	psi	50	3000
Average reverse thrust lever	%	0	100
CG position	%MAC	10	50
Crosswind at touchdown	$\mathrm{m\,s^{-1}}$	-20	20
Groundspeed at touchdown	$\mathrm{m\,s^{-1}}$	50	100
Headwind at touchdown	$\mathrm{m\,s^{-1}}$	-15	30
Aircraft mass	kg	4×10^4	9.5×10^4
Lateral deviation at touchdown	m	-25	25
QNH pressure at touchdown	hPa	850	1050
Heading deviation at touchdown	°	-10	10
Touchdown distance	m	0	2000
Temperature at touchdown	K	240	340
Time of spoiler deployment	s	0	10
Time of begin of braking	s	0	10
Time of reverser deployment	s	0	10
Time of end of braking	s	20	200
Approach speed deviation	$\mathrm{m\,s^{-1}}$	-20	20

Table 8.3: *Truncation limits for the contributing factors*

9

Accident Prediction

9.1 Introduction

After all the steps of the Predictive Analysis (PA) are described and the required tools are presented, this chapter finally performs the prediction, i.e. the computation of the accident probabilities. It combines the aforementioned methods into an entire tool chain:

1. The processing of Flight Data Monitoring (FDM) data from the aircraft (see chapter 2)
2. The implementation of the PA (see chapter 4) for Runway Excursion (RE), in particular the following steps:
   (a) *Modeling* of the aircraft's behavior during landing roll, including the system logics and pilot behavior (see chapter 6 and chapter 7)
   (b) *Cumulation* of measurements from FDM and distribution fitting (see chapter 8)
   (c) Accident *prediction* using Subset Simulation (see chapter 5)

For the analysis, recorded FDM data from landings at Munich Airport (MUC/EDDM) is used. Table 9.1 shows the available landings in the database on each runway for the aircraft types of the Airbus A320 family, i.e. A319, A320 and A321.

The data was provided by the operator without the detailed information about the specific aircraft type within the A320 family. Therefore, the distinction had to be made using the available data. The differentiation of the A321 data is based on the engine type installed. While the A319 and the A320 aircraft in the fleet are equipped with CFM56-5 engines by CFM International, the A321 in the fleet uses V2500 engines manufactured by International Aero Engines (IAE). Since the two engines use different con-

Rwy \ A/C	A319	A320	A321	Total
08L	470	2058	2540	5068
08R	152	980	2317	3449
26L	259	1307	3201	4767
26R	513	3303	3935	7751
Total	1394	7648	11993	21035

Table 9.1: *Available data for each scenario, sorted by aircraft type (A/C) and runway (Rwy); The baseline scenario is highlighted.*

trol parameters, there are distinct properties in the Dataframe Layout (DFL) structure. While the CFM56 uses the rotational speed of the low pressure shaft N1 to control the thrust, the V2500 uses the Engine Pressure Ratio (EPR). The separation of the A319 data proves to be more difficult since they share the same engine type with the A320. It was performed using the flap deflection angle when the configuration is set to *CONF Full*. In this configuration, the flaps on the A320 extend to $35°$ while on the A319, the angle reaches $40°$ [Deu09a]. However, for landings performed using configuration *CONF 3*, this distinction is not possible since the deflection angle on both aircraft types are identical. A separation based on the aircraft's mass was tested since both aircraft differ in Maximum Take-off Mass (MTOM) and Maximum Landing Mass (MLM). However, this turned out to be difficult since there are still significant overlaps in the mass range of the two aircraft types.

A small number of flights was excluded from the analysis because the data enhancing algorithm using the Rauch-Tung-Striebel (RTS) smoother could not perform successfully. The reason for this is mainly the fact that an Instrument Landing System (ILS) approach is required to perform the smoothing, i.e. a localizer frequency corresponding to the ILS of one of the runways has to be recorded along with the measurements of the Difference in Depth of Modulation (DDM) of both the localizer and the glideslope. If one of these parameters is not available, the smoothing algorithm fails. As the number of affected flights is very small compared to the total available amount of data, these flights are simply excluded.

The Subset Simulation runs were, unless otherwise stated, performed using a conditional probability of $p_0 = 0.1$ and a sample size of $N = 2 \times 10^3$. Infinity Sampling is used to generate the samples for the Markov Chain. These parameters were chosen as a trade-off: Higher number of samples lowers the Coefficient of Variation (c.o.v.), meaning that the obtained accident probability is more reliable, but considering computational effort, the number of samples should be reduced to a minimum.

For the analysis, the landing of the Airbus A320 on runway 26R at MUC/EDDM with fully extended flaps and slats (*CONF Full*) under dry runway conditions is used as the

baseline. This scenario is highlighted in table 9.1. Runway 26R was chosen because it has the highest number of landings based on the available data. An Airport Ground Chart (AGC) of MUC/EDDM can be found in the appendix C. All other scenarios are derived from and compared with the baseline. Table 9.2 shows the properties that can be varied and the possible states they can adopt. The baseline scenario is written in *italic*.

Property	**Possible States**
Aircraft Type	A319; *A320*; A321
Flap / Slat Configuration	CONF 3; *CONF Full*
Runway Condition	*Dry*; Wet
Runway	08L; 08R; 26L; *26R*
Distribution fitting	*Parametric distribution*; Kernel density

Table 9.2: *Possible variations from the baseline scenario, which is highlighted in italic.*

For the Airbus A320 family, two possible configurations can be used for landing: *CONF 3* and *CONF Full*. The decision is up to the flight crew and it depends on operational and environmental conditions. For each configuration, different approach target speeds are used, see table 7.4. The approach target speed is typically higher when using *CONF 3* instead of *CONF Full* since the zero lift coefficient C_{L0} is higher if the flaps and slats are further extended. The runway condition is reflected in the friction coefficient, represented by the slip-to-friction curve by Pacejka introduced in section 6.3.3.2. The maximum achievable friction coefficient is always lower for wet runways compared to dry runways, but the overall shape of the curve described by equation (6.37) can be different as well. All four possible landing runways at MUC/EDDM airport, i.e. two runways with two directions each, are considered. All of them have a length of $4000\,\mathrm{m}$ and a width of $60\,\mathrm{m}$. As described in section 8.4, the distribution fitting of the available data can be done by using either given parametric distributions, listed in the appendix B, or by using Kernel Density Estimation (KDE). The difference of the results are shown here as well.

In the following sections of this chapter, the computed results for both runway overrun (section 9.2) and runway veer-off (section 9.3) are presented for the baseline scenario and the derived scenarios for comparison.

9.2 Runway Overrun Probability

9.2.1 Baseline Scenario

For the baseline scenario, the overrun probability is shown in figure 9.1. The Probability Density Function (PDF) of the Beta distribution is shown along with the mean and

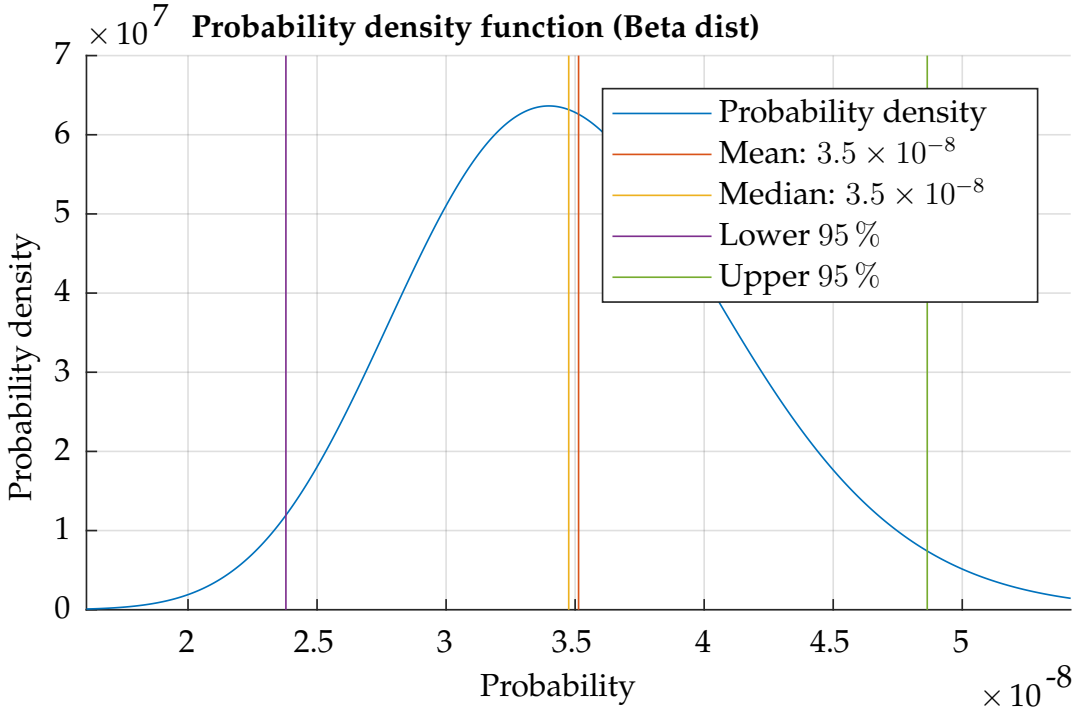

Figure 9.1: *The Beta distribution (PDF) of the overrun probability for the baseline scenario, along with the mean and the median value as well as the boundaries for the 95% confidence interval*

the median. Both of them are at around 3.5×10^{-8} per flight, the standard deviation of the Beta distribution is at 6.4×10^{-9}, which is almost one order to magnitude lower than the mean value, resulting in a c.o.v. of 0.18. Figure 9.1 also shows the lower and the upper boundaries of the 95% confidence interval based on the Beta distribution.

Figure 9.2 shows how samples are generated in each subset and how they move towards lower stop margins as the Subset Simulation progresses. The number of samples in each subset is identical. As the conditional probability is introduced by the Markov Chain Monte Carlo (MCMC) algorithm, samples start moving towards lower stop margins. The intermediate failure domains are very well visible in this figure, it is indicated by the upper boundaries of the samples in each subset. The intermediate failure threshold moves towards smaller stop margins with each subset until a sufficient number of samples fulfilling *stop margin* < 0 is obtained. According to the MCMC algorithm, it can be said that the histogram of the samples in subset i is a magnification of the histogram from subset $i-1$ for the area below the intermediate failure threshold C_{i-1}. According to the MCMC algorithm, newly generated samples are rejected and reverted back to the seed sample if the new sample is located outside of the intermediate failure region. The simulation stops when at least $p_0 N$ samples are located below a stop margin of zero, i.e. indicating an overrun, which is achieved in subset eight in this particular example.

It is important to identify the influence of each contributing factor. Therefore, some

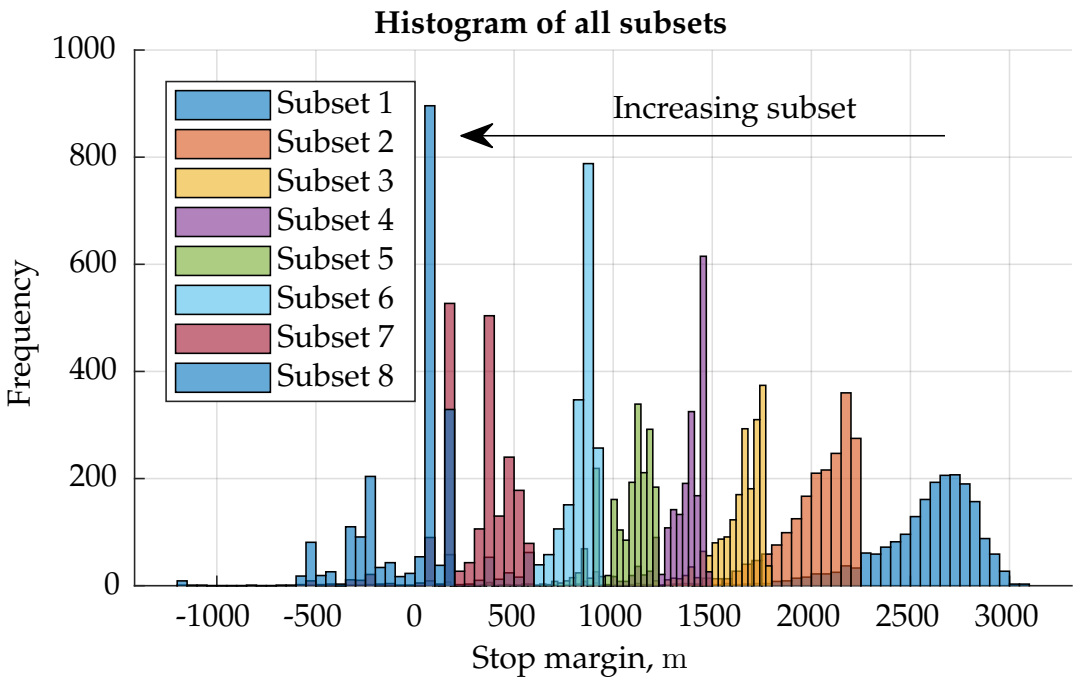

Figure 9.2: *Histogram of all samples generated across all subsets*

figures were created that show how the samples move towards lower stop margins when the contributing factors move to either higher or lower values with each subset.

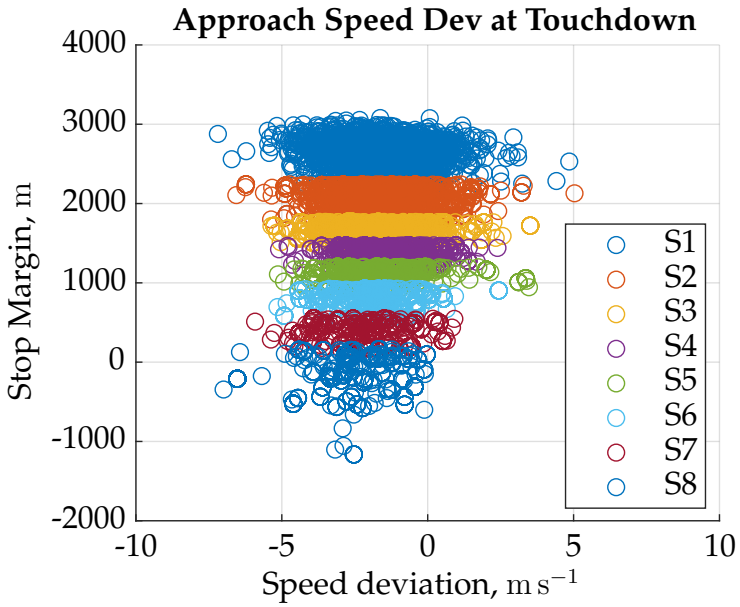

Figure 9.3: *The influence of speed deviation at touchdown*

Figure 9.3 shows the influence of the approach speed deviation. Negative values indicate that the actual approach speed is lower than the target approach speed. Samples from the same subset are drawn using an identical color. It is well visible that the speed deviation does not significantly change as the Subset Simulation progresses from one subset to the next.

As the value is obtained at the time of touchdown, it is plausible that the deviation of the approach speed are mostly below zero, which means that the Indicated Airspeed (IAS) of the aircraft is lower than the target reference speed. Shortly before the touchdown, the aircraft performs the flare maneuver, enabling a smooth touchdown and some reduction in speed as the throttles are retarded back to idle. In figure 9.3, one can see that, as the stop margin decreases, the approach speed deviation moves slightly towards lower values, but not significantly, though the spread of the samples becomes smaller. This behavior is surprising as a higher touchdown speed would certainly lead to longer braking distances and, thus, increase the risk of an overrun.

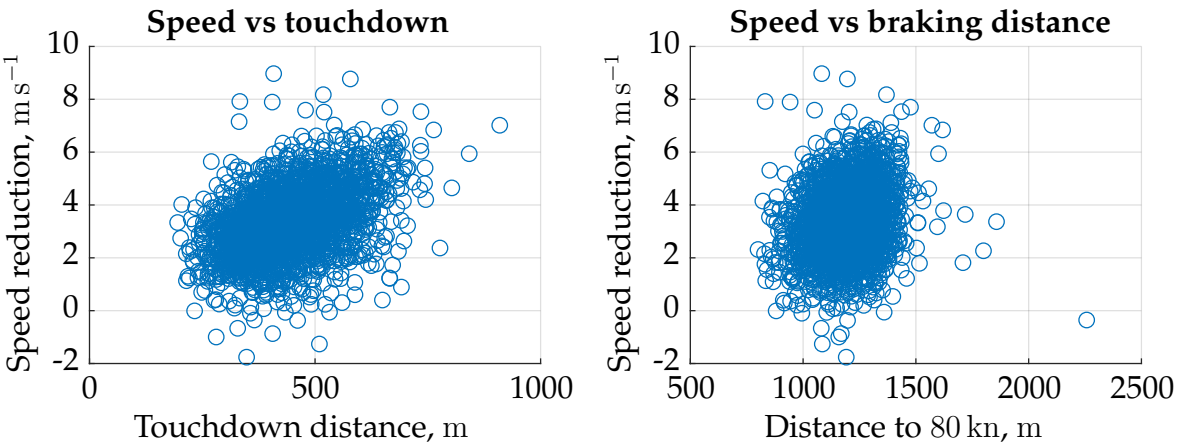

(a) *Correlation of the touchdown distance* **(b)** *Correlation of the distance to* 80 kn

Figure 9.4: *Correlation to the approach speed at touchdown*

A possible explanation can be found in figure 9.4. In figure 9.4a, the touchdown distance is plotted against the change in speed during the last part before touchdown. To be more precise, the speed at touchdown and the speed at the point at which the aircraft is at 50 ft Above Ground Level (AGL) are extracted and subtracted from each other. Positive values indicate that the aircraft was faster when passing 50 ft which is essentially when it overflies the runway threshold for a standard ILS configuration. It is well visible that a higher reduction in speed in general leads to a longer touchdown distance. This means that the aircraft floats longer above the runway, the speed reduces in the meanwhile, but the aircraft touches down later. Figure 9.4b shows the same relationship for the distance until the aircraft reaches a Groundspeed (GS) of 80 kn. This speed is considered as the value until which sufficient braking should be applied regardless of the available margin. A correlation is visible here as well and it shows that if the speed reduction is higher, the flare is longer and the touchdown is later, leading to a longer braking distance. The important statement is that deceleration on the ground is much more effective than while airborne. Therefore, a higher touchdown speed does not necessarily lead to a higher probability of overrun as it is most often the result of an earlier touchdown, meaning that the aircraft has a longer distance available to apply braking and other deceleration means.

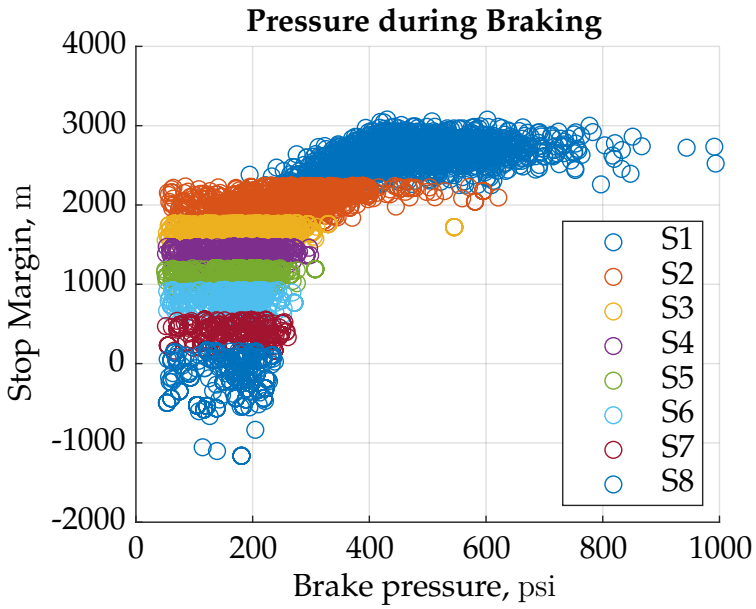

Figure 9.5: *The influence of the average brake pressure on the stop margin*

Figure 9.5 shows the same samples along with their corresponding stop margins and the average brake pressure that was applied. It is clearly visible that the influence of the brake pressure on the stop margin is extremely high. The samples move towards lower brake pressure values with each subset and decreasing stop margin values. The samples that represent overruns, i.e. where the stop margin is smaller than zero, are all associated with brake pressures of no greater than 300 psi whereas the first subset, which is created by simple Monte Carlo Simulation (MCS), contains samples of up to 1000 psi.

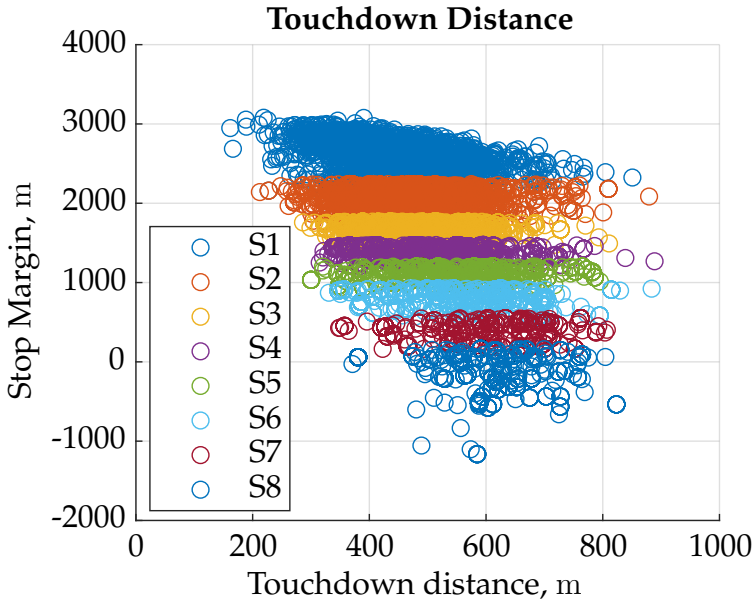

Figure 9.6: *The influence of touchdown distance on the stop margin*

In figure 9.6, the influence of the touchdown distance is shown. The desired touch-

down point for runway 26R at Munich airport is located $1000\,\mathrm{ft}$, i.e. $305\,\mathrm{m}$, behind the runway threshold. In figure 9.6, one can see that most landings touched down significantly further down the runway, reaching values of up to $1000\,\mathrm{m}$. An increase of the touchdown distance leads to an decrease of the stop margin. The spread between the samples becomes smaller as the lower limit increases while the upper limit remains constant. This shows that even though the Landing Distance Available (LDA) at MUC/EDDM is much longer than what the Airbus A320 requires, a late touchdown still increases the probability of suffering from a runway overrun. For the analysis, one has to keep in mind that the touchdown point is also heavily influenced by operational factors, such as the location of the parking position. A smooth and late touchdown occurs more often if the parking position is located towards the end of the runway [WF12].

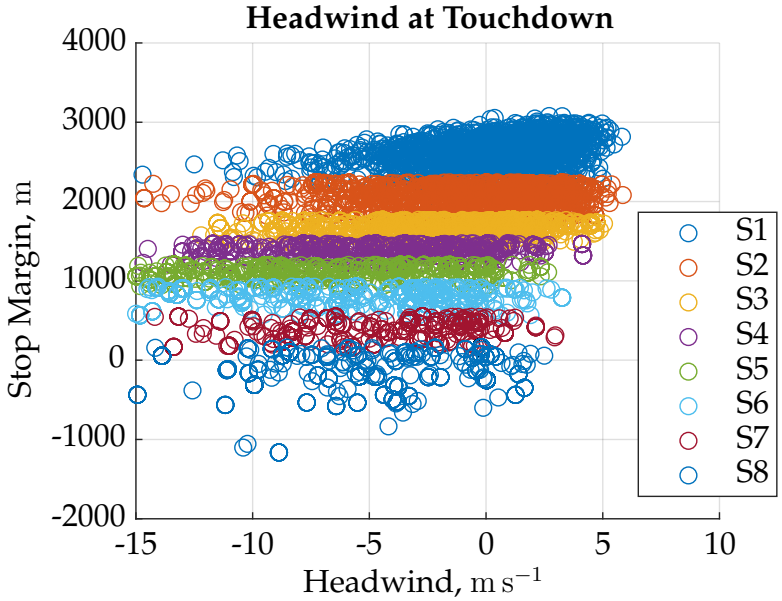

Figure 9.7: *The influence of wind on the stop margin*

The influence of the wind is shown in figure 9.7, where negative values indicate tailwind and positive values indicate headwind. It is clearly visible that stronger tailwinds moves the samples towards lower stop margins, which is consistent with flight physics considerations. The effect is caused by two main effects:

1. As the approach reference speed is always the IAS, stronger tailwinds will increase the GS of the aircraft, which implies a longer distance to slow down. For headwinds, the opposite effect applies. Although equation (7.1) indicates that only a third of the headwind must be added to obtain the target speed, the influence is still significant as the remaining two thirds of the wind speed can be used to benefit the landing performance.

2. As the aircraft is on the ground, stronger tailwinds will lead to lower IASs, which reduce the effect of aerodynamic braking and engine thrust reverse.

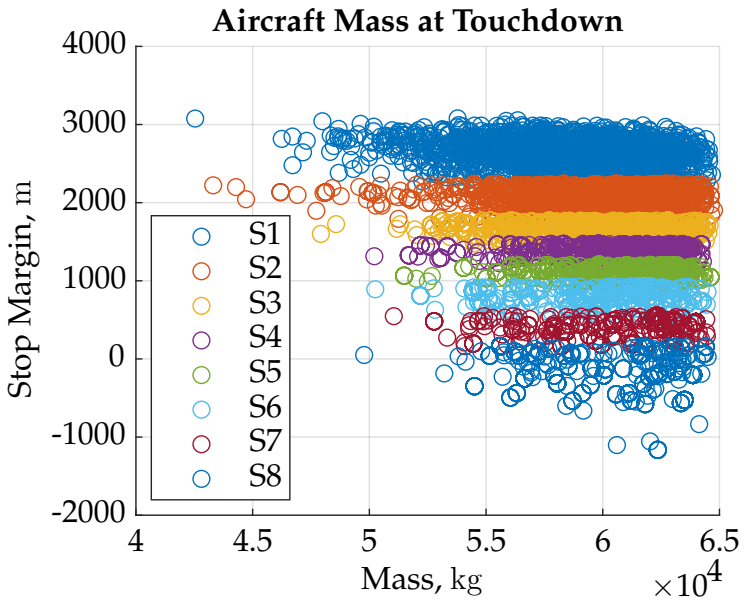

Figure 9.8: *The influence of aircraft mass on the stop margin*

The aircraft's mass at touchdown is shown in figure 9.8. The MLM of the Airbus A320 is limited to $64\,500\,\mathrm{kg}$ [Air18c], which is well visible as the upper boundary of the data. The Maximum Certified Take-off Mass (MCTOM) of the A320 is, depending on the exact version, between $70\,400\,\mathrm{kg}$ and $77\,400\,\mathrm{kg}$. In general, the landing mass of the aircraft must not exceed the MLM, but overweight landings can be performed in emergency situations. It is, however, clear that the landing weight can never be higher than the MCTOM because this would indicate a prohibited departure configuration. As there were no overweight landings in the data, the generated samples are also all located within the boundaries of the MLM. Figure 9.8 clearly indicates that the samples move towards higher masses as the simulation progresses and the stop margin decreases. This is consistent with the physical understanding of the aircraft dynamics. All samples that indicate an overrun have MLMs greater than $50\,000\,\mathrm{kg}$. The typical Operating Weight Empty (OWE) is provided by Airbus to be $42\,600\,\mathrm{kg}$ [Air09], which means that in order to be exposed to a high risk of overrun, the aircraft should have at least $5000\,\mathrm{kg}$ of fuel and payload on board at the time of touchdown.

Besides of the braking system, the reverse thrust is used as well to slow down the aircraft after landing. Figure 9.9 shows the influence of the use of reverse thrust. According to the system logics of the A320, the reverse thrust has to be manually activated and modulated by the flight crew. However, reverse thrust is inhibited until the aircraft detects the ground condition. The horizontal axis is the normalized thrust lever position when set to reverse thrust with 100% being the maximum possible reverse and zero being idle reverse. The values are average values during the time frame when reverse thrust is activated. The significance can be well seen as all overrun samples use very little reverse thrust. For all samples, the amount of thrust reverse used is quite

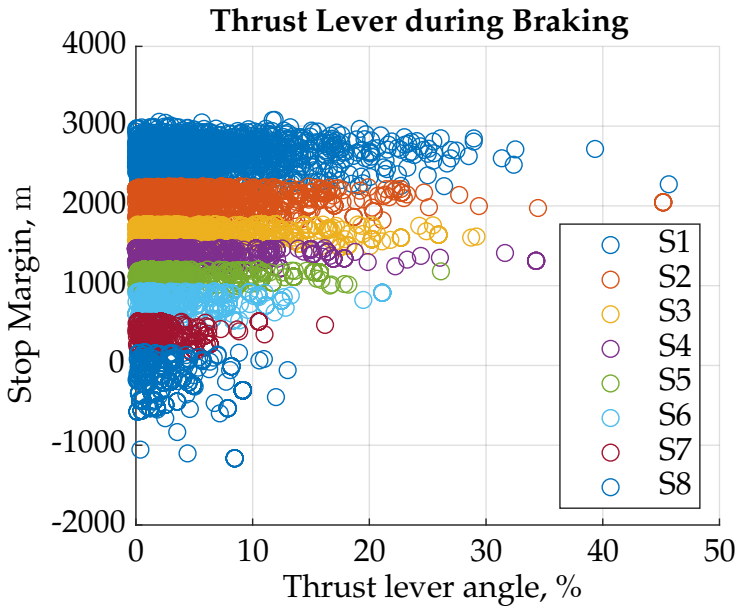

Figure 9.9: *The influence of reverse thrust on the stop margin*

low, never exceeding 50%. This is caused by local procedures at MUC/EDDM as pilots are strongly discouraged from selecting more than idle reverse at MUC/EDDM due to noise abatement.

9.2.2 Scenario Comparison

9.2.2.1 Variation of Runway

In the previous section, the baseline scenario, i.e. the Airbus A320 on runway 26R, was presented. The results for the remaining three runways are shown and compared here. Table 9.3 shows the overrun probability for the other runways or landings directions 26L, 08L and 08R.

	A320 Flaps Full Dry Runway	
	μ	σ
08L	4.7×10^{-6}	7.2×10^{-7}
08R	2.2×10^{-4}	2.7×10^{-5}
26L	2.4×10^{-7}	4.1×10^{-8}
26R	3.5×10^{-8}	6.4×10^{-9}

Table 9.3: *Runway overrun risk for different runways at Munich airport; the baseline scenario is highlighted.*

While the c.o.v. for the other three landing runways are in the same order to magnitude as the results for 26R, which is an indication that the method of distribution

propagation using Subset Simulation delivers results with the same confidence, the actual overrun probabilities are significantly different. The probability for 26L, which is the parallel southern runway, is one order of magnitude higher than for 26R. For 08L, which is the opposite landing direction of 26R, the probability is two orders of magnitude higher. The overrun probability for runway 08R is even larger by a factor of 10^4 compared to 26R.

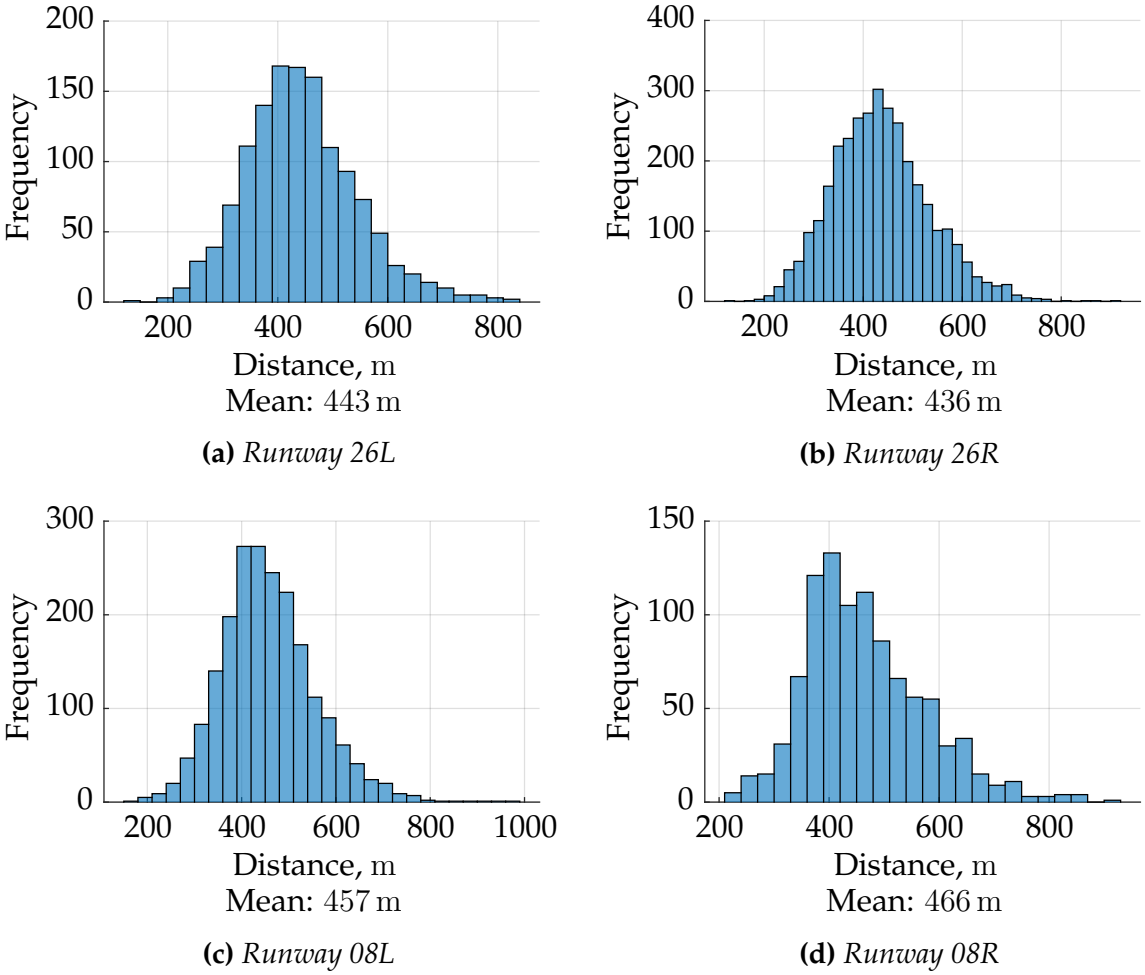

(a) *Runway 26L* **(b)** *Runway 26R*

(c) *Runway 08L* **(d)** *Runway 08R*

Figure 9.10: *Comparison of the touchdown distance for different runways*

Explanations for these numbers are found in the contributing factors for the four runways. Some differences become visible that explain the differences between the results in table 9.3. Figure 9.10 shows the touchdown distances for the four runways. The mean value is also displayed at the bottom of each histogram. The touchdown distances vary slightly across the runways, but the mean is the shortest for 26R, followed by 26L and 08L while touchdown occurs the latest in average on runway 08R, though the mean is only $30\,\mathrm{m}$ longer compared to 26R. In addition, the histogram for 08R shows a heavy tail on the right end, which indicates that a larger share of landings touch down very late on the runway, some more than $800\,\mathrm{m}$.

While some differences are visible when it comes to the touchdown point, they are

not significant between the runways. The reason could be that a vast majority of the approaches are performed at MUC/EDDM using the ILS. This means that the guidance of the localizer and the glideslope always leads to the same desired touchdown point on the runway. Variation is only injected during the very last part of the final approach, when the pilot transitions from the instruments to visual cues for flying. The differences become much more significant when comparing the braking behavior after touchdown.

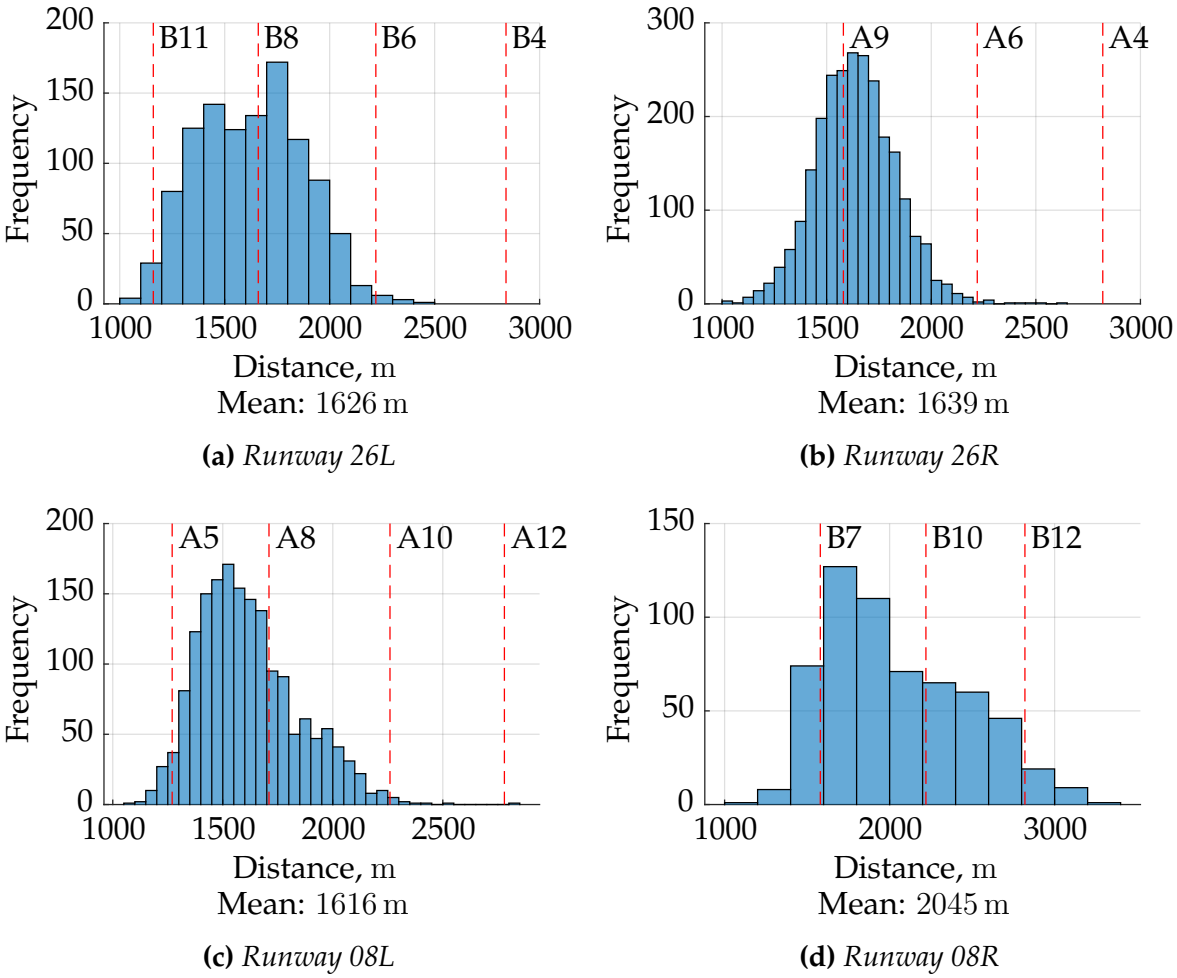

(a) *Runway 26L*

(b) *Runway 26R*

(c) *Runway 08L*

(d) *Runway 08R*

Figure 9.11: *Comparison of the distances between runway threshold and reaching* 80 kn*, with the available exit taxiways shown for each runway*

In figure 9.11, the distances between the runway threshold and the point on the runway at which the aircraft's GS decreases below 80 kn is extracted from the data. The value of 80 kn was chosen because this is the reference value pilots typically use to slow down the aircraft in the first phase of braking. The purpose is to ensure that deceleration is always the top priority until reaching this speed. Below it, other operational conditions, such as the location of the parking position, can become more relevant. In fact, during the type certification phase for an aircraft, the values are even lower. It is typically assumed that any overrun with more than 60 kn or veer-off with more than

30 kn leads to *catastrophic* consequences [FAA17]. Figure 9.11 clearly shows that the distance is, in average, similar on the three runways 26L, 26R and 08L. Runway 08R is an exception with an average value of 400 m higher than the other three. In addition, the spread of the values is lower on the northern runway (26R/08L) compared to the southern runway (26L/08R). The dashed lines indicate the positions of available taxiways that can be used to vacate the runway. Their significance is explained later in this section.

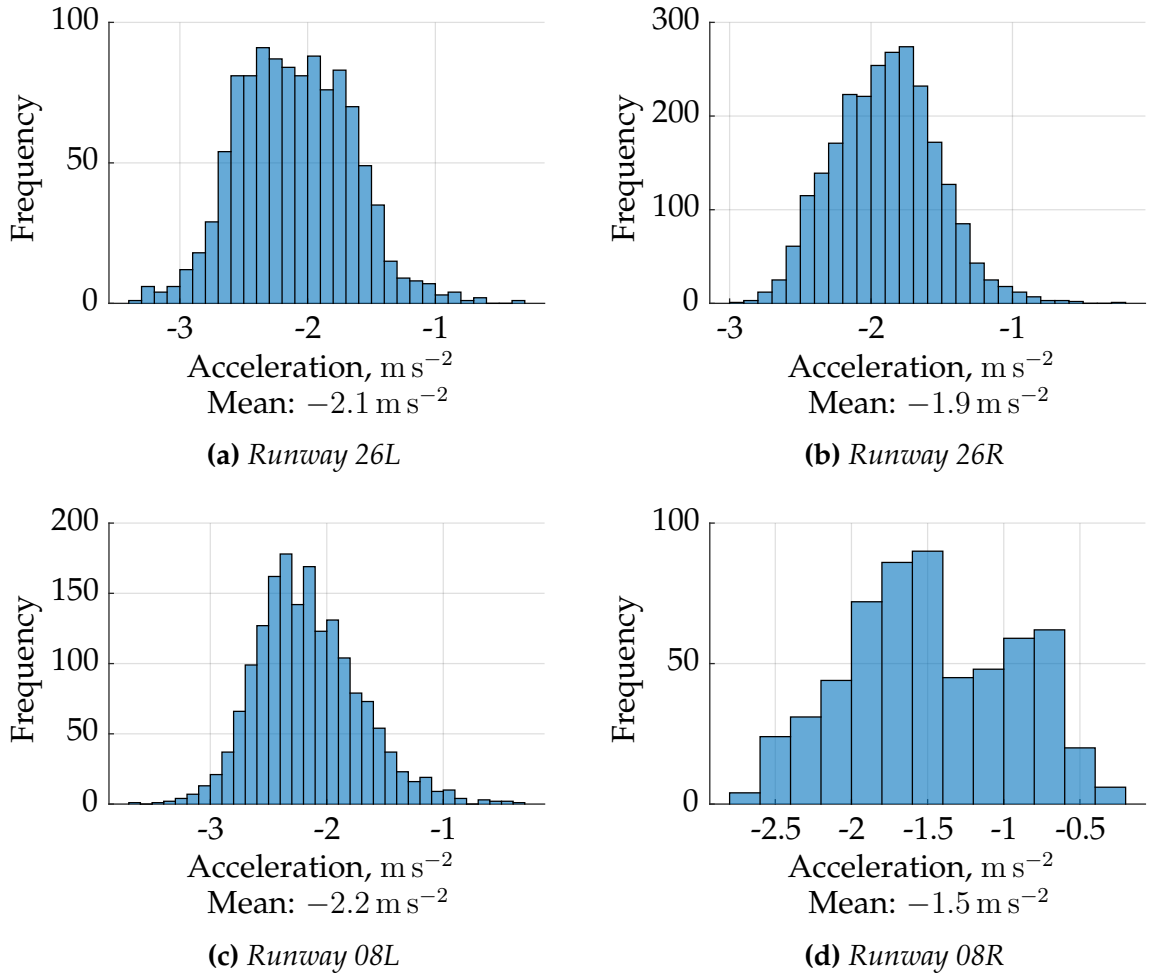

(a) *Runway 26L* **(b)** *Runway 26R*

(c) *Runway 08L* **(d)** *Runway 08R*

Figure 9.12: *Comparison of the mean acceleration during braking*

This observation is consistent with the acceleration data, which is presented in figure 9.12 for all four runways. Again, the values for the three runways 26L, 26R and 08L are close to each other while for 08R, the value is significantly lower. In addition, the data is multi-modal, i.e. there are two visible peaks in the histogram in figure 9.12d.

Similar observations can be found in figure 9.13. The same comparison is done for the brake pressure. The applied average braking pressure during braking is much lower on 08R than on all other runways along with a very heavy tail for low pressure values. As figures 9.5 and 9.6 highlight the influence of the brake pressure and the touchdown

distance on the overrun probability, these differences between the data of different runways explain the difference in the accident probability.

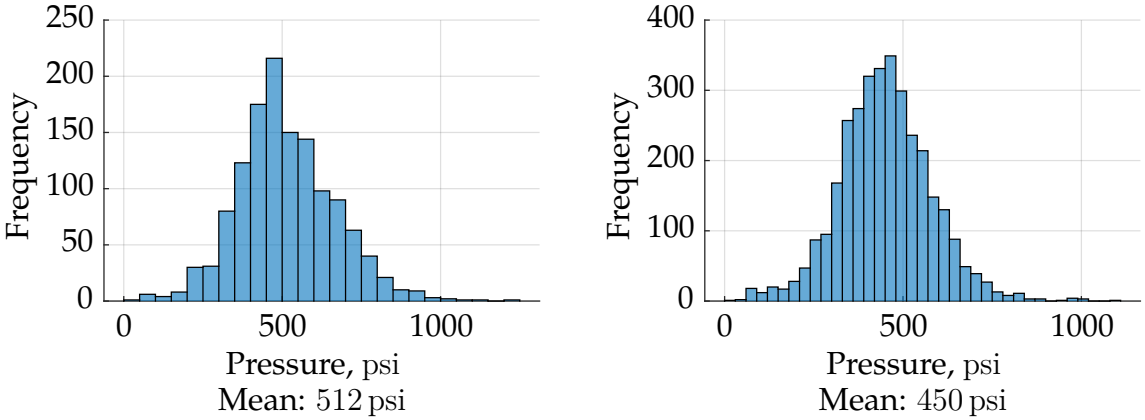

(a) *Runway 26L*

(b) *Runway 26R*

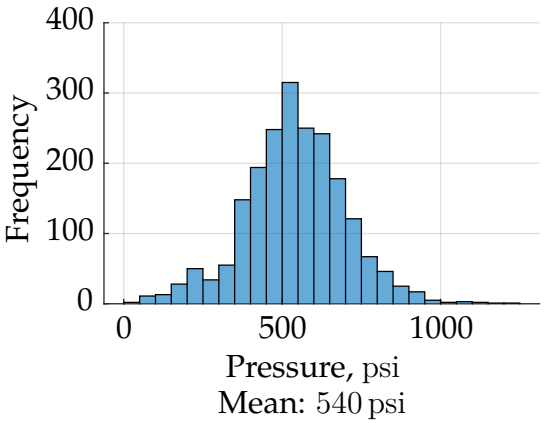

(c) *Runway 08L*

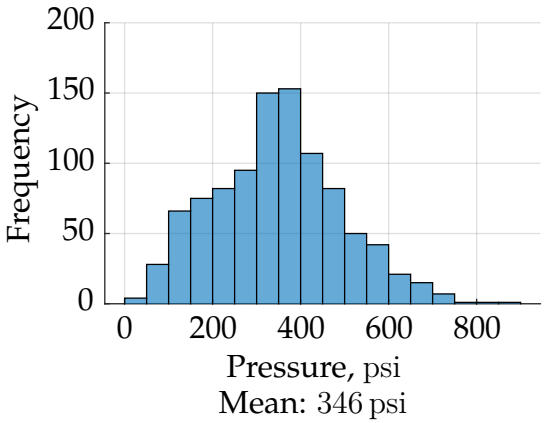

(d) *Runway 08R*

Figure 9.13: *Comparison of the brake pressure for different runways*

The reason for this particular behavior on runway 08R that is reflected in the figures can be found in the layout of Munich Airport. The operator from whom the available flight data was obtained uses gate positions on apron 2 for which the entries S7 and S8 are used when arriving on the southern runway. For the northern runway, this applies to the entries N3 and N4. An aerodrome chart of MUC/EDDM is included in the appendix C which is published by the German state in the Aeronautical Information Publication (AIP) [DFS18]. For the northern runway, i.e. 26R and 08L, in order to reach apron 2, the quickest way is to use the first high-speed exit for both directions, A9 and A5, which are located 1580 m and 1270 m behind the threshold, respectively. In contrast, on the southern runway, the entrance to the apron is located abeam to the touchdown point of runway 26L, which implies that the aircraft has to taxi back even if the first exit (B11, 1160 m behind the threshold) is used. For 08R, the first exit is B7 which is 1580 m behind the threshold. However, exit B12, which is 2820 m behind the threshold is preferably used – traffic permitting – since the aircraft can make a long

roll-out and exit at B12 with the application of minimum braking. During high-traffic hours, as the runway has to be vacated as soon as possible for following traffic, the aircraft can still exit the runway on B10, which is located $2220\,\mathrm{m}$ behind the threshold. Therefore, the location of the taxiways along with the gate positions explain the heavy tail in the brake pressure histogram of runway 08R in figure 9.13d. Munich Airport publishes recommended exit taxiways for all four runways when High Intensity Runway Operation (HIRO) is in progress, depending on the weight category of the aircraft. The table is also included in the appendix C.

Going back to figure 9.11, the location of the high speed taxiways that can be used to vacate are added for each runway along with the taxiway identifier. It is well visible that peaks in the histogram are correlated with the taxiway positions. At MUC/EDDM, high-speed taxiways are available that have an offset of $30°$ in direction relative to the runway. According to the *Aerodrome Design Manual* published by the International Civil Aviation Organization (ICAO) [Int05], these are *rapid exit taxiways* with code number 3 or 4, their design speed is standardized to be $30\,\mathrm{kn}$. Assuming an average deceleration of $2\,\mathrm{m\,s^{-2}}$, slowing down from $80\,\mathrm{kn}$ to $30\,\mathrm{kn}$ would require a distance of $364\,\mathrm{m}$. This value is consistent with the distance between the peaks in the data in figure 9.11 and the location of the taxiways. This clearly proves that, even at high speed, the braking behavior is such that the pilot already aims for a specific exit taxiways.

For the analysis and the computation of overrun probabilities, this has two significant implications:

1. The deceleration behavior can be clustered, i.e. depending on which taxiway is aimed for, the braking process can be significantly different.

2. In order to optimize for a specific taxiway, the braking behavior can differ from the common, i.e. braking with a much lower magnitude may be applied. This also has an influence on the level of safety with respect to overrun.

Having found the explanation for the differences, it can be said that the number for the overrun probability does not necessarily imply that landings on 08R are significantly less safe than on other runways. The operational dependencies are incorporated in the method by using the data containing the information, but they are not fully considered in the context of *all* contributing factors within flight operations. For example, the applied brake pressure will not be low if the landing becomes more critical due to environmental factors, such as weather. It is less likely that the pilot chooses to perform a long roll-out if the touchdown point is already very far down the runway. This calls for incorporating the dependency structure within the data and during its propagation, which is covered in the *Revise* step of the PA, described briefly in section 4.2.6. The details are further explored in other publications outside of, but related to this work [HWK+18].

9.2.2.2 Usage of Kernel Density

Distribution fitting can be performed using either parametric distributions as listed in the appendix B or by using KDE, see section 8.4. The Subset Simulation algorithm is run twice for the runways 26L and 26R each, once using parametric distributions and once using KDE. Table 9.4 shows the results compared with the baseline scenario.

	Parametric		KDE	
	A320 Flaps Full Dry Runway		A320 Flaps Full Dry Runway	
	μ	σ	μ	σ
26L	2.4×10^{-7}	4.1×10^{-8}	1.9×10^{-8}	3.6×10^{-9}
26R	3.5×10^{-8}	6.4×10^{-9}	2.2×10^{-8}	4.0×10^{-9}

Table 9.4: *Runway overrun risk as comparison with KDE; the baseline scenario is highlighted.*

In general, overrun probability values obtained by using KDE are smaller compared to using parametric distributions. The results for runway 26R are very close to each other. For runway 26L, the difference between KDE and parametric distribution is more than one order of magnitude apart. Figure 9.14 shows the histogram of two datasets for runway 26L, along with the fitting of a parametric distribution, in both cases a Generalized Extreme Value (GEV) distribution, and the fitted KDE. The two contributing factors that are chosen here have a particular high influence on the outcome, which was already demonstrated in section 9.2.1. The KDE tends to underestimate the tails of the distributions compared to the GEV. For the average brake pressure in figure 9.14a, the underestimation of the lower tail (smaller than $500\,\mathrm{psi}$) leads to lower accident probabilities as well as for the lower tail of the headwind distribution, particularly between $-5\,\mathrm{m\,s^{-1}}$ and $0\,\mathrm{m\,s^{-1}}$ in figure 9.14b.

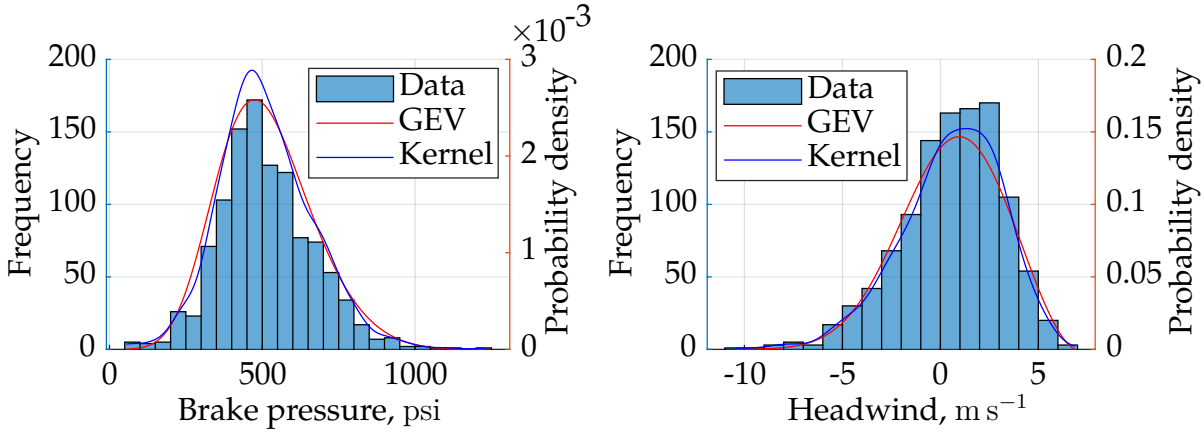

(a) *Average pressure during braking* **(b)** *Headwind at touchdown*

Figure 9.14: *Comparison of fit between parametric distributions and KDE, for runway 26R*

A KDE fit follows the available data much more closely than a parametric distribution. In addition, a KDE can be multi-modal and the PDF can quickly reach zero if there is no data available in a certain area. Especially when it comes to the tails of the distributions, the KDE will, therefore, take up the value of zero if there is simply no measurement in the data while a parametric distribution will decrease slower towards both tails. This behavior explains the computed overrun probabilities that are, in general, lower when using KDE rather than parametric distributions. From the computational point of view, using KDEs can be less efficient because the generation of samples requires more computational effort since KDEs are composed of multiple parametric distributions. Therefore, it always depends on the specific case whether a parametric distribution should be preferred to a KDE.

The differences in the numbers also demonstrate that further effort should be taken to refine the distribution fitting (*Cumulate*) and especially the *Calibrate* step of the PA, which is not the focus of this work. For the remaining part of this work, parametric distributions are used.

9.2.2.3 Variation of Aircraft Type

The Airbus A320 family consists of four members: A318, A319, A320 and A321, listed in ascending order of MCTOM. Data is available only for the A319, A320 and A321. The A318, however, is only utilized by a very few operators worldwide as it only contributes to 80 of 8512 aircraft of the A320 family that have been delivered as of November 2018 with no more outstanding orders [Air18a]. Therefore, the A318 will be excluded from further analysis. Table 9.5 shows the MCTOM and the MLM of each of the three aircraft types according to their certification. As there are many sub-versions of each type, the minimum and the maximum values of each subversion are presented.

	A319	A320	A321
MCTOM	75 900 kg	78 000 kg	93 500 kg
	61 000 kg	70 000 kg	78 000 kg
MLM	62 500 kg	77 800 kg	93 500 kg
	61 000 kg	64 500 kg	73 500 kg

Table 9.5: *Technical specifications for the three members of the Airbus A320 family, showing maximum and minimum values [Air18b] [Air18d] [Air18c]*

Table 9.6 shows the computed overrun probabilities for each of the three aircraft types. The values for the A319 is close to that of the A320 while the probability for the A321 is significantly higher. Some of the contributing factors are shown in figure 9.15 that explain the differences. Every histogram shows the distribution of the data separately for each aircraft type in a different color: blue for A321, brown for A320 and yellow for A319.

	A319 Flaps Full Dry Runway		A320 Flaps Full Dry Runway		A321 Flaps Full Dry Runway	
	μ	σ	μ	σ	μ	σ
26R	1.0×10^{-7}	1.8×10^{-8}	3.5×10^{-8}	6.4×10^{-9}	2.0×10^{-7}	3.5×10^{-8}

Table 9.6: *Runway overrun risk for different aircraft types of the Airbus A320 family; the baseline scenario is highlighted.*

In figure 9.15a, the distribution of the landing mass is shown. It is not surprising that the distribution for the A319 is lower in value compared to the A320 while the A321 has highest values. The masses are compliant with the certified numbers in table 9.5 though it is unknown which exact version the individual aircraft are from which the FDM data was obtained.

All aircraft types share a similar wing. The high-lift system is somewhat different. while the A319 and A320 have double-slotted flaps, however, with different extension angles, the A321 is equipped with triple-slotted flaps. In general, higher mass also leads to a higher approach speed, as shown in figure 9.15b, which is reflected in a higher deceleration distance until reaching a GS of $80\,\mathrm{kn}$ in figure 9.15c. The touchdown distance does not vary significantly among the aircraft types in figure 9.15d, but it is the lowest for the A319. Again, the approaches are typically performed using the ILS, which explains the little variation in touchdown point. The comparison of the average deceleration in figure 9.15f and the applied brake pressure in figure 9.15e suggests that significantly less pressure was applied on the A319, which also leads to a slightly lower deceleration value. However, as the initial approach speed is lower on the A319, it is still capable of achieving a shorter stopping distance.

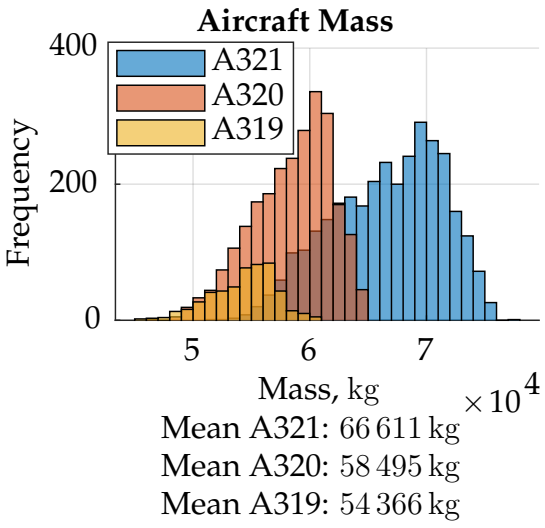

Mean A321: 66 611 kg
Mean A320: 58 495 kg
Mean A319: 54 366 kg

(a) *Aircraft mass*

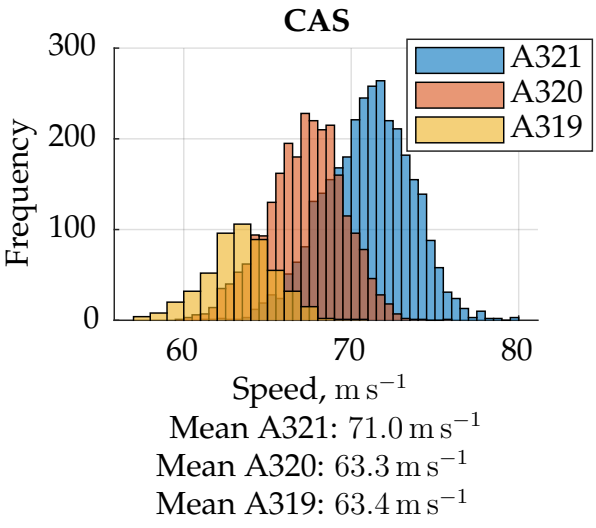

Mean A321: 71.0 m s^{-1}
Mean A320: 63.3 m s^{-1}
Mean A319: 63.4 m s^{-1}

(b) *Calibrated Airspeed (CAS)*

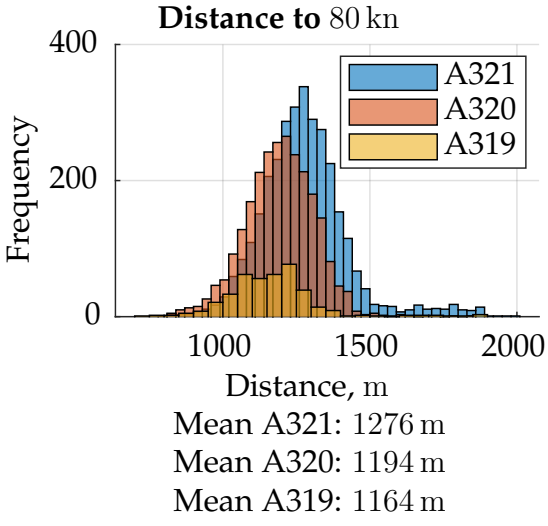

Mean A321: 1276 m
Mean A320: 1194 m
Mean A319: 1164 m

(c) *Distance from threshold to* 80 kn

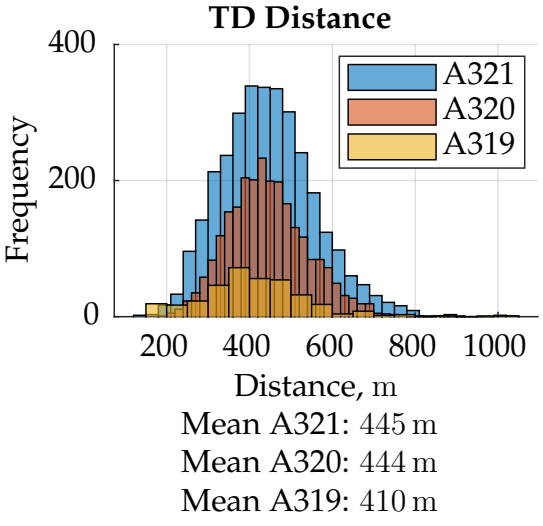

Mean A321: 445 m
Mean A320: 444 m
Mean A319: 410 m

(d) *Touchdown distance*

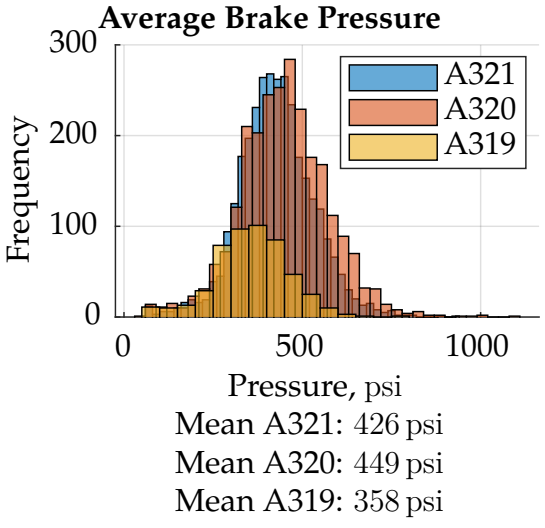

Mean A321: 426 psi
Mean A320: 449 psi
Mean A319: 358 psi

(e) *Average brake pressure*

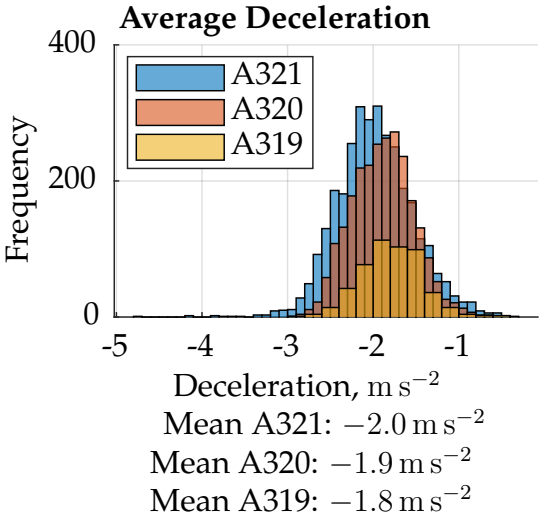

Mean A321: −2.0 m s^{-2}
Mean A320: −1.9 m s^{-2}
Mean A319: −1.8 m s^{-2}

(f) *Average deceleration*

Figure 9.15: *Comparison between different aircraft types of the A320 family*

9.2.2.4 Variation of Landing Configuration

On the Airbus A320 family, two landing configurations are available, *CONF 3* and *CONF Full*. *CONF Full* is the default setting and the flaps ($35°$ instead of $20°$) and slats ($27°$ instead of $22°$) are further extended compared to *CONF 3*. The values provided are specifically for the A320 and vary slightly across the members of the family [Deu09a]. A lower setting is typically used during high turbulence as the wing loading is higher due to the smaller wing area. The drawback is the higher approach speed caused by a higher stall speed, which increases the landing distance. In addition, a higher angle of attack during approach is required, which can be critical during the flare. An excessive flare maneuver will lead to a tailstrike while flaring not sufficiently will increase the risk of a hard landing resulting from the higher approach speed.

	A320 CONF 3 Dry Runway		A320 CONF Full Dry Runway	
	μ	σ	μ	σ
26R	1.2×10^{-8}	2.2×10^{-9}	3.5×10^{-8}	6.4×10^{-9}

Table 9.7: *Runway overrun risk as comparison between different landing configurations; the baseline scenario is highlighted*

Out of the 3033 available flights of the A320 on runway 26R in table 9.1, 2501 were performed using *CONF Full* while 802 used *CONF 3*, which is about $26\,\%$. Table 9.7 shows the result for the overrun probability using *CONF 3* compared to the baseline scenario using *CONF Full*. Both results are close to each other, both being in the order of 10^{-8}. The probability for *CONF 3* is even slightly lower than for *CONF Full*, which is unexpected because of the higher approach speed when using *CONF 3*. According to the Operations Manual (OM) Part B [Deu09a], on the A320, the approach speed (CAS) is between $4\,\mathrm{kn}$ and $5\,\mathrm{kn}$ higher for *CONF 3*, provided all other influencing factors are identical.

Figure 9.16 shows the histograms of some contributing factors, separately for both configurations. In all histograms, the blue color indicates the data for *CONF Full* while the brown data indicates the values for *CONF 3*. The mean values for both configurations are listed below each figure. As there is less data for *CONF 3*, the brown histogram is always drawn in front of the blue histogram to easy the visualization.

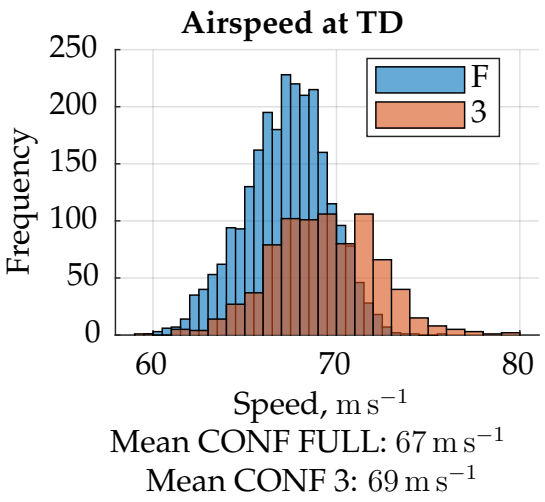

(a) *CAS at touchdown*

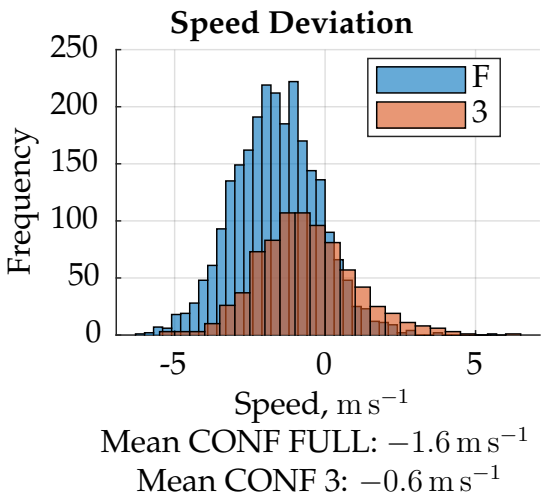

(b) *Approach speed deviation at touchdown*

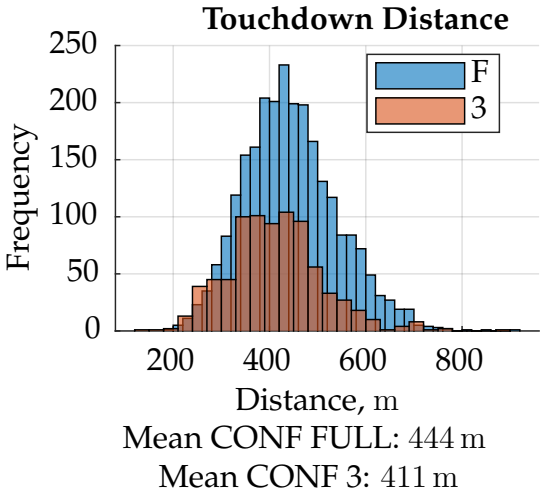

(c) *Touchdown distance*

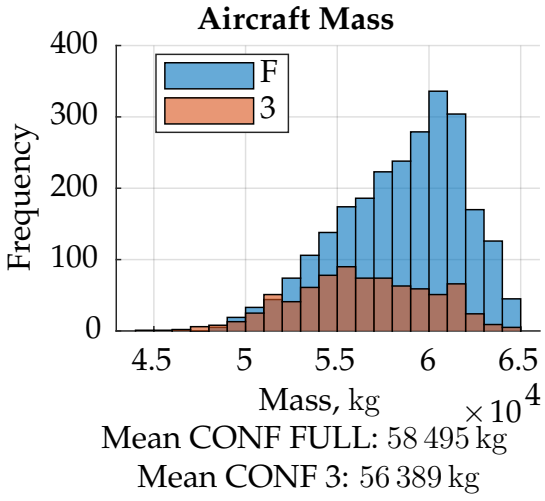

(d) *Aircraft mass at touchdown*

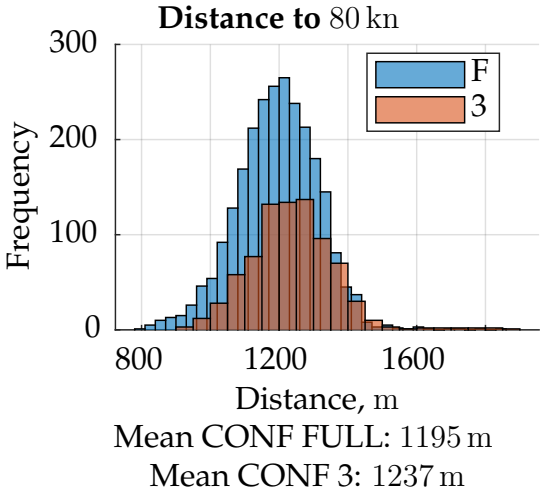

(e) *Distance from threshold until reaching* 80 kn

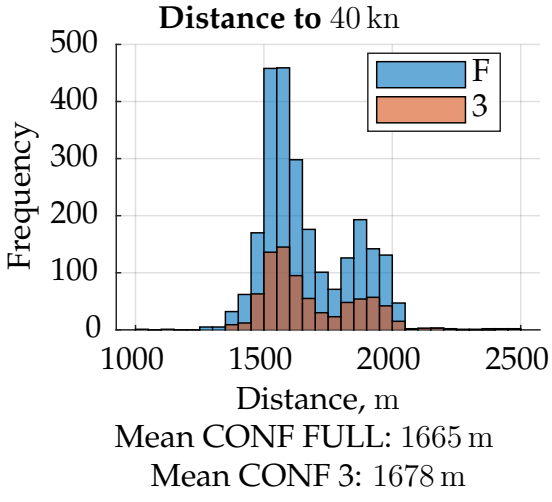

(f) *Distance from threshold until reaching* 40 kn

Figure 9.16: *Comparison between different landing configuration, for runway 26R*

Figure 9.16a shows the CAS of the aircraft at touchdown. In general, the CAS is higher for the configuration *CONF 3*, the mean value is higher by $2\,\mathrm{m\,s^{-1}}$, which is consistent with the numbers provided in the OM-B. The deviation from the approach target speed is provided in figure 9.16b. For both configurations, the speed at touchdown is, in average, smaller than the target speed, which is indicated by the negative sign. However, the deviation for *CONF 3* is, in average, smaller than for *CONF Full*. A reason for this difference can be found in figure 9.16c, which shows the touchdown distance for both landing configurations. While the spread of the values is much smaller for *CONF 3*, the mean value is also smaller compared to *CONF Full*. This suggests that landings performed using *CONF 3* tend to touch down earlier on the runway. Though the speed at touchdown is higher compared to *CONF Full*, we may expect the same effect that was also observed in figure 9.4 earlier. Although landing with higher speed increases the stopping distance, it is often related to an earlier touchdown point, which, in contrast, decreases the stopping distance because the wheel brakes are applied earlier to slow down the aircraft.

Another significant reason for the smaller overrun probability when using *CONF 3* is presented in figure 9.16d. The average aircraft mass is more than $2\,\mathrm{t}$ less for *CONF 3*. According to the OM, for landings performed using *CONF Full* and an aircraft weight of $58\,\mathrm{t}$ requires a landing distance of $1654\,\mathrm{m}$ while a landing with *CONF 3* and a weight of $56\,\mathrm{t}$ would require a landing distance of $1740\,\mathrm{m}$ [Deu09a]. All values are obtained for International Standard Atmosphere (ISA) conditions at Mean Sea Level (MSL) using autobrake LOW on a dry runway. The difference between the two values is merely $100\,\mathrm{m}$ and it shows how a higher approach speed can be compensated by a smaller mass. This is also easily visible when looking at the distances from the threshold until the aircraft reaches a GS of $80\,\mathrm{kn}$ and $40\,\mathrm{kn}$, respectively in figures 9.16e and 9.16f. For the distance to $80\,\mathrm{kn}$, both datasets are very similar with a difference in mean of only $40\,\mathrm{m}$ while for the distance to $40\,\mathrm{kn}$, the difference is merely $13\,\mathrm{m}$. For the latter, two peaks are visibly in the data for both configurations. This is caused by the two available taxiways A9 and A6, which are located $1580\,\mathrm{m}$ and $2200\,\mathrm{m}$ after the threshold, respectively. This, again, shows the strong impact of the exiting taxiway on the braking behavior.

Considering that the share of landings performed using *CONF 3* decreases significantly as the aircraft mass increases and the fact that the touchdown point tends to be closer to the threshold when landing in *CONF 3*, it is clearly explained why the risk for an overrun is lower when using *CONF 3*. However, one has to keep in mind that this is not primarily caused by using a lower landing configuration, but rather by other factors. A landing does not become less risky with respect to overrun if conducted in *CONF 3*, it is rather caused by other factors associated to it. A verifiable explanation for the correlation between landing configuration and the aircraft mass could not be

found. One possible motivation could be the reduction of fuel burn and the reduction of the noise level since the aerodynamic efficiency is higher if flaps and slats are less extended. Pilots might select *CONF 3* if the aircraft mass is low since the approach speed as well as the landing distance decreases with decreasing landing mass while accepting the higher approach target speed associated with a lower setting of flaps and slats.

9.2.2.5 Variation of Runway Condition

The runway condition is varied in the model by introducing different slip-friction curves previously obtained by experiments in other studies [Eng95]. The input data into the Subset Simulation containing the contributing factors remain unchanged since there is no possibility to clearly separate the data according to the runway condition. Meteorological Aerodrome Report (METAR) data is recorded for each landing, but efforts to distinguish between wet and dry runway proved to deliver very inaccurate results due to several reasons:

1. METAR is only published and recorded every 30 minutes and the closest METAR report is available for each landing. Thus, there could be a time offset of up to 15 minutes back or forth.

2. It is very often not possible to unambiguously reconstruct the runway condition based on METAR. Rain does not necessarily imply a wet runway if it was observed shortly after the landing. Heavy thunderstorms during the summer can quickly lead to contaminated runways with standing water, but it can also dry up quickly if the cells have moved and the surface temperature is still high.

These factors either lead to a high number of false positives (dry runway but classified as wet) or false negatives (wet runway but classified as dry). Therefore, no further effort was made to separate the input data. Instead, only the model is changed to reflect changing friction coefficients on the runway.

	A320 Flaps Full Dry Runway		A320 Flaps Full Wet Runway	
	μ	σ	μ	σ
26R	3.5×10^{-8}	6.4×10^{-9}	4.8×10^{-7}	8.0×10^{-8}

Table 9.8: *Runway overrun risk as comparison between different runway conditions; the baseline scenario is highlighted.*

Table 9.8 shows the results obtained for wet runway compared with the baseline scenario. The overrun probability is approximately one order of magnitude higher than

for dry runway. This is a plausible result since the friction coefficient that can be achieved is lower for both a given brake pressure that is applied and globally.

9.3 Runway Veer-Off Probability

9.3.1 Baseline Scenario

For the quantification of the runway veer-off probability, the same model is used as for runway overrun analysis in the previous section. The only difference is that for the *incident metric*, the shortest distance to the runway edge on either side is used, which is referred to as the *shoulder margin* in the following. The entire landing roll is simulated and the smallest shoulder margin that occurs during the landing is taken as the overall shoulder margin. As the width of the runway at MUC/EDDM is $60\,\mathrm{m}$, the largest possible shoulder margin is $30\,\mathrm{m}$. Of course, each aircraft has a certain track width, i.e. the distance between the outer wheels on each side. In this case, the shoulder margin is always computed with respect to the aircraft reference point or the Center of Gravity (CG), the actual distance between the runway edge and the outer wheel is smaller.

The baseline scenario is defined to be the Airbus A320 landing on runway 26R at MUC/EDDM using *CONF Full* on a dry runway, which is identical to the runway overrun examination in the previous section. Again, the selection was driven by the fact that this is the scenario with the highest number of flights available in the data. After presenting the baseline scenario, a comparison for different runways and other aircraft types of the Airbus A320 family is carried out.

	A320 Flaps Full Dry Runway	
	μ	σ
26R	2.9×10^{-7}	4.8×10^{-8}

Table 9.9: *Runway veer-off risk for the baseline scenario*

Table 9.9 shows the probability of runway veer-off for the baseline scenario obtained from the Subset Simulation. The mean value is almost one order of magnitude larger than the standard deviation, resulting in a c.o.v. of 0.17, indicating the confidence of the Subset Simulation propagation. Figure 9.17 shows how the samples move with each subset.

Similar to section 9.2.1, some of the contributing factors for runway veer-off are presented, particularly those with a high influence on the accident probability. It should be

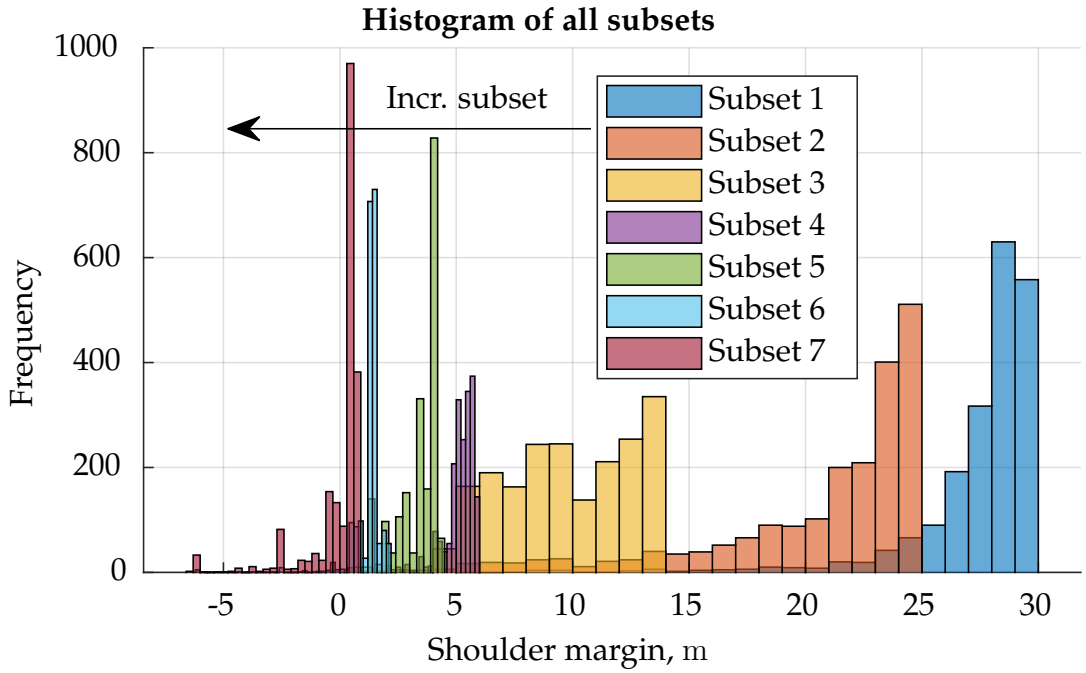

Figure 9.17: *Histogram of all samples generated across all subsets*

noted that many contributing factors that have high influence on the overrun probability, such as brake pressure, deviation from the approach reference speed, headwind or the touchdown distance do not significantly influence the veer-off probability, which is consistent with the expectation knowing the flight physics as they mainly contribute to the longitudinal motion of the aircraft.

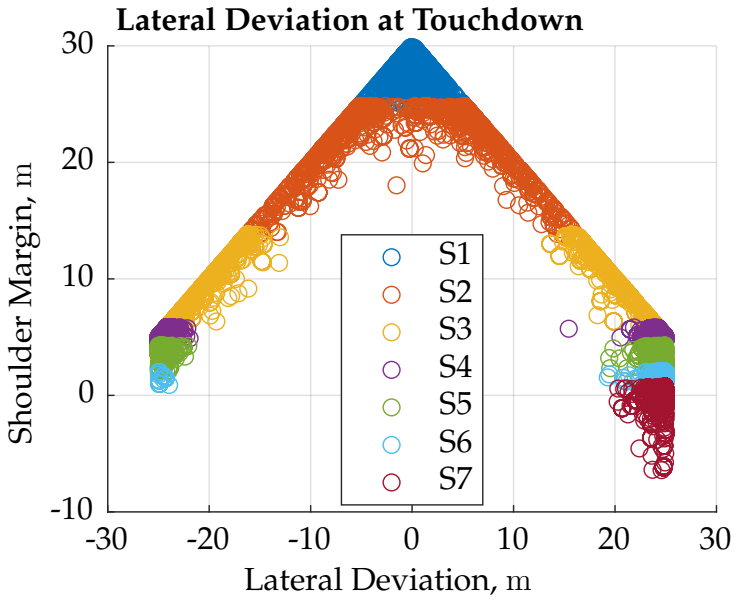

Figure 9.18: *The influence of the lateral touchdown point on the shoulder margin*

The lateral deviation at touchdown is obviously directly affecting the overall shoulder margin of the entire landing. Though the aircraft immediately tries to correct the offset

after landing by applying nosewheel steering and rudder, the initial lateral deviation will sometimes also be the maximum lateral deviation. Figure 9.18 shows this clear relationship. A clear boundary is visible on the upper side as the maximum shoulder margin is $30\,\mathrm{m}$ while the maximum possible shoulder margin for a particular flight is always

$$30\,\mathrm{m} - \text{lateral deviation at touchdown.}$$

The values for the lateral deviation that can be sampled is truncated to $\pm 25\,\mathrm{m}$. This boundary is also well visible in figure 9.18. It should be noted that there is an asymmetry in the location of the sample as the branch with deviations to the right is much larger than the left one. This is caused by an asymmetry of the input distribution of the lateral offset at touchdown.

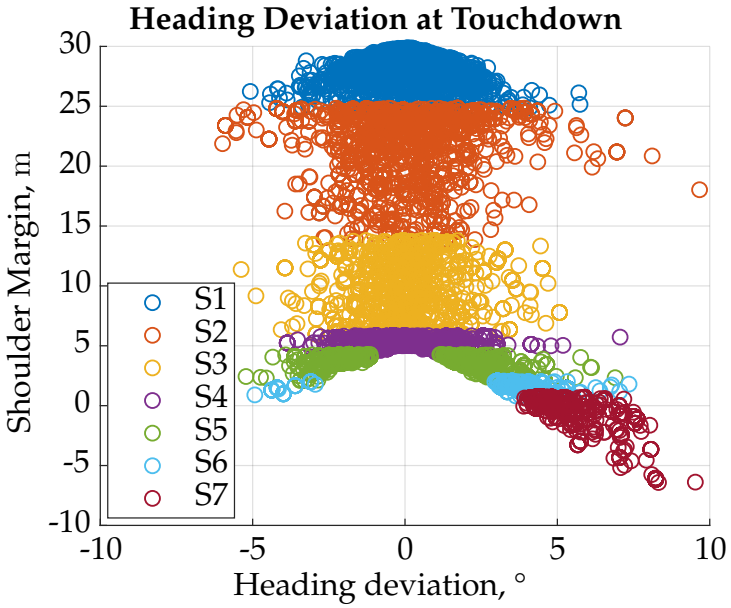

Figure 9.19: *The influence of the crab angle on the shoulder margin*

Figure 9.19 shows how the samples move with each subset with respect to the heading deviation at touchdown, i.e. the crab angle between the aircraft's heading and the runway heading. Two branches are well visible, indicating veer-off samples to the left and to the right of the runway. The maximum value that can be sampled is truncated to $\pm 10°$. One has to keep in mind that the limit set out by Airbus for the remaining crab angle at touchdown is $\pm 5°$. The majority of samples shown in figure 9.19 that constitute a veer-off, i.e. a shoulder margin of less than zero, violate this limit. It is also noteworthy that if the aircraft touches down with zero crab, the shoulder margin will not decrease below $5\,\mathrm{m}$, i.e. the maximum distance from the runway centerline is $25\,\mathrm{m}$. The bifurcation of the two branches seems to already occur during the first two subsets, however, the samples move slightly closer to the center again before the actual bifurcation. This behavior can be observed in all the following figures visualizing the contributing factors. The reason for this is that the main contributing factor driving

the shoulder margin in this stage is the lateral deviation, i.e. as the samples move towards smaller shoulder margins, this is their main driver while other contributing factors have much smaller influences. In this case, the Markov Chain tends to generate samples in areas where the input PDFs have high values for all the contributing factors except the one that is currently dominating the outcome.

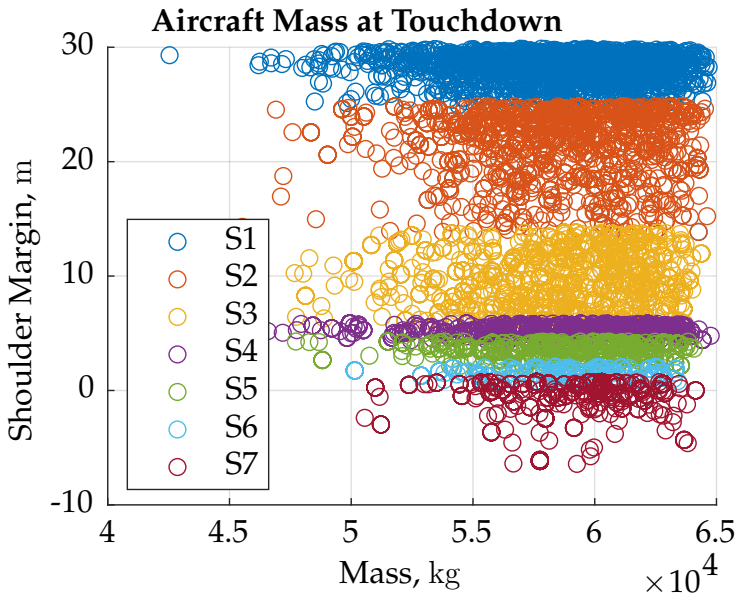

Figure 9.20: *The influence of aircraft mass on the shoulder margin*

Figure 9.20 shows that the mass of the aircraft also has significant influence on the veer-off occurrence probability. As the shoulder margin decreases with each subset, the mass of the aircraft at touchdown increases. A heavier aircraft is less agile and more difficult to control, which leads to a higher probability of veer-off. The mass is limited by the upper boundary which is the MLM. Again, one can see that the samples move towards higher masses and then spread out in the first three subsets before returning to high values again. This is also caused by the lateral deviation being the dominant contributing factor in this phase.

The CG does not have an influence on the overrun probability, but it does influence the outcome for veer-off, which is visible in figure 9.21. A tendency to a narrower span of CG values is shown. A reason for this could be the effectiveness of nosewheel and rudder when it comes to steering. A forward CG reduces the lever arm of the nosewheel and increases the lever arm of the rudder. However, the nosewheel steering could also become more effective since the weight on the nosewheel increases with a more forward CG. In general, the rudder is used for higher speeds and the nosewheel steering is used for lower speeds, as the dynamic pressure enables rudder control. It seems that a CG position between 22 and 35 % of the Mean Aerodynamic Chord (MAC) is the least favorable. This could be caused by a minimum of the overall effectiveness of both steering devices.

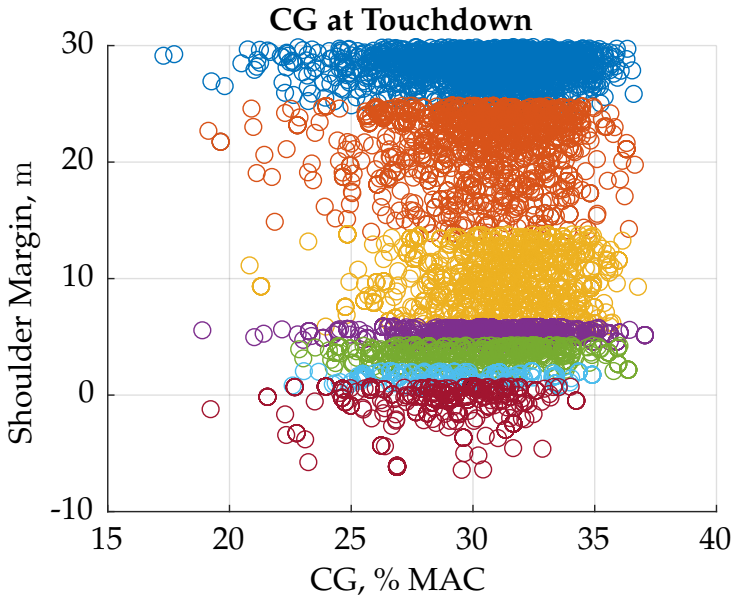

Figure 9.21: *The influence of CG on the shoulder margin*

However, the influences of the CG could also result from the fact that there is a dependency between the aircraft's mass and its CG, as shown in figure 9.22. A higher mass is typically associated with to a more aft CG.

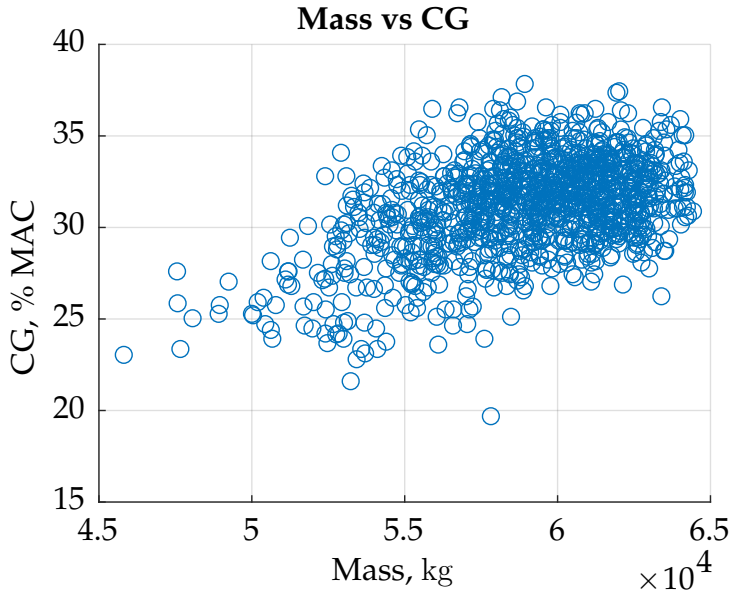

Figure 9.22: *Dependency between mass and CG*

When creating the same plot showing the influence of the crosswind, one might expect a similar behavior as the lateral deviation in figure 9.18 or the crab angle in figure 9.19. However, figure 9.23 shows that the shoulder margin is not significantly affected by the crosswind. Instead, samples with crosswind values across the entire range exist throughout all subsets with a slight tendency to zero crosswind. This, however, is not consistent with the knowledge about the flight dynamics. The issue that actually arises

here is not that the crosswind does not directly influence the probability of runway veer-off but rather the dependency with other contributing factors. Deviations from the nominal value, i.e. zero, typically does not occur for the crosswind only, but also for other contributing factors at the same time, such as the crab angle.

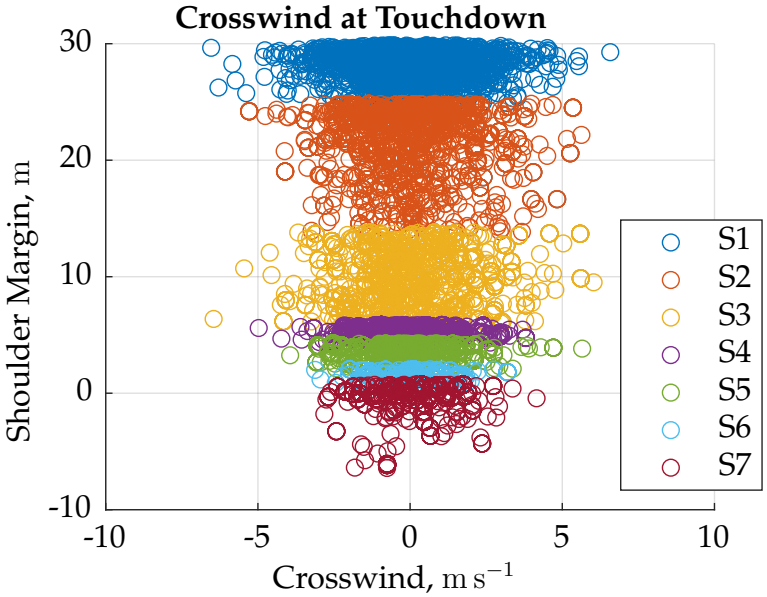

Figure 9.23: *The influence of crosswind on the stop margin*

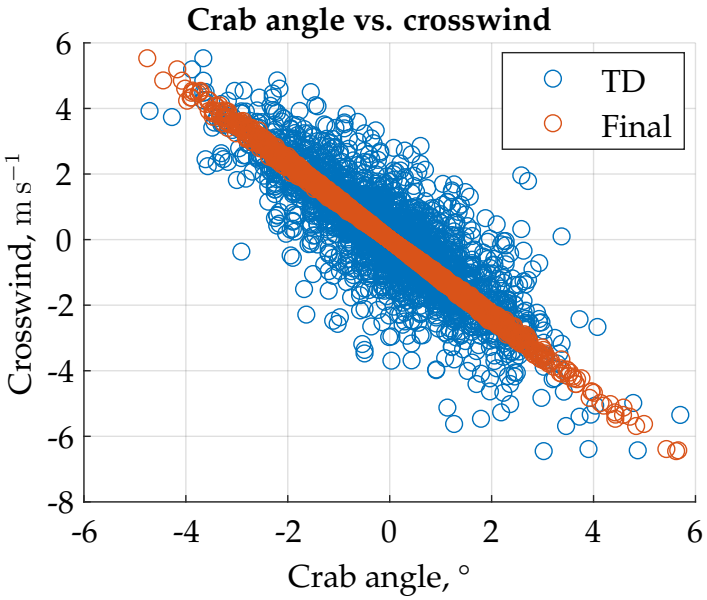

Figure 9.24: *Dependency between crab angle and crosswind*

Figure 9.24 shows the dependency between the crab angle and the crosswind. Positive values of the crab angle indicate that the aircraft heading is deviating to the right compared to the runway heading. Positive crosswind values indicate wind blowing towards the right side of the aircraft, i.e. the wind is coming from the left. Two sets of data are shown. The blue dataset indicates the measured crab angle at touchdown

Ψ_{TD}. The red data is the computed crab angle that the aircraft should have during the final approach Ψ_{Final} assuming the aerodynamic angle of sideslip is zero: $\beta_A = 0$. It is obtained using equation (9.1) from the crosswind speed $V_{\text{W, cross}}$ and the IAS V_{IAS}. For the sake of simplicity, the IAS and the True Airspeed (TAS) are considered to be the same at this stage of flight as the speeds are low.

$$\Psi_{\text{Final}} = \arctan \frac{V_{\text{W, cross}}}{V_{\text{IAS}}} \tag{9.1}$$

The computed crab angle for the final approach is almost entirely on a straight line with little deviation. This is straightforward, as the IAS of the aircraft at touchdown only varies within a small range. The crab angle at touchdown provides more interesting facts.

1. Only one flight in the available dataset actually touched down outside of the crab angle range of $\pm 5°$ set out by Airbus.
2. The figure clearly shows a correlation between the two parameters. Positive crab angle values are likely to be related to negative crosswind values, which applies to both the blue and the red data points. This indicates that a small crab angle still exists at the moment of touchdown, i.e. it is not completely reduced to zero or reverted to the opposite direction, indicating that the aircraft's nose is still pointing slightly towards the wind.
3. The spread of the blue data points for small crosswind values is larger than for high crosswinds. It can be concluded that for light crosswinds, the pilot tends to accept the crab angle and to keep it until touchdown to avoid destabilization of the aircraft's attitude and trajectory during the final seconds prior touchdown.

For runway 26R, the maximum crosswind value in the data is $6.5\,\mathrm{m\,s^{-1}}$, while for the entire dataset at MUC/EDDM, the maximum value is $13.0\,\mathrm{m\,s^{-1}}$, which is still within the limits of the Airbus A320 for dry runways, see table 8.2. This is attributed to the environmental conditions at MUC/EDDM, as the prevalent wind directions are east and west and both runways are aligned accordingly. This explains figure 9.23 in which the crosswind apparently does not influence the veer-off probability. The crosswind is reflected in the crab angle of the aircraft at touchdown, which heavily influences the veer-off probability. If the crab angle would be set to a constant value, e.g. zero, the direct influence of the wind would be able to stand out in the analysis. However, this is not physical from the perspective of flight dynamics.

Figure 9.25 shows the ILS localizer deviation and the lateral position deviation at touchdown for runway 26R, respectively. The localizer deviation is measured in DDM, which results from the $90\,\mathrm{Hz}$ and the $150\,\mathrm{Hz}$ signal transmitted by the localizer antenna [Men14]. According to regulation, the signal must be configured such that a linear

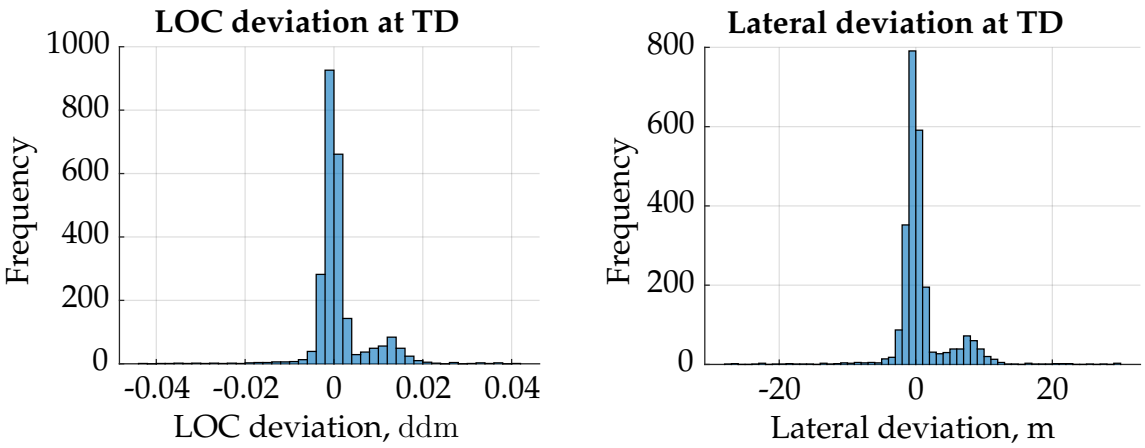

(a) *Localizer deviation at touchdown*

(b) *Lateral deviation at touchdown*

Figure 9.25: *Comparison between the localizer deviation and the lateral deviation of the touchdown point for runway 26R*

relationship is established between the DDM values in the range of ± 0.155 and the angular deviation from the runway centerline. In addition, at runway threshold, a lateral deviation of $300\,\mathrm{ft}$ must correspond to a DDM value of ± 0.155 [Int06]. For runway 26R at MUC/EDDM, a lateral deviation of $30\,\mathrm{m}$ to either side abeam the runway threshold corresponds to a localizer offset of $\pm 0.0435\,\mathrm{ddm}$. Therefore, the measurements in figure 9.25a are truncated to this value. Out of the 2501 flights available, 20 flights have measurements outside of this range. It can be assumed that no aircraft landed outside of the runway edge as this would be an incident that must be reported to the authorities. These measurements could be caused by disturbances in the localizer signal.

Figure 9.25a also shows an unexpected peak at approximately $0.013\,\mathrm{DDM}$. No plausible explanation for this could be found in the data. As this corresponds to a lateral deviation of approximately $7\,\mathrm{m}$, see figure 9.25b, it is still well within the limits. As it appears to be a systematic deviation, possible explanation could also be erroneous ILS measurements resulting from reflections of the localizer signal by buildings or by other aircraft waiting at the holding point, if the airport is not operating under CAT II or III conditions, requiring a larger runway protection zone in order to be able to conduct automatic landings. This hypothesis would imply that the actual touchdown points are located around the centerline as flight crew performs the landing visually, but the measured localizer deviation is biased. The lateral deviation in figure 9.25b reflects this behavior, but one has to keep in mind that the data has been processed by the trajectory smoothing algorithm described in section 8.2, so the lateral deviation is adjusted according to the measured localizer deviation. This bi-modally distributed data could only be found for landings on runway 26R for all three aircraft types, but on no other runway. Further investigations have shown that the second, smaller peak also exists for localizer deviations when overflying the runway threshold.

9.3.2 Scenario Comparison

9.3.2.1 Variation of Runway

The veer-off probabilities for different runways is presented in table 9.10. The runways, sorted by descending order of probability, is 26R, 08R, 26L, 08L. The highest and the lowest value are less than two orders of magnitude apart.

	A320 Flaps Full Dry Runway	
	μ	σ
08L	8.4×10^{-9}	1.6×10^{-9}
08R	6.2×10^{-8}	1.1×10^{-8}
26L	3.3×10^{-8}	6.0×10^{-9}
26R	2.9×10^{-7}	4.8×10^{-8}

Table 9.10: *Runway veer-off risk for different runways at Munich airport; the baseline scenario is highlighted.*

A reason for the difference can be found in figure 9.26, showing the distributions of the lateral deviation for the four runways. As the nominal mean value should be zero for all distributions, the standard deviation, indicating the spread of the values, is also displayed below each figure. Though it can be questioned whether the lateral offset of the touchdown point on runway 26R is really bi-modal with a second peak around $7\,\mathrm{m}$, propagating this data in figure 9.26b leads to a higher spread of the lateral touchdown point and thus also a higher probability for veer-off. Landings on runway 08L, which is the same runway, but opposite direction as 26R, also have, in average, a small offset to the left, though no second peak is visible.

Figure 9.27 shows the crab angle at touchdown for the four runways. Like the lateral deviation, both the mean value and the standard deviation are displayed. No significant differences could be found between the runways, the mean values are all closely located at zero, with a standard deviation between $1.1°$ and $1.3°$.

The crosswind data is shown in figure 9.28. The mean value for all runways are positive, indicating that the wind, in average, is coming from the left side of the aircraft. This indicates that, assuming landings are performed with a headwind component rather than tailwind, the prevailing wind direction at MUC/EDDM is not exactly the runway direction, i.e. $81°$ and $261°$ magnetic or $83°$ and $263°$ true [DFS18], but slightly rotated counter-clockwise. In addition, the variation of the crosswind, when the 08 direction is in use, is smaller compared to landings in the 26 direction.

To sum up the runway comparison, the veer-off probability for 26R is higher than for the other three runways due to the larger lateral offset of the touchdown point. The

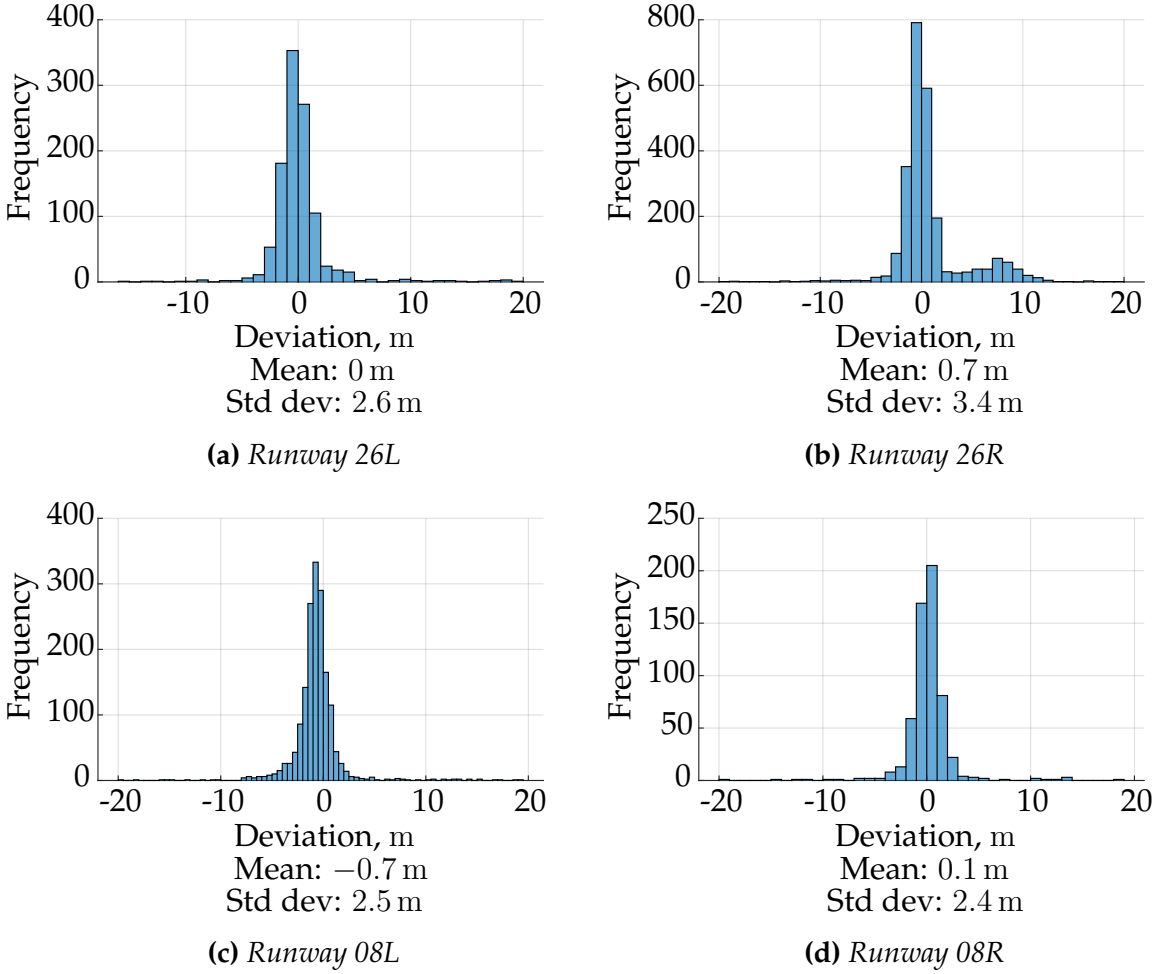

(a) *Runway 26L* **(b)** *Runway 26R*

(c) *Runway 08L* **(d)** *Runway 08R*

Figure 9.26: *Comparison of the lateral deviation of the touchdown point for different runways. The mean and the standard deviation of the respective dataset is also provided.*

differences between the other three runways are minor and no significant differences could be found in the data of the contributing factors that would lead to differences in the veer-off probability.

9.3.2.2 Variation of Aircraft Type

Similar to section 9.2.2.3, a comparison between the Airbus A320 family aircraft types A319, A320 and A321 is made for runway veer-off. The results are shown in table 9.11. The probabilities of the A319 and the A320 are all close to each other while for the A321, it is slightly higher. The higher mass of the A321 causes the aircraft to be less agile and more difficult to control. However, this effect is not visible for the A319, which can be explained by the fact that the fuselage of the A319 is shorter, resulting in less control authority of both the rudder and the nose landing gear due to the shorter lever arm. The A319 features the same vertical stabilizer as the other types in the A320 family and, therefore, the controllability is slightly reduced. The A318, which is

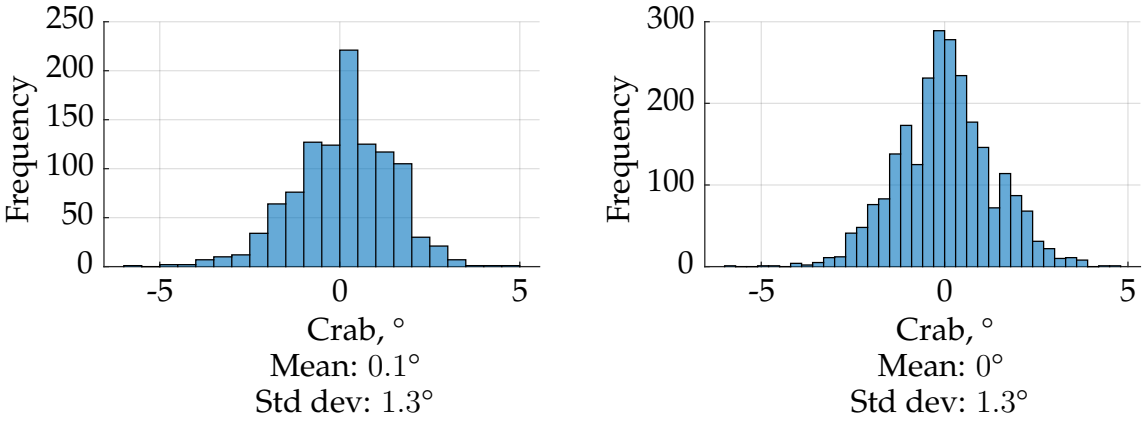

(a) *Runway 26L*

(b) *Runway 26R*

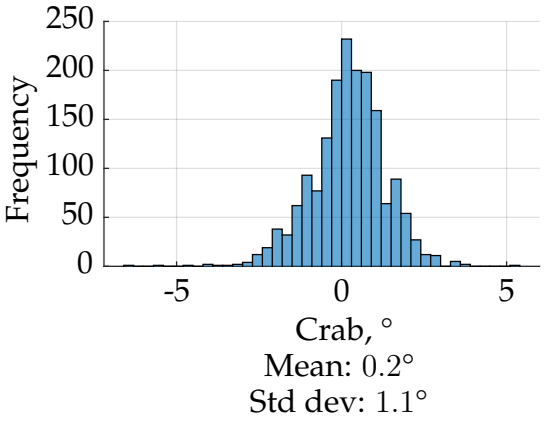

(c) *Runway 08L*

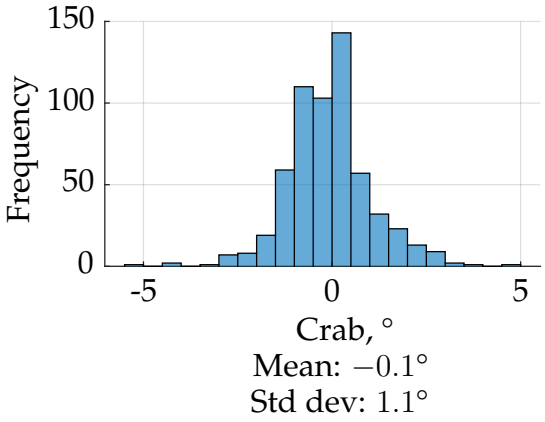

(d) *Runway 08R*

Figure 9.27: *Comparison of the crab angle at touchdown*

a further shortened version of the A319, features a larger stabilizer in order to achieve the required directional stability, compensating for the shorter fuselage.

	A319 Flaps Full Dry Runway		A320 Flaps Full Dry Runway		A321 Flaps Full Dry Runway	
	μ	σ	μ	σ	μ	σ
26R	5.5×10^{-7}	9.1×10^{-8}	2.9×10^{-7}	4.9×10^{-8}	1.2×10^{-6}	2.0×10^{-7}

Table 9.11: *Runway veer-off risk for different aircraft types of the Airbus A320 family; the baseline scenario is highlighted.*

9.3.2.3 Variation of Landing Configuration

A comparison between landing in the two possible configurations *CONF 3* and *CONF Full* in table 9.12 shows that landing with a lower flaps setting leads to a slightly lower occurrence probability for runway veer-off. However, both values are very close to

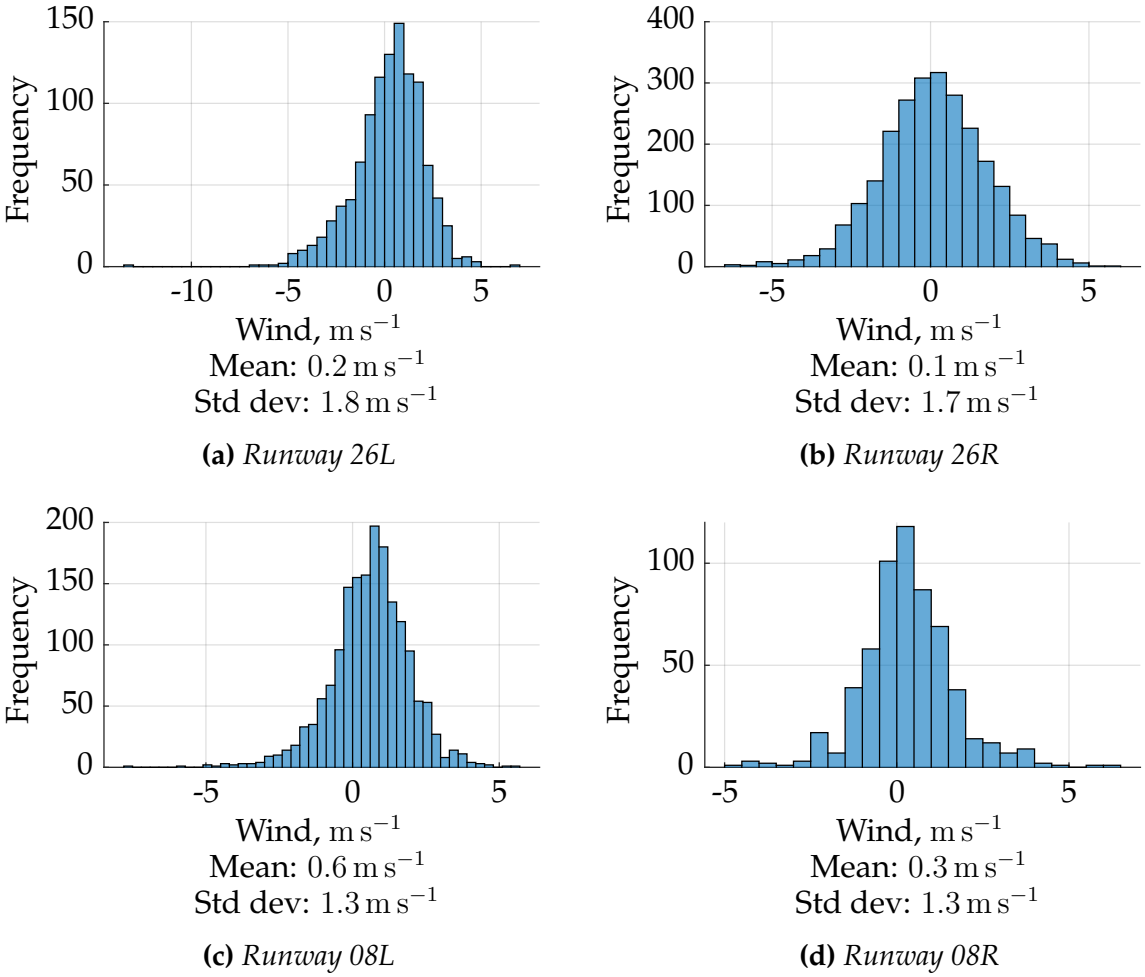

(a) *Runway 26L* **(b)** *Runway 26R*

(c) *Runway 08L* **(d)** *Runway 08R*

Figure 9.28: *Comparison of the crosswind component for different runways*

each other.

	A320 CONF 3 Dry Runway		A320 CONF Full Dry Runway	
26R	8.5×10^{-8}	1.5×10^{-8}	2.9×10^{-7}	4.9×10^{-8}

Table 9.12: *Runway veer-off risk as comparison between different landing configurations; the baseline scenario is highlighted*

When comparing the contributing factors for both configurations, no significant differences can be found, which is consistent with both numbers being very close to each other. The bi-modal input data of the lateral offset of the touchdown point is also reflected in the data for landings using *CONF 3*. The slightly lower probability in *CONF 3* could result from the fact that the aircraft's mass is typically lower when conducting landings in this configuration, which has already been shown in section 9.2.2.4 and figure 9.16d for the overrun scenario.

9.3.2.4 Variation of Runway Condition

As previously described in section 9.2.2.5, it is not possible to separate the available flights in the data according to the runway condition during landing. Therefore, the Subset Simulation is conducted based on the same set of data, however, using friction coefficient values describing a wet runway. The results are displayed in table 9.13.

	A320 Flaps Full Dry Runway		A320 Flaps Full Wet Runway	
	μ	σ	μ	σ
26R	2.9×10^{-7}	4.9×10^{-8}	1.0×10^{-4}	1.4×10^{-5}

Table 9.13: *Runway veer-off risk as comparison between different runway conditions; the baseline scenario is highlighted*

The probability for runway veer-off is significantly higher if the runway is wet compared to a dry runway. The difference is almost a factor of 10^3, which is much larger compared to the overrun scenario in table 9.8. An explanation can be found when looking closely at the dynamics of the aircraft after touchdown. Figure 9.29 shows a simulated flight with an initial lateral offset of the touchdown point of $10\,\mathrm{m}$ right of the centerline and a crab angle of $5°$ to the right. Immediately after touchdown, the lateral deviation increases towards the direction of the crab angle, see figure 9.29a. In this case, the aircraft deviates to the right, leading to an additional increase of the lateral deviation. The controller immediately corrects the aircraft's heading towards the runway centerline, see figure 9.29b, resulting in a minimum phase behavior with an overshoot. During this phase, as the aircraft is steering, the traction relies on the friction coefficient between the tire and the runway. If the achievable friction coefficient is smaller due to different runway conditions, the overshoot of the lateral position will further increase, resulting in higher veer-off probabilities for wet runways.

However, the probabilities are computed based on the assumption that the contributing factors are independent. When the aircraft performs the de-crab maneuver shortly before touchdown, its nose is rotated such that the aerodynamic angle of sideslip increases, thus its lateral position will move towards the direction of the wind. As already shown in figure 9.24, the crab angle is typically reduced, but rarely changes to the opposite direction. This means that at the moment of touchdown, the aircraft's nose is often still pointed into the wind, which is also the direction of the runway centerline. This means that the remaining crab angle will lead to a reduction of the lateral offset immediately after touchdown. If this dependency between the lateral offset and the crab angle is taken into account, the actual veer-off probability will decrease. The current approach of independent contributing factors overestimates the accident probability. Based on the numbers in figure 9.13, veer-off accident at MUC/EDDM on wet

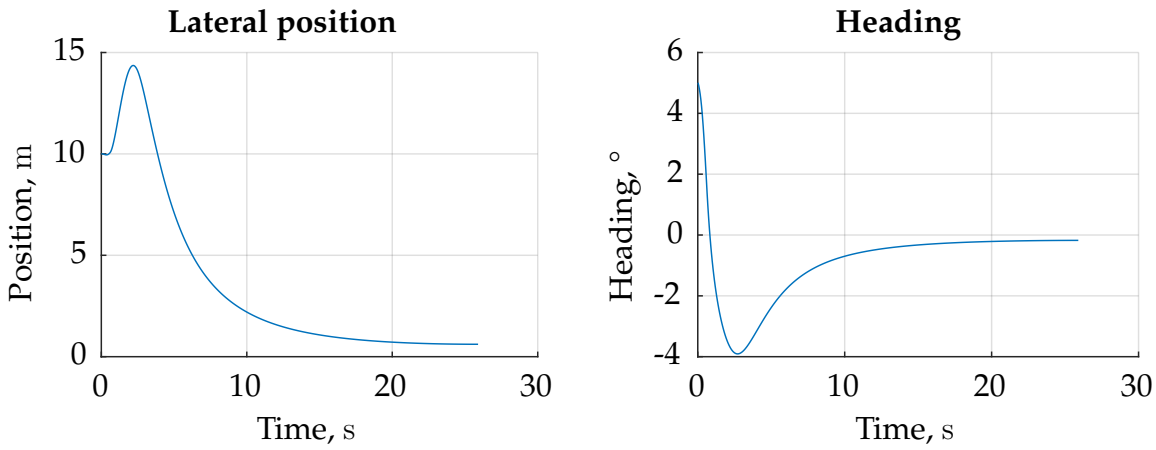

(a) *Lateral position of the aircraft*

(b) *Heading of the aircraft*

Figure 9.29: *Heading and lateral position for a simulated landing roll with inital crab angle and lateral deviation*

runways should already be well observable from the number of movements. However, this has not emerged in the flight operations.

9.4 Summary of Results

In this chapter, the probabilities for both runway overrun and runway veer-off have been computed. A baseline scenario, i.e. Airbus A320 on dry runway 26R at Munich Airport using full flaps and slats configuration, is presented and other scenarios are derived from it, the results are compared with the baseline. Based on these quantitative results, the influence of the contributing factors are highlighted qualitatively. Some interesting information in the data could be derived based on the analysis results. Dependencies between the contributing factors in the data could be identified.

As of December 2018, no runway overrun at MUC/EDDM could be found in publicly accessible databases. Two runway veer-off accidents occurred since the opening of the airport in 1992, both during landing. One of them involved an Avions de Transport Régional (ATR)-72 turboprop aircraft, which suffered an engine failure during take-off and subsequently returned for an emergency landing. Due to blockage of the rudder pedals, the yaw moment caused by the asymmetric thrust could not be compensated and the aircraft veered off from runway 26L after touchdown [Bun12]. The final position of the aircraft is shown in figure 9.30, the tire marks in the grass are well visible.

The second accident involved a Boeing 777-300ER. The aircraft performed an automatic landing assuming CAT III meteorological conditions, though the airport was not operating under CAT III since the visibility was much better. However, the aerodrome controller was not informed about the flight crew's decision to perform au-

Figure 9.30: *The RE (veer-off) accident at MUC/EDDM in 2012 involving an ATR-72 aircraft [Bun12]*

toland. Therefore, the runway protection zone was not sufficiently cleared of objects and other traffic. As the aircraft was shortly before touchdown on runway 08R, a departing traffic on the same runway flew above the ILS localizer, causing the signal to be disturbed. The aircraft slightly banked to the left as it touched down and departed from the runway to the left. As the pilots tried to correct, the aircraft returned to the runway, but departed again to the right before coming to a stop [Bun18].

Both accidents did not cause any fatalities. While some passengers were injured in the ATR and the aircraft was severely damaged due to collapse of one main landing gear, the Boeing only received minor damages with no harm to passengers and crew.

Compared to the total number of aircraft movements at MUC/EDDM, which sums up to $9\,228\,000$ – half of them being landings, i.e. $4\,614\,000$ – from the opening in 1992 until the end of 2018 [Flu], the numbers are consistent with the accident probabilities computed in this chapter. Two veer-off accidents out of $4\,614\,000$ movements and zero overrun accident would result in a veer-off probability of 4.3×10^{-7} and an overrun probability of less than 1.1×10^{-7}. However, one has to keep in mind that these two accidents that have occurred, apart from the fact that the sample size is fairly small, are primarily caused by technical failures. The primary cause for the ATR accident was an engine failure combined with rudder blockage and for the Boeing, it was the incorrect signal from the ILS localizer combined with the inappropriate handling of the fight crew and the lack of necessary exchange of information between flight crew and the tower controller. Though the aircraft model is capable of including technical failures, they were excluded during the computation of the numbers presented in this chapter. These system failures and their influences should be included in the model for future work.

9.5 Assessment of the Subset Simulation Algorithm

Some remarks concerning the behavior of the Markov Chain were already made as certain properties had become visible. Two aspects are further discussed in the following.

Contributing factors with large differences in impact

The movement of the Markov Chain was discussed for figure 9.19. The MCMC algorithm explores the parameter space in all directions using the Infinity Sampling method. Newly generated samples are only rejected if they are not located in the failure space. However, if the motion of the Markov Chain in one component is capable of compensating any contrary effect coming from other components, their values can quickly take up the entire parameter space according to the input distributions. For example, for the veer-off, the lateral offset of the touchdown position is the main driver during the first three subsets. When the Markov Chain explores the parameter space individually for each component, an increase of the lateral offset is capable of compensating for most changes in other contributing factors, such as the crab angle, with respect to the shoulder margin as the lateral offset is much more dominant compare to others, at least during this stage. This means that values generated in the other components do not make a difference or at least no significant difference. The result is that samples are generated over the entire range defined by the input PDF and most samples are generated in the center, i.e. where the PDF has the highest value.

The behavior vanishes as the effect of the contributing factors become more equally distributed. In the veer-off example, the lateral offset is truncated to certain values and cannot be further increased at a certain point. In this case, other contributing factors start to move faster towards values leading to further decreasing shoulder margins.

Model singularities

This problem arose during the assessment of runway veer-off. For certain initial conditions at touchdown, the model shows singularities with respect to the shoulder margin. This phenomena occurs when the crab angle at touchdown is very high and the aircraft touches down with a bank angle and the controller immediately tries to correct the offset combined with braking. This combination rarely occurs, but in this case, the lateral friction coefficient is not sufficient any more to keep the aircraft on track and it starts skidding laterally and spinning around the yaw axis. The violation of the overall shoulder margin in this case is very high, often beyond $-100\,\mathrm{m}$. The Anti-Lock Braking System (ABS) is not capable of regaining the control of the aircraft if the sideslip angle is already close to $90°$.

If one of the samples during the first few subsets shows this behavior, it will be automatically used as a seed for the next sample as the corresponding shoulder margin is well in the negative. However, as one of the input factors is changed, the aircraft becomes controllable again and the shoulder margin becomes positive. However, this also means that the generate candidate sample is often not in the failure domain of the previous subset. Therefore, it is rejected and the newly generated sample is set to be the seed. As N_C Markov Chains exist, each of them does this again and the seed is effectively copied N_C times to form the samples for the next subset. Ultimately, in each of the i succeeding subsets, the same sample occurs $(N_C)^i$ times, the correlation in the samples increase significantly as the same sample appears several times and the result becomes erroneous.

10

Conclusion and Outlook

10.1 Summary

In this work, novel methods contributing fo the *Predictive Analysis (PA)* have been presented. It consists of seven steps. Three of them, namely *Model*, *Cumulate* and *Predict*, are the foci of this work. The enablers and techniques underlying this approach are explained in the first chapters. The necessity of the PA results from the continuously decreasing accident rates in commercial aviation. As the number of accidents decreases, the classical *reactive safety management* by analyzing accidents that have happened in the past gradually loses its effectiveness. Accident investigation has led to significant improvement of the level of safety in aviation over the last decades. However, the current low number of accidents does not only imply a small amount of data, but also very different factors that contribute to an accident. Thus, the lessons learned have become less transferable and less useful to derive safety recommendations from. The PA aims at quantifying accident probabilities and identifying the main drivers without requiring actual accident data for individual organizations. It enables the further reduction of accident rates and, therefore, can become a useful tool for airline safety managers.

For the demonstration of the PA, the example of Runway Excursion (RE) during landing is used, including both runway overrun and runway veer-off. To explain the method, an introduction to an airline's Safety Management System (SMS) has been given in which the Flight Data Monitoring (FDM) system is a key element. To understand FDM, it is essential to understand how flight data is measured, acquired, recorded and – finally – transferred and processed within the operator's IT system. After the data has become available and accessible, key characteristics at specific points in time, the so-called *timepoints* and *measurements*, are extracted from the data, creating distributions that represent the airline's entire flight operations without the focus on single flights.

In order to perform the PA, a model of the aircraft is required. The model is mainly a physical model, incorporating the laws of motion based on the forces and moments acting on the aircraft. As the landing gear forces are essential when it comes to the behavior of the aircraft on the ground within the scope of RE, the landing gears are extensively modeled. In addition to the flight physics, the system logics of the aircraft are included as well as the braking and steering behavior of the pilot.

For the propagation of the distributions obtained from FDM data through the aircraft model within the scope of the *Predict* step, the *Subset Simulation* is used that is particularly suitable for the quantification of small probabilities as a classical Monte Carlo Simulation (MCS) approach would require an unreasonably high computational effort, providing a lower confidence at the same time. The results are computed for both accident types, runway *overrun* and runway *veer-off*. Based on the available FDM data, accident probabilities are obtained for the runways at Munich Airport (MUC/EDDM) and members of the Airbus A320 family aircraft. Two possible configurations of the high-lift system that can be used for landing are compared as well as dry and wet runways. The most influential contributing factors are identified for each scenario. In addition, some findings, such as dependencies between the contributing factors and operational influences with impact on the level of safety, are highlighted, they are summarized in section 10.2. The obtained numbers serve three main purposes:

1. They *quantify the absolute occurrence probability* for given scenarios and thus provide a direct measure for the level of safety within the flight operations of an airline.

2. They *quantify the differences* in the level of safety with respect to RE between aircraft types, landing runways, landing configurations and runway conditions.

3. They represent the starting point for further analysis to explore *the reasons in the contributing factors* for the differences between the numbers as well as how to influence them, ultimately with the goal to further decrease the accident probabilities and to increase the level of safety.

10.2 Key Findings for Runway Excursion

During the analysis of the results obtained in chapter 9, the key findings concerning the hazards affecting RE accidents are obtained which are summarized and listed in the following.

Late touchdown with lower speed

If the flare is performed too firmly, the aircraft will float above the runway for a long time as the speed decreases. This leads to a touchdown with a lower speed, but at the same time a longer touchdown distance. The probability for an overrun increases as the means for deceleration on the ground are much more powerful compared to those available in-air due to the use of brakes, the extension of ground spoilers and the deployment of reverse thrust.

Landing with lower flap setting and mass dependency

Landings with a lower flap setting, namely *CONF 3* instead of *CONF Full* on the Airbus A320 family, have a lower probability for overrun because it is typically performed when the aircraft's mass is low, thus compensating for the higher approach speed. An important advantage of lower flap settings is the reduced fuel consumption and noise level due to the higher aerodynamic efficiency during the approach. This example clearly shows that, even though landings with *CONF 3* are less risky than *CONF Full*, the level of safety will not improve by simply performing all landings using *CONF 3* because the reason for this – the difference in average mass between the two configurations – is not directly visible, but hidden in the data of the contributing factors.

Low brake application due to operational reasons

Although applying brakes and other deceleration devices should be done immediately after touchdown to slow down the aircraft to a sufficiently safe Groundspeed (GS), braking is sometimes delayed and/or heavily reduced due to operational reasons, e.g. the fact that the parking position is located towards the end of the runway. This behavior, which becomes eminent when comparing different runways at the same airport, significantly increases the probability for runway overrun as well as the severity in case of an overrun caused by the higher speed. The difference in braking behavior becomes particularly observable for long runways, such as those in MUC/EDDM.

Impact of wet runways

Wet runways significantly reduces the friction coefficient that can be achieved between the runway surface and the aircraft's tires. While for the overrun scenario, the increase of the accident probability is significant, but not major, the increase for the veer-off scenario is tremendous. However, the influence on the overrun probability should increase if the available runway length is shorter than the $4000\,\mathrm{m}$ at MUC/EDDM and

thus more critical. For veer-off, the impact will be even higher when landing on runways with widths less than $60\,\mathrm{m}$. Therefore, special attention should be paid by the flight crew when performing landings on wet, or even contaminated runways under high crosswind conditions with respect to veer-off and when performing landings on short runways with respect to overrun.

Dependency between the contributing factors

Some contributing factors are closely related to each other. Examples include the crab angle versus the crosswind or the speed reduction during flare versus the touchdown distance. One effect resulting from this is that certain contributing factors can shadow the influence of other contributing factors. A clear distinction should be made between a causal relationship and a simple data-based correlation. Furthermore, these dependencies should be included for future assessments.

10.3 Outlook and Perspectives

Despite the fact that the Predictive Analysis has proven to be a useful and reliable method to quantify the occurrence probabilities for given accident types and its applicability has been shown for the use-case of Runway Excursion, more work is in progress or still to be done. The steps *Identify*, *Calibrate* and *Revise* are covered in other works, on which the results obtained in this work also rely. The parameters required to build the aircraft model is taken from the step *Identify*, the distributions to be propagated through the model using Subset Simulation are finalized in the step *Calibrate* and the dependency structures between all the contributing factors are derived in the step *Revise*. Especially with respect to the dependency in the data, the results obtained in this work have shown that they should be included to improve the quality of the results.

Several sources of error exist in the entire chain leading from processed flight data to accident probabilities besides the errors in the data, which is thoroughly described in chapter 3. Modeling errors are introduced when the aircraft model is created due to simplifications that have to be made. The extraction of measurements is associated with errors when it comes to correctly detecting timepoint and measurement values. The fitting of distributions causes errors as the available data does not necessarily follow one of the available parametric distributions. The data can be limited to certain values or be multi-modal. Kernel Density Estimations (KDEs) can be used in this case to minimize the fitting error, but can also lead to other errors. For example, a KDE will return a Probability Density Function (PDF) value of zero if no data is present in

a sufficiently large span. However, that does not mean that there cannot be any data. The recorded data is just a sample representing the flight operations.

In order to improve the quality of the data, particularly the kinematic parameters of the aircraft, it is enhanced using the Rauch-Tung-Striebel (RTS) smoother. For landings on runway 26R, it was shown that there is a smaller peak in the localizer position offset right to the centerline. It should be further investigated whether this error is caused by erroneous signal of the localizer or whether it actually represents the real trajectory. Reflections of Instrument Landing System (ILS) signal by buildings, ground vehicles and other aircraft is not uncommon and was one of the main causes for one veer-off accident at Munich Airport.

For the detection of the runway condition, further sources of data have to be included in order to reliably detect whether the runway was dry, wet or contaminated. An alternative approach would be to treat the runway condition as a continuous variable. The maximum achievable friction coefficient could be identified from the data and a distribution of the friction coefficient can be obtained, serving as an input into the Subset Simulation.

When it comes to the overall safety assessment of RE, the model should be enhanced in the future to include technical failures on-board the aircraft. A classification should be made to include only those failure conditions that occur with a frequency that is relevant to the overall safety assessment. The occurrence probability of failure conditions should always be, if possible, directly obtained from operational data rather than certification requirements to account for the difference between actual real-life reliability values and theoretical ones. Furthermore, the model should be modified such that the singularities mentioned in section 9.5 do not occur or at least in such a ways that the overall result is not affected.

To extend the safety assessment for RE, an assessment of the approach phase should be conducted to determine unstabilized approaches and possible decisions for conducting a missed approach. As the assessment of RE begins at the time of touchdown, unfavorable conditions during touchdown, e.g. the combination of late touchdown and high approach speed or excessive crab angle, are caused by events during the final approach. A similar model-based procedure based on the Predictive Analysis can be used. This work is already in progress [WSK+19]. The output will be the inputs for RE assessment, but will also include occurrence probabilities for other types of accidents, such as Abnormal Runway Contact (ARC), including hard landing, tailstrike and wingtip strike. Other accident types that can occur during the approach, such as Loss of Control In-Flight (LOC-I) as well as Controlled Flight Into Terrain (CFIT) can be assessed. Combined with the methods presented in this work, an overall risk picture of the entire approach and landing phase can be obtained, which is the most critical part of a flight with respect to safety.

Appendix A

Definition of Coordinate Frames

Aerodynamic Frame A

The A frame translates with the aircraft and rotates with the airflow. It is suitable to describe the aerodynamic forces and moments.

Property	**Description**
Origin	Aircraft reference point R
x axis	Pointing towards the airflow relative to the aircraft, parallel to the aerodynamic velocity
y axis	Perpendicular to the x and z axes
z axis	Pointing down within aircraft's symmetry plane

Body-Fixed Frame B

The B frame is fixed with the aircraft and rotates with the motion of the aircraft. It is often suitable to express the position of certain point with respect to the aircraft reference point as it does not change in the B frame when the aircraft is considered as a rigid body. For some applications, the aircraft reference point can set to be the Center of Gravity (CG).

Property	**Description**
Origin	Aircraft reference point R
x axis	Pointing towards the nose of the aircraft within the aircraft's symmetry plane
y axis	Pointing towards the right wing
z axis	Pointing down within aircraft's symmetry plane, perpendicular to the x and y axes

Earth-Centered-Earth-Fixed Frame E

The E is fixed to the earth and rotates with the earth. It is suitable for navigation applications.

Property	**Description**
Origin	Center of the earth
x axis	Pointing towards the prime meridian within the equatorial plane
y axis	Pointing towards the $90°$ meridian within the equatorial plane
z axis	Pointing towards the true north pole. It is the rotation axis of the earth.

Instead of Cartesian coordinates, the position on the earth can also be expressed with the geodetic latitude μ, the longitude λ and the height above the reference ellipsoid h when the World Geodetic System 1984 (WGS84) is used.

Kinematic Frame K

The K translates with the aircraft and rotates with the kinematic velocity.

Property	**Description**
Origin	Center of the earth
x axis	Pointing towards the direction of motion, parallel to the kinematic velocity
y axis	Perpendicular to the x and z axes
z axis	Pointing down within aircraft's symmetry plane

North-East-Down Frame O

The O translates along with the aircraft, but maintains a fixed orientation relative to the local earth's surface. It can be used to express the gravitational forces and for navigation purposes.

Property	**Description**
Origin	Aircraft reference point R
x axis	Pointing towards the true north pole
y axis	Pointing towards the east, parallel to the circles of latitude
z axis	Pointing downwards, perpendicular to the earth local surface and parallel to the direction of the earth's gravitation

Navigation Frame N

The N is a local navigation frame that was introduced in section 6.1. The N is obtained from the O by rotating around the z axis. A picture showing the N frame is shown in figure 6.1.

Property	**Description**
Origin	On the runway centerline, either on the threshold or abeam the touchdown point of the aircraft
x axis	Pointing towards the direction of the runway
y axis	Pointing towards the side of the runway, perpendicular to the x and z axes
z axis	Pointing downwards, perpendicular to the earth local surface and parallel to the direction of the earth's gravitation

Appendix B

Probability Distributions

The following probability distributions are used in the scope of this work as inputs to the Subset Simulation.

Distribution	**Parameters**	**PDF**
Beta $\mathcal{Be}(a,b)$	$a>0$ $b>0$	$f(x)=\frac{x^{a-1}(1-x)^{b-1}}{\int_0^1 u^{a-1}(1-u)^{b-1}\mathrm{d}u}$
Birnbaum-Saunders $\mathcal{Bs}(\beta,\gamma)$	$\beta>0$ $\gamma>0$	$f(x)=\frac{\sqrt{\frac{x-\mu}{\beta}}+\sqrt{\frac{\beta}{x-\mu}}}{2\gamma(x-\mu)}f_N(x)\left(\frac{\sqrt{\frac{x-\mu}{\beta}}-\sqrt{\frac{\beta}{x-\mu}}}{\gamma}\right)$
Burr $\mathcal{Bu}(\alpha,c,k)$	$\alpha>0$ $c>0$ $k>0$	$f(x)=\frac{ck}{\alpha}\left(\frac{x}{\alpha}\right)^{c-1}\left[1+\left(\frac{x}{\alpha}\right)^{c}\right]^{-k-1}$
Exponential $\mathcal{Exp}(\mu)$	$\mu>0$	$f(x)=\mu\exp(-\mu x)$
Gamma $\mathcal{Ga}(a,b)$	$a>0$ $b>0$	$f(x;\alpha,\beta)=\frac{\beta^{\alpha}x^{\alpha-1}e^{-\beta x}}{\Gamma(\alpha)}$
GEV $\mathcal{Gev}(k,\sigma,\mu)$	$-\infty\leq k\leq\infty$ $\sigma\geq 0$ $-\infty\leq\mu\leq\infty$	$\frac{1}{\sigma}t(x)^{\xi+1}e^{-t(x)}$, where $t(x)=\begin{cases}\left(1+\xi(\frac{x-\mu}{\sigma})\right)^{-1/\xi} & \text{if } \xi\neq 0\\ e^{-(x-\mu)/\sigma} & \text{if } \xi=0\end{cases}$
Inverse-Gaussian $\mathcal{N}^{-1}(\mu,\lambda)$	$\mu>0$ $\lambda>0$	$f(x)=\sqrt{\frac{\lambda}{2\pi x^3}}\exp\left(\frac{-\lambda(x-\mu)^2}{2\mu^2 x}\right)$
Logistic $\mathcal{Log}(\mu,\sigma)$	$-\infty<\mu<\infty$ $\sigma\geq 0$	$f(x)=\frac{e^{-\frac{x-\mu}{\sigma}}}{\sigma\left(1+e^{-\frac{x-\mu}{\sigma}}\right)^2}$
Log-Logistic $\mathcal{Ll}(\mu,\sigma)$	$\mu>0$ $\lambda>0$	$f(x)=\frac{(\lambda/\mu)(x/\mu)^{\lambda-1}}{\left(1+(x/\mu)^{\lambda}\right)^2}$
Log-Normal $\mathcal{Ln}(\mu,\sigma)$	$-\infty<\mu<\infty$ $\sigma\geq 0$	$f(x)=\frac{1}{x\sigma\sqrt{2\pi}}e^{-\frac{(\ln x-\mu)^2}{2\sigma^2}}$

Nakagami $\mathcal{Na}(\mu, \omega)$	$\mu > 0$ $\omega > 0$	$f(\mu, \omega) = \frac{2\mu^{\mu}}{\Gamma(\mu)\omega^{\mu}} x^{2\mu-1} \exp\left(-\frac{\mu}{\omega} x^2\right)$
Normal $\mathcal{N}(\mu, \sigma)$	$-\infty < \mu < \infty$ $\sigma \geq 0$	$f(x) = \frac{1}{\sqrt{2\pi\sigma^2}} e^{-\frac{(x-\mu)^2}{2\sigma^2}}$
Rayleigh $\mathcal{Ra}(b)$	$b > 0$	$f(x) = \frac{x}{b^2} e^{-x^2/\left(2b^2\right)}$
Rician [1] $\mathcal{Ri}(s, \sigma)$	$s \geq 0$ $\sigma > 0$	$f(x) = \frac{x}{\sigma^2} \exp\left(\frac{-(x^2+s^2)}{2\sigma^2}\right) I_0\left(\frac{xs}{\sigma^2}\right)$
t-Location Scale $\mathcal{Lo}(\mu, \sigma, \nu)$	$-\infty < \mu < \infty$ $\sigma > 0$ $\nu > 0$	$f(x) = \frac{\Gamma\left(\frac{\nu+1}{2}\right)}{\sigma\sqrt{\nu\pi}\Gamma\left(\frac{\nu}{2}\right)} \cdot \left(\frac{\nu+\left(\frac{x-\mu}{\sigma}\right)}{\nu}\right)^{-\left(\frac{\nu+1}{2}\right)}$
Uniform $\mathcal{U}(a, b)$	$-\infty \leq a \leq \infty$ $-\infty \leq b \leq \infty$ $-\infty \leq \mu \leq \infty$	$f(x) = \begin{cases} \frac{1}{b-a} & \text{for } x \in [a, b] \\ 0 & \text{otherwise} \end{cases}$
Weibull $\mathcal{Wb}(a, b)$	$a > 0$ $b > 0$	$f(x) = \begin{cases} \frac{b}{a}\left(\frac{x}{a}\right)^{b-1} e^{-(x/a)^b} & x \geq 0, \\ 0 & x < 0 \end{cases}$

[1] I_0 represents the first kind Bessel function with an order of zero.

Appendix C

Aeronautical Charts

Exit Taxiway Positions for Munich Airport

According to the Aeronautical Information Publication (AIP), the following taxiways should be used to vacate the runways at Munich Airport (MUC/EDDM) when High Intensity Runway Operation (HIRO) is in progress [DFS18]. The distance from runway threshold is also provided.

Aircraft Type	**08L**	**08R**	**26L**	**26R**
Heavy	A10	B10	A6	B6
Distance	2260 m	2200 m	2200 m	2220 m
Medium	A7	B7	A9	B8
Distance	1710 m	1580 m	1580 m	1660 m
Light	A5	B7	A9	B11
Distance	1270 m	1580 m	1580 m	1160 m

Airport Ground Chart for Munich Airport

On the following page, the Airport Ground Chart (AGC) for MUC/EDDM is shown [DFS18].

AERODROME CHART - ICAO

ARP 1470 ft
N 48° 21' 13,62"
E 011° 47' 09,91"

AERODROME ELEVATION
1487 ft

MUENCHEN

INTERSECTION TAKE-OFF

RWY	TWY	TORA	TODA	ASDA
08L	A3	3800	3860	3800
	A4	2820	2880	2820
	A6	2200	2260	2200
26R	A10	2260	2320	2260
	A12	2780	2840	2780
	A13	3800	3860	3800
08R	B3	3800	3860	3800
	B4	2840	2900	2840
	B6	2220	2280	2220
26L	B10	2200	2260	2200
	B12	2820	2880	2820
	B13	3800	3860	3800

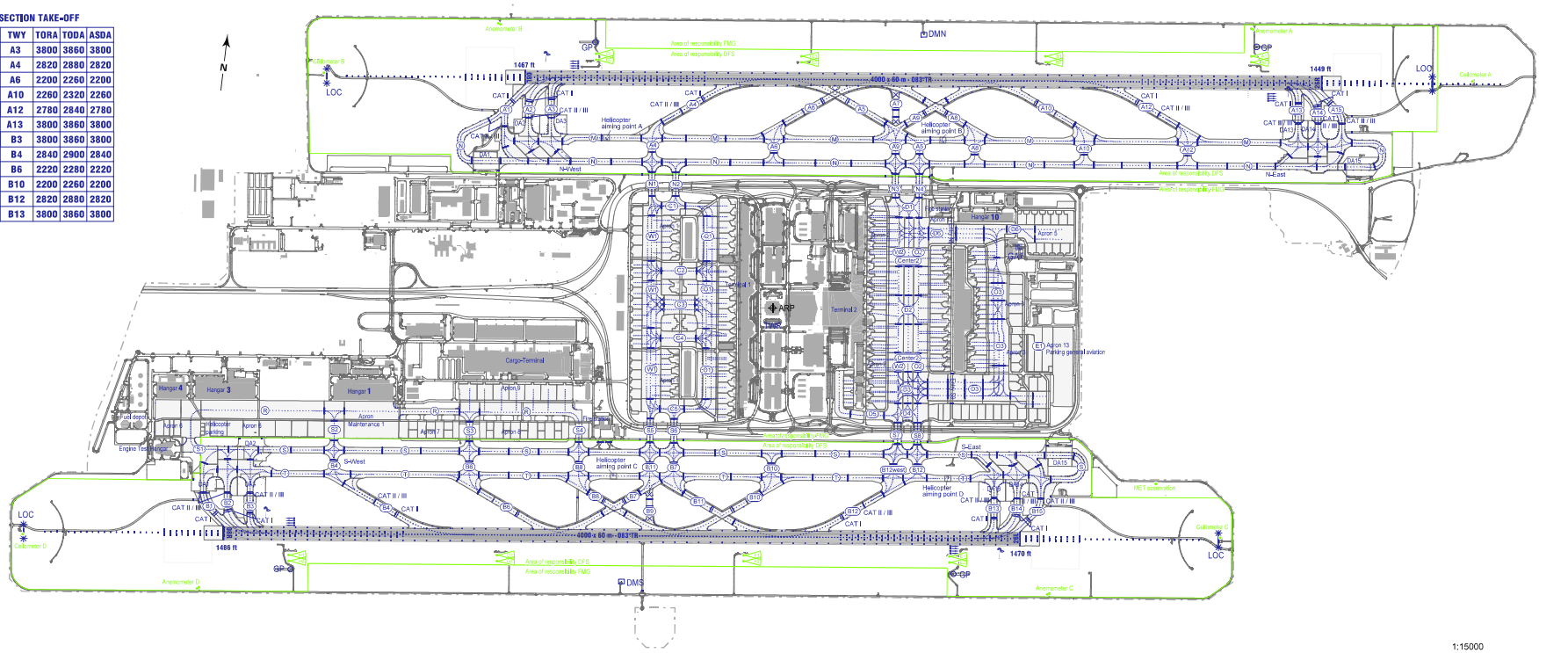

Correction: TWYs C3, C4, C5, Intersection take-off.

Appendix D

Data Measurements for the Baseline Scenario

The baseline scenario is set to be the landing of the Airbus A320 on runway 26R at MUC/EDDM using *CONF Full* on a dry runway surface.

Measurements as Direct Model Input

The distributions that are fitted using the following measurements serve as direct inputs into the model that are propagated using Subset Simulation.

For each histogram, a distribution is fitted. The type of the distribution and the value of the distribution parameters are shown. In addition, a Kolmogorov-Smirnov (KS) test is performed that is an indication of how well the data actually follows the fitted distribution.

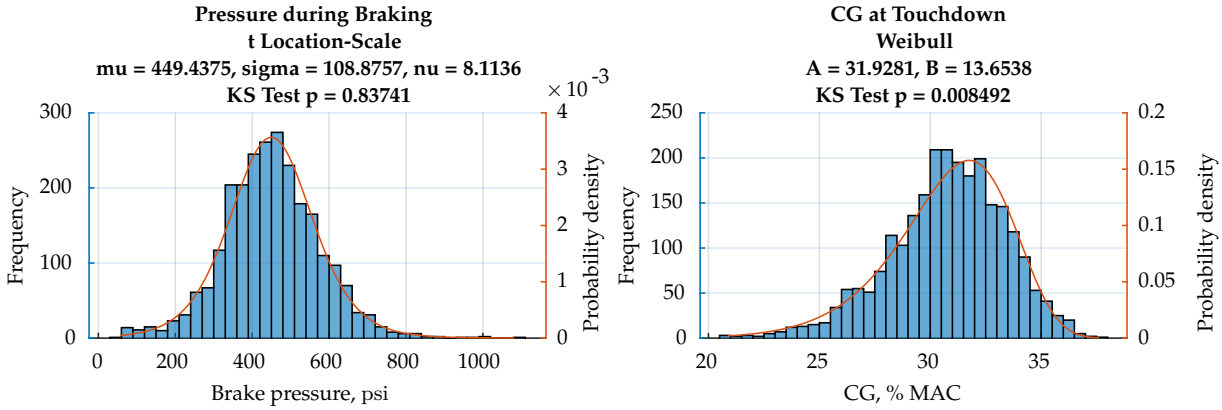

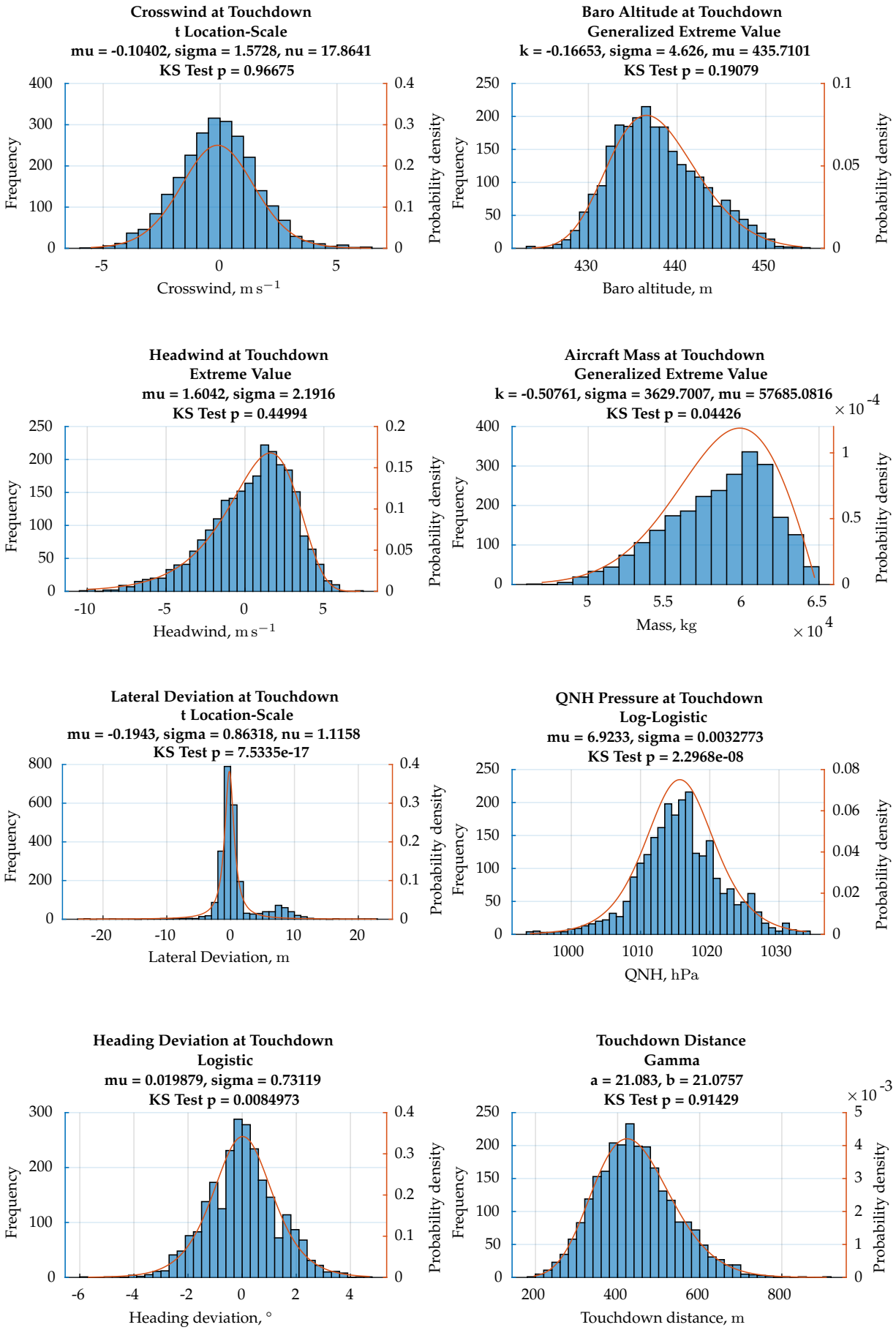
Crosswind at Touchdown
t Location-Scale
mu = -0.10402, sigma = 1.5728, nu = 17.8641
KS Test p = 0.96675
Frequency
Probability density
Crosswind, m s−1
Baro Altitude at Touchdown
Generalized Extreme Value
k = -0.16653, sigma = 4.626, mu = 435.7101
KS Test p = 0.19079
Frequency
Probability density
Baro altitude, m
Headwind at Touchdown
Extreme Value
mu = 1.6042, sigma = 2.1916
KS Test p = 0.44994
Frequency
Probability density
Headwind, m s−1
Aircraft Mass at Touchdown
Generalized Extreme Value
k = -0.50761, sigma = 3629.7007, mu = 57685.0816
KS Test p = 0.04426
× 10-4
× 10 4
Frequency
Probability density
Mass, kg
Lateral Deviation at Touchdown
t Location-Scale
mu = -0.1943, sigma = 0.86318, nu = 1.1158
KS Test p = 7.5335e-17
Frequency
Probability density
Lateral Deviation, m
QNH Pressure at Touchdown
Log-Logistic
mu = 6.9233, sigma = 0.0032773
KS Test p = 2.2968e-08
Frequency
Probability density
QNH, hPa
Heading Deviation at Touchdown
Logistic
mu = 0.019879, sigma = 0.73119
KS Test p = 0.0084973
Frequency
Probability density
Heading deviation, °
Touchdown Distance
Gamma
a = 21.083, b = 21.0757
KS Test p = 0.91429
× 10-3
Frequency
Probability density
Touchdown distance, m

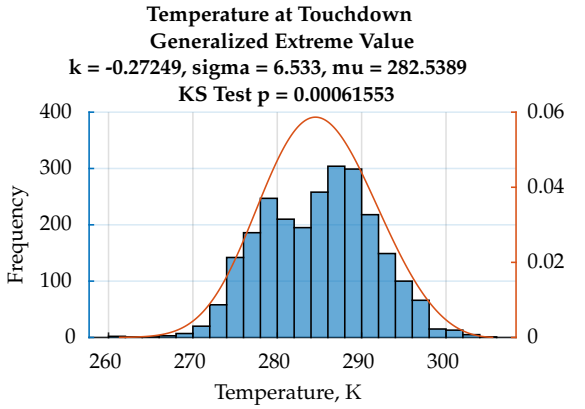

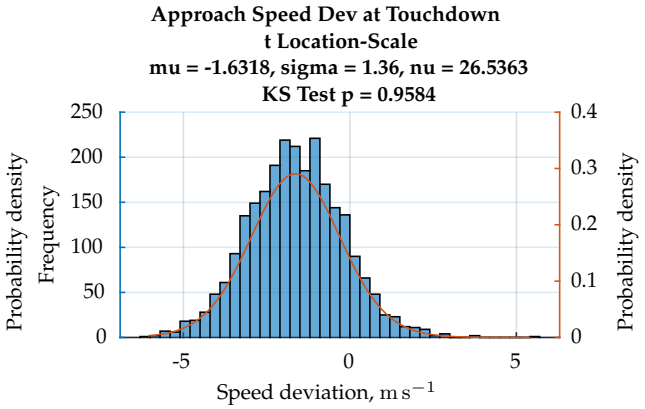

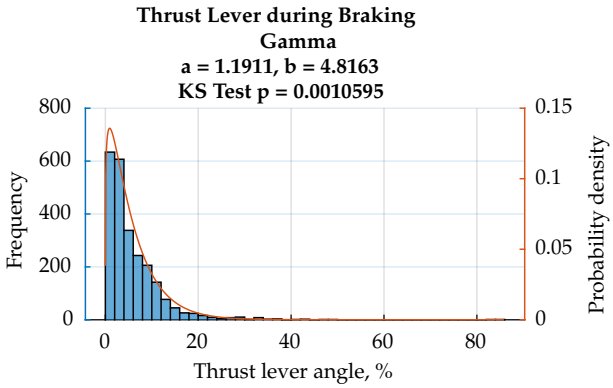

Timepoints as Direct Model Input

Timepoints are used to activate or deactivate deceleration devices during the simulation of the landing. They include the deployment of spoilers, the deployment and retraction of thrust reverse as well as the activation and deactivation of braking.

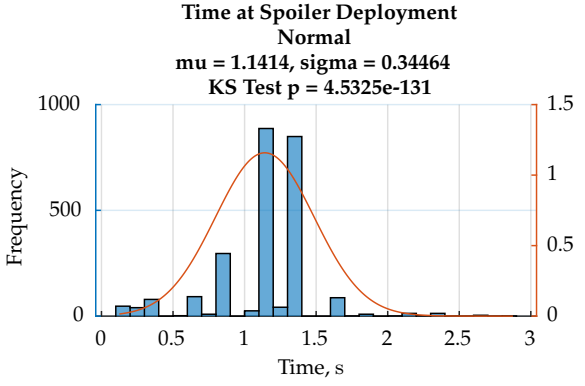

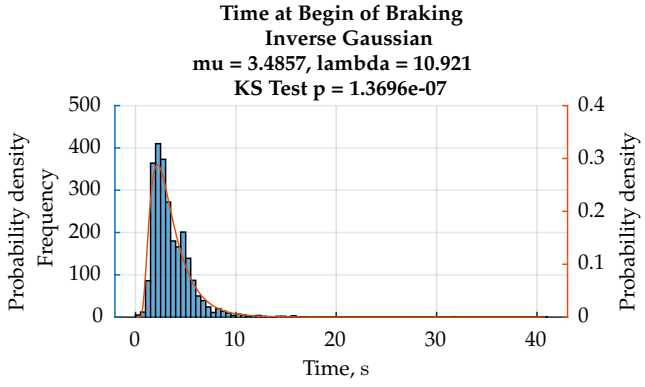

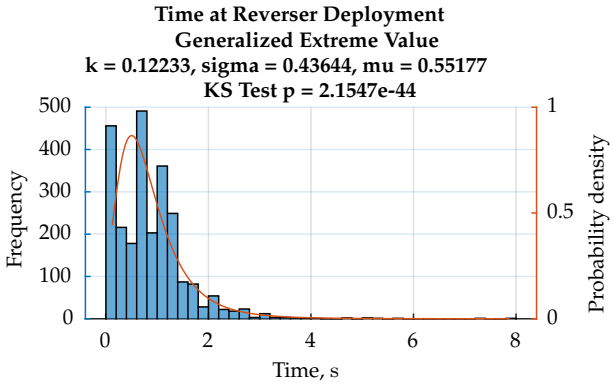

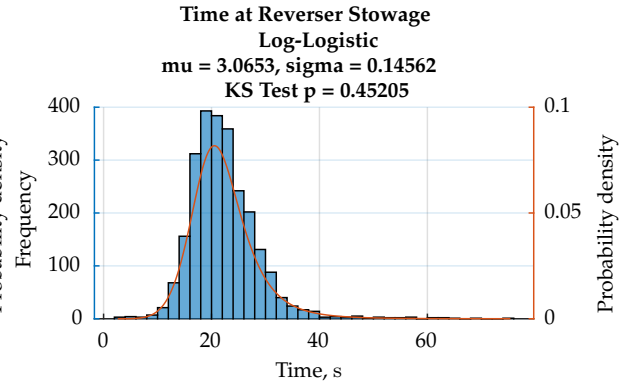

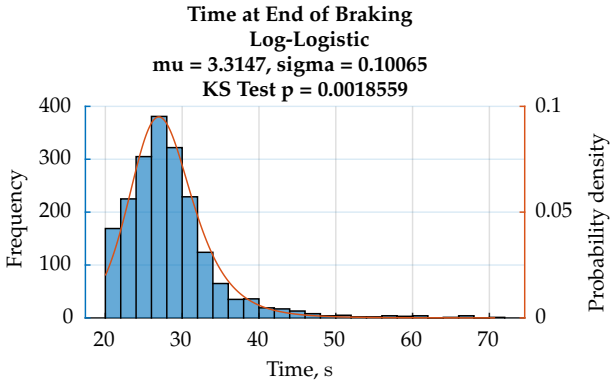

Supplementary Measurements

Supplementary measurements are not directly fed into the model. However, they are used to make adjustments to the model and to perform further analysis within the contributing factors. The fitted distributions are often not used, but only the data histograms to explain the influences of contributing factors and to assess the results obtained from the Subset Simulation.

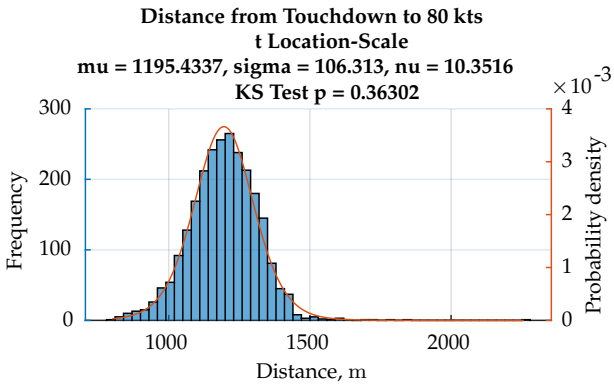

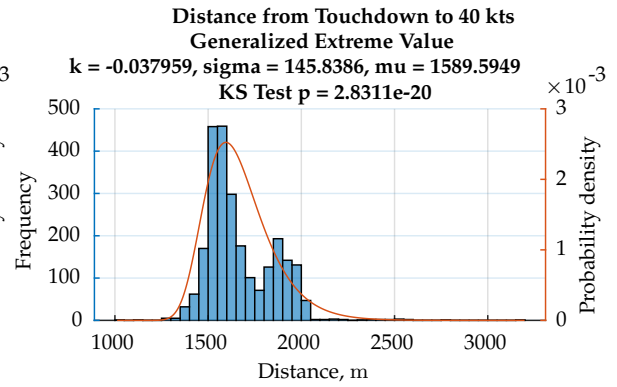

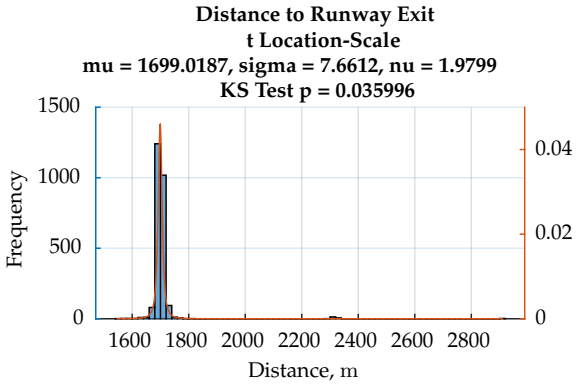

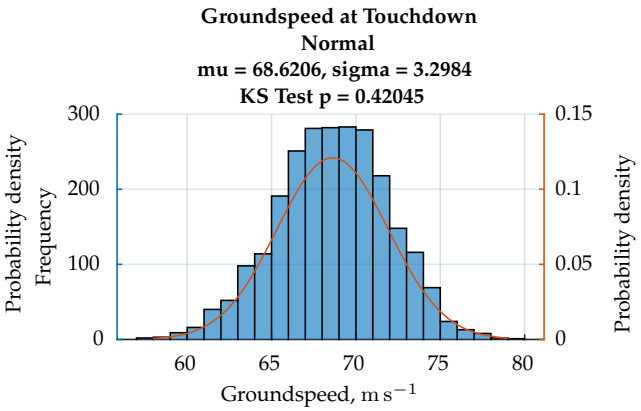

Additional Measurements

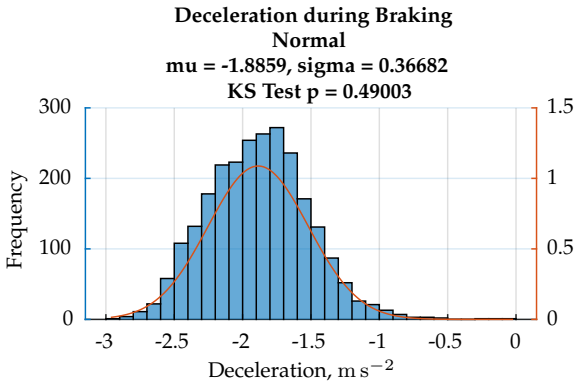

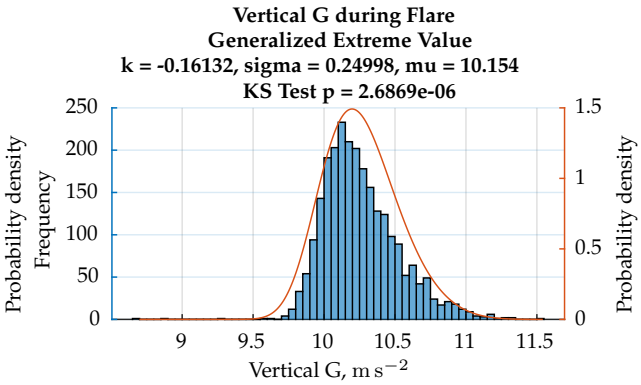

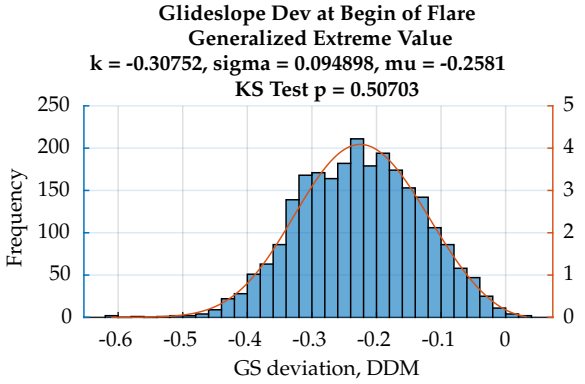

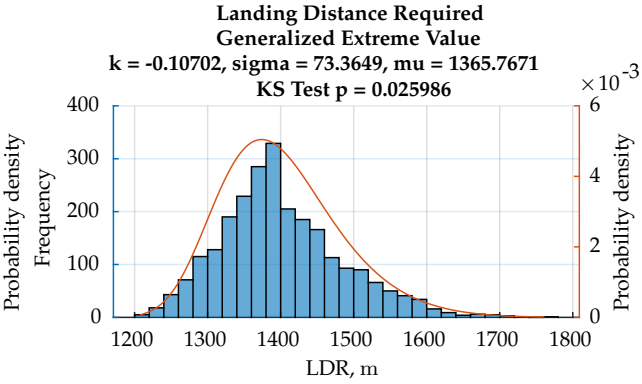

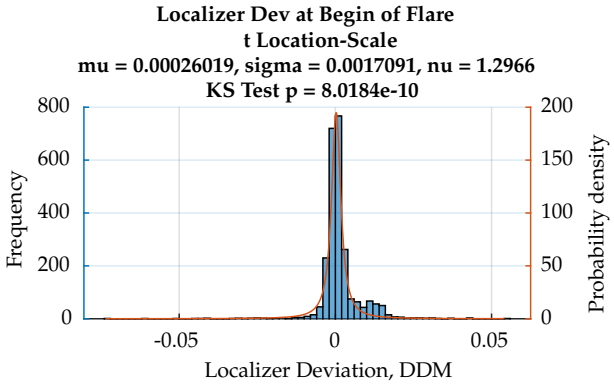
Localizer Dev at Begin of Flare
t Location-Scale
mu = 0.00026019, sigma = 0.0017091, nu = 1.2966
KS Test p = 8.0184e-10
Frequency
Probability density
Localizer Deviation, DDM

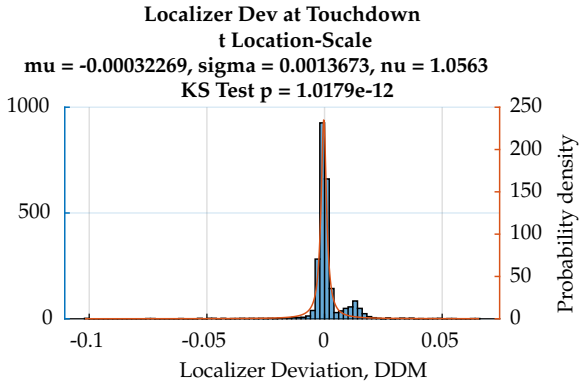
Localizer Dev at Touchdown
t Location-Scale
mu = -0.00032269, sigma = 0.0013673, nu = 1.0563
KS Test p = 1.0179e-12
Frequency
Probability density
Localizer Deviation, DDM

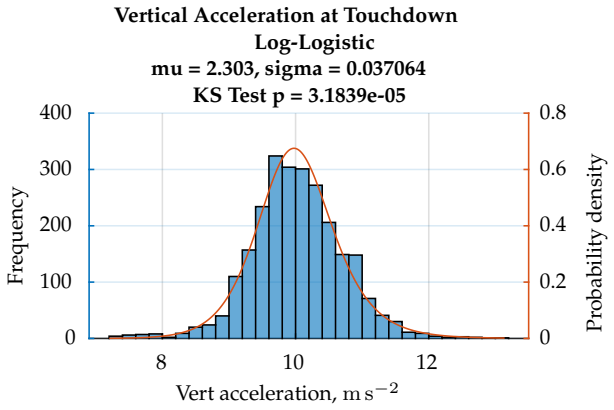
Vertical Acceleration at Touchdown
Log-Logistic
mu = 2.303, sigma = 0.037064
KS Test p = 3.1839e-05
Frequency
Probability density
Vert acceleration, m s^{-2}

Scientific Publications by the Author

[WDG+14] WANG, Chong; DREES, Ludwig; GISSIBL, Nadine; HÖHNDORF, Lukas; SEMBIRING, Javensius; HOLZAPFEL, Florian: Quantification of Incident Probabilities Using Physical and Statistical Approaches. In: *6th International Conference on Research in Air Transportation*. Istanbul, Turkey, 2014

[WDH14] WANG, Chong; DREES, Ludwig; HOLZAPFEL, Florian: Incident Prediction using Subset Simulation. In: *29th Congress of International Council of the Aeronautical Sciences (ICAS)*. St. Petersburg, Russia: International Council of the Aeronautical Sciences, 2014

[WDH16a] WANG, Chong; DREES, Ludwig; HOLZAPFEL, Florian: Extracting measurements from operational flight data using the flare example. Version: 2016. http://dx.doi.org/10.2514/6.2016-0175. In: *AIAA Modeling and Simulation Technologies Conference*. San Diego, CA, USA: American Institute of Aeronautics and Astronautics, 2016 (AIAA SciTech Forum). – DOI 10.2514/6.2016–0175

[WDH16b] WANG, Chong; DREES, Ludwig; HOLZAPFEL, Florian: Fuel Starvation Caused by Hub Closure. In: *30th International Congress of the International Council of the Aeronautical Sciences (ICAS)*. Daejeon, Korea: International Council of the Aeronautical Sciences, 2016

[WMH16] WANG, Chong; MOHR, Nils; HOLZAPFEL, Florian: Decoding of Binary Flight Data in ARINC 717 Format. In: *1st International Conference in Aerospace For Young Scientists (ICAYS)*. Beijing, China: Beihang University, 2016

[WH18b] WANG, Chong; HOLZAPFEL, Florian: Modeling of the Aircraft Landing Behavior for Runway Excursion and Abnormal Runway Contact Analysis. Version: 2018. http://dx.doi.org/10.2514/6.2018-1166. In: *2018 AIAA Modeling and Simulation Technologies Conference*. Kissimmee, FL, USA:

American Institute of Aeronautics and Astronautics, 2018 (AIAA SciTech Forum). – DOI 10.2514/6.2018–1166

[WMH18] WANG, Chong; METGE, Sylvain; HOLZAPFEL, Florian: Quantification of Accident Probabilities for a Risk Observatory. Version: 2018. http://dx.doi.org/10.5281/zenodo.1484912. In: *7th Transport Research Arena*. Vienna, Austria, 2018. – DOI 10.5281/zenodo.1484912

[WH18a] WANG, Chong; HOLZAPFEL, Florian: Evaluation of Aircraft Braking Performance Based on Operational Flight Data. In: *31st Congress of the International Council of the Aeronautical Sciences (ICAS)*. Belo Horizonte, Brazil: International Council of the Aeronautical Sciences, 2018

[DSH+13] DREES, Ludwig; SEMBIRING, Javensius; HÖHNDORF, Lukas; WANG, Chong; HOLZAPFEL, Florian: *IATA Safety Report 2013, Section 9: Predictive Analysis*. Montreal, Canada, 2014

[DWH14] DREES, Ludwig; WANG, Chong; HOLZAPFEL, Florian: Using Subset Simulation to Quantify Stakeholder Contribution to Runway Overrun. In: *Probabilistic Safety Assessment and Management (PSAM)*. Honolulu, HI, USA, 2014

[HHD+15] HÖHNDORF, Lukas; HOLZAPFEL, Florian; DREES, Ludwig; SEMBIRING, Javensius; WANG, Chong; KOPPITZ, Phillip; SCHIELE, Stefan; ZAGLAUER, Christopher: Predictive Flight Data Analysis. In: *3rd Data Science in Aviation Workshop*. Brussels, Belgium: The Innaxis Foundation & Research Institute, 2015

[DMSM+17] DREES, Ludwig; MÜLLER, Manfred; SCHMIDT-MOLL, Carsten; GONTAR, Patrick; ZWIRGLMAIER, Kilian; WANG, Chong; BENGLER, Klaus; HOLZAPFEL, Florian; STRAUB, Daniel: Risk analysis of the EASA minimum fuel requirements considering the ACARE-defined safety target. In: *Journal of Air Transport Management* 65 (2017), S. 1–10. http://dx.doi.org/10.1016/j.jairtraman.2017.07.003. – DOI 10.1016/j.jairtraman.2017.07.003

[HWK+18] HÖHNDORF, Lukas; WANG, Chong; KOPPITZ, Phillip; WEISS, Sebastian; OLMOS, Sergio; CZADO, Claudia; HOLZAPFEL, Florian: Integration of Vine Copula Dependence Structures into Subset Simulation for Accident Probability Quantifications. In: *31st Congress of the International Council of the Aeronautical Sciences (ICAS)*. Belo Horizonte, Brazil: International Council of the Aeronautical Sciences, 2018

[KWH+19] KOPPITZ, Phillip; WANG, Chong; HÖHNDORF, Lukas; SEMBIRING, Javensius; WANG, Xiaolong; HOLZAPFEL, Florian: From Raw

Operational Flight Data to Incident Probabilities using Subset Simulation and a Complex Thrust Model. Version: 2019. http://dx.doi.org/10.2514/6.2019-2233. In: *AIAA Scitech 2019 Forum*. San Diego, CA, USA: American Institute of Aeronautics and Astronautics, 2019. – DOI 10.2514/6.2019–2233

[WSK+19] WANG, Xiaolong; SEMBIRING, Javensius; KOPPITZ, Phillip; HÖHNDORF, Lukas; WANG, Chong; HOLZAPFEL, Florian: Modeling of the Aircraft's Low Energy State During the Final Approach Phase Using Operational Flight Data. Version: 2019. http://dx.doi.org/10.2514/6.2019-0989. In: *AIAA Scitech 2019 Forum*. San Diego, CA, USA: American Institute of Aeronautics and Astronautics, 2019. – DOI 10.2514/6.2019–0989

Bibliography

[AB01] AU, Siu-Kui; BECK, James L.: Estimation of small failure probabilities in high dimensions by subset simulation. In: *Probabilistic Engineering Mechanics* 16 (2001), Nr. 4, S. 263–277. http://dx.doi.org/10.1016/S0266-8920(01)00019-4. – DOI 10.1016/S0266–8920(01)00019–4. – ISSN 0266–8920

[Air93] AIRCRAFT ACCIDENT INVESTIGATION COMMITTEE, MINISTRY OF TRANSPORT AND COMMUNICATIONS: *Lauda Air Luftfahrt Aktiengesellschaft, Boeing 767-300ER, Registration OE-LAV, Dan Chang District, Sphan Buri Province, Thailand, May 26, 1991*. Bangkok, Thailand, July 21, 1993

[Air07] AIRBUS S.A.S. - CUSTOMER SERVICES DIRECTORATE: *Getting to Grips with FOM: Flight Operations Monitoring Handbook*. Toulouse, France, September 2007

[Air08] AIRBUS S.A.S. - CUSTOMER SERVICES DIRECTORATE: *Flight Operations Briefing Notes: Landing Techniques – Crosswind Landings*. Toulouse, France, March 2008

[Air09] AIRBUS S.A.S.: *All about the A320 Family: Technical Appendices*. Toulouse, France, May 2009

[Air11a] AIRBUS S.A.S. - CUSTOMER SERVICES DIRECTORATE: *Airbus A380 Flight Crew Operating Manual (FCOM)*. Toulouse, France, November 3, 2011

[Air11b] AIRBUS S.A.S. - CUSTOMER SERVICES DIRECTORATE: *A350-900 Flight Deck and Systems Briefing for Pilots*. Toulouse, France, September 2011

[Air16] AIRBUS S.A.S. - CUSTOMER SERVICES, TECHNICAL DATA SUPPORT AND SERVICES: *Aircraft Characteristics: Airport and Maintenance Planning: A380*. Toulouse, France, December 1, 2016

[Air17] AIR FRANCE INDUSTRIES, KLM ENGINEERING & MAINTENANCE: *PROGNOS - Predictive Aircraft Maintenance*. Version: June 2017.

http://www.afiklmem.com/AFIKLMEM/en/g_page_standard/MRO_lab_Innovations/BigData.html, last accessed: July 16, 2018

[Air18a] AIRBUS S.A.S.: *O&Ds Airbus Commercial Aircraft November 2018*. Version: November 30, 2018. https://www.airbus.com/content/dam/corporate-topics/publications/o&d/ODs-Airbus-Commercial-Aircraft-November-2018.xlsx, last accessed: December 19, 2018

[Air18b] AIRBUS S.A.S. - CUSTOMER SERVICES, TECHNICAL DATA SUPPORT AND SERVICES: *Aircraft Characteristics: Airport and Maintenance Planning: A319*. Toulouse, France, February 1, 2018

[Air18c] AIRBUS S.A.S. - CUSTOMER SERVICES, TECHNICAL DATA SUPPORT AND SERVICES: *Aircraft Characteristics: Airport and Maintenance Planning: A320*. Toulouse, France, February 1, 2018

[Air18d] AIRBUS S.A.S. - CUSTOMER SERVICES, TECHNICAL DATA SUPPORT AND SERVICES: *Aircraft Characteristics: Airport and Maintenance Planning: A321*. Toulouse, France, February 1, 2018

[Air18e] AIRBUS S.A.S. - CUSTOMER SERVICES, TECHNICAL DATA SUPPORT AND SERVICES: *Aircraft Characteristics: Airport and Maintenance Planning: A330*. Toulouse, France, Juli 1, 2018

[Air18f] AIRBUS S.A.S. - CUSTOMER SERVICES, TECHNICAL DATA SUPPORT AND SERVICES: *Aircraft Characteristics: Airport and Maintenance Planning: A340-500/-600*. Toulouse, France, July 1, 2018

[Air18g] AIRBUS S.A.S. - CUSTOMER SERVICES, TECHNICAL DATA SUPPORT AND SERVICES: *Aircraft Characteristics: Airport and Maintenance Planning: A340-200/-300*. Toulouse, France, July 2, 2018

[Air18h] AIRBUS S.A.S. - CUSTOMER SERVICES, TECHNICAL DATA SUPPORT AND SERVICES: *Aircraft Characteristics: Airport and Maintenance Planning: A350*. Toulouse, France, June 1, 2018

[ARI09] ARINC INDUSTRY ACTIVITIES: *767 Enhanced Airborne Flight Data Recorder*. Rev. 1. Bowie, MD, May 29, 2009

[ARI11] ARINC INDUSTRY ACTIVITIES: *717-15 Flight Data Acquisition and Recording System*. Rev. 15. Bowie, MD, June 1, 2011. (717)

[Aus13] AUSTRIAN WINGS: *Vor 20 Jahre verunglückte der Lufthansa A320 Kulmbach in Warschau*. Version: September 14, 2013. https://www.austrianwings.info/2013/09/

vor-20-jahren-lufthansa-crash-in-warschau/, last accessed: August 8, 2018

[AW14] AU, Siu-Kui; WANG, Yu: *Engineering Risk Assessment with Subset Simulation*. Wiley, 2014. – ISBN 978–111839807–4

[Bau06] BAULCH, Vivian: *Selfridge Field and the beginnings of air power*. http://blogs.detroitnews.com/history/2000/07/18/selfridge-field-and-the-beginnings-of-air-power/. Version: 2006, last accessed: August 20, 2018

[Bau16] BAUMÜLLER, Tobias: *Development of Generic Calibration Algorithms for Contributing Factors of Physics-Based Incident Models*. Garching, Technical University of Munich, Master's Thesis, March 21, 2016

[BMMP17] BIEBER, Pierre; METGE, Sylvain; MOREL, Marion; PLE, Julien: Aircraft Safety Model Development and Integration in a Risk Observatory. In: *7th EASN International Conference on Innovation in European Aeronautics Research*. Warsaw, Poland, 2017

[BNP87] BAKKER, E.; NYBORG, L.; PACEJKA, H. B.: *Tyre Modelling for Use in Vehicle Dynamics Studies*. Version: 1987. http://dx.doi.org/10.4271/870421. – DOI 10.4271/870421

[Bra99] BRADY, Chris: *The Boeing 737 Technical Site: Landing Gear*. http://www.b737.org.uk/landinggear.htm. Version: 1999, last accessed: August 10, 2018

[BS10] BOISSENIN, Stephane; SALAVY, Elisabeth: A320 Family / Evolution of Ground Spoiler Logic. In: *Safety First: The Airbus Safety Magazine* February 2010 (February 2010), Nr. 9, S. 3–6

[Bun06] BUNDESANSTALT FÜR VERKEHR - UNFALLUNTERSUCHUNGSSTELLE: *Flugunfall mit dem Motorflugzeug Typ Airbus A310 am 12. Juli 2000 am Flughafen Wien-Schwechat, Niederösterreich*. Vienna, Austria, 2006. (GZ. 85.007/0001-FUS/2006)

[Bun11] BUNDESSTELLE FÜR FLUGUNFALLUNTERSUCHUNG: *Status Report - BFU EX010-11*. Braunschweig, Germany, 2011

[Bun12] BUNDESSTELLE FÜR FLUGUNFALLUNTERSUCHUNG: *Bulletin: Unfälle und Störungen beim Betrieb ziviler Luftfahrzeuge, Mai 2012*. Braunschweig, Germany, May 2012

[Bun18] BUNDESSTELLE FÜR FLUGUNFALLUNTERSUCHUNG: *Investigation Report - BFU EX010-11*. Braunschweig, Germany, December 2018

[Bur05] BUREAU D'ENQUÊTES ET D'ANALYSES POUR LA SECURITÉ DE L'AVIATION CIVILE: *Flight Data Recorder Read-Out: Technical and Regulatory Aspects*. Le Bourget, France, May 2005

[Bur16] BUREAU D'ENQUÊTES ET D'ANALYSES POUR LA SECURITÉ DE L'AVIATION CIVILE: *Final Report: Accident on 24 March 2015 at Prads-Haute-Bléone (Alpes-de-Haute-Provence, France) to the Airbus A320-211 registered D-AIPX operated by Germanwings*. Le Bourget, France, March 2016

[Cam17] CAMILLE, Jerome: Runway Overrun Risk. In: *EASA FDM Conference 2017*. Cologne, Germany: European Aviation Safety Agency, 2017

[Civ13] CIVIL AVIATION AUTHORITY: *Flight Data Monitoring: CAP 739*. Ed. 2. West Sussex, United Kingdom, June 2013

[Coc14] COCUZ, Alexander: *Treibstoffmangel im Anflug durch Kapazitätsengpässe*. Garching, Technical University of Munich, Master's Thesis, January 1, 2014

[Com13] COMISION DE INVESTIGACION DE ACCIDENTES E INCIDENTES DE AVIACION CIVIL, CENTRO DE PUBLICACIONES, SECRETARIA GENERAL TECNICA, MINISTERIO DE FOMENTO: *Report IN-010/2010: Incident occured on 14 May 2010, to aircraft Boeing 737-800, registration EI-DYX, operated by Ryanair during approach to Valencia Airport (LEVC), Spain*. Madrid, Spain, June 24, 2013

[Deg16] DEGLMANN, Jen: Cockpit Products Top to Bottom: Maintenance, Repair & Overhaul. In: *MRO-Network.com* (November 3, 2016). http://www.mro-network.com/maintenance-repair-overhaul/cockpit-products-top-bottom, last accessed: July 12, 2018

[Deu09a] DEUTSCHE LUFTHANSA AG: *Operations Manual: Part B: Aeroplane Operating Matters A320 Family*. Frankfurt am Main, Germany, February 23, 2009

[Deu09b] DEUTSCHE LUFTHANSA AG: *Operations Manual: Part B: Aeroplane Operating Matters Airbus A330-A340*. Frankfurt am Main, Germany, March 3, 2009

[Deu13] DEUTSCHE LUFTHANSA AG: *Operations Manual Part A*. Frankfurt am Main, Germany, November 30, 2013

[Deu18a] DEUTSCHE LUFTHANSA AG: *Operations Manual: Part B: Aeroplane Operating Matters A350*. Frankfurt am Main, Germany, August 29, 2018

[Deu18b] DEUTSCHE LUFTHANSA AG: *Geschäftsbericht 2017*. Frankfurt am Main, Germany, March 15, 2018

[DFS18] DFS DEUTSCHE FLUGSICHERUNG GMBH: *Luftfahrthandbuch Deutschland, AIP Germany: AD EDDM 2-5*. AMDT 10/18. Langen, Germany, September 13, 2018

[DH11] DREES, Ludwig; HOLZAPFEL, Florian: Predicting the Occurrence of Incidents Based on Flight Operation Data. In: *AIAA Modeling and Simulation Technologies Conference*. Portland, OR, USA: American Institute of Aeronautics and Astronautics, 2011

[DH12] DREES, Ludwig; HOLZAPFEL, Florian: Determining and Quantifying Hazard Chains and their Contribution to Incident Probabilities in Fight Operation. In: *AIAA Modeling and Simulation Technologies Conference*. Minneapolis, MN, USA: American Institute of Aeronautics and Astronautics, 2012

[DHSH13] DREES, Ludwig; HASELHOFER, Heiko; SEMBIRING, Javensius; HOLZAPFEL, Florian: Modeling the Flare Maneuver Performed by Airline Pilots Using Flight Operation Data. In: *AIAA Modeling and Simulation Technologies Conference*, American Institute of Aeronautics and Astronautics, 2013 (AIAA SciTech Forum)

[DMSM+17] DREES, Ludwig; MÜLLER, Manfred; SCHMIDT-MOLL, Carsten; GONTAR, Patrick; ZWIRGLMAIER, Kilian; WANG, Chong; BENGLER, Klaus; HOLZAPFEL, Florian; STRAUB, Daniel: Risk analysis of the EASA minimum fuel requirements considering the ACARE-defined safety target. In: *Journal of Air Transport Management* 65 (2017), S. 1–10. http://dx.doi.org/10.1016/j.jairtraman.2017.07.003. – DOI 10.1016/j.jairtraman.2017.07.003

[Dre16] DREES, Ludwig: *Predictive Analysis: Quantifying Operational Airline Risks*. München: Verlag Dr. Hut, 2016. – ISBN 978–384392987–5

[DS12] DEGROOT, M. H.; SCHERVISH, M. J.: *Probability and Statistics*. Addison-Wesley, 2012. – ISBN 978–032150046–5

[DSH+14] DREES, Ludwig; SEMBIRING, Javensius; HÖHNDORF, Lukas; WANG, Chong; HOLZAPFEL, Florian: *IATA Safety Report 2013, Section 9: Predictive Analysis*. Montreal, Canada, 2014

[Dub14] DUBOIS, Marc: *Flight Data Analysis*. Lima, 2014

[eas12] EASYJET AIRLINE COMPANY LIMITED: *A319/A320 Flight Crew Operating Manual (FCOM)*. Luton, United Kingdom, August 3, 2012

[Emi13] EMIRATES GROUP: *Emirates Airline Operations Manual Part C*. Dubai, United Arab Emirates, April 4, 2013

[Eng95] ENGINEERING SCIENCES DATA UNIT: *Frictional and Retarding Forces on Aircraft Tyres Part II: Estimation of Braking Force*. June 1995. (ESDU 71026d)

[Eur03] EUROPEAN AVIATION SAFETY AGENCY: *Decision No. 2003/6/RM of the Executive Director of the Agency of 17 October 2003 on certification specification, including airworthiness codes and acceptable means of compliance, for all weather operations (CS-AWO). CS-AWO*. October 17, 2003

[Eur08a] EUROPEAN COMMISSION: *Commission Regulation (EC) No 859/2008 of August 2008 amending Council Regulation (EEC) No 3922/91 as regards common technical requirements and administrative procedures applicable to commercial transportation by aeroplane: EU-OPS*. August 20, 2008

[Eur08b] EUROPEAN COMMISSION: *Regulation (EC) No 1008/2008 of the European Parliament and the Council of 24 September 2008 on common rules for the operation of air services in the Community (Recast): EG 1008/2008*. September 24, 2008

[Eur11a] EUROPEAN COMMISSION: *Flightpath 2050 - Europe's Vision for Aviation: Report of the High Level Group on Aviation Research*. Luxembourg, 2011

[Eur11b] EUROPEAN COMMISSION: *Commission Regulation (EU) No 1178/2011 of November 2011 laying down technical requirements and administrative procedures related to civil aviation aircrew pursuant to Regulation (EC) No 216/2018 of the European Parliament and of the Council*. November 3, 2011

[Eur12] EUROPEAN AVIATION SAFETY AGENCY: *Acceptable Means of Compliance (AMC) and Guidance Material (GM) to Part-ORO*. October 25, 2012

[Eur14] EUROPEAN COMMISSION: *Commission Regulation (EU) No 1321/2014 of November 2014 on the continuing airworthiness of aircraft and aeronautical product, parts and appliances, and on the approval of organizations and personnel involved in these tasks*. November 26, 2014

[Eur17a] EUROPEAN AUTHORITIES COORDINATION GROUP ON FLIGHT DATA MONITORING: *Good Practice on the Oversight of Flight Data Monitoring Programmes*. 2. Cologne, Germany, April 2017

[Eur17b] EUROPEAN AVIATION SAFETY AGENCY: Data4Safety: The European Big Data Programme for Aviation Safety. In: *EASA FDM Conference 2017*. Cologne, Germany: European Aviation Safety Agency, 2017

[Eur18] EUROPEAN AVIATION SAFETY AGENCY: *Certification Specifications and Acceptable Means of Compliance for Large Aeroplanes CS-25: CS-25*. March 27, 2018

[FAA17] FAA AVIATION RULEMAKING ADVISORY COMMITTEE: *Recommendation Report - Rev A*. Version: April 2017. https://www.faa.gov/regulations_policies/rulemaking/committees/documents/media/09%20-%20FTHWG_Final_Report_Phase_2_RevA__Apr_2017.pdf, last accessed: January 16, 2019

[FHK+16] FAHRMEIR, L.; HEUMANN, C.; KÜNSTLER, R.; PIGEOT, I.; TUTZ, G.: *Statistik: Der Weg zur Datenanalyse*. Berlin, Heidelberg, Germany: Springer, 2016 (Springer-Lehrbuch). – ISBN 978–366250372–0

[Flu] FLUGHAFEN MÜNCHEN GMBH: *Verkehrszahlen*. https://www.munich-airport.de/verkehrszahlen-88506, last accessed: January 16, 2018

[Gam10] GAMBINO, Megan; THE SMITHSONIAN INSTITUTION (ed.): *Q and A: Capt. Chesley "Sully" Sullenberger: The pilot of US Airways Flight 1549 talks about that fateful day, being a pilot and his future*. Version: November 2010. https://www.smithsonianmag.com/science-nature/q-and-a-capt-chesley-sully-sullenberger-63542623/, last accessed: July 12, 2018

[Geo96] GEORGE S. FISHMAN: *Monte Carlo: Concepts, Algorithms and Applications*. New York, NY, USA: Springer Verlag, 1996. – ISBN 978–038794527–9

[GPHB15] GONTAR, Patrick; PORSTNER, V.; HOERMANN, H.-J.; BENGLER, Klaus: Pilots' Decision-Making under High Workload: Recognition-Primed or Not – An Engineering Point of View. In: LINDGAARD, G. (ed.); MOORE, D. (ed.): *Proceedings of the 19th Treinnial Congress of the International Ergonomics Association (IEA) 2015*, 2015

[Has70] HASTINGS, W. K.: Monte Carlo sampling methods using Markov chains and their applications. In: *Biometrika* 57 (1970), Nr. 1, S. 97–109. http://dx.doi.org/10.1093/biomet/57.1.97. – DOI 10.1093/biomet/57.1.97

[HCB+17] HÖHNDORF, Lukas; CZADO, Claudia; BIAN, Huanglei; KNEER, Jennifer; HOLZAPFEL, Florian: Statistical Modeling of Dependence Structures of Operational Flight Data Measurements not Fulfilling the I.I.D. Condition. In: *2017 AIAA AVIATION Forum*. Denver, CO, USA: American Institute of Aeronautics and Astronautics, 2017

[Her17] HERREMA, Floris: A Novel Machine Learning Model to Predict Abnormal Runway Occupancy Times and Observe Related Precursors. In: *EASA FDM Conference 2017*. Cologne, Germany: European Aviation Safety Agency, 2017

[HGS12] HASLBECK, A.; GONTAR, Patrick; SCHUBERT, E.: The way pilots handle their control stick - effects shown in a flight simulator study. In: *Proceedings 30th European Annual Conference on Human Decision-Making and Manual Control* Bd. 19, DLR, 2012 (Berichte aus dem DLR-Institut für Verkehrssystemtechnik), S. 21–26

[HHD+15] HÖHNDORF, Lukas; HOLZAPFEL, Florian; DREES, Ludwig; SEMBIRING, Javensius; WANG, Chong; KOPPITZ, Phillip; SCHIELE, Stefan; ZAGLAUER, Christopher: Predictive Flight Data Analysis. In: *3rd Data Science in Aviation Workshop*. Brussels, Belgium: The Innaxis Foundation & Research Institute, 2015

[Hit17] HITZBLECK, Frank: Individual Flight Data Monitoring Report for Flight Crews as Part of a University Study. In: *EASA FDM Conference 2017*. Cologne, Germany: European Aviation Safety Agency, 2017

[Höh14] HÖHNDORF, Lukas: Copulas applied to flight data analysis. In: *11th German Probability and Statistics Days*. Ulm, Germany, 2014

[Höh16] HÖHNDORF, Lukas: Analysis of Operational Flight Data in Hadoop using MapReduce and the MATLAB Distributed Computing Server (MDCS). In: *MATLAB Expo 2016*. Munich, Germany: The MathWorks, Inc., 2016

[Höh17] HÖHNDORF, Lukas: Trajectory and Attitude Reconstruction within AGS. In: *10th Safran FDM Users Conference*, SAFRAN Sagem, 2017

[Hra14] HRADECKY, Simon: *Accident: ANA B788 near Takamatsu on Jan 16th 2013, battery problem and burning smell on board (including JAL Boston, Ethiopian London and JAL Tokyo events)*. Version: September 25, 2014. http://avherald.com/h?article=45c377c5&opt=0, last accessed: July 31, 2018

[HS17] HÖHNDORF, Lukas; SEMBIRING, Javensius: *FDR Raw Data: Why Binary Data and How to Decode it?* Version: July 20, 2017. http://innaxis.org/fdm-raw-data-why-binary-data-and-how-to-decode-it/, last accessed: July 11, 2018

[HSGB12] HASLBECK, A.; SCHUBERT, E.; GONTAR, Patrick; BENGLER, Klaus: The relationship between pilots' manual flying skills and their visual behavior: a flight simulator study using eye tracking. In: LAUNDRY, S. (ed.); SALVENDY, G. (ed.); KARWOWSKI, Waldemar (ed.): *Advances in Human Aspects of Aviation*, CRC Press, 2012 (Advances in Human Factors and Ergonomics). – ISBN 978–143987116–4, S. 561–568

[HSH14] HÖHNDORF, Lukas; SEMBIRING, Javensius; HOLZAPFEL, Florian: Copulas applied to Flight Data Analysis. In: *Probabilistic Safety Assessment and Management (PSAM)*. Honolulu, HI, USA, 2014

[HWK+18] HÖHNDORF, Lukas; WANG, Chong; KOPPITZ, Phillip; WEISS, Sebastian; OLMOS, Sergio; CZADO, Claudia; HOLZAPFEL, Florian: Integration of Vine Copula Dependence Structures into Subset Simulation for Accident Probability Quantifications. In: *31st Congress of the International Council of the Aeronautical Sciences (ICAS)*. Belo Horizonte, Brazil: International Council of the Aeronautical Sciences, 2018

[Int05] INTERNATIONAL CIVIL AVIATION ORGANIZATION: *Aerodrome Design Manual - Doc 9157*. Fourth Edition. 2005

[Int06] INTERNATIONAL CIVIL AVIATION ORGANIZATION: *Annex 10 to the Convention on International Civil Aviation, Volume I, Radio Navigation Aids*. Montreal, Canada, July 2006. (Sixth Edition)

[Int13] INTERNATIONAL CIVIL AVIATION ORGANIZATION: *Safety Management Manual - Doc 9859: SMM*. 2013

[Int15] INTERNATIONAL CIVIL AVIATION ORGANIZATION: *Manual of Aircraft Accident and Incident Investigation - Doc 9756*. 2015

[Int16] INTERNATIONAL CIVIL AVIATION ORGANIZATION: *Annex 13 to the Convention on International Civil Aviation - Aircraft Accident and Incident Investigation*. Montreal, Canada, July 2016. (Eleventh Edition)

[Int17] INTERNATIONAL AIR TRANSPORT ASSOCIATION: *IATA Safety Report 2017*. Montreal, Canada, April 2017

[Int18] INTERNATIONAL AIR TRANSPORT ASSOCIATION: *Flight Data Connect: World leading flight data analysis service*. August 2018

[JHZ17] JIANG, Shui-Hua; HUANG, Jinson; ZHOU, Chuang-Bing: Efficient system reliability analysis of rock slopes based on Subset simulation. In: *Computers and Geotechnics* 82 (2017), S. 31–42. http://dx.doi.org/10.1016/j.compgeo.2016.09.009. – DOI 10.1016/j.compgeo.2016.09.009. – ISSN 0266–352X

[KHK15] KLÜPPELBERG, C.; HAUG, S.; KUHN, G.: Copula structure analysis based on extreme dependence. In: *Statistics and its Interface* 8 (2015), Nr. 1, S. 93–107

[KKC18] KILLICHES, Matthias; KRAUS, Daniel; CZADO, Claudia: Model distances for vine copulas in high dimensions. In: *Statistics and Computing* 28 (2018), Nr. 2, S. 323–341

[Kop17] KOPPITZ, Phillip: Comparing Fuel Flow using a Cluster Method. In: *EASA FDM Conference 2017*. Cologne, Germany: European Aviation Safety Agency, 2017

[KSH16] KOPPITZ, Phillip; SAUTERLEUTE, Daniel; HOLZAPFEL, Florian: Cluster Analysis of Fuel Flow in Operational Flight Data. In: *16th AIAA Aviation Technology, Integration, and Operations Conference*. Washington, DC, USA: American Institute of Aeronautics and Astronautics, 2016 (AIAA AVIATION Forum)

[KSR+18] KOPPITZ, Phillip; SIEGEL, Joachim; ROMANOW, Nikolaus; HÖHNDORF, Lukas; HOLZAPFEL, Florian: Touchdown Point Detection for Operational Flight Data using Quality Measures and a Model Based Approach. In: *2018 AIAA Atmospheric Flight Mechanics Conference*. Kissimmee, FL, USA, 2018 (AIAA SciTech Forum)

[KT16] KHAN, Lutfor R.; TEE, Kong F.: Risk-Cost Optimization of Buried Pipelines Using Subset Simulation. In: *Journal of Infrastructure Systems* 22 (2016), Nr. 2, S. 4016001. http://dx.doi.org/10.1061/(ASCE)IS.1943-555X.0000287. – DOI 10.1061/(ASCE)IS.1943–555X.0000287

[KWH+19] KOPPITZ, Phillip; WANG, Chong; HÖHNDORF, Lukas; SEMBIRING, Javensius; WANG, Xiaolong; HOLZAPFEL, Florian: From Raw Operational Flight Data to Incident Probabilities using Subset Simulation and a Complex Thrust Model. Version: 2019. http://dx.doi.org/10.2514/6.2019-2233. In: *AIAA SciTech 2019 Forum*. San Diego, CA, USA: American Institute of Aeronautics and Astronautics, 2019. – DOI 10.2514/6.2019–2233

[LCM+17] LLOBET LOPEZ, Marta; CARBO, Laura; METGE, Sylvain; BIEBER, Pierre; WANG, Chong; SCHMIDT-MOLL, Carsten; KAAKAI, Fateh; PLE, Julien; MOREL, Marion; VAN BIRGELEN, Tom; VERSTRAETEN, Joram; FUTURE SKY SAFETY (ed.): *Risk Assessment Models: Deliverable D4.4 Future Sky Safety*. September 20, 2017

[LH15] LÖBL, David; HOLZAPFEL, Florian: Subset Simulation for Estimating Small Failure Probabilities of an Aerial System Subject to Atmospheric Turbulences. In: *AIAA Atmospheric Flight Mechanics Conference*. Kissimmee, FL, USA: American Institute of Aeronautics and Astronautics, 2015 (AIAA SciTech Forum)

[LH17] LOW, Ying M.; HUANG, Xiaoxu: Long-term extreme response analysis of offshore structures by combining importance sampling with subset simulation. In: *Structural Safety* 69 (2017), S. 79–95. http://dx.doi.org/10.1016/j.strusafe.2017.08.001. – DOI 10.1016/j.strusafe.2017.08.001. – ISSN 0167–4730

[Luf] LUFTHANSA TECHNIK AG: *Haifisch lernt fliegen: Forschungsprojekt FAMOS: System zum Aufbringen von Haifischhautstruktur*. https://www.lufthansa-technik.com/de/famos, last accessed: July 12, 2018

[Luf14] LUFTHANSA CITYLINE GMBH: *Operations Manual Part A*. Munich, Germany, May 23, 2014

[Luf17] LUFTHANSA TECHNIK AG: *Lufthansa Technik präsentiert AVIATAR: Erste Innovation des neu geschaffenen Geschäftsbereichs*. Version: April 24, 2017. https://www.lufthansa-technik.com/de/press-releases-content/-/asset_publisher/9Mf5/content/press-release-aviatar/10165, last accessed: July 16, 2018

[LZK18] LI, Yuyin; ZHANG, Yahui; KENNEDY, David: Reliability analysis of subsea pipelines under spatially varying ground motions by using subset simulation. In: *Reliability Engineering & System Safety* 172 (2018), S. 74–83. http://dx.doi.org/10.1016/j.ress.2017.12.006. – DOI 10.1016/j.ress.2017.12.006. – ISSN 0951–8320

[Mai94] MAIN COMMISSION AIRCRAFT ACCIDENT INVESTIGATION WARSAW: *Report on the Accident to Airbus A320-211 Aircraft in Warsaw: On September 14, 1993*. Version: March 1994. http://www.rvs.uni-bielefeld.de/publications/Incidents/DOCS/ComAndRep/Warsaw/warsaw-report.html, last accessed: July 17, 2018

[Men14] MENSEN, H.: *Moderne Flugsicherung: Organisation, Verfahren, Technik*. Springer Berlin Heidelberg, 2014 (VDI-Buch). – ISBN 978–364254294–7

[MK16] MORELLI, E. A.; KLEIN, V.: *Aircraft System Identification: Theory and Practice*. Second Edition. Sunflyte Enterprises, 2016. – ISBN

978–099743061–5

[MMAR16] MISHRA, Chinmaya; MASKELL, Simon; AU, Siu-Kui; RALPH, Jason F.: Efficient estimation of probability of conflict between air traffic using Subset Simulation. In: *CoRR* abs/1604.07363 (2016)

[Moh16] MOHR, Nils: *Flight Data Decoding used for Generating En-Route Information based on Binary Quick Access Recorder Data*. Garching, Technical University of Munich, Master's Thesis, January 7, 2016

[Mor17] MORIOKA, HIDEO: Furikaeri - Looking Back to One's Behavior. In: *EASA FDM Conference 2017*. Cologne, Germany: European Aviation Safety Agency, 2017

[MRR+] METROPOLIS, Nicholas; ROSENBLUTH, Arianna W.; ROSENBLUTH, Marshall N.; TELLER, Augusta H.; TELLER, Edward: Equation for State Calculations by Fast Computing Machines. In: *The Journal of Chemical Physics* Bd. 21-6. Melville, NY, USA: American Institute of Physics (AIP), S. 1087–1092

[Mül16] MÜLLER, Manfred: Quantitative Risk Management. In: *7th International Conference on Research in Air Transportation*. Philadelphia, PA, USA, 2016

[Nat08] NATIONAL COORDINATION OFFICE FOR SPACE-BASED POSITIONING, NAVIGATION, AND TIMING: *Global Positioning System Standard Positioning Service Performance Standard*. September 2008

[Oeh17] OEHLING, Julian: Machine Learning in FDM: Extracting new safety knowledge from FDM. In: *EASA FDM Conference 2017*. Cologne, Germany: European Aviation Safety Agency, 2017

[PA15] PATELLI, Edoardo; AU, Siu-Kui: Efficient Monte Carlo algorithm for rare failure event simulation. Version: 2015. http://dx.doi.org/10.14288/1.0076089. In: *International Conference on Applications of Statistics and Probability in Civil Engineering (ICASP)*. 2015. – DOI 10.14288/1.0076089

[Pac12] PACEJKA, Hans B. (ed.): *Tire and Vehicle Dynamics (Third Edition)*. Third Edition. Oxford: Butterworth-Heinemann, 2012. – ISBN 978–008097016–5

[PBZS15] PAPAIOANNOU, Iason; BETZ, Wolfgang; ZWIRGLMAIER, Kilian; STRAUB, Daniel: MCMC algorithms for Subset Simulation. In: *Probabilistic Engineering Mechanics* 41 (2015), S. 89–103. http://dx.doi.org/10.1016/j.probengmech.2015.06.006. – DOI 10.1016/j.probengmech.2015.06.006. – ISSN 0266–8920

[PHD+09] PAPAIOANNOU, Iason; HEIDKAMP, H.; DÜSTER, Alexander; KOLLMANNSBERGER, Stefan; RANK, Ernst; KATZ, Casimir: The subset simulation applied to the reliability analysis of a nonlinear geotechnical finite element model. In: *Proceedings of the 7th International Probabilistic Workshop*. 2009

[QJ17] QUIELLO, Michael; JANGELIS, Steve: Aviation Safety Information Analysis and Sharing (ASIAS). In: *EASA FDM Conference 2017*. Cologne, Germany: European Aviation Safety Agency, 2017

[Rap09] RAPS, Jürgen: *Sicherheit muss jeden Tag neu produziert werden: Risk Management bei Lufthansa*. Version: September 24, 2009. www.luftfahrt-presse-club.de/files/lufthansa_vortrag_sicherheitskultur.ppt, last accessed: July 3, 2018

[Rea00] REASON, James: Human error: models and management. In: *BMJ* 320 (2000), Nr. 7237, S. 768–770. http://dx.doi.org/10.1136/bmj.320.7237.768. – DOI 10.1136/bmj.320.7237.768. – ISSN 0959–8138

[Reu09] REUSCHENBACH, Daniel: Nichtparametrische Testverfahren. Version: 2009. http://dx.doi.org/10.1007/978-3-322-96406-9{_}32. In: ALBERS, Sönke (ed.); KLAPPER, Daniel (ed.); KONRADT, Udo (ed.); WALTER, Achim (ed.); WOLF, Joachim (ed.): *Methodik der empirischen Forschung*. Wiesbaden: Gabler Verlag, 2009. – DOI 10.1007/978–3–322–96406–9_32. – ISBN 978–332296406–9, S. 501–520

[RK17] RUBINSTEIN, Reuven Y.; KROESE, Dirk P.: *Simulation and the Monte Carlo Method*. 3. John Wiley & Sons, Inc., 2017. – ISBN 978–111863216–1

[Roc17] ROCKWELL COLLINS INC.: *Airbus selects Rockwell Collins for FOMAX program to digitally connect A320 aircraft and operators*. Version: June 21, 2017. https://www.rockwellcollins.com/Data/News/2017-Cal-Yr/CS/20170621-FOMAX.aspx, last accessed: July 22, 2018

[RvS+08] ROELEN, A.L.C.; VAN DOORN, B. A.; SMELTINK, J. W.; VERBEEK, M. J.; WEVER, Rombout: *Quantification of Event Sequence Diagrams for a Causal Risk Model of Commercial Air Transport*. October 2008

[Sch15] SCHNEIDER, Kate: Flying into failure: Airlines that no longer exist. In: *News Pty Limited* (March 16, 2015). https://www.news.com.au/travel/travel-updates/flying-into-failure-airlines-that-no-longer-exist/

news-story/c71c826106c228d56e32a631732cac96, last accessed: January 10, 2019

[SDH13] SEMBIRING, Javensius; DREES, Ludwig; HOLZAPFEL, Florian: Extracting Unmeasured Parameters Based on Quick Access Recorder Data Using Parameter-Estimation Method. In: *AIAA Atmospheric Flight Mechanics Conference*. Boston, MA, USA: American Institute of Aeronautics and Astronautics, 2013

[SH17] SEIFERTH, David; HELLER, Matthias: Testing and performance enhancement of a model-based designed ground controller for a diamond-shaped unmanned air vehicle (UAV). In: *IEEE Conference on Control Technology and Applications (CCTA)*. Kohala Coast, HI, USA, 2017, S. 1988–1994

[SHH14] SEMBIRING, Javensius; HÖHNDORF, Lukas; HOLZAPFEL, Florian: Bayesian Approach Implementation on Quick Access Recorder Data for Estimating Parameters and Model Validation. In: *Probabilistic Safety Assessment and Management (PSAM)*. Honolulu, HI, USA, 2014

[SHH18] SEIFERTH, David; HELLER, Matthias; HOLZAPFEL, Florian: Automatic Safe Area Detection for novel Unmanned Air Vehicle. In: *4th International Conference on Control, Automation and Robotics (ICCAR)*. Auckland, New Zealand: Institute of Electrical and Electronics Engineers (IEEE), 2018

[SKHH18] SEIFERTH, David; KÜGLER, Martin E.; HELLER, Matthias; HOLZAPFEL, Florian: In-Flight Verification of a model-based designed Ground Controller for an innovative Unmanned Air Vehicle (UAV). In: *2018 AIAA Flight Testing Conference*. Dallas, TX, USA, 2018 (AIAA AVIATION Forum)

[Soc96] SOCIETY OF AUTOMOTIVE ENGINEERS (SAE) INTERNATIONAL: *ARP4761: Guidelines and Methods for Conducting the Safety Assessment Process on Civil Airborne Systems and Equipment*. Rev. A. Warrendale, PA, USA, December 1996. (ARP4761)

[Soc12] SOCIETY OF AUTOMOTIVE ENGINEERS (SAE) INTERNATIONAL: *ARP4754: Guidelines for Development of Civil Aircraft Systems*. Rev. A. Warrendale, PA, USA, December 2012. (ARP4754)

[Sor18] SORIANO TORRES, Juan: *Optimization of the Maintenance Program of an Airline by Means of Reliability Engineering / Optimierung des Wartungsprogramms einer Fluggesellschaft mittels*

Zuverlässigkeitsmodellierung. Garching, Technical University of Munich, Master's Thesis, May 17, 2018

[Sri14] SRINIVASAN, R.: *Importance Sampling*. Berlin, Germany: Springer, 2014. – ISBN 978–366205053–8

[Str17] STRASSL, Florian: *Auswirkung von Bahnschließungen am einem Drehkreuzflughafen*. Garching, Technical University of Munich, Bachelor's Thesis, October 2, 2017

[The09] THE BOEING COMPANY: *Boeing 737-804/-8K5 Flight Crew Operations Manual (FCOM): Thomson Airways*. Seattle, WA, March 27, 2009

[Tra05] TRANSPORTATION SAFETY BOARD OF CANADA: *Aviation Ingestigation Report: Runway Overrun and Fire: Air France, Airbus A340-313 F-GLZQ, Toronto/Lester B. Pearson Internationa Airport, Ontario, 2 August 2005*. August 2, 2005. (A05H002)

[van17a] VAN DER GEEST, Peter: Reconstruction fo Cross- and Tailwind Components from Flight Data. In: *EASA FDM Conference 2017*. Cologne, Germany: European Aviation Safety Agency, 2017

[van17b] VAN ES, Gerard: Braking Capabilities on Flooded Runways: Flight Test Results Obtained with a Business Jet. Version: 2017. http://dx.doi.org/10.2514/6.2017-3651. In: *AIAA Flight Testing Conference*. Denver, CO, USA: American Institute of Aeronautics and Astronautics, 2017 (AIAA AVIATION Forum). – DOI 10.2514/6.2017–3651

[VvW] VERSTRAETEN, Joram; VAN BAREN, Gerben; WEVER, Rombout: The Risk Observatory: Developing an Aviation Safety information Sharing Platform in Europe. http://dx.doi.org/10.5296/jss.v2i2.10443. In: *Journal of Safety Studies*. Las Vegas, NV, USA: Macrothink Institute. – DOI 10.5296/jss.v2i2.10443

[vWC] VAN EEKEREN, Rob; WRIGHT, Stephen; COKORILO, Olja: Early Cost Safety Analysis of Runway Events. http://dx.doi.org/10.7708/ijtte.2018.8(3).01. In: *International Journal for Traffic and Transport Engineering* Bd. 2018, 8(3). Belgrade, Serbia, . – DOI 10.7708/ijtte.2018.8(3).01, S. 261–270

[vWVv16] VAN BAREN, Gerben; WEVER, Rombout; VERSTRAETEN, Joram; VAN MILTENBURG, Maykel: *Risk Observatory Design and Early Prototype*. Version: June 28, 2016.

https://www.futuresky-safety.eu/wp-content/uploads/2016/08/FSS_P4_NLR_D4.2_v2.0-1.pdf, last accessed: July 10, 2018

[Wan00] WANG, Ximing: *Fortschritt-Berichte VDI. Reihe 12, Verkehrstechnik /Fahrzeugtechnik, 0178-9449*. Bd. Nr. 445: *Ein Beitrag zur Entwicklung semiaktiver Flugzeugfahrwerksysteme*. Düsseldorf: VDI Verlag, 2000. – ISBN 978–318344512–7

[WDG+14] WANG, Chong; DREES, Ludwig; GISSIBL, Nadine; HÖHNDORF, Lukas; SEMBIRING, Javensius; HOLZAPFEL, Florian: Quantification of Incident Probabilities Using Physical and Statistical Approaches. In: *6th International Conference on Research in Air Transportation*. Istanbul, Turkey, 2014

[WDH14] WANG, Chong; DREES, Ludwig; HOLZAPFEL, Florian: Incident Prediction using Subset Simulation. In: *29th Congress of International Council of the Aeronautical Sciences (ICAS)*. St. Petersburg, Russia: International Council of the Aeronautical Sciences, 2014

[WDH16a] WANG, Chong; DREES, Ludwig; HOLZAPFEL, Florian: Extracting measurements from operational flight data using the flare example. Version: 2016. http://dx.doi.org/10.2514/6.2016-0175. In: *AIAA Modeling and Simulation Technologies Conference*. San Diego, CA, USA: American Institute of Aeronautics and Astronautics, 2016 (AIAA SciTech Forum). – DOI 10.2514/6.2016–0175

[WDH16b] WANG, Chong; DREES, Ludwig; HOLZAPFEL, Florian: Fuel Starvation Caused by Hub Closure. In: *30th International Congress of the International Council of the Aeronautical Sciences (ICAS)*. Daejeon, Korea: International Council of the Aeronautical Sciences, 2016

[WF12] WENDT, Michael; FABREGAS, Pere: Characterization of Deep and Long Landings and of the Runway Excursion Risk. In: *EOFDM Conference 2012*. Cologne, Germany: European Aviation Safety Agency, 2012

[WH18a] WANG, Chong; HOLZAPFEL, Florian: Evaluation of Aircraft Braking Performance Based on Operational Flight Data. In: *31st Congress of the International Council of the Aeronautical Sciences (ICAS)*. Belo Horizonte, Brazil: International Council of the Aeronautical Sciences, 2018

[WH18b] WANG, Chong; HOLZAPFEL, Florian: Modeling of the Aircraft Landing Behavior for Runway Excursion and Abnormal Runway Contact Analysis. Version: 2018. http://dx.doi.org/10.2514/6.2018-1166. In: *2018 AIAA*

Modeling and Simulation Technologies Conference. Kissimmee, FL, USA: American Institute of Aeronautics and Astronautics, 2018 (AIAA SciTech Forum). – DOI 10.2514/6.2018–1166

[WMH16] WANG, Chong; MOHR, Nils; HOLZAPFEL, Florian: Decoding of Binary Flight Data in ARINC 717 Format. In: *1st International Conference in Aerospace For Young Scientists (ICAYS)*. Beijing, China: Beihang University, 2016

[WMH18] WANG, Chong; METGE, Sylvain; HOLZAPFEL, Florian: Quantification of Accident Probabilities for a Risk Observatory. Version: 2018. http://dx.doi.org/10.5281/zenodo.1484912. In: *7th Transport Research Arena*. Vienna, Austria, 2018. – DOI 10.5281/zenodo.1484912

[WSK+19] WANG, Xiaolong; SEMBIRING, Javensius; KOPPITZ, Phillip; HÖHNDORF, Lukas; WANG, Chong; HOLZAPFEL, Florian: Modeling of the Aircraft's Low Energy State During the Final Approach Phase Using Operational Flight Data. Version: 2019. http://dx.doi.org/10.2514/6.2019-0989. In: *AIAA SciTech 2019 Forum*. San Diego, CA, USA: American Institute of Aeronautics and Astronautics, 2019. – DOI 10.2514/6.2019–0989

[ZBAK12] ZUEV, Konstantin M.; BECK, James L.; AU, Siu-Kui; KATAFYGIOTIS, Lambros S.: Bayesian post-processor and other enhancements of Subset Simulation for estimating failure probabilities in high dimensions. In: *Computers & Structures* 92-93 (2012), S. 283–296. http://dx.doi.org/10.1016/j.compstruc.2011.10.017. – DOI 10.1016/j.compstruc.2011.10.017. – ISSN 0045–7949